Physics of Atomic Nuclei, Vol. 68, No. 8, 2005, pp. 1263–1264. Translated from Yadernaya Fizika, Vol. 68, No. 8, 2005, pp. 1315–1317.

TRIBUTE TO THE 90th BIRTHDAY OF V.V. VLADIMIRSKY

V. V. Vladimirsky and Charged-Particle Accelerators

D. G. Koshkarev*

Institute of Theoretical and Experimental Physics, Bol'shaya Cheremushkinskaya ul. 25, Moscow, 117259 Russia

Received February 28, 2005

Abstract—The main advances made in the field of accelerator science and technology at the Institute of Theoretical and Experimental Physics (ITEP, Moscow) within the ten years between 1953 and 1963 under the supervision of V.V. Vladimirsky and with his participation are described. © *2005 Pleiades Publishing, Inc.*

The proposal of E. Courant, M. Livingston, and H. Snyder (1952) that concerned the creation of strongly focusing accelerators changed radically the situation around the construction of high-energy accelerators and, hence, in high-energy physics. However, this proposal was perceived rather ambiguously in the Soviet Union. Some of the renowned authorities on accelerator physics called attention to extraordinarily stringent tolerances on magnetic elements in these accelerators and, in view of this, denied the possibility of implementing this project in practice. Under these circumstances, V.V. Vladimirsky demonstrated great scientific perspicacity and considerable courage when, contrary to the authorities' opinion, he argued that the required tolerances, albeit stringent, are quite attainable technologically. At the same time, the "nothing for nothing" principle suggested that this project is in line with technical progress; therefore, it should be started despite technological difficulties and prepared for a practical implementation in the future. It was just due to Vladimirsky's scientific intuition that the official leaders of our branch of industry decided to charge the staff of the Thermotechnical Laboratory [presently, the Institute of Theoretical and Experimental Physics (ITEP, Moscow)] with starting the development of a new generation of strongly focusing accelerators under Vladimirsky's supervision.

Even the first analysis of the situation indicated at least four problems peculiar to strongly focusing systems. First, there was the problem of a critical energy that, if attained, impaired the stability of longitudinal oscillations of accelerated protons. The remaining problems were associated with a greatly diminished transverse size of the magnetic elements and the vacuum chamber of the accelerator. This called for completely changing the design of the accelerator vacuum chamber, strengthening tolerances on a residual vacuum in it, and imposing more stringent requirements on the nonlinear components of the magnetic field. In order to solve these and other problems, Vladimirsky was able to organize a small group of researchers at ITEP within a short period of time, which included L.L. Gol'din, D.G. Koshkarev, Yu.F. Orlov, and E.K. Tarasov as the main participants; I.M. Kapchinsky joined the group later. They solved these problems successfully, and this permitted preparing physics projects of strongly focusing proton synchrotrons in the shortest possible time.

Koshkarev could understand the essence of the problem that arose upon reaching the critical energy, but the technological realization of this transition above it was dubious because of the underdevelopment of radioelectronics at that time. Vladimirsky, together with Tarasov, proposed a more reliable version where was no critical energy at all—more precisely, where it was pushed to the energy region unattainable at a particular accelerator. Unfortunately, the proposed decision led to some complication of the design of the accelerator magnetic system and to an increase in the accelerator perimeter. Nevertheless, this suggestion played a positive role, having confirmed the efficiency of employing strong focusing in circular accelerators.

The theory of nonlinear oscillations of protons in strongly focusing accelerators was developed by Orlov. This theory made it possible to determine the tolerances on the nonlinear components of the magnetic field in the operating area of the accelerator vacuum chamber. The effect of a residual vacuum on the dynamics of accelerated ions was studied by Gol'din and Koshkarev, whose results enabled them to determine an allowed value of the residual-gas pressure in the vacuum chamber of a strongly focusing accelerator.

Projects of two strongly focusing proton synchrotrons, which were the largest at that time, were prepared on the basis of the studies performed under

* e-mail: koshkarev@itep.ru

the supervision of Vladimirsky. The first project of a 7-GeV accelerator (U-7) was successfully commissioned at ITEP within the shortest period in 1961. In 1967, a 70-GeV proton accelerator constructed in accordance with the second of these projects (it was the greatest accelerator at that time) was put into operation at the Institute for High Energy Physics, which was organized on the basis of this accelerator near Serpukhov in Protvino, Moscow region, in 1964.

Injectors were needed for the circular accelerators under development, but only electrostatic generators could be used for that purpose at that time, their energy not exceeding 5 MeV. This energy was barely sufficient for injection into U-7, but it was absolutely inadequate for a more sizable accelerator. Under these circumstances, Vladimirsky made the only possible decision to construct U-7 with an 5-MeV electrostatic generator as an injector and to initiate, at the same time, the development of two new injectors—specifically, 25- and 100-MeV linear proton accelerators for the U-7 and U-70 facilities, respectively. Vladimirsky invited Kapchinsky, whom he knew well since their cooperation in the field of radiolocation, to develop the projects of these strongly focusing linear proton accelerators.

Since the advent of the strong focusing principle, Vladimirsky realized that this principle can be of advantage not only in circular accelerators but also in channels for ion-beam transportation in linear accelerators. However, major difficulties were associated with the use of magnetic quadrupole lenses in the initial segment of a linear proton accelerator, where the speed of accelerated particles is considerably below the speed of light; in some cases, their use even appeared to be impossible. A solution to this problem via magnetic quadrupoles by electrostatic ones was rejected, since the introduction of electrostatic quadrupoles in the vacuum system would complicate the accelerator design and reduce the reliability of its operation. There remained only one way out—that which consisted in changing the design of the accelerating elements in such a way that the high-frequency field would generate a quadrupole focusing component, along with a dipole accelerating component. Vladimirsky was the first to find a rather simple solution to this problem—he proposed using "horn" electrodes. Later, V.A. Teplyakov independently arrived at the same solution. Kapchinsky found another solution, suggesting to change the structure of the accelerating system radically in such a way that the focusing quadrupole field would be the main excited component of the high-frequency field in it, in which case only due to a violation of quadrupole symmetry would the focusing quadrupole field generate a dipole component needed for proton acceleration. Both these suggestions are widely used in practice now, although Kapchinsky's solution is applied more frequently.

For their outstanding contribution to the practice of linear-accelerator construction, the authors of these innovations received, in 1968, inventor's certificate and, in 1991, a diploma for their discovery of a new phenomenon of the focusing of charged-particle beams in a varying electric field that is uniform along the beam axis. This research work was subsequently awarded a Lenin prize.

In developing contemporary accelerators, the intensity of the accelerated beam and its luminosity, which characterize the possibility of producing ion beams of high electric-charge density, are the most important parameters along with the ion energy. In order to find out which accelerator parameters determine the intensity and the luminosity of accelerated ion beams, one needed a theory that would correctly describe the dynamics of ion beams with allowance for the effect of the electromagnetic fields of accelerated ions. Such a theory was developed by Kapchinsky and Vladimirsky. The results of that study were first presented at the conference on charged-particle accelerators in Geneva in 1959. The main result known as the KV equation has been extensively applied both in theory and in the calculations of the dynamics of intense ion beams in accelerators and charged-particle storage rings. Later, the main ideas of that study were developed in many investigations, but, undeniably, the priority belongs to the discoverers, Kapchinsky and Vladimirsky.

The report of Vladimirsky at the International Conference on Charged-Particle Accelerators in Dubna in 1963 appeared to be his last research work in the field of accelerators. In his report, Vladimirsky demonstrated that U-70, which was then under construction near Serpukhov, could serve as an appropriate basis for developing, in the Soviet Union, the next generation of giant accelerators for the energy region around 1 TeV.

Vladimirsky's disciples and colleagues regretted deeply that he stopped his active research in the field of charged particle accelerators after 1963, concentrating his main efforts on studies in the realms of elementary-particle physics, nuclear-force physics, and nuclear reactors.

Vladimirsky's achievements in developing the complex of contemporary accelerator facilities in the Soviet Union were highly appreciated by the scientific community and the government. Vladimirsky was elected a corresponding member of the USSR Academy of Sciences after the commissioning of U-7 in 1961; in 1970, he was awarded a Lenin prize for his participation in the construction of the 70-GeV proton synchrotron, the greatest facility in the world at that time.

Translated by E. Kozlovsky

Physics of Atomic Nuclei, Vol. 68, No. 8, 2005, pp. 1265–1270. Translated from Yadernaya Fizika, Vol. 68, No. 8, 2005, pp. 1318–1323.

TRIBUTE TO THE 90th BIRTHDAY OF V.V. VLADIMIRSKY

Influence of Irradiation Conditions on the Retention of Hydrogen Isotopes in Structural Materials

A. G. Zaluzhnyi, V. P. Kopytin, M. A. Kozodaev, and A. L. Suvorov[†]

Institute of Theoretical and Experimental Physics, Bol'shaya Cheremushkinskaya ul. 25, Moscow, 117259 Russia

Received October 26, 2004; in final form, March 17, 2005

Abstract—The influence of irradiation conditions on the retention of hydrogen isotopes in structural materials (austenitic steel) under heating is considered. The specimens under study were irradiated either in a reactor or by bombarding them with hydrogen-isotope ions of variable fluence and energy at accelerators. An investigation of irradiated specimens with an EM-300 transition electron microscope was accompanied by studying the kinetics of hydrogen release from samples with a high-vacuum mass spectrometer. Also, the kinetics of hydrogen-isotope release from specimens of structural materials treated with a deuterium plasma was studied. It was found that, under the effect of irradiation, the materials being studied develop radiation defects, which appear to be efficient traps for hydrogen atoms, retaining them up to rather high temperatures (650 K). It is also shown that blisters formed in the materials treated with a hydrogen plasma contain both molecular hydrogen and hydrocarbons—in particular, methane.

1. INTRODUCTION

In connection with the problem of creating materials for the first wall of thermonuclear reactors, it is of paramount importance to study processes of hydrogen-isotope retention in them. This in turn is associated with possible losses of expensive fuel (tritium) and with the problems of safe reactor operation.

In the present study, we explore the influence of irradiation on hydrogen-isotope retention in austenitic-steel samples under heating. Specimens of the materials being studied were irradiated either in a reactor or by bombarding them with hydrogen-isotope ions of variable energy and fluence at accelerators. We also study the kinetics of hydrogen-isotope release from specimens treated with a deuterium plasma.

2. EXPERIMENTAL PROCEDURE

The kinetics of hydrogen-isotope release from austenitic-steel specimens was studied by using a high-vacuum mass spectrometer whose operational concept was described in [1]. The specimens under study were heated at a constant rate of 10 K/min within the temperature range 300–1300 K, the hydrogen evacuation rate being 4.8 ± 0.5 l/s. The specimens were prepared in the form of foils 200 μm thick. The foil surface was cleaned with CCl_4 before the experiments. The electron-microscopic studies of the specimens were performed with an EM-300 transition electron microscope [2].

3. EXPERIMENTAL RESULTS

Figure 1 shows a typical kinetic dependence of hydrogen release from specimens of 0X16H15M3B austenitic steel that were irradiated in the 18-keV H_2^+-ion beam up to a fluence of 1×10^{18} ions/cm^2 at an ILU-100 magnetic mass-separating facility. In this case, the hydrogen-ion free path in the material being studied was about 0.1 μm. There are two peaks at about 420 and 570 K in Fig. 1.

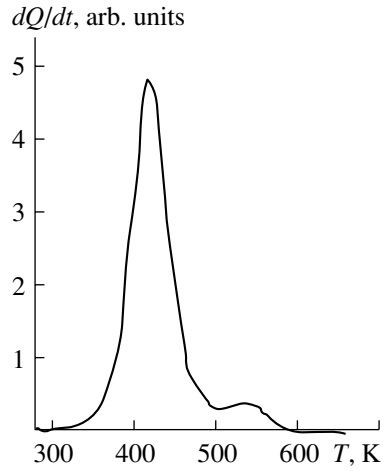

Fig. 1. Curve of hydrogen thermal desorption from specimens of 0X16H15M3B steel that were irradiated up to a fluence of 10^{18} ions/cm^2 with a 18-keV hydrogen-ion beam at an accelerator. The curve was obtained under conditions of uniform heating.

[†] Deceased.

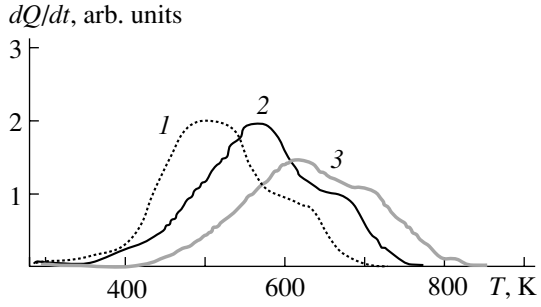

Fig. 2. Deuterium-thermal-desorption curves obtained under a uniform heating of specimens of 0X16H15M3B steel that were irradiated up to a fluence of 10^{18} ions/cm^2 with a 3-MeV deuterium-ion beam: (*1*) calculated curve and (*2, 3*) results obtained, respectively, 1.5 and 9 months after irradiation.

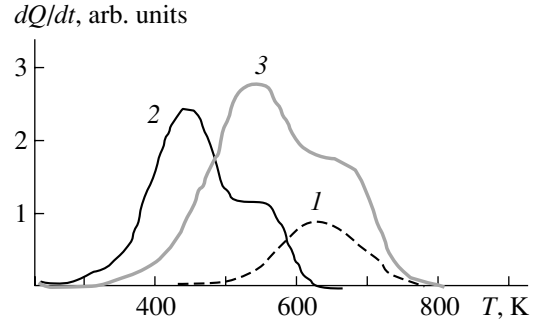

Fig. 3. Hydrogen-thermal-desorption curves obtained under a linear heating at rate of 0.15-K/s for (*1*) a specimen irradiated with neutrons, (*2*) an unactivated specimen that is saturated electrolytically with hydrogen, and (*3*) a specimen irradiated with neutrons and additionally saturated electrolytically with hydrogen.

Figure 2 displays a typical kinetic dependence of deuterium release from specimens of 0X16H15M3B austenitic steel that were held at room temperature for 1.5 and 9 months after irradiation with 3-MeV deuterium ions at fluences up to 1×10^{18} ions/cm^2. Just as in Fig. 1, the curves in Fig. 2 exhibit two peaks within the temperature range 550–700 K. In this case, the particle free path was about 20 μm. Irradiation was performed at an electrostatic accelerator by using a well-known procedure that guaranteed the reliable cooling of the specimens to 373 K for ion-current densities of $(3–5) \times 10^{-2}$ A/m^2 [3] up to fluences of $10^{16}–10^{18}$ ions/cm^2. An electron-microscopic investigation could not reveal any noticeable defects in the implanted layer of the specimens irradiated up to a fluence of 1×10^{16} ions/cm^2 (the investigation was performed 3 months after irradiation). Implantation dislocation loops were observed after a heavier dose. At a fluence of 1×10^{17} ions/cm^2, the density of such loops was 7×10^{22} m^{-3}, their mean size being 4.5 nm. At a fluence of 1×10^{18} ions/cm^2, these parameters were 1×10^{23} m^{-3} and 7.0 nm, respectively. In studying gas thermal desorption under the heating of the specimens irradiated in a deuterium-ion beam up to a fluence of 10^{16} ions/cm^2, no deuterium was found for specimens held at room temperature for 1.5 months after their irradiation.

Figure 3 (curve *1*) shows a typical dependence of hydrogen thermal desorption under a linear heating of austenitic-steel specimens irradiated in a PWR reactor at about 590 K up to a neutron fluence of $(0.4–0.9) \times 10^{21}$ cm^{-2} after storing the specimens at room temperature for five years. The kinetic curve of hydrogen release has one peak (at about 680 K). Hydrogen release stops completely at about 740 K. Curve *2* represents hydrogen thermal desorption from a specimen that was not irradiated, but which was saturated with hydrogen electrolytically. Curve *3* corresponds to an irradiated specimen that was electrolytically saturated with hydrogen after its irradiation in the reactor. Electron-microscopic studies of specimens irradiated in the reactor revealed implantation dislocation loops of density about 4×10^{22} m^{-3}, their mean diameter being 60 nm.

Figure 4 presents the curves of deuterium thermal desorption from specimens of 12X18H10T austenitic steel that were irradiated with four pulses of deuterium plasma, the energy content per pulse being 40–60 kJ. The studies were performed 3 to 5 days after irradiation. The central part of the specimens was melted, and blisters of various size were formed at the periphery of the specimens [4]. Curve *2*, which has one peak at about 600 K, was obtained with a specimen from the assembly center where there were no blisters because of the melting of the material surface. Curve *1*, which was obtained with a sample from the assembly periphery, where blisters were identified, has three peaks at about 500, 600, and 900 K.

4. DISCUSSION OF THE RESULTS

In Fig. 1, the first two peaks in the curves of hydrogen release from specimens preliminarily irradiated with 18-keV hydrogen ions correspond to diffusive hydrogen escape from planar specimens in the case of an asymmetric gas distribution with respect to the specimen surfaces [5]. The first peak is associated with gas escape through the specimen surface closest to the saturated layer, while the second peak corresponds to hydrogen escape through both specimen surfaces. A sharp shape of the low-temperature peak suggests that hydrogen escaped from a thin irradiated layer near the specimen surface.

Figure 2 shows the kinetic curves of hydrogen release from austenitic-steel specimens irradiated with

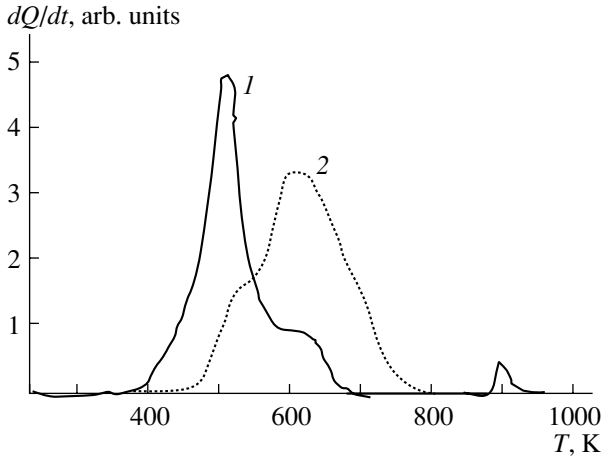

Fig. 4. Deuterium-thermal-desorption curves obtained under a uniform heating of specimens of 12X18H10T steel that were subjected to the effect of four pulses of deuterium plasma: (*1*) results for a specimen containing blisters and (*2*) results for a specimen having a fused surface and not containing blisters.

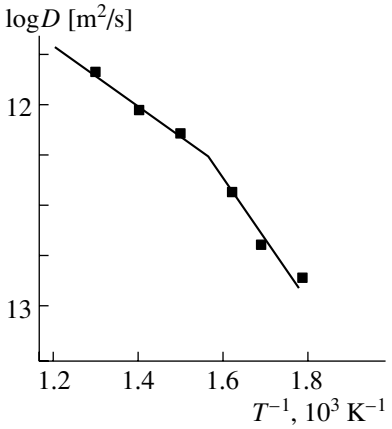

Fig. 5. Arrhenius dependence plotted on the basis of the experimental curves of hydrogen thermal desorption from a specimen saturated with a gas by means of deuterium-ion bombardment.

3-MeV deuterium ions. As mentioned above, the double peak corresponds to diffusive hydrogen release from planar specimens in the case of an asymmetric gas distribution with respect to the specimen surfaces. Curve *1* is the calculated curve of deuterium thermal desorption from a nonirradiated specimen 200 μm thick, in which deuterium was initially concentrated in a thin layer at a distance of 25 μm from one of the specimen surfaces. The following data from [6] were used in our calculation: the activation energy of hydrogen diffusion, 50 kJ/mol, and a preexponential factor, $D_0 = 3 \times 10^{-7}$ m^2/s. The shift of the peaks toward higher temperatures in the case of irradiated specimens can be explained by hydrogen diffusion slowed down in irradiated specimens because of the formation of radiation defects.

Our calculations revealed that, if there were no radiation defects (hydrogen traps), deuterium contained initially in a thin specimen layer at a depth of 25 μm would diffuse uniformly throughout the whole volume of the 200-μm thick specimen in just 1.5 months of specimen storage at room temperature. In view of this, the thermal-desorption curve should have only one peak. However, thermal-desorption curves have a double peak even nine months after irradiation, this suggesting deuterium retention by radiation defects in the damaged region of the specimen. This conclusion is in good agreement with known data obtained by studying the effect of the prolonged storage of specimens irradiated with 17-MeV protons on variation of their microhardness [7].

The Arrhenius dependence (Fig. 5) plotted on the basis of the curves of hydrogen thermal desorption from an irradiated specimen according to the procedure described in [5] has an inflection point at $T \approx 650$ K. The activation energy for hydrogen diffusion was found to be about 70 kJ/mol in the temperature range up to 650 K and about 50 kJ/mol for $T > 650$ K, the latter being close to the activation energy for deuterium-atom diffusion in the nonirradiated austenitic steel [6]. These data indicate that the radiation defects formed are traps for deuterium atoms up to rather high temperatures of about 650 K.

From an analysis of deuterium-release curves (Fig. 2), it is obvious that storage of irradiated specimens at room temperature results in a shift of the double peak toward higher temperatures. The observed shift of the peaks of deuterium release from the specimens being studied with increasing time of specimen storage at room temperature after irradiation may be due to hydrogen redistribution among radiation defects—that is, the migration of the hydrogen atoms from traps of lower binding energy to those of higher binding energy.

The presence of two peaks in Fig. 3 (curves *2, 3*) is explained by a nonuniform initial saturation of specimens with hydrogen. The shift of the peaks corresponding to hydrogen release from irradiated specimens that are subjected to additional electrolytic saturation with hydrogen in relation to those caused by hydrogen release from nonirradiated specimens is explained by the fact that the irradiated specimens contain hydrogen traps, which are free from gas atoms and which are filled in the course of electrolytic saturation. The shape of the curve of hydrogen thermal desorption from an irradiated material (curve *1*) corresponds to hydrogen escape from a specimen that is uniformly saturated with a gas (symmetrically over its thickness). It follows from Fig. 3 that irradiation

results in a shift of the hydrogen-release peaks toward higher temperatures.

We plotted the Arrhenius dependence on the basis of curve *1* (Fig. 3) by using the method described in [5]; just as in the case of specimens irradiated with 3-MeV deuterium ions, this curve has an inflection point, this time at 600 K. The distinction between the temperature values corresponding to the inflection points can possibly be explained by the difference in the saturating agent—hydrogen in the present case (Fig. 4) and deuterium in the case of irradiation at an accelerator (Fig. 2)—and by different irradiation conditions. The most probable reason for the appearance of the inflection point is that, at temperatures above 600 K, radiation defects formed in this case by reactor irradiation lose their efficiency as traps for hydrogen atoms. This is confirmed by the calculation of the activation energy: it appears to be 65 kJ/mol or 50 kJ/mol if calculated on the basis of, respectively, the low- or the high-temperature section of the Arrhenius curve. The latter value is in good agreement with data from [8, 9] on hydrogen diffusion in nonirradiated austenitic steel. We used the procedure described in [8] to determine the binding energy of hydrogen in traps; it appeared to be 33 kJ/mol. Vacancy complexes can be supposed to be traps of this type [10].

It was found experimentally that specimens irradiated in a reactor contained 1.3×10^{-2} at % hydrogen. As was indicated in [11], the nuclear reaction $^{59}\mathrm{Ni}(n,p)^{59}\mathrm{Co}$, whose cross section for thermal neutrons is $\sigma = 2.0$ b, can yield one hydrogen atom per every six helium atoms produced in the nuclear reaction $^{58}\mathrm{Ni}(n,\gamma)^{59}\mathrm{Ni}(n,\gamma)^{56}\mathrm{Fe}$ ($\sigma = 13$ b). Starting from this fact and using experimental data reported in [12], we find that the calculated amount of hydrogen produced in a particular material irradiated in a PWR reactor is two orders of magnitude less than the values obtained in our experiment. The specimens being studied can be assumed to contain hydrogen of a nonradiation origin, or hydrogen can be assumed to originate in the specimens from some unknown nuclear reactions, but the latter is less probable.

Figure 4 presents the kinetic curves of deuterium release in the course of a uniform heating of 12X18H10T steel specimens that were subjected to the effect of four pulses of deuterium plasma: curves *1* and *2* represent relevant results for specimens containing blisters and having a fused surface without blisters.

It was found in [4] that, in the case of a high energy content in the plasma flows, the surface of the specimens being studied is predominantly melted, blisters not being formed. At a lower energy content, anomalously large blisters, with top layer about 1 μm thick (this value is an order of magnitude greater than the free path of hydrogen ions at the energy value used), are formed on austenitic steel specimens. Heating to about 900 K gives rise only to additional smaller blisters without destruction of already available ones or variations in their size. Only upon heating to 1020 K does there occur a partial cracking of the domes of the largest blisters, but, even at 1300 K, a lot of blisters remain undamaged.

In addition to the peak at $T \sim 600$ K, curve *1* (Fig. 4) for specimens from the periphery of the assembly has two peaks—a low-temperature one at about 500 K and a high-temperature one at about 900 K. It is possible that these peaks are associated with deuterium release from the blisters, where it can be both in a molecular form and in the form of chemical compounds—for instance, hydrocarbons.

In order to confirm the above conjectures, we will consider the kinetics of hydrogen release from the blisters. For structures similar to hydrogen blisters, it was shown in [8] that the concentration of hydrogen at the blister top decreases linearly with depth as the blisters are degassed, whereby there arises a hydrogen distribution typical of experiments studying permeability in the mode of a steady-state flow. An estimate of the permeability of austenitic steel [10] revealed that the redistribution of molecular hydrogen released from blisters of particular geometry under a uniform heating at a rate of about 10 K/min generates a gas-release peak in the range 400–600 K.

Thus, the first peak of the curve of gas release from austenitic-steel specimens containing blisters (Fig. 4) can be explained by the redistribution of molecular deuterium accumulated in the blisters. This conclusion is confirmed by data from [13], where it was shown that radiation pores in austenitic steels do not retain molecular hydrogen at 800 K. Therefore, molecular hydrogen cannot cause the observed destruction of blisters under heating and the formation of second-generation blisters.

The high-temperature peak of the curve of deuterium release from austenitic-steel specimens containing blisters (Fig. 4) is possibly associated with deuterium release in the dissociation of hydrocarbon compounds contained in the blisters. The most probable reasons for the absence of a high-temperature peak (900–1000 K) on the curves of the thermal desorption of hydrogen isotopes from 0X16H15M3B steel specimens (Figs. 1–3) are the following: on one hand, we did not observe any porosity in these particular specimens; on the other hand, there was an insufficient amount of hydrogen for the formation of hydrocarbon compounds.

The hypothesis put forth in [10, 14] that hydrocarbons—in particular, methane—are formed in metals irradiated with hydrogen ions explains rather

well the destruction of blisters and the formation of second-generation blisters in the course of heating after irradiation. Since methane is not soluble in a metal, it will behave as an inert gas (for instance, helium) under heating. If, at the dissociation temperature, the methane pressure in the blisters is not sufficient for their destruction, then blisters must survive further heating. In order to test this conjecture, we studied thermal desorption of gases from specimens of 0X16H15M3B austenitic steel at a heating rate of 0.3 K/s. The surface topography was studied before and after heating [4].

In order to determine the composition of chemical compounds within blisters directly, we used the effect of blister destruction under heating. Since the destruction of blisters depends on the plasma-flow power and, hence, on the distance between the specimens and the assembly center, it is impossible to pinpoint, from the outset, specimens for which the effect will be maximal. In view of this, we studied a group of specimens that contained blisters and which were irradiated with three pulses of a hydrogen plasma. We chose hydrogen plasma in this case, since it is more difficult to isolate CD_4 peaks than CH_4 peaks in their detection with a mass spectrometer. The possible presence of water vapor at the surface of setup elements was the main obstacle, which generated a series of peaks corresponding to atomic masses of 18, 17, and 16, this complicating the detection of peaks corresponding to methane (masses of 16, 15, and 13) [15]. The mass spectrometer used was tuned to recording compounds of mass in the range from 15 to 27.

The corresponding gas-release curves are presented in Fig. 6. The first peak was observed for all specimens. Probably, it is associated with degassing of the specimen surface. The second peak was observed only for specimens in which the blisters appeared to be destroyed after heating. An analysis of the resulting spectra gives grounds to state that, at a temperature of about 750 K, methane and some other compound of the C_XH_Y type (a peak at a mass of 26 corresponds to it) are released upon the destruction of blisters. The high-temperature peaks on the thermal-desorption curves for specimens irradiated with 18-keV and 3-MeV hydrogen-isotope ions are also likely associated with the dissociation of chemical compounds contained in microcracks that we did not observe.

Knowing the evacuation rate for our system and considering the gas-desorption curves corresponding to specimens containing intact blisters as a "background," we estimated the amount of hydrocarbons released from a specimen upon the destruction of blisters. We determined the gas pressure in blisters

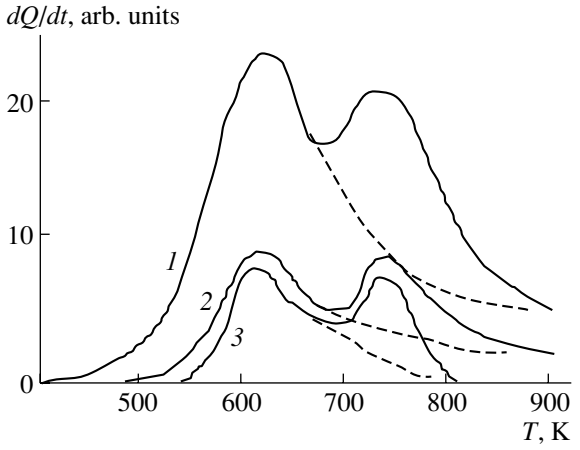

Fig. 6. Gas-release curves obtained under a uniform heating of specimens from 12X18H10T austenitic steel that were subjected to the effect of four pulses of deuterium plasma. The dashed and solid lines correspond to specimens containing nondestructed and destructed blisters. Curves *1*, *2*, and *3* represent results corresponding to masses of 16, 15, and 26, respectively.

at the instant of their destruction from the electron-microscopy data on the volume of destroyed blisters and obtained a value of about 100 MPa, which, according to the known estimates from [16], is quite sufficient for their destruction. The mechanism of formation of the observed anomalous blisters was considered in [17]. According to this concept, some prerequisites for methane-blister formation (micropores, sufficient amount of hydrogen and carbon, temperature) appear at some depth from the plasma-irradiated surface (about 1 μm in our case) under certain conditions.

5. CONCLUSION

We have found that, upon heating austenitic-steel specimens that were irradiated in a reactor or by means of bombarding them with hydrogen-isotope ions and which were stored up to 9 months at room temperature, there arises a "high-temperature" peak of hydrogen release (600–700 K). This suggests that irradiation generates some defects in the material, which are efficient traps for hydrogen up to rather high temperatures (650 K).

If austenitic-steel specimens are irradiated in a PWR reactor, the amount of hydrogen accumulated in the material being studied considerably exceeds the yield from known nuclear reactions of the (n, p) type.

Our study of deuterium thermal desorption from austenitic-steel specimens irradiated with 3-MeV deuterium ions show that preliminary storage of irradiated specimens at room temperature (for 1.5 and 9 months) causes a shift of the gas-desorption

peaks toward higher temperatures. This may be due to the redistribution of hydrogen atoms in specimens among traps of different binding energy in the course of specimen storage at room temperature.

In relation to what was observed for nonirradiated specimens, two additional peaks (at about 500 and 1000 K) have been found on the kinetic curve of deuterium thermal desorption from austenitic-steel specimens subjected to the effect of deuterium plasma. The high-temperature peak of deuterium release (at about 1000 K) is caused by the dissociation of hydrogen-containing compounds accumulated in micropores. The low-temperature peak of deuterium release (at about 500 K) is associated with its escape from the material under study upon the dissociation of deuterium molecules contained in blisters.

We heartily congratulate V.V. Vladimirsky on the occasion of his 90th birthday and wish him good health and further years of creative activity.

REFERENCES

1. A. G. Zaluzhnyi, V. P. Kopytin, and M. V. Cherednichenko-Alchevsky, Fusion Technol. **2**, 1815 (1996).
2. A. G. Zholnin, A. G. Zaluzhnyĭ, and V. P. Kopytin, At. Energ. **61**, 5 (1986); **61**, 350 (1986).
3. V. D. Onufriev, Yu. N. Sokursky, and V. I. Chuev, Preprint No. 3070, IAÉ (Institute of Atomic Energy, Moscow, 1978).
4. V. I. Pol'skiĭ, B. A. Kalin, P. I. Kartsev, *et al.*, At. Energ. **56** (2), 83 (1984).
5. A. G. Zholnin and A. G. Zaluzhnyĭ, Poverkhnost **10**, 33 (1986).
6. T. J. Dolan and R. A. Anderi, Idaho 83415, Idaho National Engineering Laboratory (EG&G Idaho, Idaho Falls, 1994).
7. Sh. Sh. Ibragimov, V. F. Reutov, and K. G. Farhudinov, *Radiation-Induced Defect in Metallic Crystals* (Nauka, Alma-Ata, 1978), p. 78 [in Russian].
8. A. G. Zholnin and A. G. Zaluzhnyĭ, Poverkhnost **11**, 27 (1986).
9. P. A. Platonov, I. E. Tursunov, A. G. Zholnin, *et al.*, Preprint No. 4086, IAÉ (Institute of Atomic Energy, Moscow, 1984).
10. A. G. Zaluzhnyĭ, D. M. Skorov, A. G. Zholnin, *et al.*, *Radiation-Induced Defect in Metallic Crystals* (Nauka, Alma-Ata, 1981), p. 278 [in Russian].
11. L. R. Greenwood and F. A. Garner, Fusion Reactor Mater. **VII**, 1530 (1995).
12. A. G. Zaluzhnyĭ, Yu. N. Sokurskiĭ, and V. N. Tebus, *Helium in Reactor Materials* (Énergoatomizdat, Moscow, 1988), p. 135 [in Russian].
13. D. Keefer and A. Pard, J. Nucl. Mater. **47**, 97 (1973).
14. V. N. Chernikov, A. P. Zakharov, and A. A. Pisarev, Izv. Akad. Nauk SSSR, Ser. Fiz. **44**, 1210 (1980).
15. G. L. Saksaganskiĭ, Yu. N. Kotel'nikov, M. D. Maneev, *et al.*, *Ultrahigh Vacuum in Radiophysical Apparatus Building* (Atomizdat, Moscow, 1976), p. 36 [in Russian].
16. B. A. Kalin, D. M. Skorov, and V. T. Fedorov, *Interaction of Atomic Particles with Solids* (Izd. Kharkov. Univ., Kharkov, 1976), Part 1, p. 120 [in Russian].
17. A. G. Zaluzhnyi, B. A. Kalin, A. L. Suvorov, and M. A. Kozodaev, in *Proceedings of the 11th Conference on Radiation Physics and Chemistry of Condensed Matter, Tomsk, Russia, 2000*, p. 462.

Translated by E. Kozlovsky

Physics of Atomic Nuclei, Vol. 68, No. 8, 2005, pp. 1271–1282. Translated from Yadernaya Fizika, Vol. 68, No. 8, 2005, pp. 1324–1335.

TRIBUTE TO THE 90th BIRTHDAY OF V.V. VLADIMIRSKY

Discovery of a Narrow Resonance at 1070 MeV in the System of Two K_S Mesons

V. K. Grigor'ev*, V. V. Vladimirsky, I. A. Erofeev, O. N. Erofeeva, Yu. V. Katinov, V. I. Lisin, V. N. Luzin, V. N. Nozdrachev, V. V. Sokolovsky, E. A. Fadeeva, and Yu. P. Shkurenko

Institute of Theoretical and Experimental Physics, Bol'shaya Cheremushkinskaya ul. 25, Moscow, 117259 Russia

Received January 12, 2005

Abstract—Results are presented that were obtained by studying the previously unknown narrow resonance of mass about 1070 MeV. This state was discovered in the system of two K_S mesons. The experimental data subjected to the analysis here come from the 6-m spectrometer created at the Institute of Experimental and Theoretical Physics (ITEP, Moscow) and irradiated with a 40-GeV beam of negatively charged pions from the U-70 accelerator at the Institute for High Energy Physics (IHEP, Protvino) with the aim of studying $\pi^- p$ and π^-C interactions. At the respective maximum, there are 69 events, the statistical significance being not less than six standard deviations. The mass and width of the observed meson are $M = 1072.4 \pm 0.8$ MeV and $\Gamma = 3.5^{+1.5}_{-1.0}$ MeV, respectively, the product of the cross section for its formation and the relevant branching ratio being not less than 20 nb. The preferable J^{PC} assignment for this resonance is 0^{++}. Its extraordinary small width has no satisfactory theoretical explanation.

1. INTRODUCTION

Over the past few years, seven narrow mesons of width not larger than 15 MeV have been discovered in the $K_S K_S$ system in the effective-mass range from the threshold to about 2200 MeV by exposing the 6-m spectrometer created at the Institute of Theoretical and Experimental Physics (ITEP, Moscow) to a 40-GeV beam of negatively charged pions from the U-70 accelerator of the Institute for High Energy Physics (IHEP, Protvino) [1–7].

One of the resonances that we observed, that of mass 1450 MeV [6], was known previously [8–11]. Indications of the existence of resonances at 1245, 1768 and 1786 MeV were obtained by the authors of [12] at the L3 facility (CERN), but those authors gave their own interpretation of the data that they obtained. The remaining resonances have not been observed by other experimental groups. In the present study, we consider a new narrow resonance of mass 1072 MeV and width ~3.5 MeV, which was discovered in the system of two K_S mesons by using the aforementioned 6-m spectrometer.

It should be emphasized that, in the system of two K_S mesons, a maximum in the mass region around 1070 MeV was previously observed in 1976 [13] (see Fig. 3 there) and in 1986 [14] (see Fig. 5 in [14]; that investigation was performed by our group, but the data from [14] are not used here). In those publications, no particular attention was given to the maxima in the mass region around 1070 MeV since their statistical significance did not exceed three standard deviations (SD). In light of our present results, however, those data appear to be of importance.

In the hadron-spectroscopy realms, interest in narrow resonances has quickened sharply in the past two years. This was due largely to the appearance of the article by Diakonov, Petrov, and Polyakov [15] in 1997, who indicated that a baryon of width about 15 MeV may exist in the mass region around 1530 MeV. The quark content of the predicted state is unusual: it contains a strange antiquark and four light quarks. The discovery of this baryon (culled the Θ^+ pentaquark) initiated an enormous number of both theoretical and experimental studies. Although many experiments have been conducted, the situation remains unclear: some experimental groups "see" this resonance, while others do not. A comprehensive review on the subject can be found in [16].

Pieces of evidence have been obtained for the existence of other narrow baryons as well [17, 18], which also have a pentaquark composition but different masses and different decay modes. However, the situation there is even more uncertain than in the case of Θ^+. In analyzing early experimental publications, studies that resulted in observing narrow baryons of

*e-mail: vkgrigor@rambler.ru

mass 3170 [19] and 3520 MeV [20] have attracted considerable attention.

In the meson-spectroscopy realms, narrow resonances whose width could not be explained on the basis of standard theoretical models have been observed experimentally since the mid-1960s. As was mentioned above, several groups claimed the observation of a resonance at a mass value of 1450 MeV [8–11]. The resonance was observed in the $\pi^+\pi^-$, K^+K^-, and K_SK_S meson systems. In [9], the measured width of this resonance was about 15 MeV. Data obtained at the ITEP 6-m spectrometer [6] corroborate the existence of this resonance and its small width. However, the resonance in question was not observed by all experimental groups, and it was excluded from the main tables of the Particle Data Group [21]. The question of why some experimental groups see this resonance, while the others do not, was addressed in [9]; the same question as applied to pentaquarks was discussed in [22].

Yet another narrow resonance was observed at one of the facilities at the Stanford Linear Accelerator Center (SLAC, USA) [23] in the K_SK_S and K^+K^- systems in the radiative decays of J/ψ particles and was confirmed at the BES facility (China) [24]. The mass and width of this resonance are 2230 and 15 MeV, respectively. The BES group observed this state in several decay modes: $p\bar{p}$, $\pi^+\pi^-$, and $K\bar{K}$. However, the history of this resonance is similar in many respects to the history of the resonance of mass 1450 MeV: it was seen in some studies but was not observed in others. Ultimately, this resonance (of mass 2230 MeV) was also excluded from the main tables of the Particle Data Group.

The narrow meson recently discovered in the $D_s^+\eta$ and D^0K^+ systems at the SELEX spectrometer [25] also attracts the attention of researchers. The mass of this state is 2636 MeV. Its decay modes and mass suggest that this meson consists of c and $\bar{s}$ quarks. It could decay via strong interaction and have a width of about 100 MeV; nevertheless, the width of this resonance is less than 17 MeV.

From the above brief survey, it follows that, both in the class of baryons and in the class of mesons, there are presently experimental indications of the existence of narrow hadrons whose small width presents a challenge to modern theoretical approaches. It is quite feasible that this phenomenon has the same explanation both for baryons and for mesons.

An experimental observation of narrow resonances involves considerable difficulties associated with the following circumstances:

(i) The product of the resonance-formation cross section and the relevant branching ratio is small, which complicates the accumulation of sufficient statistics. In the majority of studies, there are not more than a few tens of events at the corresponding peak, but, at a low background level, the statistical significance may exceed five standard deviations even in this case.

(ii) As a rule, the resonance widths are less than the resolution of the experimental facilities used.

(iii) Since the production dynamics of these resonances is unusual, the possibility of observing them may depend on experimental conditions.

(iv) For experimental facilities of the electronic type, it is not clear how one should organize a trigger. It is little wonder that a considerable number of studies where narrow states were observed were performed by using bubble chambers.

In the present study, we explore in detail the properties of a newly discovered narrow resonance of mass about 1070 MeV and width amounting to a few megaelectronvolts. An observation of such a narrow resonance is an extraordinary fact. There are no clear-cut theoretical arguments in favor of the existence of new states in this region, especially such narrow ones. In view of this, we investigated the effect of various selections of the statistical significance of this resonance and subjected our data to various tests.

2. EXPERIMENTAL CONDITIONS

The experimental data employed in the present analysis were obtained over a period between 1985 and 1996 by using the ITEP 6-m spectrometer. A detailed description of the spectrometer was given elsewhere [26, 27]. The spectrometer records, with a high efficiency, K_S mesons traveling in the forward direction and decaying to two charged pions. A large volume covered by a magnetic field and filled with detectors makes it possible to identify K_S mesons reliably and to measure the effective mass of the K_SK_S system in the region around 1100 MeV to a high precision (to within a few megaelectronvolts).

The data analyzed in the present study come from exposures where we employed liquid-hydrogen and carbon targets. The K_SK_S system recorded under experimental conditions of the 6-m spectrometer is produced in the following two reactions on a hydrogen target:

$$\pi^-p \to K_SK_Sn \qquad (1)$$

and

$$\pi^-p \to K_SK_S + (n + m\pi^0, p + \pi^-, \ldots). \qquad (2)$$

The reaction in (1) is selected by means of a triggering device that is based on veto counters surrounding the liquid-hydrogen target. The counters form a double veto layer around the target. In order to suppress events where not only charged particles but also photons are emitted from the target, lead

converters of thickness about two radiation-length units are arranged in between the counters. Because of an imperfect operation of the trigger, some events of the reaction in (2) are recorded in the apparatus.

A trigger that selects low-multiplicity events (two to three charged particles escaping from the target) accompanied by the production of additional charged particles beyond the target was applied in the case of a carbon target. This trigger also recorded events involving the production of K_S mesons. In the data sample obtained in this way, we selected events featuring two K_S mesons. The recorded K_S-meson pair was predominantly produced in the reaction

$$\pi^- A \to K_S K_S + (A' + m\pi^0 + n\pi^+ + l\pi^-, \ldots). \quad (3)$$

By A', we imply here not only excited nuclei but also reaction products formed in the final state, which possibly include isobars.

Product K_S mesons are identified by their decays to a $\pi^+\pi^-$ pair. For the $K_S K_S$ system, the detection efficiency is 45% at the threshold and is about 35% in the mass region around 2000 MeV. For events where the momentum of each of the two K_S mesons does not fall below 7 GeV, the main contribution to the calculated efficiency comes from the suppression of events involving the decay of one or both K_S mesons within the volume surrounded by the veto counters. The contribution of such events is determined by the relative disposition of the target and these counters and can easily be taken into account. In the present study, we consider events where the effective mass of two K_S mesons does not exceed 1150 MeV, while their total momentum is not less than 37 GeV. Under these conditions, the momentum of an individual K_S meson cannot be less than 10 GeV, 13 GeV in the band of the resonance being studied.

For kinematical variables that are used in our analysis of the $K_S K_S$ system, we took the effective mass M_{KK} of a K_S pair, the squared mass MM^2 of particles that are produced in association with the $K_S K_S$ system and which are not recorded by the spectrometer (missing mass squared), the 4-momentum transfer from the beam to the system under study ($-t$), the cosine $\cos\theta$ of the Gottfried–Jackson angle, and the Treiman–Yang angle ϕ. The angles are calculated in the rest frame of the K_S-meson pair, the beam-axis direction in this frame being taken for the polar axis. The plane from which we measure the Treiman–Yang angle is spanned by the beam and target-proton momenta.

For a K_S-meson system produced on carbon nuclei, the missing mass squared is calculated by the same formulas as in the case of production on protons. It is assumed that intranuclear protons and neutrons are in a "quasifree" state. But in fact, the very concept of a missing mass loses meaning in many respect in the case of production on nuclei. Nevertheless, practice revealed that, even in this case, selections in the "quasimissing" mass may be useful in separating various mechanisms of the production of the K_S meson system.

3. DATA PROCESSING

In this section, we describe basic methods for data processing. In Subsection 3.1, we consider an algorithm for fitting a "vee" that is formed upon the decay of a K_S meson to two charged pions. The results of this fit are important for the following two reasons: first, no such procedure is used by other experimental groups; second, the fitting in question improves the resolution in the effective mass of the $K_S K_S$ system. The fitting of vees that is used here is of paramount importance for discovering narrow resonances. In Subsection 3.2, we consider the effect of various selections on the separation of a signal from the narrow resonance being studied.

3.1. Fitting the Parameters of K_S Mesons

In order to refine the particle parameters on which physically significant quantities depend (effective mass of two K_S mesons and Gottfried–Jackson and Treiman–Yang angles), the fitting procedure was performed independently for each of the two vees. The following requirements were imposed: charged-pion tracks forming a vee must intersect at one spatial point, while the effective mass of a two-pion system must be equal to the Particle Data Group value of the K_S-meson mass. As the result of fitting, we calculated χ^2_V and the kinematical features of a vee. This procedure improves the accuracy in calculating the physical parameters of K_S, as is illustrated in Fig. 1, which displays the distributions of events with respect to the vertex coordinate X_V and with respect to the distance D between the trajectories of K_S mesons. One can see that the fitting procedure (its results are shown in Figs. 1*b* and 1*d*) improves substantially the original distributions (Figs. 1*a* and 1*c*). It should be recalled that the vees are fitted independently of each other.

As follows from the data in Fig. 2, which shows the mass spectra of two K_S mesons in the resonance region, the application of the fitting procedure also improves the accuracy for the effective mass of the system of two K_S mesons. The effective mass was calculated by three methods. For Figs. 2*a* and 2*b*, the masses were calculated by using nonfitted parameters, the vee masses being taken from our experimental data for Fig. 2*a* and being set to the Particle Data Group value for the K_S-meson mass

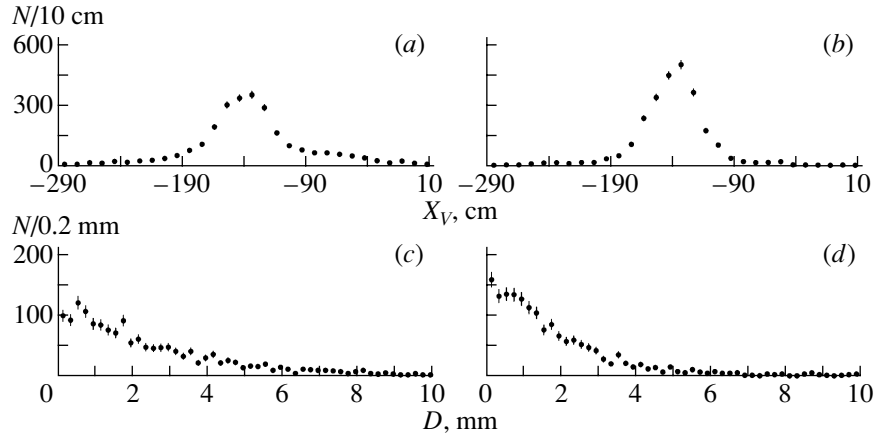

Fig. 1. Distribution of (*a*) nonfitted and (*b*) fitted events with respect to the vertex coordinate X_V; distribution of (*c*) nonfitted and (*d*) fitted events with respect to the distance D between the K_S-meson tracks at the point of their maximal approach.

for Fig. 2*b*; for Fig. 2*c*, we employed fitted parameters. As the parameters of K_S-meson vees are refined, the resonance width is seen to become narrower. This behavior of the calculated effective mass lends additional support to the statement that, here, we are dealing with a physical effect rather than with a statistical fluctuation.

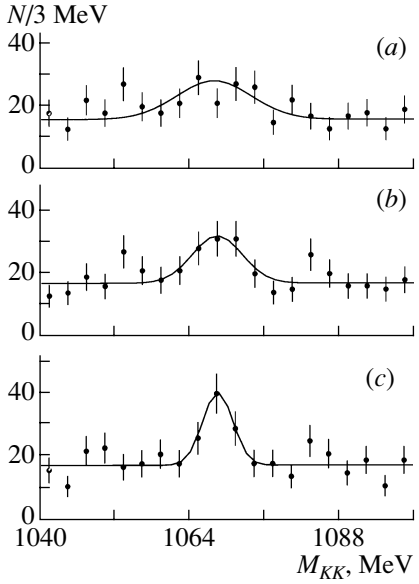

Fig. 2. Effective-mass distributions of events for the K_SK_S system: (*a*) nonfitted distribution for the case where the effective mass of two pions is calculated on the basis of experimental data, (*b*) nonfitted distribution for the case where the mass of each two-pion system is set to the Particle Data Group value of the K_S-meson mass, and (*c*) fitted data. The curves represent the results of the approximation by a Gaussian function with a parameter σ: $\sigma =$ (*a*) 6, (*b*) 4, and (*c*) 2.4 MeV.

3.2. Event Selection

In processing experimental data, we applied selections that admit a convenient separation into selections in the quality of events, in geometric variables, and in kinematical parameters. Figure 3 shows the distribution of events with respect to the variables used in standard selections and the boundaries within which events employed in a further data treatment lie. The numerical boundaries of the selections are given in Subsection 3.2.3. The distributions of events in the kinematical variables are considered in Subsection 3.2.4.

3.2.1. Selections in the quality of events. The meaning of selections in the quality of events consists in separating events that were measured most accurately. With selections in the quality of events, we class those in the deviations of the vee effective mass $M_{\pi\pi}$ from the K_S-meson mass, those in the track age T, those in χ^2_V, and those in the number N_P of points on a track.

The distributions of events with respect to the effective mass of two pions forming a vee and with respect to the track age are given in Figs. 3*a* and 3*b*, respectively. In the figures, the boundaries of the selections are indicated by the vertical lines. We do not present here the distribution with respect to χ^2_V and N_P since the number of events rejected by using these criteria is about 4%.

The track age is determined as follows. The time between the passage of a charged particle through a spark chamber and the development of a breakdown between the chamber wires is about 3 μs. Within this time interval, ions formed upon the passage of the recorded particle travel some distance in crossed electric and magnetic fields. The electric fields have opposite directions in even and odd chambers. Therefore, there is a gap (measured in millimeters) between the tracks of the same charged particle that

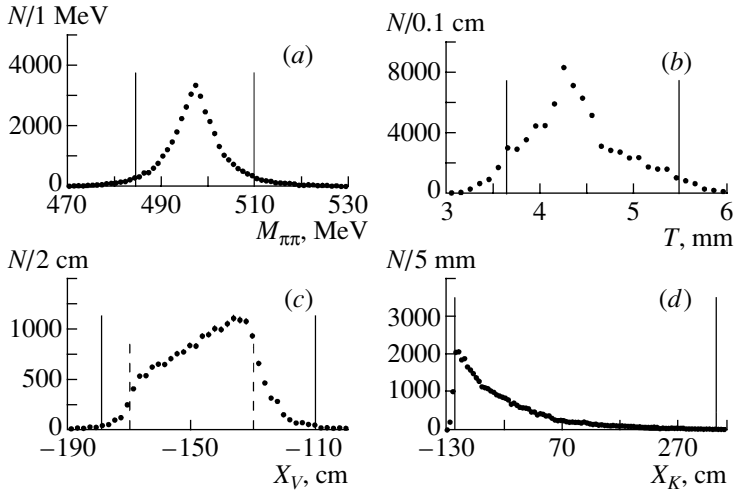

Fig. 3. Distribution of events versus the variables in which the standard selections were performed (the boundaries of the standard selections are indicated by vertical solid lines): (*a*) effective-mass distribution of K_S-meson vees, (*b*) track-age distribution, (*c*) distribution with respect to the event-vertex coordinate X_V (the dashed lines indicate the boundaries of the liquid-hydrogen target), and (*d*) distribution with respect to the coordinate X_K of the K_S-meson-decay vertices.

are drawn on the basis of sparks in even and odd chambers, and this gap is precisely the quantity that is the measure of time and which is determined in the experiment. In the following, we refer to it as the age of a track and denote it by T. This distance depends on many factors. First, it is affected by the errors in measuring the coordinates of the sparks. Second, the spark-generation instant for different spark chambers depends on the individual properties of discharge gaps. If the time interval between two successive events is not longer than 100 ms, then high-voltage capacitances do not have time to be charged to a nominal voltage, this leading to a delay of discharge-gap initiation and, accordingly, to an increase in the age. Further, the fact that a high voltage is selected for each chamber individually is also operative. The voltage is selected in such a way as to achieve the highest efficiency. In addition to the aforementioned factors, there is also the background from the tracks of particles that passed prior to ("old tracks") or after ("young tracks") the instant of trigger-signal generation.

The selection in the track age made it possible to remove cases where one of the tracks was not associated with a given event. Simultaneously, poorly measured tracks were rejected.

3.2.2. Geometric selections. Geometric selections consisted in imposing cuts on the coordinates X_V of the vertices of vee-production events and the coordinates X_K of K_S-meson-decay vertices.

The cuts on the event-vertex coordinates required that they lie in the region where the beam intersects the liquid-hydrogen target. The selections in the coordinate X_V played the most important role.

Figures 3*c* and 3*d* show the distributions of events with respect to X_V and X_K. The boundaries of the liquid-hydrogen target are indicated by the dashed lines. Use is made of fitted coordinates. The distributions of events in the plane orthogonal to the beam (coordinates Y and Z) are not presented here since

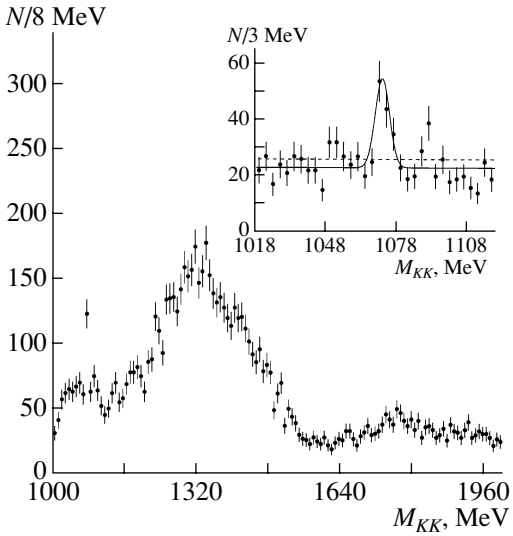

Fig. 4. Effective-mass spectrum of the system of two K_S mesons. The events included in the spectrum were selected according to quality, geometric parameters, the missing mass squared ($-0.3 < \mathrm{MM}^2 < 2.5$ GeV^2), and the momentum transfer ($-t < 0.6$ GeV^2); $N_{\mathrm{ev}} = 8158$, $S = 60$, and $S/B = 1.0$. The solid curve represents the result obtained by fitting a Breit–Wigner function to the resonance by the maximum-likelihood method, while the dashed line is a fit constructed without introducing a resonance.

Table 1

Selection	N_{ev}	Rejected events, %	K, arb. units
Without selections	1554	0	1.0
$M_{\pi\pi}$	1207	22	1.95
T	1246	20	2.15
N_P	1489	4	1.15
χ^2	1521	2	1.10
All selections in quality	913	41	3.1
X_V	1373	12	1.5
Y_V	1502	4	1.2
Z_V	1513	3	1.1
X_K	1334	13	1.5
All geometric selections	1125	28	2.5
All selections	684	55	4.75

the role of selections in these coordinates is insignificant.

The selection in the vee-vertex coordinate X_K excludes the region that contains a significant fraction of background events produced in the scintillators of the veto counters.

3.2.3. Effect of various selections on the signal-to-background ratio (S/B). We will now list once again the criteria that were used in event selections:

$487 < M_{\pi\pi} < 510$ MeV,
$3.75 < T < 5.6$ mm,
$N_P > 8$,
$\chi^2 < 80$,
$-180 < X_V < -110$ cm,
$-2.0 < Y_V < 0.3$ cm,
$-3.0 < Z_V < 2.5$ cm,
$-115 < X_K < 300$ cm.

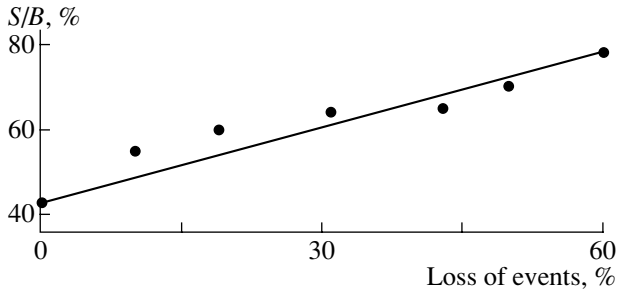

Fig. 5. Effect of the selection in $M_{\pi\pi}$ on the signal-to-background ratio S/B. The event-number loss caused by this selection is plotted along the abscissa. The straight line is drawn to guide the eye.

For the mass spectrum of the system of two K_S mesons, Fig. 4 displays the result obtained upon applying these selections. There is a distinct maximum at a mass value of 1072 MeV. In the case of 8-MeV binning, the excess of events falls within one channel almost entirely. The inset in Fig. 4 shows the respective distribution for a bin width of 3 MeV.

Table 1 illustrates the effect of each selection on the ratio of the number of events in the signal to that in the background, the signal-to-background ratio S/B; for unity, we take here the ratio $(S/B)_0$ obtained without applying any selections. In the first, second, third, and fourth columns, we present respectively, the kind of a selection, the number N_{ev} of events that survived a given selection, the fraction of rejected events in percent, and the quantity $K = (S/B)/(S/B)_0$.

From the data in Table 1, it follows that each selection improves the ratio S/B. An additional analysis reveals that, if the selection being considered is bounded from above and from below, the introduction of each of these bounds individually leads to an improvement of S/B.

In those cases where a selection affects each vee individually (χ^2, X_K, $M_{\pi\pi}$), it turns out that the ratio S/B is improved upon the effect of the selection on each vee.

The selections in $M_{\pi\pi}$ and T are especially efficient. Figure 5 demonstrates the effect of the change in the boundaries of the selection in $M_{\pi\pi}$ on S/B. The greater the number of removed events, the larger the value that the ratio S/B assumes. The behavior in response to the application of other selections is similar.

3.2.4. Selections in kinematical variables. By selections in kinematical variables, we mean selections in the missing mass and in the momentum transfer. These selections are immaterial for isolating the resonance under study, but they characterize the mechanism of its production.

Figure 6 shows the distributions of events with respect to kinematical variables (square of the missing mass and momentum transfer). The vertical lines indicate the boundaries of the selections. The removal of the kinematical selections reduces K to 3.55.

Important physical information about the properties of the $X(1070)$ resonance can be deduced from the results obtained upon applying a selection in the square of the missing mass. This selection separates events in which a neutron is produced in association with two K_S mesons and events in which a baryon accompanied by one or a few pions are produced in the lower vertex. It turns out that the ratio S/B is greater in the latter case (Fig. 7) than in the region where a neutron is predominantly produced in the

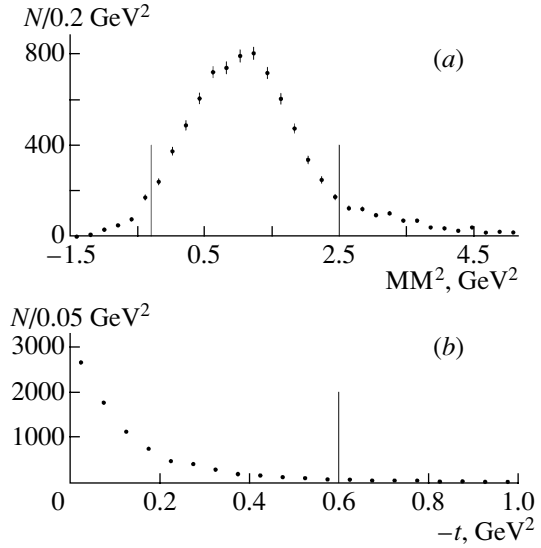

Fig. 6. (a) Missing-mass-squared and (b) momentum-transfer distributions of events ($N_{ev} = 8389$ and $N_{ev} = 8314$, respectively). The boundaries of the selections are indicated by the vertical lines.

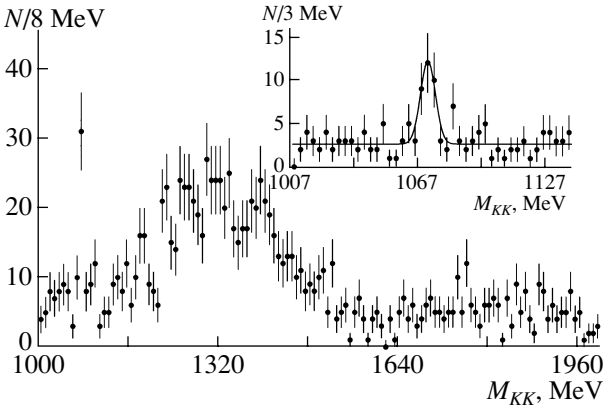

Fig. 7. Effective-mass spectrum of the system of two K_S mesons according to data from our experiment with a liquid-hydrogen target. Events were selected by applying cuts on the square of the effective mass ($1.6 < \mathrm{MM}^2 < 2.5\ \mathrm{GeV}^2$) and on the momentum transfer ($-t < 0.6\ \mathrm{GeV}^2$); $N_{ev} = 1197$, $S = 23$, and $S/B = 3.1$. The curve represents the result obtained by fitting a Breit–Wigner function to the resonance in question by the maximum-likelihood method.

lower vertex. This conclusion was confirmed by an analysis of data obtained with a carbon target.

If the above selection in the square of the missing mass is supplemented with a selection in the momentum transfer, $0.1 < -t < 0.6\ \mathrm{GeV}^2$ (this eliminates low momentum transfers), then the ratio S/B reaches a value of about 6.0. Despite a rather low statistical significance, these data may be of importance in studying the resonance-production mechanism.

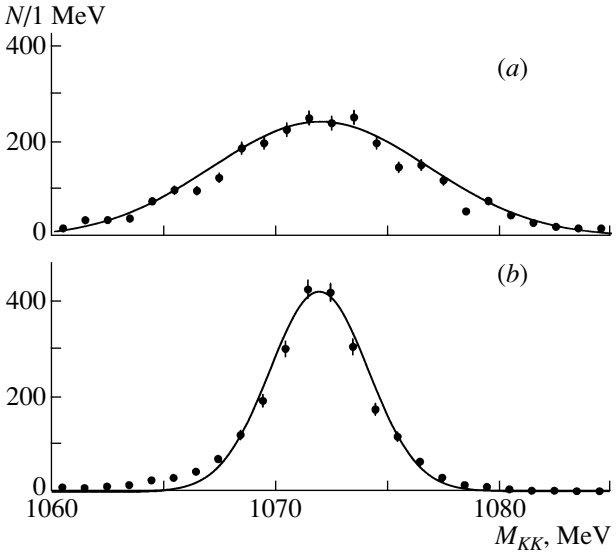

Fig. 8. Effective-mass distribution of two K_S mesons according to a Monte Carlo simulation: (a) results obtained with the vee effective mass set to the value obtained from the simulation and (b) results obtained with the vee effective mass set to the Particle Data Group value of the K_S-meson mass. The curves represent the results of the approximation by a Gaussian function with parameter $\sigma =$ (a) 4.8 and (b) 2.2 MeV.

We note that that, in studying the missing-mass dependence of the production cross sections for narrow resonances, we found that these objects may be produced via different mechanisms. Specifically, a resonance of mass 2000 MeV [7] is predominantly produced in a reaction involving a neutron, while a resonance of mass 1786 MeV [2] is not produced in the association with a neutron. The $X(1070)$ resonance, which is studied here, may be accompanied either by a neutron or by an isobar.

4. MONTE CARLO SIMULATION OF RELEVANT EVENTS

Distributions with respect to various variables were obtained from a Monte Carlo simulation, and these distributions were contrasted against our experimental results. This comparison revealed that the spectrometer model used is quite realistic, reproducing experimental data to within 20%. The most important result was obtained by calculating the effective mass of the system of two K_S mesons.

For the effective-mass distribution of the system of two K_S mesons, Fig. 8 shows the result obtained from a Monte Carlo simulation of respective events at the fixed resonance mass of 1072 MeV. The methods for calculating the effective mass were different for Figs. 8*a* and 8*b*. In Fig. 8*b*, the effective mass of each vee was set to the Particle Data Group value of

the K_S-meson mass, while, in Fig. 8*a*, it was set to the value that was obtained from the simulation. A comparison of these results with the corresponding experimental distributions (Figs. 2*a* and 2*b*) shows that, both in simulated events and in experimental data, a transition from the method where use is made of the experimental value of the K_S-meson mass to the method that employs the Particle Data Group value of the K_S-meson mass leads to a narrower maximum in the spectrum of the system of two K_S mesons.

The width of the experimental distribution (Fig. 2*b*) is larger than that obtained from the simulation (Fig. 8*b*). This suggests that the intrinsic width is somewhat smaller than the apparent one. The substitution of a Breit–Wigner function for a delta function showed that a distribution that agrees with the experimental one is obtained at $\Gamma = 3.5^{+1.5}_{-1.0}$ MeV. As usually occurs in the case where the width of the observed object is commensurate with the spectrometer resolution, it is difficult to draw a more definitive conclusion.

5. TEST INVESTIGATIONS

Test investigations consisted in verifying the existence of the $X(1070)$ resonance in individual event samples selected by different methods. First, we investigated the yield of events featuring the resonance under study in individual runs. After that, we analyzed the distribution of events with respect to the azimuthal angle determined in the laboratory frame. Also, we studied the yield of events in different samples for the same target volume and, finally, the yield of events grouped according to the coordinates of K_S-meson-decay vertices. For each sample, we tested the dependence of the signal-to-background ratio S/B on selections in the quality of events.

5.1. Analysis of the Yield of Events in the Resonance Band in Individual Runs

Three runs were performed with a hydrogen target under identical conditions. A signal from the resonance being studied was present in all three runs. The scatter of the yield of events in the resonance band from one run to another was within statistically admissible boundaries. Within each of the runs, all selections improve the ratio S/B, the statistical uncertainty being taken into account.

5.2. Analysis of the Azimuthal Dependence

In order to investigate the azimuthal dependence, we selected (as well as in other cases) events lying in the mass range 1020–1120 MeV. This range was broken down into four sectors in accordance with the direction of the K_SK_S-pair momentum.

We performed the partition by two methods, taking, for the reference plane, the horizontal plane in the first case and the plane rotated through an angle of 45° with respect to the horizontal plane in the second case. An analysis revealed that the yields of the total number of events in each of the sectors and the yields of events in the resonance band lie within the statistical errors.

In addition, we analyzed the yield of events of the double production of K_S mesons over the target volume. We chose four equal intervals in the coordinate X in the YZ plane orthogonal to the beam-axis direction, the target being partitioned into four segments of identical area. It turned out that the scatter of events in a resonance signal did not exceed that which was expected statistically.

We also investigated the yield of events involving the production of the K_SK_S system versus the coordinate X_K of the K_S-meson-decay vertex. As a result, it turned out that the number of events at the resonance was proportional to the total number of events in each of the intervals in this coordinate.

6. ANALYSIS OF DATA OBTAINED WITH A CARBON TARGET

Experimental data obtained with a carbon target in 1995 and 1996 were accumulated under conditions differing substantially from those peculiar to data acquisition with a liquid-hydrogen target.

The trigger applied in those runs was much softer: the emission of two to three charged particles from the target was allowed. In order to separate the production of neutral strange particles, a hodoscope arranged inside of the magnet between the spark chambers was included in the trigger. It was required that the number of particles recorded by the hodoscope be greater than the number of particles emitted from the carbon target.

The spectrometer resolution in the K_S-meson mass was about 1.5 times lower in the runs with a carbon target than in the runs with a hydrogen target. Nonetheless, the effective-mass distribution of the system of two K_S mesons (Fig. 9) showed a distinct peak in the region around the mass value of 1070 MeV. No selections in the quality of events were imposed. The missing-mass selection $\mathrm{MM}^2 > 2.0$ GeV^2 was introduced. The histogramming of these data yielded a mass of $M = 1070 \pm 3$ MeV

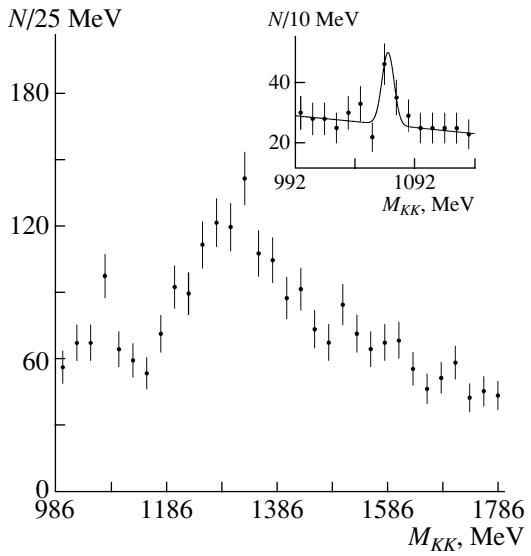

Fig. 9. Effective-mass spectrum of the system of two K_S mesons for events obtained with a carbon target. The events were subjected to a selection in the square of the missing mass ($2 < \mathrm{MM}^2 < 10$ GeV^2). The curve represents the result obtained by fitting a Breit–Wigner function to the resonance by the maximum-likelihood method, the background being described by a linear function.

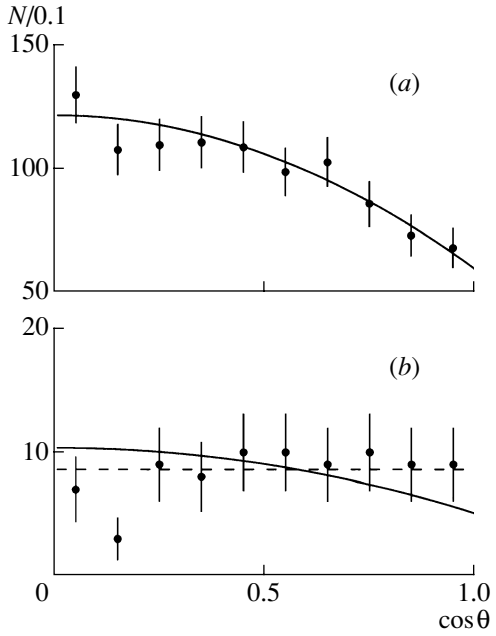

Fig. 10. Distribution of events with respect to $\cos\theta$ for events (a) off the resonance band ($1045 < M_{KK} < 1067$ MeV, $1088 < M_{KK} < 1105$ MeV; $N_{\mathrm{ev}} = 997$) and (b) in the resonance band ($1069 < M_{KK} < 1073$ MeV; $N_{\mathrm{ev}} = 84$).

and a width of $\sigma = 5 \pm 3$ MeV (the resonance was described in terms of a Gaussian function). The number of standard deviations was $N_{\mathrm{SD}} \simeq 3.7$.

The result obtained with a carbon target—namely, the fact that $X(1070)$ production occurs for $\mathrm{MM}^2 > 2.0$ GeV^2—is in accord with the result obtained with a liquid-hydrogen target, where the signal-to-background ratio S/B is higher for that sector of the missing-mass spectrum which corresponds to the production of one or a few pions at the lower vertex in the association with the baryon (see Fig. 7). It should be recalled that, in the runs with a carbon target, the production of additional pions was not suppressed by the trigger. Thus, the fact that, in the inelastic-channel region, the new resonance in question is produced more intensively is confirmed by data obtained both with a carbon and with a hydrogen target.

Although the statistical significance in experimental data coming from a carbon target is less than five standard deviations, the importance of this result is great: it was shown that the application of a nuclear target does not prevent the observation of the $X(1070)$ resonance, while the use of a trigger that is softer than a neutral one leads to an increase in the ratio S/B.

7. ANGULAR DISTRIBUTION

Figure 10 shows the distribution of events with respect to the cosine of the Gottfried–Jackson angle θ for various mass intervals. For Fig. 10a, we choose the broad mass interval 1045–1105 MeV, from which we excluded the resonance region (1067–1088 MeV). The statistical sample of 997 events available in this interval makes it possible to get quite a clear idea of the background angular distribution.

From [14], it is well known that the mass region below 1200 MeV is dominated by the S wave, which contributes more than 90% to the total cross section. The remaining cross-section fraction is described by the D_0 wave, generated by the $f_2(1270)$ resonance. Within the mass range being considered, the relative phase of the S and D_0 waves is close to π. Below, we reckon all phases from the direction of the S wave, which we assume to be real-valued. In this case, the angular distribution is described by two parameters, a constant and the coefficient of the angular momentum. The square of the D_0-wave amplitude is disregarded, since its contribution is negligible. In view of this, we describe the angular distribution in terms of the function

$$U(\cos\theta) = A^2 - 2ABY_2^0, \qquad (4)$$

where A is the S-wave amplitude, B is the D_0-wave amplitude, and Y_2^0 is a spherical harmonic. The solid

Table 2

Fitting conditions	A_S	A_{D_0}	M_0, MeV	Γ, MeV	α, deg	N	χ^2
Without introducing a resonance	1.0	0.11	–	–	–	0	100
The resonance is described	0.95	0.12	1072	5.1	86.1	79	63
by the S wave	0.95	0.12	1072	4.7	−88.7	67	60
The resonance is described	0.99	0.12	1072	1.0	75.1	10	88
by the D_0 wave	0.99	0.11	1069	1.0	−69.1	14	85

curves in Fig. 10 represent the results of approximating experimental data by the function in (4). It can be seen that, in Fig. 10*a*, this function describes the experimental distribution satisfactorily.

As to the angular distribution in the resonance band (Fig. 10*b*), it is much better described by a constant (dashed line); however, the statistical significance of the distinction between the two descriptions is not more than two standard deviations. Thus, we can state that the angular distribution in the resonance band shows no significant changes in relation to the angular distribution of the background.

8. DETERMINATION OF THE RESONANCE PARAMETERS

In order to determine the parameters of the observed resonance and its statistical significance, we fitted experimental data by the maximum-likelihood method. The main advantage of this method over that of histogramming is that, in the fitting process, the masses and angles are not averaged over the bin width, so that the result does not depend on the choice of reference point and the number of intervals into which the range of the masses being studied is partitioned.

In describing experimental data, we employed the probability-density function $F(P;\Omega)$, where P is the set of parameters and Ω is the phase space for the system of two K_S mesons. This phase space is spanned by the effective mass, the cosine of the Gottfried–Jackson angle θ, and the Treiman–Yang angle ϕ. The resonance is described by a Breit–Wigner function. The angular dependence for the background is specified by S and D_0 waves whose amplitudes are taken to be free parameters. According to our fit, the amplitudes of both background waves can be assumed to be mass-independent. Thus, the S- and D_0-wave amplitudes are the parameters P that describe the background. The amplitude A_R, the mass M_0, the phase α, and the width Γ are the resonance parameters.

We minimized the functional

$$\int_\Omega \epsilon(\Omega)F(P;\Omega)d\Omega - \sum_{i=1}^{N} \ln F(P;\Omega_i), \qquad (5)$$

where $\epsilon(\Omega)$ is the event-detection efficiency and N is the number of events. In the mass range being studied (1–1.2 GeV), the detection efficiency is virtually independent of the mass. The function $F(P;\Omega)$ has the form

$$F(P;\Omega_i) = (A_S - A_{D_0}(Y_2^0)_i \qquad (6)$$
$$+ A_R\mathrm{Re(BW)}(Y_m^0)_i)^2 + (A_R\mathrm{Im(BW)}(Y_m^0)_i)^2,$$

where A_S is the amplitude of the background S wave; A_{D_0} is the amplitude of the background D_0 wave; and BW is a Breit–Wigner function,

$$\mathrm{BW} = \exp(i\alpha)\frac{M_0\Gamma}{(M_i^2 - M_0^2) - iM_0\Gamma}. \qquad (7)$$

The quantity χ^2 is calculated by the formula

$$\chi^2 = -2\ln L + \mathrm{const}, \qquad (8)$$

where $L = \prod_{i=1}^{N} F(P;\Omega_i)$. The choice of value for the constant in (8) is immaterial since this constant does not appear in the formula for calculating the number of standard deviations:

$$N_{\mathrm{SD}} = \sqrt{\chi_B^2 - \chi_S^2 - n}. \qquad (9)$$

In this expression, χ_B^2 is the value obtained for χ^2 without introducing a resonance; χ_S^2 is its counterpart obtained upon introducing a resonance; and n is the number of degrees of freedom, which, in our case, is equal to four (amplitude, mass, width, and phase of the resonance).

For the K_SK_S system, the angular momentum J can take only even values, while P and C are positive. The resonance being studied lies near the threshold for the production of two K_S mesons. It is difficult to expect a spin value in excess of two. The possible quantum-number assignments are 0^{++} and 2^{++}. The distribution of the Treiman–Yang angle ϕ shows that spin projections for nonzero m are impossible. For the

2^{++} state, a D_0 wave was therefore chosen for a trial function.

Table 2 shows the results of fitting. The experimental data in question were approximated by formula (6), N being the number of events at the resonance.

It turned out that there are two solutions for which the values of χ^2 differ by only three units.

In describing experimental data by a D_0 wave, χ^2 is greater by 25 units than in describing them by an S wave, this corresponding to more than five standard deviations. As a result, we can rule out the 2^{++} quantum state.

Figure 11 shows the quantity χ^2 as a function of the resonance phase. One solution corresponds to a phase value of $\alpha \simeq 90°$, while the other corresponds to $\alpha \simeq -90°$. The masses and widths of these two solutions agree within the statistical errors, while the amplitudes differ by a factor of about four. The amplitudes are different because the interference is constructive in the former and is destructive in the latter case. If there were no D_0 wave in the background at all, there would be no visible distinctions between these two solutions. The difference of the χ^2 values is so small that it is impossible to choose a solution.

The important fact that, if there is yet a destructive interference, this can lead to additional difficulties in observing the resonance is noteworthy. If the resonance amplitude is twice as great as the background amplitude, the resonance as a maximum in the mass distribution disappears, the change in the phase remaining the only observable phenomenon. For a ratio of the amplitude that is close to two, the resonance-production rate may be highly sensitive to changes in experimental conditions. Possibly, this explains sometimes observed contradictions between data of different experiments.

The number of standard deviations is $N_{\mathrm{SD}} = 4.5$ in the treatment of data obtained by using only geometric selections, $N_{\mathrm{SD}} = 5.1$ for data obtained by using the selections only in the quality of events, and $N_{\mathrm{SD}} = 6.2$ upon the application of both kinds of selections. In Fig. 4, the inset shows solutions obtained (dashed line) without and (solid line) upon introducing a resonance.

For the number of events under the Breit–Wigner peak, the mass, and the width, our fitting procedure yielded the values of 69, $M = 1072.4 \pm 0.8$ MeV, and $\Gamma = 5.0^{+1.2}_{-1.0}$ MeV, respectively. A Monte Carlo simulation of the resonance width with allowance for the errors in the spectrometer measurements showed that the true width is $\Gamma = 3.5^{+1.5}_{-1.0}$ MeV.

In order to test, the above errors in the mass and width due to statistical fluctuations, our statistical sample was partitioned into four subsamples, each being treated individually. The results of this treatment confirmed the above estimates.

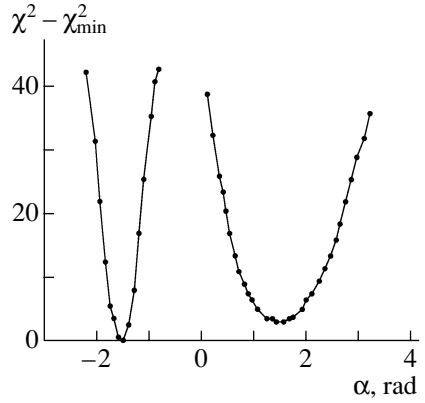

Fig. 11. Dependence of $\chi^2 - \chi^2_{\min}$ on the phase difference between the resonance amplitude and the amplitude of the background S wave.

9. ESTIMATING THE RELIABILITY OF OUR RESULTS

In the present study, it has been shown that the observed maximum in the system of two K_S mesons is a real physical object rather than a statistical fluctuation. Our confidence is based on the following facts:

(i) Any selection aimed at removing poorly measured events improves the signal-to-background ratio S/B. The selections in the vee mass (the closer the vee mass to the Particle Data Group value of the K_S-meson mass, the better obviously the measurement of an event) and in the track age play a dominant role. Other selections (in χ^2 and in the number of points) are less efficient. If they had not been applied, the results would have changed only slightly.

(ii) The selections in geometric variables also improve the ratio S/B. Under our experimental conditions, the geometric selections, as well the selections in quality, are essentially selections that make it possible to remove poorly measured events. However, the choice of boundaries for the selections in question is not arbitrary—it is determined by the target and beam dimensions, which are well known.

(iii) Various methods for calculating the effective mass have revealed that the higher the accuracy in determining the mass, the more clear-cut the manifestation of the resonance. Such a pattern inevitably takes place if we are dealing with a real object. In the case of a statistical fluctuation, the result of this would be unpredictable in advance.

10. CONCLUSION

For the mass and the width of the previously unknown narrow resonance observed in study, we have found values of $M = 1072.4 \pm 0.8$ MeV and $\Gamma = 3.5^{+1.5}_{-1.0}$ MeV; the resonance quantum numbers are $J^{PC} = 0^{++}$.

For the product of the resonance-formation cross section and the respective branching ratio, the observed number of events yields a value of 20 ± 5 nb.

ACKNOWLEDGMENTS

This investigation could not have been performed without painstaking efforts of the technical personnel of the 6-m spectrometer and the staff of the U-70 accelerator at IHEP. We are deeply indebted to them.

We are also grateful to K.G. Boreskov, V.S. Borisov, M.V. Danilov, A.G. Dolgolenko, A.M. Zaitsev, A.B. Kaidalov, L.B. Okun, and G.D. Tikhomirov for stimulating discussions and enlightening comments.

This work was supported by the Russian Foundation for Basic Research (project no. 02-02-16623) and the Ministry for Industry, Science, and Technologies of the Russian Federation (grant no. 1867.2003.2).

REFERENCES

1. V. K. Grygor'ev *et al.*, Yad. Fiz. **59**, 2187 (1996) [Phys. At. Nucl. **59**, 2105 (1996)].
2. V. K. Grygor'ev *et al.*, Yad. Fiz. **62**, 513 (1999) [Phys. At. Nucl. **62**, 470 (1999)].
3. B. P. Barkov *et al.*, Pis'ma Zh. Éksp. Teor. Fiz. **68**, 727 (1998) [JETP Lett. **68**, 764 (1998)].
4. B. P. Barkov *et al.*, Pis'ma Zh. Éksp. Teor. Fiz. **70**, 242 (1999) [JETP Lett. **70**, 248 (1999)].
5. V. V. Vladimirsky *et al.*, Pis'ma Zh. Éksp. Teor. Fiz. **72**, 698 (2000) [JETP Lett. **72**, 486 (2000)].
6. V. V. Vladimirsky *et al.*, Yad. Fiz. **64**, 1979 (2001) [Phys. At. Nucl. **64**, 1895 (2001)].
7. V. V. Vladimirsky *et al.*, Yad. Fiz. **66**, 729 (2003) [Phys. At. Nucl. **66**, 700 (2003)].
8. W. Beusch *et al.*, Phys. Lett. B **25B**, 357 (1967).
9. C. Daum *et al.*, Z. Phys. C **23**, 339 (1984).
10. T. Akesson *et al.*, Nucl. Phys. B **264**, 154 (1986).
11. DM2 Collab. (J. E. Augustin *et al.*), Z. Phys. C **36**, 369 (1987).
12. L3 Collab. (M. Acciarri *et al.*), Phys. Lett. B **501**, 173 (2001).
13. W. Wetzel *et al.*, Nucl. Phys. B **115**, 208 (1976).
14. O. N. Baloshin *et al.*, Yad. Fiz. **43**, 1487 (1986) [Sov. J. Nucl. Phys. **43**, 959 (1986)].
15. D. Diakonov, V. Petrov, and M. Polyakov, Z. Phys. A **359**, 305 (1997).
16. A. R. Dzierba *et al.*, hep-ex/0412077.
17. NA49 Collab. (C. Alt *et al.*), hep-ex/0310014.
18. H1 Collab. (A. Aktas *et al.*), hep-ex/0403017.
19. J. Amirzadeh *et al.*, Phys. Lett. B **89B**, 125 (1979).
20. V. M. Karnaukhov *et al.*, Phys. Lett. B **281**, 148 (1992).
21. Particle Data Group (K. Hagiwara *et al.*), Phys. Rev. D **66**, 010001 (2002).
22. M. Karliner and H. J. Lipkin, hep-ph/0405002 v3.
23. R. M. Baltrusaitis *et al.*, Phys. Rev. Lett. **56**, 107 (1986).
24. BES Collab. (J. Z. Bai *et al.*), Phys. Rev. Lett. **76**, 3502 (1996).
25. SELEX Collab. (A. V. Evdokimov *et al.*), hep-ex/0406045.
26. B. V. Bolonkin, O. N. Baloshin, A. M. Blagorodov, *et al.*, Preprint No. 86, ITÉF (Inst. Theor. Exp. Phys., Moscow, 1973).
27. B. V. Bolonkin, V. V. Vladimirsky, A. P. Grishin, *et al.*, Preprint No. 154, ITÉF (Inst. Theor. Exp. Phys., Moscow, 1981).

Translated by A. Isaakyan

Physics of Atomic Nuclei, Vol. 68, No. 8, 2005, pp. 1283–1287. Translated from Yadernaya Fizika, Vol. 68, No. 8, 2005, pp. 1336–1340.

TRIBUTE TO THE 90th BIRTHDAY OF V.V. VLADIMIRSKY

A Dependence of Inclusive Pion Double Charge Exchange

B. M. Abramov, L. Alvarez-Ruso[1)], Yu. A. Borodin, S. A. Bulychjov, M. J. Vicente Vacas[2)], I. A. Dukhovskoy, A. P. Krutenkova[*], V. V. Kulikov, M. A. Matsyuk, and E. N. Turdakina

Institute of Theoretical and Experimental Physics, Bol'shaya Cheremushkinskaya ul. 25, Moscow, 117259 Russia

Received December 9, 2004

Abstract—The A dependence of the forward cross section for inclusive pion double charge exchange on nine target nuclei from ^{6}Li to ^{209}Bi at $T_0 = 0.59$ GeV, as well as the cross section for ^{6}Li, ^{7}Li, and ^{12}C nuclei at $T_0 = 0.59$, 0.75, and 1.1 GeV, was measured with the 3-m magnetic spectrometer of the Institute of Theoretical and Experimental Physics (ITEP, Moscow). The resulting A dependence is well described within the model involving two sequential single charge exchanges and taking into account the renormalization of the amplitude for pion single charge exchange in a nucleus. A relatively weak energy dependence of the cross section for the ^{6}Li, ^{7}Li, and ^{12}C nuclei agrees with the analogous dependence obtained previously for the ^{16}O nucleus, but it contradicts the predicted sharp decrease in the cross section within the model involving two sequential single charge exchanges. This result provides an additional piece of evidence that the contribution from the mechanism of inelastic Glauber rescattering is significant at $T_0 \gtrsim 0.6$ GeV. © *2005 Pleiades Publishing, Inc.*

1. INTRODUCTION

Pion double charge exchange (DCX) in a nucleus is a process in which a pion of specific charge transforms into a pion of opposite charge owing to the interaction with the nucleus. This process involves at least two identical nucleons of the nucleus. This unique feature of DCX reactions attracted attention as early as 1961 [1] in connection with the possibility of employing the DCX process in searches for two-nucleon correlations in nuclei. A process of this type was first observed in 1963 at the Joint Institute for Nuclear Research (JINR, Dubna) [2] in inclusive reactions at energies in the range 30–80 MeV; since 1977, exclusive DCX reactions have been intensively studied, first of all as an efficient method for exciting doubly isobar-analogous nuclear levels. In contrast to what we have in inclusive reactions, the final state of the nucleus involved is fixed, in which case the cross section is substantially smaller. The investigations mentioned above became feasible owing to the appearance of meson factories (for an overview, see [3]) producing meson beams of high intensity up to about 10^9 pions/s and energy in the region $T_0 \lesssim 0.5$ GeV. The mechanism of two sequential single charge exchanges (SSCX) of a π meson with π^0 in the intermediate state is the commonly adopted mechanism that is used to analyze experimental data in this energy range. The SSCX mechanism predicts a fast decrease in the DCX cross section with increasing energy [4]; therefore, interest in this process at high energies is associated with searches for new DCX mechanisms. In [5], our group proposed studying DCX in inclusive reactions by using a kinematical region at the high-energy edge of the emitted-pion spectrum ($\Delta T = T_0 - T \leq 140$ MeV, T being the kinetic energy of the emitted pion), where the production of an extra pion is forbidden by the energy-conservation law in the nucleus. We emphasize that, strictly speaking, events off this region at energies of $T_0 \gtrsim 0.17$ GeV may be due to the process in which the production of two real pions on one nucleon is followed by the absorption of an extra pion in the nucleus [6–8]. Investigation of the process in this region, which is relatively narrow in ΔT of the emitted pion, requires a high momentum resolution of the experimental facility used. The ITEP 3-m magnetic spectrometer equipped with spark chambers, which has a resolution of $\Delta p/p \simeq 1\%$, made it possible to separate and study events from this region. For example, the spectra of emitted pions were analyzed in [9] for the case where the kinetic energy of incident π^- mesons was $T_0 = 0.59$ GeV; in [10], the energy dependence of DCX on an oxygen nucleus was studied at $T_0 = 0.59$–1.1 GeV, while, in [11], preliminary data on the A dependence of DCX were obtained at $T_0 = 0.59$ GeV.

[1)]Univ. of Giessen, Germany.
[2)]Univ. de Valencia, Av. Dr. Moliner, 50; E-46100 Burjassot, Valencia, Spain.
[*]e-mail: anna.krutenkova@itep.ru

1063-7788/05/6808-1283$26.00

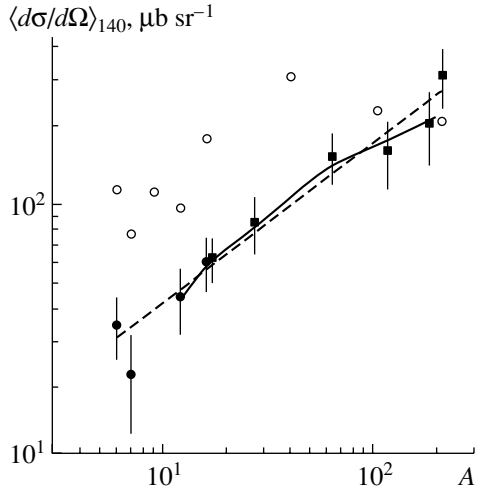

Fig. 1. A dependence of the cross section for the reaction $\pi^- A \to \pi^+ X$ at $\theta \approx 5^\circ$ and $\Delta T = T_0 - T \leq 140$ MeV ($T_0 = 0.59$ GeV) for two series of measurements: results for the ^{6}Li, ^{7}Li, ^{12}C, and ^{16}O nuclei (closed circles) and results for the Al, Cu, In, Ta, Bi, and ^{16}O nuclei (closed boxes; the point for ^{16}O is shifted to the right along the A axis in order to obtain a clearer picture). The solid curve was calculated for the SSCX mechanism on the basis of the cascade model and with allowance for the renormalization of the amplitude for pion single charge exchange in the nucleus. The dashed line is a fit of the expression A^α, where $\alpha = 0.61 \pm 0.08$, to the data. The open circles represent data from [15, 16] for $T_0 = 0.24$ GeV and $\theta = 25^\circ$.

It is worth emphasizing that the concept of the ITEP 3-m magnetic spectrometer and design of its magnet were developed under the supervision of V.V. Vladimirsky [12]. In the mid-1960s, he initiated the creation of two magnetic spectrometers supplemented with optical spark chambers. One of them was the aforementioned 3-m magnetic spectrometer based on a magnet of field volume $3 \times 0.5 \times 1.0$ m and intended for experiments at the 7-GeV ITEP accelerator, which operated at that time, while the second was a 6-m spectrometer based on a still larger magnet of field volume $6 \times 0.75 \times 1.5$ m and intended for experiments at the 70-GeV IHEP accelerator. The underlying ideas of these spectrometers proved to be so seminal that the spectrometers are still used, upon several upgrades, in physics experiments [13].

2. DESCRIPTION OF THE EXPERIMENT

In this study, we explored the A dependence of the inclusive cross section for the reaction

$$\pi^- + A \to \pi^+ + X \qquad (1)$$

on the $A =$ ^{6}Li, ^{7}Li, ^{12}C, ^{16}O, Al, Cu, In, Ta, and Bi nuclei at 0.59 GeV, and the energy dependence of the analogous cross section for the ^{6}Li, ^{7}Li, and ^{12}C nuclei in the range $T_0 = 0.59$–1.1 GeV for reaction angles of $\theta \lesssim 10^\circ$ (the average value is $\langle\theta\rangle \approx 5^\circ$) in the kinematical region where no contribution comes from reactions involving the production of an extra pion. Our measurements were performed in a negative pion beam from the ITEP 10-GeV proton synchrotron. The beam intensity amounted to about $(1$–$5) \times 10^5$ π^- mesons per second. The target was placed at the center of the ITEP 3-m magnetic spectrometer, and the trajectories of incident and final pions were recorded in multigap spark chambers arranged in the magnetic field. An incident (final) pion was separated from the electron (positron) background by Cherenkov counters. Emitted pions and protons were discriminated by the time of flight over a base of about 6 m. The equipment used and the procedures for event selection and cross-section calculations were described in detail elsewhere [9, 10].

As was shown in [9, 10], the ΔT-spectra of π^+ mesons grow with increasing ΔT. In the present experiment, these spectra are constrained by the acceptance of the setup at a value of $\Delta T \simeq 150$–180 MeV. The double-differential cross sections $d^2\sigma/d\Omega dT$ for reaction (1) that were integrated over the region $\Delta T \leq 140$ MeV, $\langle d\sigma/d\Omega\rangle_{140}$, were obtained for each target from the total number of events falling within the interval 0–140 MeV and the average value of the solid angle.

Targets from ^{12}C, Al, Cu, In, Ta, and Bi were prepared as sets of identical disks about 8 cm in diameter arranged uniformly space in thin-walled cylinders 9.5 cm long. The disk thickness was chosen in such a way that the total thickness of each target was about 0.1 of the nuclear length. Targets from ^{6}Li, ^{7}Li, H_2O, and D_2O filled the cylinders completely. Targets from H_2O and D_2O were used to study interaction with the ^{16}O nucleus and to calibrate the whole procedure for evaluating cross sections on the basis of measurements of backward elastic $\pi^- p$ scattering [10]. The background from the empty target was measured with the cylinder casing. Six target cylinders were simultaneously placed on a turntable and were in turn exposed to the beam at regular time intervals.

The measurements with Al, Cu, In, Ta, Bi, and D_2O (for calibration) were performed at $T_0 = 0.59$ GeV. The total flux of π^- mesons that traversed the set was 2.44×10^9 particles.

The energy dependence of the cross sections for reaction (1) was measured with the ^{6}Li, ^{7}Li, ^{12}C, H_2O, and D_2O targets and with an empty target at $T_0 = 0.59$, 0.75, and 1.1 GeV. For the ^{6}Li and D_2O targets, the cross sections were measured with and without the Cherenkov counters, whereby it was possible to determine the positron background, which proved to be within the range 10–40%, depending on

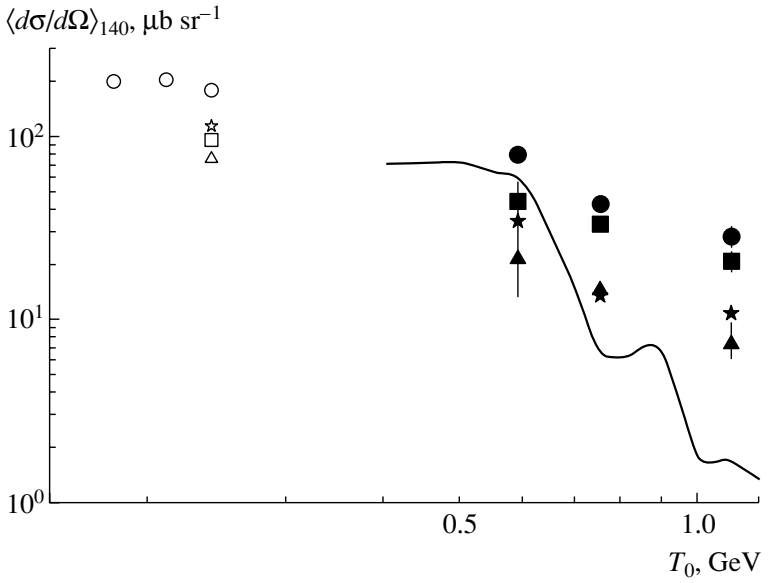

Fig. 2. Energy dependence of the cross sections for the reaction $\pi^- A \to \pi^+ X$, where A = (closed stars) ^{6}Li, (closed triangles) ^{7}Li, (closed boxes) ^{12}C, and (closed circles) ^{16}O that were integrated with respect to ΔT from 0 to 140 MeV at $\theta \approx 5^\circ$. The curve is calculated for the ^{16}O nucleus on the basis of the cascade model for the SSCX mechanism and with allowance for the renormalization of the amplitude for pion single charge exchange in the nucleus. The open symbols represent data for ^{6}Li, ^{7}Li, and ^{12}C nuclei from [16] at $T_0 = 0.24$ GeV and the ^{16}O nucleus from [15] at $T_0 = 0.18$, 0.21, and 0.24 GeV and $\theta = 25^\circ$.

the initial energy and the target type. This value was used to evaluate the cross sections for reaction (1) on the ^{7}Li and ^{12}C targets, for which the measurements were performed without the Cherenkov counters. The positron background originating from the electron contamination of the beam was removed by choosing a nonzero angle of reaction detection. The total fluxes of π^- mesons that traversed the setup with the ^{6}Li, ^{7}Li, and ^{12}C targets at $T_0 = 0.59$, 0.75, and 1.1 GeV amounted to 3.77×10^9, 8.59×10^9, and 9.21×10^9 particles, respectively.

3. *A* DEPENDENCE OF THE INCLUSIVE DCX CROSS SECTION AT $T_0 = 0.59$ GeV

Figure 1 shows the cross sections $\langle d\sigma/d\Omega\rangle_{140}$ at $T_0 = 0.59$ GeV and $\langle\theta\rangle \approx 5^\circ$ for two measurement series: for ^{6}Li, ^{7}Li, ^{12}C, and ^{16}O nuclei (closed circles) and for Al, Cu, In, Ta, Bi, and ^{16}O nuclei (closed squares; the point for ^{16}O is shifted to the right along the A axis in order to obtain a clearer presentation). The displayed errors are purely statistical; the systematic errors do not exceed 10%. The dashed line is a fit of the dependence A^α, where $\alpha = 0.61 \pm 0.08$, to the measured cross sections. The value of α in the fit allowing for the $\langle d\sigma/d\Omega\rangle_{140}$ values obtained in [9] for ^{6}Li, ^{7}Li, and ^{16}O in the case of a broader acceptance in ΔT coverage amounts to $\alpha = 0.68 \pm 0.04$. These values of α are close to 2/3, which is typical of the A dependence of the total cross sections for nuclear targets. The solid curve was calculated on the basis of the cascade model for the SSCX mechanism [10, 14], the Fermi motion of nucleons, the Pauli exclusion principle, absorptive effects, and the renormalization of the amplitude for pion single charge exchange in the nucleus (polarization of nuclear matter) according to [4] being taken into account in this calculation. The curve does not represent a power-law function, but it describes well the observed A dependence. We emphasize that, upon taking into account the renormalization of the amplitude, whereupon the cross sections decrease by a factor of about 2.5 for all nuclei, the description of the emitted-pion spectrum for the ^{16}O nucleus at $T_0 = 0.59$ GeV proved to be better in [9].

For the sake of comparison, Fig. 1 also shows data that we extracted from the π^+-meson spectra in reaction (1) on the ^{6}Li, ^{7}Li, ^{9}Be, ^{12}C, ^{16}O, ^{40}Ca, ^{103}Rh, and ^{208}Pb nuclei from [15, 16] for $T_0 = 0.24$ GeV and $\theta = 25^\circ$ (open circles). It is clear from the figure that the cross section decreases for large A at $T_0 = 0.24$ GeV, but that there is virtually no such effect at $T_0 = 0.59$ GeV. Qualitatively, this is explained by the decrease in the cross section for pion absorption in a nucleus with increasing primary energy.

4. ENERGY DEPENDENCE OF THE INCLUSIVE DCX CROSS SECTION FOR ^{6}Li, ^{7}Li, AND ^{12}C

Figure 2 displays the double-differential DCX cross section measured for the light nuclei ^{6}Li, ^{7}Li, and ^{12}C at $T_0 = 0.59$, 0.75, and 1.1 GeV and $\theta = 5^\circ$ and integrated over the region ΔT from 0 to 140 MeV ($\langle d\sigma/d\Omega\rangle_{140}$, closed stars, triangles, and boxes, respectively). The closed circles represent combined data of the present experiment and previous data for the ^{16}O nucleus from [9, 10]. The open stars, triangles, boxes, and circles correspond to the cross sections extracted from data reported in [15, 16] for $T_0 = 0.24$ GeV and $\theta = 25^\circ$. It is clear from the figure that a relatively weak (as compared to the results of the calculation based on the SSCX model, which are shown by the solid curve in Fig. 2) energy dependence observed for ^{16}O manifests itself for other light nuclei as well.

As was shown in [4], a fast decrease in the cross section for $T_0 \gtrsim 0.6$ GeV in the SSCX model with π^0 in the intermediate state (the curve in Fig. 2) is associated with the decrease in the amplitude of π^0-meson single charge exchange in this energy region and is independent of the type of target nucleus. A relatively weak energy dependence of the cross section for some nuclei is an additional argument in favor of a significant contribution from new DCX mechanisms in the region being studied. Indeed, it was shown in [17] that Glauber inelastic rescattering (first of all, the two-pion contribution) in the intermediate state must be taken into account in the calculations at $T_0 \gtrsim 0.6$ GeV. For example, the cross section (2) was represented in [18] as the sum of two contributions: that which involves intermediate π^0 and that which involves an intermediate two-pion state. The latter was estimated in the Gribov–Glauber approximation for the one-pion-exchange model. It was shown that the energy dependence of the cross section at $T_0 \gtrsim 1$ GeV is completely determined by sequential charge exchanges accompanied by Glauber inelastic rescattering in the intermediate state. We can expect that the A dependence of the cross section would also obey the $A^{2/3}$ law in this case.

5. CONCLUSION

The A dependence of the cross section for inclusive pion double charge exchange has been measured for a set of nuclei from ^{6}Li to ^{209}Bi at $T_0 = 0.59$ GeV and $\langle\theta\rangle \approx 5^\circ$ in the kinematical region where there is no contribution from reactions involving the production of an extra pion. The A dependence has been calculated within the model of two sequential single charge exchanges. The measured A dependence is in good agreement with the results of the calculation that takes into account the renormalization of the amplitude for pion single charge exchange in nuclear matter. The inclusive forward cross section for pion double charge exchange has been measured for the ^{6}Li, ^{7}Li, and ^{12}C nuclei over the energy range $T_0 = 0.59$–1.1 GeV. A relatively weak energy dependence of the cross section for the ^{6}Li, ^{7}Li, and ^{12}C nuclei agrees with the analogous dependence measured previously for the ^{16}O nucleus. These results are at odds with the predictions of the SSCX model, according to which the cross sections in question must decrease fast. We consider this as an additional piece of evidence of a dominant contribution from inelastic Glauber rescattering at $T_0 \gtrsim 0.6$ GeV.

ACKNOWLEDGMENTS

We are grateful to the personnel of the 3-m spectrometer, the PSP-2 measurement complex, and the ITEP accelerator for their assistance in performing the experiment. We are also indebted to A.B. Kaidalov for permanent interest in this study and numerous discussions.

This work was supported in part by the Federal Target-Oriented Program for Science and Technology (grant no. 40.052.1.1.1113) and the Program for Support of Leading Scientific Schools (grant no. 1867.2003.02).

REFERENCES

1. A. De Shalit, S. D. Drell, and H. Lipkin, *Nuclear News* (Weizmann Inst., Rehovot, 1961).
2. Yu. A. Batusov *et al.*, Zh. Éksp. Teor. Fiz. **46**, 817 (1964) [Sov. Phys. JETP **19**, 557 (1964)].
3. M. B. Johnson and C. L. Morris, Annu. Rev. Nucl. Part. Sci. **43**, 165 (1993); H. Clement, Prog. Part. Nucl. Phys. **29**, 175 (1992); R. P. Jibuti and R. Ya. Kezerashvili, Fiz. Élem. Chastits At. Yadra **16**, 1173 (1985) [Sov. J. Part. Nucl. **16**, 519 (1985)].
4. E. Oset and D. Strottman, Phys. Rev. Lett. **70**, 146 (1993); E. Oset, D. Strottman, H. Toki, and J. Navarro, Phys. Rev. C **48**, 2395 (1993).
5. B. M. Abramov *et al.*, in *Proceedings of the International Conference "Mesons and Nuclei at Intermediate Energies", Dubna, Russia, 1994*, Ed. by M. Kh. Khankhasayev and Zh. B. Kurmanov (World Sci., Singapore, 1995), p. 516.
6. J.-B. Jeanneret, M. Bogdanski, and E. Jeannet, Nucl. Phys. A **350**, 345 (1980).
7. A. V. Arefyev *et al.*, *Interaction of High-Energy Particles with Nuclei and New Nuclear-Like Systems* (Atomizdat, Moscow, 1974), Vol. 2, p. 35 [in Russian].
8. I. I. Vorob'ev, L. S. Novikov, and A. F. Buzulutskov, Yad. Fiz. **36**, 417 (1982) [Sov. J. Nucl. Phys. **36**, 243 (1982)].

9. B. M. Abramov *et al.*, Yad. Fiz. **65**, 253 (2002) [Phys. At. Nucl. **65**, 229 (2002)].
10. B. M. Abramov *et al.*, Nucl. Phys. A **723**, 389 (2003); Yad. Fiz. **59**, 399 (1996) [Phys. At. Nucl. **59**, 376 (1996)].
11. B. M. Abramov *et al.*, AIP Conf. Proc. **603**, 519 (2001).
12. I. A. Radkevich, V. V. Vladimirskiĭ, V. V. Sokolovskiĭ, and A. M. Blagorodov, Prib. Tekh. Éksp., No. 4, 54 (1984).
13. V. V. Vladimirsky *et al.*, Yad. Fiz. **66**, 729 (2003) [Phys. At. Nucl. **66**, 700 (2003)]; B. A. Abramov *et al.*, Pis'ma Zh. Éksp. Teor. Fiz. **80**, 244 (2004) [JETP Lett. **80**, 214 (2004)].
14. M. J. Vicente Vacas, M. Kh. Khankhasayev, and S. G. Mashnik, nucl-th/9412023.
15. S. A. Wood *et al.*, Phys. Rev. C **46**, 1903 (1992).
16. P. A. M. Gram, in *Pion–Nucleus Physics: Future Directions and New Facilities at LAMPF*, Ed. by R. J. Peterson and D. D. Strottman (AIP, New York, 1988), p. 79.
17. A. B. Kaidalov and A. P. Krutenkova, Yad. Fiz. **60**, 1334 (1997) [Phys. At. Nucl. **60**, 1206 (1997)].
18. A. B. Kaidalov and A. P. Krutenkova, J. Phys. G **27**, 893 (2001).

Translated by M. Kobrinsky

Physics of Atomic Nuclei, Vol. 68, No. 8, 2005, pp. 1288–1293. Translated from Yadernaya Fizika, Vol. 68, No. 8, 2005, pp. 1341–1346.

TRIBUTE TO THE 90th BIRTHDAY OF V.V. VLADIMIRSKY

Investigation of *pn* Correlations in ^{4}He*p* Interactions at a Momentum of 5 GeV/*c*

A. V. Blinov*, V. F. Turov, and M. V. Chadeyeva*****

Institute of Theoretical and Experimental Physics, Bol'shaya Cheremushkinskaya ul. 25, Moscow, 117259 Russia

Received November 12, 2004; in final form, February 10, 2005

Abstract—Proton–neutron correlations in ^{4}He*p* interactions are studied in an exclusive experiment by using a 2-m bubble chamber exposed to a 5-GeV/*c* beam of α particles (the kinetic energy of the protons in the nucleus rest frame is $T_p = 620$ MeV). Data on the production of *pn* pairs in 4π geometry for three channels, where it is possible to reconstruct the neutron momentum unambiguously, are used to determine the *pn* correlation function in ^{4}He*p* interactions. The experimental results are compared with the predictions of a modified Lednicky–Lyuboshitz model. The value obtained for the root-mean-square radius of the *pn*-emission region is $R_{pn} = 2.1 \pm 0.3$ fm. The dependence of the correlation function on the modulus of the total momentum of the emitted nucleon pair and on the direction of the momentum transfer is studied. An indication that the emission of a *pn* pair proceeds predominantly through the production of a virtual deuteron is obtained. © *2005 Pleiades Publishing, Inc.*

V.V. Vladimirsky has always been keenly interested in the development of the methodology of liquid-hydrogen bubble chambers. He initiated work that resulted in successfully designing and commissioning a 80-cm liquid-hydrogen bubble chamber at the Institute of Theoretical and Experimental Physics (ITEP, Moscow) by a team headed by Ya.M. Selektor. That chamber was used in a series of experiments devoted to studying the interactions of light nuclei (^{3}H and ^{3}He) with a target proton at intermediate energies. Experiments at the ITEP 2-m liquid-hydrogen bubble chamber that were aimed at exploring ^{4}He*p* interactions at 2.7 and 5 GeV/*c* were a logical development of those studies. The present article reports on a continuation of an analysis of experimental data obtained throughout these exposures.

1. INTRODUCTION

Nuclear-reaction studies based on analyzing pair correlations of emitted particles (two-particle interferometry) [1, 2] have aroused interest in recent years. For studying correlations, of particular interest are data on the production of a two-nucleon system in reactions involving the most compact nucleus ^{4}He,

$$h + {}^4\mathrm{He} \to (NN) + X. \qquad (1)$$

Here, h is an incident particle, NN is the emitted nucleon pair, and X is the system of secondary particles and nuclear fragments. Such data make it possible to study special features of the correlation function for the emitted nucleon pair, $C_{NN}(q_{\mathrm{inv}})$ ($q_{\mathrm{inv}} = \frac{1}{2}|\mathbf{p}_1^* - \mathbf{p}_2^*|$, where $\mathbf{p}_1^*$ and $\mathbf{p}_2^*$ are the nucleon momenta in the rest frame of the pair), in the case where the emission-region dimension is commensurate with the range of nuclear forces. However, there are virtually no such data in the literature.

In our previous study [3], which was devoted to exploring *pp* correlations, we used an experimental scheme where the 2-m liquid-hydrogen bubble chamber is exposed to a beam of 5-GeV/*c* ^{4}He nuclei, this corresponding to reaction (1) on protons, whose kinetic energy in the rest frame of the nucleus is $T_p = 620$ MeV. The resulting data in 4π geometry for six main ^{4}He*p*-interaction channels involving the production of two protons were used to determine the total *pp* correlation function C_{pp} and the two-proton correlation functions for individual interaction channels. Also, the root-mean-square (rms) radius of the *pp*-emission region in ^{4}He*p* interactions was found to be $R_{pp} = 1.6 \pm 0.3$ fm, which is close to the rms radius of the nucleus, $R_{^4\mathrm{He}} = 1.53$–1.66 fm (see discussion in [3]).

In [4], the correlation function for two protons in reaction (1) was determined by employing an electron beam of energy 4.46 GeV. The value of $R_{pp} = 1.6$ fm,

*e-mail: blinov@itep.ru
**e-mail: turov@itep.ru
***e-mail: marina.chadeyeva@itep.ru

which was obtained there with a systematic error of about 3%, indicates that this quantity takes close values for strong and electromagnetic interactions.

As to studying pn correlations in reaction (1), there are no relevant data in the literature, as far as we know. (The correlation function for a pn pair was determined in [5] only for heavy-ion interactions.) However, such data and their comparison with the corresponding data for pp production are obviously of great interest.

In this study, the pn correlation function and the rms radius of the pn-emission region are determined from an analysis of data accumulated over the exposure of the liquid-hydrogen bubble chamber to a 5-GeV/c ^{4}He beam. We selected only events in the ^{4}Hep-interaction channels featuring one neutron in the final state, in which case it is possible to reconstruct and kinematically balance the neutron momentum. We emphasize that, for the above primary momentum, secondary neutrons can be unambiguously identified for the above channels almost over the entire phase space.

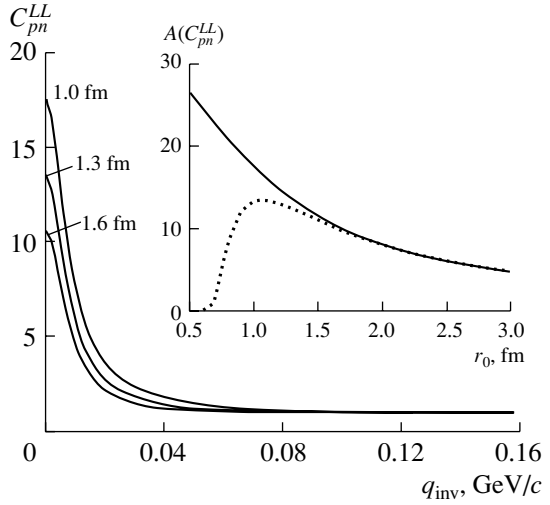

Fig. 1. Proton–neutron correlation function $C_{pn}^{LL}(q_{\text{inv}})$ calculated within the theoretical model used (see main body of the text) for the chosen values of r_0. The inset displays the r_0 dependence of the correlation-function "amplitude" $A(C_{pn}^{LL})$ within (solid curve) the theoretical model used and (dotted curve) the conventional Lednicky–Lyuboshitz model.

2. THEORETICAL MODEL

In this study, pn correlations are analyzed within the same theoretical scheme as that which was used in [3] to analyze pp correlations. We calculated the pn correlation function within the simplest modification of the Lednicky–Lyuboshitz model [6] as a function of the spacetime parameters r_0 and τ_0 (the rms radius of the emission region is $R = \sqrt{3}r_0$). For the components of the pn wave function within the range of nuclear forces ($R \leq 2$ fm), we use an exact solution to the Schrödinger equation for the square-well potential

$$U(r) = \begin{cases} -K^2/m, & r \leq D, \\ 0, & r > D, \end{cases} \qquad (2)$$

where K and D are the well parameters and m is the nucleon mass.

It is obviously of interest to calculate the pn correlation function with a realistic NN potential, but this is beyond the scope of the present study. As was stated in [4], the pp correlation function in the region $R \leq 2$ fm is weakly sensitive to the choice of potential (simple-well, Reid, or Tabakin potentials), while the values of the rms radius that appear in a fit of data from [4] with various potentials differ within 3%, which is taken in that study for the theoretical uncertainty in the calculation.

The correlation function C_{pn} averaged over the distribution of unpolarized nucleon sources has the form

$$C_{pn} = 1 + \frac{1}{4}(C^{(0)} + 3C^{(1)}), \qquad (3)$$

where the functions $C^{(0)}$ and $C^{(1)}$ describe the contributions of singlet and triplet states, respectively. In the calculations, the length and effective range of pn interaction were taken to be $f_0^{pn} = 23.7$ fm and $d_0^{pn} = 2.7$ fm in the singlet and $f_1^{pn} = -5.4$ fm and $d_1^{pn} = 1.7$ fm in the triplet state [7, 8]. For the well parameters, we used, respectively, the values of $K_0^{pn} = 0.11$ GeV/c and $D_0^{pn} = 0.983d_0^{pn}$ and the values of $K_1^{pn} = 0.18$ GeV/c and $D_1^{pn} = 1.14d_1^{pn}$ [7, 9]. We also used the approximation of equal emission times in the rest frame of nucleons ($\tau_0 = 0$).

For various values of r_0, Fig. 1 shows the pn correlation function $C_{pn}^{LL}(q_{\text{inv}})$ calculated on the basis of the theoretical model used. The inset displays the r_0 dependence of the maximum value of the correlation function, $A(C_{pn}^{LL})$, within the theoretical model used (solid curve) and the conventional Lednicky–Lyuboshitz model [6] (dotted curve). It is clear from the figure that, in the region $r_0 \geq 1.5$ fm, the curves virtually coincide, but that, for $r_0 \leq 1$ fm, the results differ significantly.

Reaction channels involving the production of the pn system in ^{4}Hep interaction at a momentum of 5 GeV/c (T_p = 620 MeV) that are chosen for our analysis

Reaction channel	Number of events	Number of events satisfying the selection rule $q_{\text{inv}} < 0.4$ GeV/c
^{4}He$p \to dppn$	2567	1871
^{4}He$p \to {}^3$ Hepn	2507	130
^{4}He$p \to tpn\pi^+$	362	323
^{4}He$p \to (pn)X$	5436	2324

3. DESCRIPTION OF THE EXPERIMENT

The 2-m ITEP liquid-hydrogen bubble chamber was exposed to a separated beam of 5-GeV/c ^{4}He nuclei. The chamber was placed in a magnetic field of strength 0.92 T. Background particles in the incident beam (predominantly, deuterons) were reliably discriminated by track ionization. About 120 00 photographs were obtained with an average load intensity of about 5 to 8 particles per chamber expansion. In all, 18 736 interactions were measured. The total cross section for ^{4}Hep interaction was determined in a standard way [10] by counting the number of interactions in a chosen chamber volume and was found to be 121.5 ± 2.9 mb (the quoted error is purely statistical). The systematic error in the absolute normalization of the cross section is about 3%. In order to identify particles in αp interactions, we used a procedure that is standard for chamber experiments and which consists in choosing mass hypotheses with allowance for data on the visible ionization of secondary-particle tracks. The methodology of the experiment and the procedure for data processing are described in more detail elsewhere [10, 11]. We note that the experimental procedure used makes it possible to analyze data in 4π geometry.

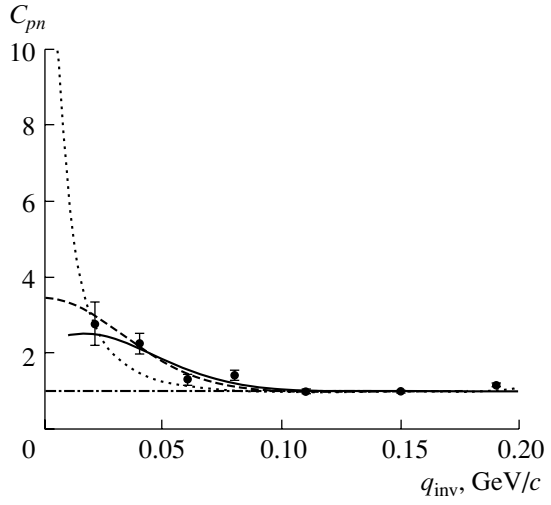

Fig. 2. Correlation function C_{pn} in ^{4}Hep interactions versus q_{inv}. The curves represent the predictions of the modified Lednicky–Lyuboshitz model with allowance for the measurement errors in the forms specified by (solid curve) Eqs. (6)–(8) and (dashed curve) Eqs. (6)–(9) and (dotted curve) without allowance for these errors.

For a further analysis, we selected only events in the ^{4}Hep-interaction channel involving one neutron in the final state, in which case it is possible to reconstruct and kinematically balance the neutron momentum. At the energy value being considered, there are three such channels, which are listed in the table, along with event statistics collected for each channel in this experiment. The total number of events in these channels exceeds 75% of total statistics for the reactions involving the simultaneous production of a proton and a neutron. For the channel ^{4}He$p \to dppn$, where two protons are produced, we selected, for our analysis, the spectator proton, which is the slowest one in the rest frame of the nucleus.

As in [3], the subsequent correlation analysis is performed for events selected according to the condition

$$q_{\text{inv}} < q_{\text{max}}, \tag{4}$$

where $q_{\text{max}} = 0.4$ GeV/c (the number of events in each channel that satisfy this selection criterion is given in the table).

For the correlation function C_{pn}, we employ the standard definition

$$C_{pn} = \text{const} \cdot \frac{N_c}{N_{\text{nc}}}. \tag{5}$$

Here const is a normalization constant that is defined in such a way that $C_{pn} \to 1$ at rather large q_{inv}, in which case there are no correlations, and N_c and N_{nc} are the numbers of events for a given q_{inv} that correspond to the experimentally observed (correlated) and background (noncorrelated) distributions, respectively. The background distribution was generated by "mixing" of the momenta of particles from different events.

4. RESULTS AND CONCLUSIONS

The points in Fig. 2 represent the pn correlation function C_{pn} in ^{4}Hep interactions versus q_{inv} according to the results of this experiment (only statistical errors are shown). In order to determine the spacetime dimension of the emission region for the pn pair, we approximated these data by the theoretical curve calculated within the modified Lednicky–Lyuboshitz model (see Section 2). In approximating experimental

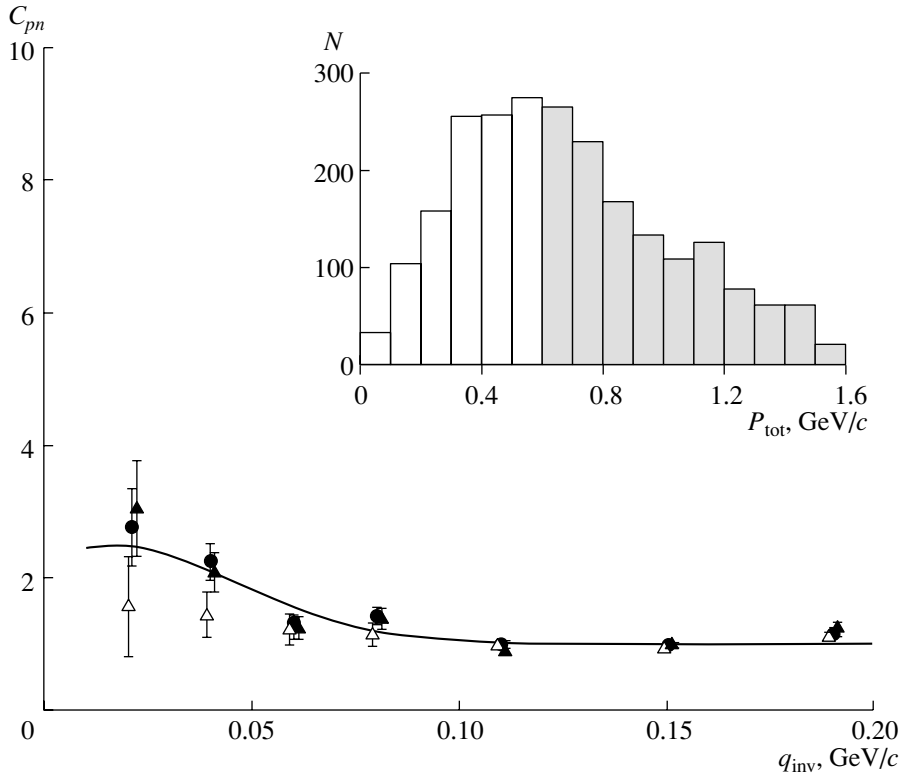

Fig. 3. Correlation function C_{pn} in ^{4}Hep interactions versus q_{inv} for P_{tot} subjected to the constraints (▲) $P_{\text{tot}} < 0.6$ GeV/c and (△) $P_{\text{tot}} > 0.6$ GeV/c and (●) for unconstrained P_{tot}. The inset displays the distribution with respect to P_{tot}, where the shadowed region corresponds to $P_{\text{tot}} > 0.6$ GeV/c. The curve represents the prediction of the modified Lednicky–Lyuboshitz model.

data, we took into account the experimental resolution as follows:

$$\tilde{C}_{pn}^{LL}(q_{\text{inv}}) = \int C_{pn}^{LL}(q'_{\text{inv}})\Phi(q_{\text{inv}}, q'_{\text{inv}}, \sigma(q'_{\text{inv}}))\, dq'_{\text{inv}}. \tag{6}$$

Here, $\tilde{C}_{pn}^{LL}$ and C_{pn}^{LL} are the model predictions with and without allowance for the measurement errors, respectively; Φ is the distribution density for the quantity q_{inv}; and $\sigma(q_{\text{inv}})$ is the experimental (systematic) error in determining q_{inv}. This error is determined primarily by the error in the reconstructed neutron momentum, is virtually independent of q_{inv} in the region of our measurement, and is on average

$$\sigma(q_{\text{inv}}) = 0.03 \text{ GeV}/c. \tag{7}$$

In approximating the data by the theoretical dependence, we employed the simplest Gaussian form for Φ,

$$\Phi = G(q_{\text{inv}}, q'_{\text{inv}}, \sigma(q'_{\text{inv}})) \tag{8}$$
$$= \frac{1}{\sqrt{2\pi}\sigma(q'_{\text{inv}})} \exp\left(-\frac{(q_{\text{inv}} - q'_{\text{inv}})^2}{2\sigma^2(q'_{\text{inv}})}\right),$$

and a form that takes into account the behavior of the distribution of the absolute value in the vicinity of zero,

$$\Phi = G(q_{\text{inv}}, q'_{\text{inv}}, \sigma(q'_{\text{inv}})) + G(-q_{\text{inv}}, q'_{\text{inv}}, \sigma(q'_{\text{inv}})). \tag{9}$$

The distinctions between the distributions in (8) and (9) become significant for $q_{\text{inv}} \leq \sigma(q_{\text{inv}})$. The value of $R_{pn} = 2.1 \pm 0.3$ fm ($\chi^2/\text{NDF} = 6.4/3$) for the rms radius of the pn-emission region corresponds to the best approximation of the data by the theoretical curve at $q_{\text{inv}} < 0.1$ GeV/c with allowance for the measurement errors in the form (8). Note that this value significantly exceeds the radius of the ^{4}He nucleus. The approximation of the data with allowance for the error by this method in the range $0.04 < q_{\text{inv}} < 0.1$ GeV/c introduces virtually no changes in this result. But if the measurement errors are taken into account in the form (9), this leads to a still greater value of $R_{pn} = 2.8 \pm 0.4$ fm ($\chi^2/\text{NDF} = 6.6/3$). It is worth noting that, in contrast to what we have for pp correlations (see [3]), the emission-region dimension determined from the approximation of the data on pn correlations proves to be highly sensitive to the method for taking into account the measurement errors. This is because the correlation function exhibits radically different types of behavior in the vicinity of

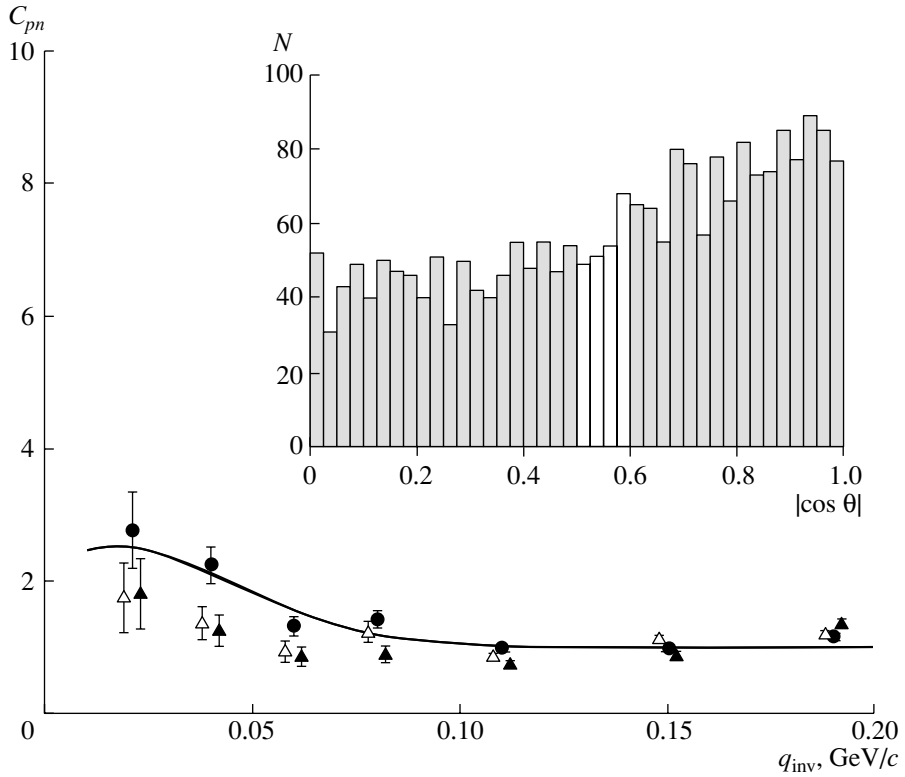

Fig. 4. Correlation function C_{pn} in ^{4}Hep interactions versus q_{inv} for $\cos\theta$ subjected to the constraints (△) $|\cos\theta| < 0.5$ and (▲) $|\cos\theta| > 0.6$ and (●) for unconstrained $|\cos\theta|$. The inset displays the distribution with respect to $|\cos\theta|$, where the shadowed regions correspond to the above constraints. The curve is the prediction of the modified Lednicky–Lyuboshitz model.

zero in these two cases; therefore, the contribution from the measurement errors for $q_{\text{inv}} \to 0$ is different. Since, however, the experimental error is not at all known for $q_{\text{inv}} < 0.015$ GeV/c, it is impossible to take completely into account the experimental resolution for the pn correlation function.

The curves in Fig. 2 represent the predictions of the modified Lednicky–Lyuboshitz model with allowance for the measurement errors in the form (6)–(8) (solid curve) or in the form (6)–(9) (dashed curve), as well as without allowance for the measurement errors (dotted curve). These curves were calculated for the parameter r_0 corresponding to $R_{pn} = 2.1$ fm (solid and the dotted curves) or $R_{pn} = 2.8$ fm (dashed curve). It is clear from the figure that the inclusion of the measurement errors significantly improves the agreement between the theoretical and experimental results (for $q_{\text{inv}} < 0.1$ GeV/c, $\chi^2 = 19.7$ for the dotted curve, this significantly exceeding the values obtained with allowance for the measurement errors).

Figure 3 displays the correlation function C_{pn} versus q_{inv} for the case where the absolute value of the sum of the particle momenta in the pn system in the rest frame of the nucleus is constrained as $P_{\text{tot}} < 0.6$ GeV/c (closed triangles) or as $P_{\text{tot}} > 0.6$ GeV/c (open triangles), as well as for the case of unconstrained P_{tot} (circles). The curve represents the predictions of the modified Lednicky–Lyuboshitz model for unconstrained P_{tot} with allowance for the measurement errors in the form specified by Eqs. (6)–(8), the parameter r_0 corresponding to the rms radius of $R_{pn} = 2.1$ fm.

The inset in Fig. 3 shows the P_{tot} distribution for events in three channels involving the production of a pn pair [for the constraint in (4)]. It is clear from Fig. 3 that, in contrast to C_{pp} (see [3]), C_{pn} is virtually independent, within the errors, of constraints imposed on P_{tot}. As differentiated from the case of pp emission, there is even some trend toward the reduction of the correlation effect for $P_{\text{tot}} > 0.6$ GeV/c. We emphasize that independent correlation experiments based on electronics are highly desirable for studying the properties of C_{pn} at high P_{tot}.

The fact that C_{pn} is independent of the total momentum of emitted particles and the fact that the value obtained for the rms radius of the emission region is nearly coincident with the charge rms radius and the close (to it) value of the rms radius of the deuteron-density distribution, $R_d = 1.96$–2.13 fm [12], suggest that the emission of pn

pairs in the case being considered is likely to occur through the production of a virtual deuteron.

For events in three channels involving the production of a pn pair [the constraint in (4) being imposed], the inset in Fig. 4 displays the distribution with respect to $|\cos\theta|$, where θ is the angle between the vectors $\mathbf{q}$ and $\mathbf{p}_{\text{in}}$ ($\mathbf{q}$ is the momentum transfer to the emitted nucleon pair, and $\mathbf{p}_{\text{in}}$ is the momentum of the incident proton in the rest frame of the nucleus).

Figure 4 presents the pn correlation function C_{pn} versus the momentum transfer q_{inv} for the case where $\cos\theta$ is constrained as $|\cos\theta| < 0.5$ (open triangles) or as $|\cos\theta| > 0.6$ (closed triangles), as well as for the case of unconstrained $|\cos\theta|$ (circles). The curve represents the predictions of the modified Lednicky–Lyuboshitz model for unconstrained $|\cos\theta|$ with allowance for the measurement errors in the form specified by Eqs. (6)–(8), the parameter r_0 corresponding to $R = 2.1$ fm. Within the errors, the distributions in Fig. 4 are in good agreement with one another. This indicates (see [2]) that the region of pn-pair emission in ^{4}Hep interactions is spherically symmetric.

5. CONCLUSION

With the aid of the 2-m liquid-hydrogen bubble chamber exposed to a 5-GeV/c beam of α particles, the correlation function for a pn pair emitted in ^{4}Hep interactions has been measured for first time. The value obtained for the rms radius of the pn-emission region in ^{4}Hep interactions is $R_{pn} = 2.1 \pm 0.3$ fm, which is close to the rms radius of the deuteron. We have studied the dependence of the correlation function on the absolute value of the total momentum of the emitted pair and on the direction of the momentum transfer. We have found that, in contrast to C_{pp}, the correlation function C_{pn} is virtually independent of the total momentum of the emitted pair. These results give reasons to assume that the emission of a pn pair proceeds predominantly through the production of a virtual deuteron.

ACKNOWLEDGMENTS

We are grateful to G.A. Leksin and A.V. Stavinsky for reading the manuscript and for valuable comments.

This work was supported in part by the Russian Foundation for Basic Research (project no. 04-02-16500).

REFERENCES

1. G. I. Kopylov and M. I. Podgoretskiĭ, Yad. Fiz. **15**, 392 (1972) [Sov. J. Nucl. Phys. **15**, 219 (1972)]; S. E. Koonin, Phys. Lett. B **70B**, 43 (1977); U. A. Wiedemann and U. Heinz, Phys. Rep. **319**, 145 (1999); R. M. Wiener, Phys. Rep. **327**, 249 (2000).
2. D. H. Boal, C.-K. Gelbke, and B. K. Jennings, Rev. Mod. Phys. **62**, 553 (1990).
3. A. V. Blinov, V. F. Turov, and M. V. Chadeeva, Yad. Fiz. **67**, 1546 (2004) [Phys. At. Nucl. **67**, 1523 (2004)].
4. CLAS Collab. (A. V. Stavinsky *et al.*), Phys. Rev. Lett. **93**, 192301 (2004).
5. R. A. Kryger *et al.*, Phys. Rev. C **46**, 1887 (1992); CHIC Collab. (M. Cronqvist *et al.*), Phys. Lett. B **317**, 505 (1993); R. Ghetti *et al.*, Nucl. Phys. A **674**, 277 (2000).
6. R. Lednitskiĭ and V. L. Lyuboshits, Yad. Fiz. **35**, 1316 (1982) [Sov. J. Nucl. Phys. **35**, 770 (1982)].
7. A. Bohr and B. R. Mottelson, *Nuclear Structure* (Benjamin, New York, 1969; Mir, Moscow, 1971).
8. L. D. Landau and E. M. Lifshitz, *Quantum Mechanics: Non-Relativistic Theory* (Nauka, Moscow, 1974; Pergamon, Oxford, 1977).
9. J. M. Blatt and J. D. Jackson, Phys. Rev. **76**, 18 (1949).
10. A. V. Blinov *et al.*, Yad. Fiz. **64**, 975 (2001) [Phys. At. Nucl. **64**, 907 (2001)].
11. A. V. Blinov, V. F. Turov, and M. V. Chadeeva, Yad. Fiz. **65**, 1340 (2002) [Phys. At. Nucl. **65**, 1307 (2002)].
12. R. W. Berard *et al.*, Phys. Lett. B **47B**, 355 (1973); G. G. Simon, Ch. Schmitt, and V. H. Walther, Nucl. Phys. A **364**, 285 (1981); S. Klarsfeld *et al.*, Nucl. Phys. A **456**, 373 (1986); I. Sick and D. Trautmann, Phys. Lett. B **375**, 16 (1996).

Translated by M. Kobrinsky

Physics of Atomic Nuclei, Vol. 68, No. 8, 2005, pp. 1294–1302. From Yadernaya Fizika, Vol. 68, No. 8, 2005, pp. 1347–1355.

TRIBUTE TO THE 90th BIRTHDAY OF V.V. VLADIMIRSKY

Dynamics of Confined Gluons*

Yu. A. Simonov

Institute of Theoretical and Experimental Physics, Bol'shaya Cheremushkinskaya ul. 25, Moscow, 117259 Russia

Received November 4, 2004

Abstract—Propagation of gluons in the confining vacuum is studied in the framework of background perturbation theory, where nonperturbative background contains confining correlators. Two settings of the problem are considered. In the first, the confined gluon evolves in time together with the static quark and antiquark forming the one-gluon static hybrid. The hybrid spectrum is calculated in terms of string tension and is in agreement with earlier analytic and lattice calculations. In the second setting, the confined gluon is exchanged between quarks and the gluon Green's function is calculated, giving rise to the Coulomb potential modified at large distances. The resulting screening radius of 0.5 fm presents a problem when confronted with lattice and experimental data. A possible solution of this discrepancy is discussed.

1. INTRODUCTION

Gluons are known to be confined, but this property is never taken into account in standard perturbation theory (SPT). As an argument, one refers to the small-distance (high-momentum) domain, where SPT is assumed to be valid. Beyond this domain, SPT displays unphysical singularities and, moreover, the very notion of gluon should be properly defined. This can be done in the framework of background perturbation theory (BPT) [1]. The formalism of this kind, where the background is assumed to be nonperturbative with confining properties, was developed in [2, 3].

One immediate consequence of this new BPT is that all gluons are confined and, moreover, the unphysical singularities of SPT (Landau ghost poles and branch points as well as IR renormalons) are removed from the theory [2, 3].

The confined gluons can form several types of systems: glueballs [4], hybrids [5, 6], and gluelumps [7]. The analytic calculations in the quoted papers predict a spectrum that, in all cases, is in good agreement with lattice data and has a very simple form depending only on string tension σ and α_s.

The main subject of the present paper is the study of the gluon-exchange interaction between Q and $\bar{Q}$ when the gluon is confined, which can be called the confined Coulomb interaction $V_{\rm C}^*(R)$. One can expect that, at small distances, say $R < 1$ GeV^{-1}, the confined Coulomb potential coincides with the standard Coulomb potential $V_{\rm C}(R) = -C_2\alpha_s(R)/R$, $C_2 = (N_c^2 - 1)/(2N_c)$.

At large R, the confined gluon is expected to produce the screening of the Coulomb interaction. At first glance, the screening mass should coincide with the lowest hybrid mass of the static hybrid. However, as will be shown below, this naive expectation fails since gluon propagation between quarks goes not only in time (where hybrid mass is in the proper place) but also in distance R (where, in addition, asymptotics of wave functions enters). As a result, one obtains a more complicated behavior, which we display both numerically and analytically.

The plan of the paper is as follows. In Section 2, the general formulas of BPT are written and approximations are discussed. In Section 3, a simple toy model is suggested to illustrate the method and possible qualitative outcome.

In Section 4, the method is applied to calculate the static hybrid Green's function and spectrum in a way different from that used before, in [6]. In Section 5, results of the previous section are used to calculate the Green's function of the confined gluon exchanged between static quarks, and the resulting screened Coulomb potential. Physical consequences and prospects are discussed in the concluding section.

2. DYNAMICS OF A CONFINED GLUON: GENERALITIES

In the field correlator method (FCM), the dynamical picture of a confined gluon is simple and self-consistent: the gluon (its corresponding field is a_μ) moves in the strong and disordered vacuum field B_μ

*This article was submitted by the author in English.

characterized by the correlators of the field $F_{\mu\nu}(B)$, so that the total gluonic field A_μ can be written as

$$A_\mu = B_\mu + a_\mu. \tag{1}$$

Here, the problem of separation of A_μ into B_μ and a_μ and that of double counting are resolved technically by the use of the so-called 't Hooft identity [3], and one can integrate and average over both DB_μ and Da_μ, so that the partition function is

$$Z = \frac{1}{N'}\int DB_\mu Z(J,B), \tag{2}$$

$$Z(J,B) = \int Da_\mu \exp(-S(a+B) + J(a+B))$$

and S is the standard QCD Euclidean action including ghost and gauge-fixing terms (see [2, 3] for details).

In what follows, we shall be interested in the gluon propagation in the field of static (confined) quark Q and antiquark $\bar{Q}$. The starting point for the gauge-invariant study of this process is the total Green's function of the $Q\bar{Q}$ system, which is proportional to the Wilson loop:

$$\langle W(A)\rangle \equiv \langle\langle W(B+a)\rangle\rangle_{B,a} = \langle\langle W(B+a)\rangle_a\rangle_B, \tag{3}$$

$$W(A) = \mathrm{tr}P\exp\left[ig\int\limits_C A_\mu dz_\mu\right]. \tag{4}$$

The Wilson loop is assumed to be the closed rectangular contour $R\times T_0$ in the (x_1, x_4) plane.

One may expand in ga_μ keeping B_μ intact and this will give the BPT series ([1, 2]; see [3] for details), the first terms being

$$\langle\langle W(B+a)\rangle\rangle_{B,a} = \langle W^{(0)}(B)\rangle_B - g^2\langle W^{(2)}(B,x,y)G_{\mu\nu}(x,y)\rangle_B dx_\mu dy_\nu + \ldots. \tag{5}$$

For the chosen contour C and the Feynman gauge of field B_μ and Fock–Feynman–Schwinger representation (FFSR) for $G_{\mu\nu}$, $W^{(2)}$ and $G_{\mu\nu}$ can be written as

$$W^{(2)} = C_2(f)\Phi^{(-)}_{\alpha\beta}(x,y)\Phi^{(+)}_{\alpha'\beta'}(y,x), \tag{6}$$

$$G_{\mu\nu}(x,y) = \int\limits_0^\infty ds(Dz)_{xy}e^{-K} \times \left\{\Phi^{(\mathrm{adj})}(x,y)P\exp\left(2g\int\limits_0^s F_{\rho\sigma}(z(\tau))dz\right)\right\}^{(\mu\nu)}_{\beta\alpha,\beta'\alpha'}, \tag{7}$$

where $\Phi^{(\pm)}(x,y)$ are the future/past pieces of the Wilson loop $W^{(0)}(B) = P\exp(ig\oint B_\mu dz_\mu)$, obtained by cutting it at points x and y. Note that the adjoint phase factor $\Phi^{(\mathrm{adj})}(x,y) \equiv \exp(ig\int_y^x B_\mu dz_\mu)$ from $G_{\mu\nu}$, which can be written as the product

$$\Phi^{(\mathrm{adj})}(x,y) = \Phi_{\beta\alpha}(y,x)\Phi_{\beta'\alpha'}(x,y), \tag{8}$$

produces in the total construction two closed Wilson loops (see [2, 3, 6] for pictures and discussion):

$$\Phi^{(-)}\Phi^{(\mathrm{adj})}\Phi^{(+)} = W^{(-)}_\sigma(x,y)W^{(+)}_\sigma(y,x). \tag{9}$$

Note the subscript σ in (9) which implies the color-magnetic spin factor [the last factor on the right-hand side of (7)] entering into all Wilson lines including $\Phi^{(\mathrm{adj})}$. The averaging of (9) over fields B_μ can be easily done at large N_c:

$$\langle W^{(2)}_{\mu\nu}G_{\mu\nu}\rangle_B = G^{(0)}\langle W^{(-)}_\sigma(x,y)\rangle_B\langle W^{(+)}_\sigma(y,x)\rangle_B, \tag{10}$$

where $G^{(0)}$ denotes the integral $\int ds(Dz)_{xy}e^{-K}$. In the FCM, one obtains for $\langle W\rangle$ the area-law behavior at large distances $R, T \gg \lambda$:

$$\langle W\rangle = \exp(-\sigma S_{\min}), \tag{11}$$

and λ is the gluon correlation length [8], characterizing the fall-off in x of the field correlator $D(x) \sim \langle \mathrm{tr}F(x)\Phi F(0)\rangle$, and $S_{\min}$ is the area, which is assumed to be minimal for the given contour C.

Note that, at large distances, the spin factor does not contribute to the area law [4–7] and, therefore, the subscript σ in (11) is omitted.

To describe $S_{\min}$, one can parametrize first the trajectory $z_\mu(t)$ of the gluon between the initial point x and the final point y (both on the contour C),

$$z_\mu: \quad (z_1(t) \equiv \xi(t), z_2(t), z_3(t), z_4(t) \equiv t), \quad h^2(t) = z_2^2(t) + z_3^2(t). \tag{12}$$

We choose the Nambu–Goto ansatz for the minimal area surface (or rather for its increase over the plane area $S_0 = RT$):

$$\Delta S = \Delta S_1 + \Delta S_2, \tag{13}$$

$$\Delta S_i = \int\limits_{y_4}^{x_4} dt\int\limits_0^1 d\beta\sqrt{(\dot{w}_i w_i')^2 - \dot{w}_i^2 w_i'^2},$$

where $w_{i\mu}(\tau,\beta)$: $w_{i4} = t$, $\mathbf{w}_{1,2} = (1-\beta)(\mathbf{R},0) + \beta\mathbf{z}$. Note that, in our case, two different processes can be initiated by the exchanged gluon:

(i) Points x and y are at $x_4 = T_0$, $\mathbf{x} = (R/2,0,0)$ and $y_4 = 0$, $\mathbf{y} = (R/2,0,0)$, the situation which is ensured on the lattice by the insertion of plaquettes at these sides of the Wilson loop. In this case, one obtains the hybrid excitation of the Wilson loop, and this form was used before to compute hybrid spectra analytically [5, 6] and on the lattice [9].

(ii) The points x and y belong to the trajectories of Q and $\bar{Q}$, respectively, so that $G_{\mu\nu}(x,y) = G_{44}(R,T)$, $T < T_0$, describes the propagation of the Coulomb gluon between the quarks.

In what follows, we shall study both cases using for that the final form resulting from (5), (7), (11), and (13)

$$\langle G_{44}(x,y)\rangle_B \equiv G(x,y) = \int\limits_0^\infty ds (Dz)_{xy} e^{-K-\sigma\Delta S}. \tag{14}$$

To treat the awkward roots in ΔS [Eq. (13)], one can introduce the einbein parameters $\nu(t)$ and $\bar{\nu}(t)$ [10], obtaining in the small oscillation limit

$$G(x,y) = \int\limits_0^\infty ds (Dz)_{xy} D\nu D\bar{\nu} e^{-K-\sigma\Delta\tilde{S}(\nu,\bar{\nu})}, \tag{15}$$

where

$$\Delta\tilde{S}(\nu,\bar{\nu}) = \int\limits_{y_4}^{x_4} dt \left\{ \frac{\nu+\bar{\nu}}{2}\left(1 - \frac{1}{3}\dot{z}_\perp^2\right) + \frac{h^2+\xi^2}{2\nu} + \frac{h^2+(R-\xi)^2}{2\bar{\nu}} - R \right\}. \tag{16}$$

For $x = (R/2, 0, 0, T_0)$, $y = (R/2, 0, 0, 0)$, one will have from (14) the static hybrid spectrum, to be compared with previous calculations, and for case (ii), one can define the generalized Coulomb interaction as

$$\int\limits_0^{T_0} dx_4 \int\limits_0^{T_0} dy_4 G(x,y) = \int\limits_0^{T_0} d\frac{x_4+y_4}{2} \times \int\limits_{-T_0/2}^{T_0/2} G(R,T) dT \equiv T_0 V_{\rm C}^*(R). \tag{17}$$

In the limit $\sigma \to 0$, one obtains the free gluon propagator $G^{(0)}(x,y) = 1/[4\pi^2(x-y)^2]$ in case (i) and the Coulomb interaction $V_{\rm C}^*(R) = V_{\rm C}(R) = -C_2\alpha_s/R$ in case (ii). Our purpose in what follows is to obtain a modification of these results for nonzero σ. To grasp the idea, we shall start with a toy model as a warm-up.

3. A SIMPLE TOY MODEL FOR THE CONFINED GLUON

Consider a gluon propagating from static quark Q with coordinate $(0, \mathbf{0})$ to antiquark $\bar{Q}(T, R, 0, 0)$.

The world sheet of the $Q\bar{Q}$ system with the string from Q to $\bar{Q}$ sweeps the strip in the (x_4, x_1) plane, and one expects that gluons are confined dynamically to some region around this strip. This means that the running away of gluons from the plane (x_4, x_1) is damped by some function, which we take in the form of the confining "potential" V,

$$V(\mathbf{z}) = \frac{\omega^2}{4}(z_2^2 + z_3^2). \tag{18}$$

The Green's function of the gluon can be written in the FFSR [11]

$$G(T,R) = \int\limits_0^\infty ds (Dz_1)_{0R} (Dz_4)_{0T} \times (Dz_2)_{00}(Dz_3)_{00} \exp\left(-K - \int\limits_0^s V d\tau\right), \tag{19}$$

where $K = \frac{1}{4}\int_0^s d\tau\, (dz_\mu/d\tau)^2$ and

$$(Dz_i)_{ab} = \prod_{n=1}^N \frac{dp_i}{2\pi} e^{ip_i(a_i-b_i)} \frac{d\Delta z_i(n)}{4\pi\varepsilon}.$$

The integration in Dz_i factorizes and can be performed immediately, with the result (see Appendix 1 for details)

$$G(T,R) = \frac{1}{16\pi^2}\int\limits_0^\infty \frac{ds}{s^2}\varphi(\omega s)\exp\left(-\frac{x^2}{4s}\right), \tag{20}$$

$$\varphi(t) = \frac{t}{\sinh t}; \quad x^2 = R^2 + T^2.$$

The integral (20) can be estimated by the stationary-point method and one obtains

$$G(T,R) \cong \frac{\psi(\omega x^2)}{4\pi^2 x^2}, \tag{21}$$

$$\psi(t) \approx \begin{cases} \dfrac{t}{8\sinh(t/8)}, & t \ll 1, \\ \sqrt{t}e^{-\sqrt{t}}, & t \gg 1. \end{cases}$$

One can see that, at large x^2, $x^2\omega \gg 1$, there appears in (21) the damping factor signaling the mass gap $m = \sqrt{\omega}$, i.e., the confined gluon acts at large distances as a massive particle, while at small distances, $x^2 \to 0$, it behaves as an ordinary unconfined gluon. When $\omega \to 0$, one recovers from (17) the standard Coulomb interaction,

$$V_{\rm C}(R) = -g^2 C_2(f) \times 2\int\limits_0^\infty G(T,R) dT = -\frac{\alpha_s C_2(f)}{R},$$

and in the opposite limit, $\omega R^2 \gg 1$, $V_C(R)$ is multiplied by the factor

$$\frac{4\sqrt{2}}{(\omega R^2)^{1/4}} \exp(-(\omega R^2)^{1/2}).$$

This screening factor is equal to $1/2$ at $R \approx \sqrt{4/\omega}$ and decays exponentially at large R, as is commonly expected. In Section 5, a more complicated behavior will be obtained in the realistic case when the gluon is confined by the string world sheet. To this end, we develop in the next section the necessary formalism for the hybrid Green's function.

4. SPECTRUM OF THE CONFINED GLUONS: STATIC HYBRID

In this section, we shall calculate the gluon Green's function in the hybrid situation, i.e., when boundary conditions are given in (i) [see Section 2 below Eq. (13)], and one can identify $T \equiv T_0$. One can introduce the einbein variable $\mu(t)$ as in [10] (see Appendix 2 for details) and write

$$G(x,y) = \int \frac{D\mu}{2\bar{\mu}} D\nu D\bar{\nu} e^{-\Gamma} G_3(R,T,\nu,\bar{\nu},\mu), \quad (22)$$

where we have defined

$$\Gamma = \int_0^T \frac{\mu}{2} dt + \frac{\sigma}{2}\int_0^T (\nu+\bar{\nu})dt + \sigma R^2 \int_0^T \frac{dt}{2(\nu+\bar{\nu})}, \quad (23)$$

$$G_3 = \int (D^3 z)_{xy} \quad (24)$$

$$\times \exp\left(-\int_0^T \left(\frac{\mu}{2}\dot{z}_1^2 + \frac{\mu + J_1 + J_2}{2}\dot{z}_\perp^2\right) dt - \frac{\sigma}{2\tilde{\nu}}\int_0^T [(z_1 - \tilde{R})^2 + h^2] dt\right),$$

$\tilde{R} = R\nu/(\nu+\bar{\nu})$, and we take $x = (R/2,0,0,0)$, $y = (R/2,0,0,T)$, $J_i = \sigma\nu_i/3$.

The integration over $(D^3 z)$ can be immediately done using the standard path integral formula (see Appendix 1):

$$G_3 = \left(\frac{\mu\omega_1}{2\pi\sinh(\omega_1 T)}\right)^{1/2} \quad (25)$$

$$\times \frac{(\mu + J_1 + J_2)\omega_\perp}{2\pi\sinh(\omega_\perp T)} \exp\left\{-\frac{\mu\omega_1}{2\sinh(\omega_1 T)} \times \frac{R^2(\nu-\bar{\nu})^2}{2(\nu+\bar{\nu})^2}(\cosh(\omega_1 T) - 1)\right\},$$

where

$$\omega_1 = \sqrt{\frac{\sigma}{\mu\tilde{\nu}}}, \quad \omega_\perp = \sqrt{\frac{\sigma}{\tilde{\nu}(\mu + J_1 + J_2)}},$$
$$\tilde{\nu} = \frac{\nu\bar{\nu}}{\nu+\bar{\nu}}.$$

The next step is the stationary point analysis of Eqs. (22), (25) with respect to variables ν, $\bar{\nu}$, μ. We relegate the details of this analysis to Appendix 2 and here only quote the result. Minimizing the expression in the exponent of (25) with respect to $(\nu - \bar{\nu})$, one obtains $\nu = \bar{\nu}$, and the stationary point in ν, $\nu = \nu_0$ is found from the equation

$$\frac{\partial}{\partial\nu}\left(\sigma\nu + \frac{\sigma R^2}{4\nu} + \frac{\omega_\perp}{2} + \omega_\perp\right) = 0. \quad (26)$$

One can distinguish two cases: (a) $\sigma R^2 \gg 1$; (b) $\sigma R^2 \ll 1$.

In case (a), taking into account that $\mu_0 \lesssim \sqrt{\sigma}$ (which will be confirmed afterwards), one has

$$\nu_0 = \frac{R}{2}, \quad \omega_1^{(0)} \to \left(\frac{4\sigma}{\mu R}\right)^{1/2}, \quad (27)$$
$$\omega_\perp^{(0)} \to \frac{\sqrt{12}}{R},$$

and Eq. (22) with $\nu = \bar{\nu} = \nu_0$ assumes the form for large ωT

$$G(x,y) \quad (28)$$
$$= \int D\mu \exp\left[-\left(\sigma R + \omega_\perp^{(0)} + \frac{\mu}{2} + \frac{1}{2}\sqrt{\frac{4\sigma}{\mu R}}\right) T\right].$$

The stationary point $\mu = \mu_0$ is found from the exponential of (28) to be

$$\mu_0 = \left(\frac{\sigma}{R}\right)^{1/3},$$

and the resulting static hybrid mass at large R is

$$M_{\text{hybrid}}(R) = \sigma R + \frac{3}{2}\left(\frac{\sigma}{R}\right)^{1/3} + \frac{\sqrt{12}}{R}. \quad (29)$$

The second term on the right-hand side of (29) is the characteristic $R^{-1/3}$ law for large-R hybrid excitations, studied in [6], and one can distinguish the longitudinal and transverse branches of the spectrum with higher excitations generated by $\sinh(\omega_1 T)$ and $\sinh(\omega_\perp T)$ in (25), which we write as in [6]:

$$M_{\text{hybrid}}^{(\text{long})} = \frac{3}{2^{1/3}}\left(\frac{\sigma}{R}\right)^{1/3}\left(n_z + \frac{1}{2}\right)^{2/3}, \quad (30)$$
$$M_{\text{hybrid}}^{(\text{trans})} = \frac{\sqrt{12}}{R}(n_\perp + \Lambda + 1),$$

where Λ is angular momentum projection on the x axis. Note that $\sqrt{12} = 3.46 \approx \pi$ and transverse spectrum is very close to the flux tube excitations, while the longitudinal one found in [6] is new.

The resulting spectrum (30) is in a good agreement with lattice calculations [9] (see also discussion in [6]).

We now turn to case (b), $\sigma R^2 \ll 1$, and from (26) find that $\nu = \nu_0 = (9/(\sigma\mu))^{1/3}$ and the equivalent of Eq. (28) is

$$G(x,y) = \int D\mu \tag{31}$$
$$\times \exp\left\{-\left[\frac{\mu}{2} + \frac{3}{2}\frac{(3\sigma)^{2/3}}{\mu^{1/3}} + \frac{\sigma R^2}{2}\left(\frac{\sigma\mu}{9}\right)^{1/3}\right]T\right\}.$$

To check the accuracy of our approach, we can calculate the hybrid mass in the limit $R \to 0$, which coincides with the gluelump case [7]. Defining for $R \to 0$ the stationary point $\mu = \mu_0$ from the exponent of (31), one has $\mu = \mu_0 = \sqrt{3\sigma}$ and the gluelump mass is

$$M_{\text{gluelump}} = 2\sqrt{3\sigma}, \tag{32}$$

which should be compared with the dedicated gluelump calculations in [7]: $M_0 = 2\,(a/3)^{3/4}\left(2\sigma_{\text{adj}}\right)^{1/2} = 2\sqrt{3.096\sigma}$, where we have used the value of the first zero of the Airy function, $a = 2.338$. One can see agreement on the level of 1.5%.

Taking into account the last term in the exponent of (31), one obtains the lowest hybrid mass at small $\sigma R^2 \ll 1$

$$M_{\text{hybrid}}(R) = 2\sqrt{3\sigma} + \frac{\sigma R^2}{2}\sqrt{\frac{\sigma}{3}} + O(R^4), \tag{33}$$

which coincides with the mass spectrum obtained in [6] for this limiting case by a different method.

Thus, our approach can be used as a good zeroth-order approximation for the confined gluon Green's function and its spectrum.

In what follows, we shall use the dependence $\mu_0(R) = \bar{\mu}$ given above in two limiting cases:

$$\mu_0(R) = \left(\frac{\sigma}{R}\right)^{1/3}, \quad \sigma R^2 \gg 1, \tag{34}$$

$$\mu_0(R) = \sqrt{3\sigma}, \quad \sigma R^2 \ll 1.$$

5. THE CONFINED COULOMB INTERACTION

In this section, we consider the confined gluon Green's function for the initial and final conditions corresponding to the Coulomb gluon exchange.

With the same notation as in (22)–(24), one has

$$G(R,T) = \int D\nu D\bar{\nu}\frac{D\mu}{2\bar{\mu}}e^{-\Gamma}G_3^{(\mathrm{C})}(R,T,\nu,\bar{\nu},\mu), \tag{35}$$

where Γ is the same as in (23), but now $G_3^{(\mathrm{C})}$ is not given by (25), but has another form, due to different initial and final condition, $x = (0,0,0,0)$, $y = (R,0,0,T)$, and the same simple general formula of Appendix 1 yields

$$G_3^{(\mathrm{C})} = \left(\frac{\bar{\mu}\omega_1}{2\pi\sinh(\omega_1 T)}\right)^{1/2} \tag{36}$$
$$\times \frac{(\bar{\mu} + J_1 + J_2)\omega_\perp}{2\pi\sinh(\omega_\perp T)}\exp\left\{-\frac{\bar{\mu}\omega_1}{2\sinh(\omega_1 T)}\right.$$
$$\left.\times\left[R^2\cosh(\omega_1 T) + 2R^2\frac{\tilde{\nu}}{\nu+\bar{\nu}}(1-\cosh(\omega_1 T))\right]\right\},$$

where we have defined $\omega_\perp$ as in the previous section, while

$$\omega_1 = \sqrt{\frac{4\sigma}{\bar{\mu}(\nu+\bar{\nu})}}, \quad D\mu = \prod_n \frac{d\mu(n)\sqrt{\Delta t}}{\sqrt{2\pi\mu(n)}},$$

so that $\int D\mu \exp\left\{-\frac{1}{2}\int_0^T \mu(t)dt\right\} = 1$. Minimizing in $(\nu - \bar{\nu})$, one obtains $\nu = \bar{\nu}$,

$$\omega_1 \to \omega_1^{(0)} = \sqrt{\frac{2\sigma}{\bar{\mu}\nu}},$$
$$\omega_\perp \to \omega_\perp^{(0)} = \sqrt{\frac{2\sigma}{(\bar{\mu} + J_1 + J_2)\nu}},$$

and one has

$$G(R,T) = \int \frac{D\nu}{(2\pi)^{3/2}\times 2\bar{\mu}}\exp(-\Gamma_0), \tag{37}$$

where

$$\Gamma_0 = \sigma\nu T + \frac{\sigma R^2 T}{4\nu} + \frac{1}{2}\ln\sinh(\omega_1^{(0)}T) \tag{38}$$
$$-\frac{1}{2}\ln(\bar{\mu}\omega_1^{(0)}) + \frac{\bar{\mu}R^2}{2T}\varphi(\omega_1^{(0)}T) + \ln\sinh(\omega_\perp^{(0)}T)$$
$$-\ln\left((\bar{\mu} + J_1 + J_2)\omega_\perp^{(0)}\right)$$

and

$$\varphi(x) = \frac{x(1+\cosh x)}{2\sinh x}, \tag{39}$$
$$\varphi(0) = 1, \quad \varphi(x\to\infty) \approx \frac{x}{2}.$$

To proceed, one should find the stationary point of Γ_0 with respect to ν, $\partial\Gamma_0/\partial\nu|_{\nu=\nu_0} = 0$. This is easy to do at large R since then $\nu_0 \sim R/2$ and

The screening factor $\xi(R)$ and $f(\lambda)$ as functions of distance R

λ	0.1	0.2	0.4	0.6	0.8	1.0	2.7	5.4
$f(\lambda)$	4.60	1.91	0.74	0.41	0.26	0.18	0.024	0.0029
R [fm]	0.084	0.14	0.23	0.32	0.39	0.46	0.98	1.645
$\xi(R)$	0.929	0.796	0.656	0.577	0.515	0.469	0.241	0.086

$\omega_1^{(0)} = \sqrt{2\sigma/(\bar{\mu}\nu_0)} \to 0$, $\omega_\perp^{(0)} \to 0$, so that the last three terms on the right-hand side of (38) do not contribute:

$$\frac{\partial\Gamma_0}{\partial\nu} = 0 = \sigma T\left(1 - \frac{R^2}{4\nu_0^2}\right), \qquad (40)$$
$$\nu_0 = \frac{R}{2}, \quad R \to \infty,$$

and

$$\Gamma_0(\nu = \nu_0) - \sigma RT = \frac{1}{2}\ln\sinh\left(\sqrt{\frac{4\sigma}{\bar{\mu}R}}T\right) \qquad (41)$$
$$-\frac{1}{2}\ln\left(\bar{\mu}\sqrt{\frac{4\sigma}{\bar{\mu}R}}\right) + \frac{\bar{\mu}R^2}{2T}\varphi\left(\sqrt{\frac{4\sigma}{\bar{\mu}R}}T\right)$$
$$+\ln\sinh\left(\frac{\sqrt{12}}{R}T\right) - \ln\left(\left(\bar{\mu} + \frac{\sigma R}{3}\right)\frac{\sqrt{12}}{R}\right).$$

To get the modified Coulomb interaction at large R, one considers the integral

$$V^*(R) \equiv \int_{-\infty}^{\infty} dT G(R,T) \qquad (42)$$
$$= 2\int_0^\infty dT G(R,T) = \frac{2}{(2\pi)^{3/2}\times 2\bar{\mu}}\int_0^\infty e^{-\Gamma_0}dT.$$

Here, the modified Coulomb potential is connected to $V^*(R)$ as $V_C^*(R) = g^2C_2V^*(R)$. Inserting (41) into (42), one obtains

$$V^*(R) = \frac{2\sqrt{3}\,(\bar{\mu}/R + \sigma/3)}{2\pi^{3/2}} \qquad (43)$$
$$\times\int_0^\infty \frac{dT}{\sinh\left(\sqrt{12}T/R\right)\left[\sinh\left(\sqrt{4\sigma/(\bar{\mu}R)}T\right)\right]^{1/2}}$$
$$\times\exp\left(-\frac{\bar{\mu}R^2}{2T}\varphi\left(\sqrt{\frac{4\sigma}{\bar{\mu}R}}T\right)\right).$$

Introducing a new variable $\tau = \bar{\mu}R^2/(2T)$, this integral can be reduced to the form

$$V^*(R) = \frac{\sqrt{3}\left((\bar{\mu}R)^2 + \frac{\lambda^2}{3}\right)}{2\pi^{3/2}R} \qquad (44)$$
$$\times\int_0^\infty \frac{d\tau}{\tau^2}\frac{e^{-\tau\varphi(\lambda/\tau)}}{(\sinh(\lambda/\tau))^{1/2}\sinh\left(\sqrt{3}\bar{\mu}R/\tau\right)} \equiv \frac{\xi(R)}{4\pi R},$$

where we have defined $\lambda = (\sigma\bar{\mu}R^3)^{1/2} \underset{R\to\infty}{\to} (\sigma R^2)^{2/3}$. Finally, $\xi(R)$ can be written as

$$\xi(R) = \sqrt{\frac{3}{\pi}}\times 2\lambda\left(1 + \frac{\lambda}{3}\right)f(\lambda), \qquad (45)$$
$$\lambda = (\sigma R^2)^{2/3},$$

$$f(\lambda) = \int_0^\infty dy\frac{e^{-\varphi(\lambda y)/y}}{\sqrt{\sinh(\lambda y)}\sinh(\sqrt{3\lambda}y)}. \qquad (46)$$

For $\lambda \to 0$, one has $f(\lambda) \approx \dfrac{1}{2\lambda}\sqrt{\dfrac{\pi}{3}}$, and $\xi(\lambda \to 0)$ is close to unity. The explicit behavior of $\xi(R)$ is given in the table.

For $\sigma R^2 \to \infty$, one has from (34) $\bar{\mu} = (\sigma/R)^{1/3}$, and inserting this into (44), one obtains the asymptotics

$$V^*(R) \approx \sqrt{\frac{2}{3\pi}}\frac{\lambda\exp\left(-\dfrac{\lambda}{2}\right)}{R} \qquad (47)$$
$$\approx \frac{\sqrt{2}(\sigma R^2)^{2/3}\exp\left[-\dfrac{1}{2}(\sigma R^2)^{2/3}\right]}{\sqrt{3}\pi^{3/2}R}, \quad \sigma R^2 \gg 1.$$

One can see in the table that the screening starts at rather small values of R, and at $R \sim 0.5$ fm, the coefficient $\xi(R) \sim 0.5$.

6. CONCLUSIONS

The overall static interaction between Q and $\bar{Q}$ can be derived from Eq. (5), where the term $\langle W^{(0)}(B)\rangle$

gives the confining term $V_{\rm conf}(R)$, while the second term on the right-hand of (5) provides the screened Coulomb potential $V_{\rm C}^*(R)$, so that one has for $R \gg \lambda$, $\lambda \approx 0.2$ fm,

$$V_{\rm static}(R) = \sigma R + V_{\rm C}^*(R), \qquad (48)$$
$$V_{\rm C}^*(R) = -\frac{C_2\alpha_s}{R}\xi(R),$$

where $\xi(R)$ is given in (45), (46) and in the table.

In (48), the interference of perturbative field a_μ and nonperturbative B_μ is taken into account. At small R, $R \lesssim \lambda$, there exists another interference effect, which was treated before in [12] and which provides linear behavior of $V_{\rm conf}(R)$ at very small R, while without this interference $V_{\rm conf}(R) \sim {\rm const}\cdot R^2$, for $R \lesssim \lambda$ [13].

The behavior $\sigma R - e/R$ was checked on the lattice in the interval $0.1 < R < 1$ fm with good accuracy [14], and the region $0.8 < R < 1.5$ fm was also measured [15] in the regime where string breaking is expected. Recently, a thorough analysis of the region $R \lesssim 1$ fm [16] has revealed that $\xi(R)$ is approximately constant in this interval and coincides within 15% with the bosonic string Casimir energy prediction (see [16] for discussion and earlier references). Also, the heavy quarkonia spectrum calculated assuming $\xi(R) \equiv 1$ is in good agreement with experiment including high excited bottomonium states [17, 18], and deviation of $\xi(R)$ from unity for $R \gtrsim 0.5$ fm seems to deteriorate this agreement. Thus, the screening factor $\xi(R)$ calculated in this paper [Eq. (45) and table] may be in conflict with lattice and phenomenological (experimental) data. A possible solution of this paradox lies in adopting the bosonic string term [16] at distances beyond 0.5 fm, so that the sum of the screened Coulomb term and the bosonic string term could imitate the original unscreened Coulomb interaction. This picture of transmutation of the Coulomb into the string vibration term, if realistic, can be supported by the Casimir scaling study of the Coulomb-like term at distances around 1 fm. The accuracy of the previous study by Bali [14] was insufficient to draw definite conclusions about the presence of the bosonic string term in this region.

In addition, one should recalculate the bosonic string term using the realistic hybrid spectrum found in [6], which will be reported elsewhere.

ACKNOWLEDGMENTS

I am grateful to A.M. Badalian, N.O. Agasyan, A.B. Kaidalov, Yu.S. Kalashnikova, and V.I. Shevchenko for useful discussions.

This work is supported by the Federal Program of the Russian Ministry of Industry, Science, and Technology, no. 40.052.1.1.1112.

APPENDIX 1

DERIVATION OF THE GLUON GREEN'S FUNCTION IN THE TOY MODEL OF THE CONFINING PLANE

Equation (19) describes the Green's function of free motion in the plane (x_1, x_4) and factorizable motion in oscillator potential in the directions x_2 and x_3. For the latter, one can use the standard textbook formula (see, e.g., [19]) for the Green's function $G(x_a, t_a; x_b, t_b)$ corresponding to the Lagrangian

$$L = \frac{m\dot{x}^2}{2} - \frac{m\omega_0^2 x^2}{2},$$

which we write in the Euclidean metrics

$$G(x_a, t_a; x_b, t_b) = \left(\frac{m\omega_0}{2\pi\sinh(\omega_0 T)}\right)^{1/2} \times \exp\left\{-\frac{m\omega_0}{2\sinh(\omega_0 T)}[(x_a^2 + x_b^2) \times \cosh(\omega_0 T) - 2x_a x_b]\right\},$$

where $T = t_a - t_b$. Changing $m\omega_0^2 \to \omega^2/4, m = 1/2$, and identifying $x_a = x_b = 0$, one arrives at the result written in Eq. (20).

APPENDIX 2

THE GLUON PROPAGATOR IN THE EINBEIN PATH-INTEGRAL REPRESENTATION

One starts with FSR for the free propagator, which can be written as

$$G(x, y) = \int_0^\infty ds (Dz)_{xy} \exp(-K), \qquad (A.1)$$

and introduces the einbein variable-dynamical mass $\mu(t)$ as in [10], so that K can be rewritten as

$$K = m^2 s + \frac{1}{4}\int_0^s \left(\frac{dz_\mu(\tau)}{d\tau}\right)^2 d\tau \qquad (A.2)$$
$$= \int_0^T dt \left\{\frac{m^2}{2\mu(t)} + \frac{\mu(t)}{2} + \frac{\mu(t)}{2}\left(\frac{dz_i(t)}{dt}\right)^2\right\}.$$

In $(Dz)_{xy}$, there is integration over time components of the path, namely,

$$(Dz_4) \equiv \prod_n \frac{d\Delta z_4(n)}{(4\pi\varepsilon)^{1/2}} \delta\left(\sum \Delta z_4 - T\right), \qquad (A.3)$$

where $T \equiv x_4 - y_4$, and using the definition of $\mu(t), \mu(t) = \frac{1}{2}\frac{dt}{d\tau}$, one can rewrite the integration element in (A.3) as follows ($t \equiv z_4$):

$$\frac{d\Delta z_4(n)}{\sqrt{4\pi\varepsilon}} = 2d\mu(n)\sqrt{\frac{\varepsilon}{\pi}} = \frac{d\mu(n)\sqrt{\Delta t}}{\sqrt{2\pi\mu(n)}}, \qquad (A.4)$$

$$\sqrt{\varepsilon} = \sqrt{\frac{\Delta t}{2\mu(n)}}.$$

Moreover, the δ function acquires the form

$$\delta\left(\sum \Delta z_4 - T\right) = \delta(s \times 2\bar{\mu} - T), \qquad (A.5)$$

where we have defined

$$\bar{\mu} = \frac{1}{s}\int_0^s 2\mu(\tau)d\tau. \qquad (A.6)$$

As a result, one can integrate in (A.1) over ds using δ function (A.5) and rewrite $ds(Dz)_{xy}$ as $ds(D^4z)_{xy} = (D^3z)_{\mathbf{xy}}D\mu$. One can write the Green's function as follows:

$$G(x,y) = \int \prod \frac{d^3\Delta z_i(n)}{l^3} \qquad (A.7)$$

$$\times\, e^{-K}\frac{d\mu(n)}{l_\mu(n)}\frac{d^3p}{(2\pi)^3}e^{i\mathbf{p}\cdot(\mathbf{x}-\mathbf{y}-\sum\Delta\mathbf{z}(n))},$$

where K is given in (A.2), and l, l_μ are

$$l(n) = \left(\frac{2\pi\Delta t}{\mu(n)}\right)^{1/2},$$

$$l_\mu(n) = \left(\frac{2\pi\mu(n)}{\Delta t}\right)^{1/2}, \quad N\Delta t = x_4 - y_4 \equiv T.$$

The integration over $d^3\Delta z_i(n)$ yields

$$G(x,y) = \int \frac{d^3p}{(2\pi)^3}\exp\left(i\mathbf{p}\cdot(\mathbf{x}-\mathbf{y}) \qquad (A.8)\right.$$

$$\left. -\frac{1}{2}\int_0^T dt\mu(t)\left(1 + \frac{\mathbf{p}^2+m^2}{\mu^2(t)}\right)\right)\frac{1}{2\bar{\mu}}(D\mu).$$

Taking into account the integral

$$\int_0^\infty \frac{d\mu(n)}{\sqrt{\mu(n)}}\exp\left[-\frac{\Delta t}{2}\left(\mu(n) + \frac{\mathbf{p}^2+m^2}{\mu(n)}\right)\right] \qquad (A.9)$$

$$= \sqrt{\frac{2\pi}{\Delta t}}e^{-\Delta t\sqrt{\mathbf{p}^2+m^2}},$$

one has finally

$$G(x,y) = \int \frac{d^3p}{(2\pi)^3}\frac{e^{i\mathbf{p}\cdot(\mathbf{x}-\mathbf{y})-\int_0^T dt\sqrt{\mathbf{p}^2+m^2}}}{2\sqrt{\mathbf{p}^2+m^2}}, \qquad (A.10)$$

where we have used the relation following from the stationary point in the integral (A.9)

$$\bar{\mu} = \int_0^s \mu(\tau)d\tau = \sqrt{\mathbf{p}^2+m^2}. \qquad (A.11)$$

This can be compared with the integral

$$G(\mathbf{r},T) = \int \frac{d^4p}{(2\pi)^4}\frac{e^{i\mathbf{p}\cdot\mathbf{r}+ip_4T}}{p_4^2+\mathbf{p}^2+m^2}, \qquad (A.12)$$

$$\mathbf{r} = \mathbf{x} - \mathbf{y},$$

which reduces to (A.10) after integrating over dp_4 for $T > 0$. Equation (A.12) is the standard form of the free propagator. Now, in the case of interacting gluon as in Section 4, one can still use (A.5), (A.6) with the result that $\bar{\mu} = \mu_0$, with μ_0 defined in (34), since μ_0 does not depend on time.

REFERENCES

1. B. S. De Witt, Phys. Rev. **162**, 1195 (1967); **162**, 1239 (1967); J. Honerkamp, Nucl. Phys. B **48**, 269 (1972); G. 't Hooft, Nucl. Phys. B **62**, 444 (1973); Acta Univ. Wratislaviensis **368**, 345 (1976); L. F. Abbot, Nucl. Phys. B **185**, 189 (1981).
2. Yu. A. Simonov, Yad. Fiz. **58**, 113 (1995) [Phys. At. Nucl. **58**, 107 (1995)].
3. Yu. A. Simonov, Lect. Notes Phys. **479**, 144 (1996).
4. A. B. Kaidalov and Yu. A. Simonov, Phys. Lett. B **477**, 163 (2000); hep-ph/9912434; Yad. Fiz. **63**, 1507 (2000) [Phys. At. Nucl. **63**, 1428 (2000)]; hep-ph/9911291.
5. Yu. A. Simonov, Nucl. Phys. B (Proc. Suppl.) **23**, 283 (1991); Yu. S. Kalashnikova and Yu. B. Yufryakov, Phys. Lett. B **359**, 175 (1995).
6. Yu. S. Kalashnikova and D. S. Kuzmenko, Yad. Fiz. **64**, 1796 (2001) [Phys. At. Nucl. **64**, 1716 (2001)]; **66**, 988 (2003) [**66**, 955 (2003)]; hep-ph/0203128; hep-ph/0302070.
7. Yu. A. Simonov, Nucl. Phys. B **592**, 350 (2001); hep-ph/0003114.
8. A. Di Giacomo and H. Panagopoulos, Phys. Lett. B **285**, 133 (1992); A. Di Giacomo, E. Meggiolaro, and H. Panagopoulos, Nucl. Phys. B **483**, 371 (1997); M. D'Elia, A. Di Giacomo, and E. Meggiolaro, Phys. Lett. B **408**, 315 (1997).
9. K. J. Juge, J. Kuti, and C. Morningstar, Nucl. Phys. B (Proc. Suppl.) **73**, 360 (1999); hep-lat/9809015; Phys. Rev. Lett. **90**, 161601 (2003).

10. A. Yu. Dubin, A. B. Kaidalov, and Yu. A. Simonov, Phys. Lett. B **323**, 41 (1994); Yad. Fiz. **56** (12), 213 (1993) [Phys. At. Nucl. **56**, 1745 (1993)]; hep-ph/9311344.
11. Yu. A. Simonov and J. A. Tjon, Ann. Phys. (N.Y.) **228**, 1 (1993); **300**, 54 (2002); hep-ph/0205165.
12. Yu. A. Simonov, Phys. Rep. **320**, 265 (1999); Pis'ma Zh. Éksp. Teor. Fiz. **69**, 471 (1999) [JETP Lett. **69**, 505 (1999)].
13. H. G. Dosch, Phys. Lett. B **190**, 177 (1987); H. G. Dosch and Yu. A. Simonov, Phys. Lett. B **205**, 339 (1988); Yu. A. Simonov, Nucl. Phys. B **307**, 512 (1988).
14. G. Bali, Nucl. Phys. B (Proc. Suppl.) **83**, 422 (2000); Phys. Rev. D **62**, 114503 (2000); A. Hasenfratz, R. Hoffmann, and F. Knechtli, Nucl. Phys. B (Proc. Suppl.) **106**, 418 (2002).
15. B. Bolder, T. Struckmann, G. S. Bali, *et al.*, Phys. Rev. D **63**, 074504 (2001).
16. M. Lüscher and P. Weisz, J. High Energy Phys. **0207**, 049 (2002).
17. E. Eichten *et al.*, Phys. Rev. D **21**, 203 (1980); E. J. Eichten, K. Lane, and C. Quigg, Phys. Rev. Lett. **89**, 162002 (2002).
18. A. M. Badalian and B. L. G. Bakker, Phys. Rev. D **67**, 071901 (2003); A. M. Badalian, B. L. G. Bakker, and A. I. Veselov, Phys. At. Nucl. **67**, 1367 (2004); hep-ph/0311010.
19. R. P. Feynman and A. R. Hibbs, *Quantum Mechanics and Path Integrals* (McGraw-Hill, New York, 1965; Mir, Moscow, 1968), Problem 3.8.

Physics of Atomic Nuclei, Vol. 68, No. 8, 2005, pp. 1303–1313. Translated from Yadernaya Fizika, Vol. 68, No. 8, 2005, pp. 1356–1367.

NUCLEI
Experiment

Scattering of α Particles on ^{11}B Nuclei at Energies 40 and 50 MeV

N. Burtebaev[1)], M. K. Baktybaev[1)], B. A. Duisebaev[1)], R. J. Peterson[2)], and S. B. Sakuta[3)]

Received April 27, 2004; in final form, October 1, 2004

Abstract—The differential cross sections for elastic and inelastic scattering of α particles on ^{11}B nuclei at energies of 40 and 50 MeV were measured in the entire angular range. The measured angular distributions were analyzed in terms of the optical model, the distorted-wave Born approximation, and the coupled-channel method. Optical model potentials and quadrupole (β_2) and hexadecapole (β_4) deformation parameters were found from this analysis. The rise in the cross sections at backward angles was shown to be associated with the transfer mechanism of the heavy ^{7}Li cluster. © *2005 Pleiades Publishing, Inc.*

1. INTRODUCTION

The elastic and inelastic scattering of hadrons on ^{11}B nuclei has been the subject of much research. The largest number of works were performed with protons of various energies up to 1 GeV (see [1–5] and references therein). The scattering of ^{3}He [6–9] and α particles [10–12] has been investigated to a much lesser extent. In these papers, the measured angular distributions were analyzed mainly in terms of the optical model and the distorted-wave Born approximation. However, belonging to the nuclei of the middle of the p shell, the ^{11}B nucleus has an extremely large quadrupole deformation [13]. Therefore, it is natural that the low-lying states of this nucleus at energies 2.125 ($1/2^-$), 4.445 ($5/2^-$), 5.021 ($3/2^-$), and 6.743 MeV ($7/2^-$) are interpreted as the members of two rotational bands. These bands are built on the ground ($3/2^-$) and first excited ($1/2^-$) states and have the quantum numbers $K = 3/2$ and $K = 1/2$, respectively. In this case, the channel-coupling effects are significant. Disregarding them can be responsible both for the nonphysical values of the potential parameters extracted from a phenomenological optical-model analysis of the elastic scattering and for the inability to achieve an acceptable description of the experimental data with folding potentials. Therefore, the coupled-channel method is more suitable for analyzing ^{11}B. In addition, not only the absolute value but also the sign of the deformation can be determined in principle by using this method.

A coupled-channel analysis was performed only in two papers in which the elastic and inelastic scattering of ^{3}He at energies of 74 MeV [7] and 17.5 and 40 MeV [8] was investigated. In the former paper, an equally good description of the measured angular distributions was achieved for both negative and positive quadrupole deformation parameters ($\beta_2 = +0.43$ and $\beta_2 = -0.5$). In the latter paper, it was pointed out that the negative sign is preferred. This is consistent with the conclusions set out in [14] and corresponds to the physical picture where, in a simple shell model, ^{11}B has the configuration of a $p_{3/2}$ hole in the core of ^{12}C, a nucleus that is known to have a negative quadrupole deformation. At the same time, the most recent result was in conflict with the data of the earlier paper [15], in which a positive quadrupole deformation of the ^{11}B nucleus was obtained by analyzing the ^{12}C(d, ^{3}He)^{11}B reaction at deuteron energy 80 MeV. However, if this were the case, then the shape of the nucleus in the above reaction would change sharply from highly oblate (^{12}C) to highly prolate (^{11}B). As was noted in [14], such a significant change in deformation would yield a large suppression factor in the cross sections for the single-nucleon pickup reaction on ^{12}C nuclei, which is not observed experimentally.

In light of the foregoing, investigating the scattering of α particles is of considerable interest. The point is that the scattering of "isoscalar" particles ($T_z = 0$) provides information about the mass deformation of the target nucleus, while the scattering of e, p, and ^{3}He is also sensitive to other isospin components. Therefore, the deformation parameters determined in both cases may not be identical. Another special feature associated with the use of α particles is the absence of spin–orbit coupling, which makes it easier

[1)]Institute of Nuclear Physics, National Nuclear Center, Almaty, Republic of Kazakhstan.
[2)]University of Colorado, USA.
[3)]Russian Research Centre Kurchatov Institute, pl. Akademika Kurchatova 1, Moscow, 123182 Russia; e-mail: sakuta@dni.polyn.kiae.su

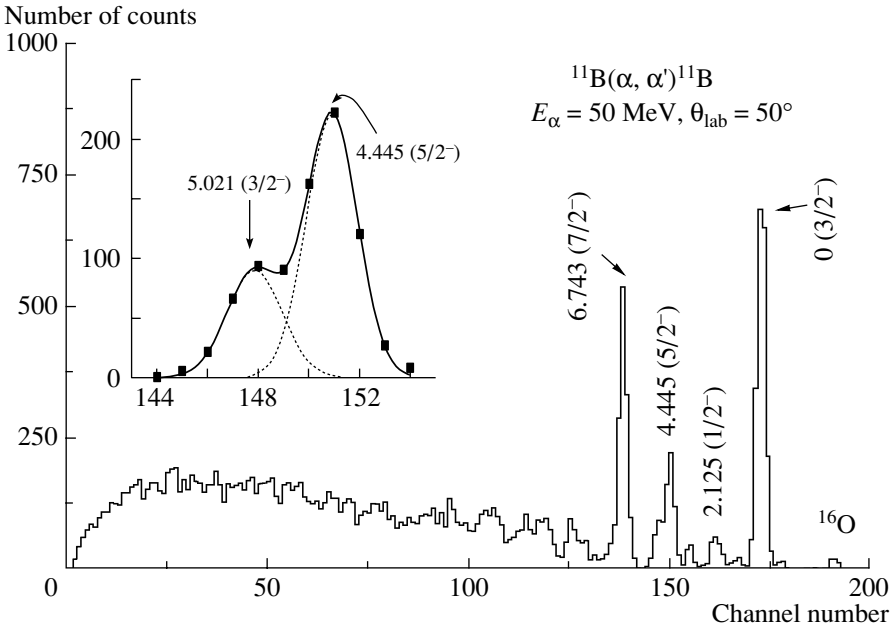

Fig. 1. The energy spectrum of α particles scattered from ^{11}B nuclei at beam energy 50 MeV measured at an angle of 50°.

to analyze the measured cross sections in the range of intermediate and backward angles.

In this paper, we investigate the elastic and inelastic scattering of α particles at energies 40 and 50 MeV with the excitation of low-lying states in the ^{11}B nucleus. Our mail goal was to extract the quadrupole and hexadecapole deformation parameters for the ^{11}B nucleus from the analysis of experimental data by using the coupled-channel method and to study the dependence of the results obtained on the choice of an optical model potential and the possible contribution of the heavy stripping mechanism to the scattering.

2. THE EXPERIMENTAL TECHNIQUE AND RESULTS OF THE MEASUREMENTS

The measurements were made with beams of α particles at energies of 40 and 50 MeV that emerged from the U-150M isochronous cyclotron at the Institute of Nuclear Physics, National Nuclear Center, Republic of Kazakhstan. The angular spread in the beam was $\pm 0.5°$.

Self-supported ^{11}B foils enriched up to 99% were used as the targets. The target thickness ranged from 0.1 to 0.2 mg cm^{-2} and was determined from the energy losses by α particles from a radioactive source with an accuracy of about 8%.

The scattered particles were detected by a telescope consisting of two silicon counters: one thin (ΔE) and one total absorption (E) counter 30 μm and 1 mm in thickness, respectively. The scattered α particles were separated from other charged reaction products by a system of two-dimensional ΔE–E analysis using CAMAC electronic modules and a special code running on a personal computer. The charged particle detection technique was described in more detail in [16].

The overall energy resolution, 400–500 keV, was determined mainly by the energy spread in the cyclotron beam.

The measurements were performed in the range of angles $\theta_{l.s.} = 10°$–$170°$. A typical spectrum of scattered α particles is shown in Fig. 1. The spectra exhibit no strong transitions at ^{11}B excitation energies above 7 MeV. Apart from the elastic scattering peak, intense transitions to the $E_x = 4.445$ MeV ($J^\pi = 5/2^-$) and 6.743 MeV ($7/2^-$) states are observed; the latter are the members of the rotational $K = 3/2$ band of the ^{11}B ($3/2^-$) ground state. The $E_x = 2.125$ MeV ($1/2^-$) and 5.021 MeV ($3/2^-$) levels, which belong to the $K = 1/2$ band, are excited weakly. This is to be expected, since the K selection rule forbids collective transitions between states with different K.

The 4.445-MeV ($5/2^-$) and 5.021-MeV ($3/2^-$) levels were not completely separated in our experiment. The standard fitting procedure with the decomposition of the structure at $E_x = 4.45$ MeV into two Gaussian peaks with the width equal to the energy resolution was used to separate them. An example of this decomposition is shown in the inset in Fig. 1.

The differential cross sections were measured only for the members of the rotational band of the ^{11}B

ground state. As will be seen from the figures below, the diffraction structure in the angular distributions, which is distinct at forward angles, gradually disappears with increasing angle. At beam energy 50 MeV, the oscillations are smoothed out in the range of intermediate angles. An increase in the cross sections, particularly significant at energy 40 MeV, is observed at backward angles (more than 120°).

We estimated the systematic error of the measured cross sections to be no larger than 10%. The statistical error was 1–5% during our measurements in the region of the forward hemisphere and increased at backward angles, but nowhere exceeded 10%.

3. ANALYSIS AND DISCUSSION OF RESULTS

3.1. Elastic Scattering: Optical-Model Analysis

The potentials describing the interaction of α particles with ^{11}B nuclei were initially sought in terms of the optical model. We restricted our analysis to the central Woods–Saxon potential with volume absorption

$$U(r) = -Vf(r) - iWg(r) + V_{\mathrm{C}} \qquad (1)$$

and the radial dependence

$$f(r) = \{1 + \exp[(r - r_V A_t^{1/3})/a_V]\}^{-1}, \qquad (2)$$

$$g(r) = \{1 + \exp[(r - r_W A_t^{1/3})/a_W]\}^{-1}, \qquad (3)$$

where $r_{V(W)}$ and $a_{V(W)}$ are, respectively, the reduced radii and diffuseness for the real (V) and imaginary (W) parts of the nuclear potential. The last term in Eq. (1) is the Coulomb potential of a uniformly charged sphere of radius $R_{\mathrm{C}} = 1.3A_t^{1/3}$, where A_t is the target mass.

We computed the elastic scattering cross sections and sought the optical-potential parameters that described best the experimental data using the well-known SPI-GENOA code [17] modified by Nilsson [18] and Goncharov [19].

The ratios of the differential cross sections for elastic scattering of α particles at energies of 40 and 50 MeV to the Rutherford cross section are shown in Figs. 2 and 3, respectively. Our data for $E_\alpha =$ 50 MeV are identical to the previous measurements at energy 48.7 MeV [12]. As we see from the figures, the diffraction structure, which clearly shows up in the forward hemisphere, decreases with increasing angle. At backward angles, the differential cross sections exhibit a rise that is the most pronounced at an energy of 40 MeV. Note that this rise is absent in the scattering of ^{3}He from ^{11}B at energies 40 MeV [8] and 45 MeV [9], where the angular distributions show a rainbow pattern that manifests itself in a broad maximum near 70° followed by an exponential decrease up to 150°.

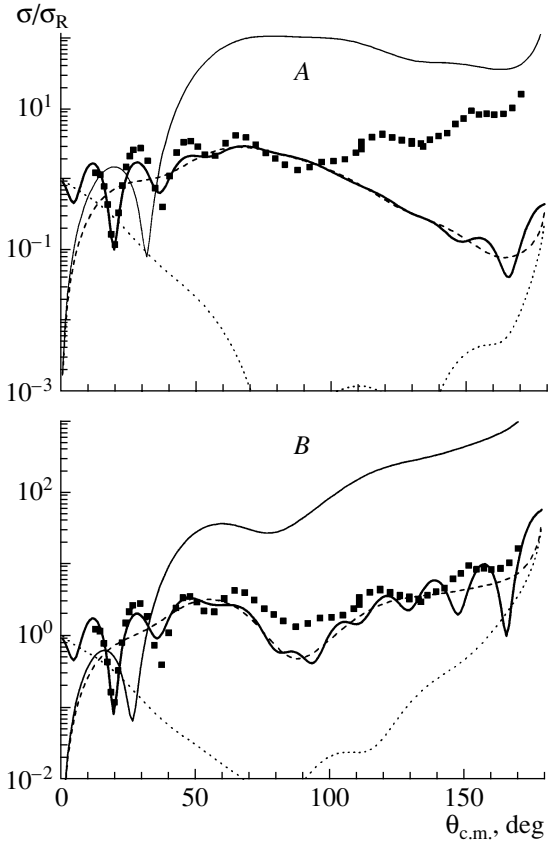

Fig. 2. Angular distributions for the elastic scattering of α particles from ^{11}B nuclei at a beam energy of 40 MeV (points). The curves represent the differential cross sections computed using the optical model with the potentials *A* and *B* from Table 1: the heavy solid curves indicate the total differential cross sections; the dotted and dashed curves indicate the cross sections for the scattering on the "near" and "far" edges of the nucleus; the thin solid curves indicate the computed differential cross sections for the far component with $W = 0$.

The rise in the cross sections at backward angles is a well-known phenomenon. It often cannot be explained in terms of the standard optical model, and other mechanisms different from the potential scattering [20] have to be included in the analysis. The scattering of d, t, ^{3}He, and α particles from light, strongly clustered nuclei (^{6}Li, ^{7}Li, ^{9}Be, etc.) represents a special case. Here, the main mechanism of anomalous backward-angle scattering is the cluster transfer between the target nucleus and the projectile particle [21, 22] in which the core of the target nucleus is identical to the projectile particle.

In seeking the potential parameters that describe best the experimental differential cross sections, we

Table 1. The potential parameters found from the optical-model analysis

Potential	V, MeV	r_V, fm	a_V, fm	W, MeV	r_W, fm	a_W, fm	$I_V/4A$, MeV fm^3	$I_W/4A$, MeV fm^3	χ^2/N
$E_\alpha = 40$ MeV									
A	76.51	1.245	0.866	16.37	1.57	0.790	305	100	7.2
				13.0*					
B	130.7	1.245	0.762	18.40	1.57	0.641	463	99.4	18.8
				12.44*					
$E_\alpha = 50$ MeV									
A	74.88	1.245	0.856	16.86	1.57	0.829	295	106.4	4.51
				13.9*					
B	124.2	1.245	0.753	19.29	1.57	0.692	435	108.5	11.36
				14.4*					

* The values used in the calculations by the coupled-channel method.

took into account the fact that the rise in the cross sections at backward angles observed in the scattering of α particles may not be associated with the ordinary potential scattering. Therefore, we found two potentials. One (A) potential was obtained from the condition for the best description of the experimental data in the angular range of the forward hemisphere, where the contribution from the potential scattering is certain to dominate. The other (B) potential was found from a fit over the entire angular range.

As the starting potential, we used the global potential [23] that describes well the elastic scattering of α particles on nuclei from ^{12}C to ^{208}Pb at energies above 80 MeV. The radii $r_V = 1.245$ fm and $r_W = 1.57$ fm were fixed, and only the four remaining parameters (V, W, a_V, a_W) were varied. The results of our search for optimal potential parameters carried out by minimizing the functional χ^2/N are presented in Table 1. The two potentials found (A and B) were used in our subsequent calculations by the coupled-channel method.

The radial dependences of the potentials for energies 40 and 50 MeV are shown in Fig. 4. As we see from this figure, the potentials A and B on the surface of the nucleus ($r \approx 3$–5 fm) have close imaginary parts and greatly differing real parts (the potential B is much deeper). In the former and latter cases, the volume integral of the real part (J_V) normalized to the pair of interacting particles is about 300 and 430–460 MeV fm^3, respectively. The computed curves for the potential A (Figs. 2 and 3) describe satisfactorily the experimental cross sections up to 80°–90°. The calculations with the potential B give quite a satisfactory global description of the behavior of the differential cross sections. However, the computed cross sections are in poor agreement with the experimental ones in the range of intermediate (60°–90°) and backward (more than 150°) angles, where, in contrast to the experimental data, the predicted curves have a distinct oscillatory structure.

Note that the theoretical angular distributions corresponding to the potential A show a rainbow pattern. The latter shows up as strong oscillations observed in the range of forward angles that are damped with increasing angle and that transform into a broad maximum followed by an exponential decrease. For greater clarity, we decomposed the cross sections into two components corresponding to the scattering from the near and far edges of the nucleus by using a standard procedure [24]. The result of this decomposition is indicated in Figs. 2 and 3 by the dotted and dashed curves. We see that the cross sections at angles larger than 30° are entirely determined by the far component attributable to the negative-angle scattering on the far (from the detector) edge of the nucleus under the nuclear field of attraction. The strong cross-section oscillations observed in the range of forward angles (where the two components have close amplitudes) are attributable to the Fraunhofer diffraction. The special features of the refractive part of the nuclear potentials A and B are seen most clearly in the behavior of the cross sections for the far component at $W = 0$. The corresponding computed cross sections are shown in Figs. 2 and 3 (thin solid curves). We see that (in contrast to the calculations with the potential B) the angular distributions computed with the potential A exhibit a broad maximum in the range 70°–80° with

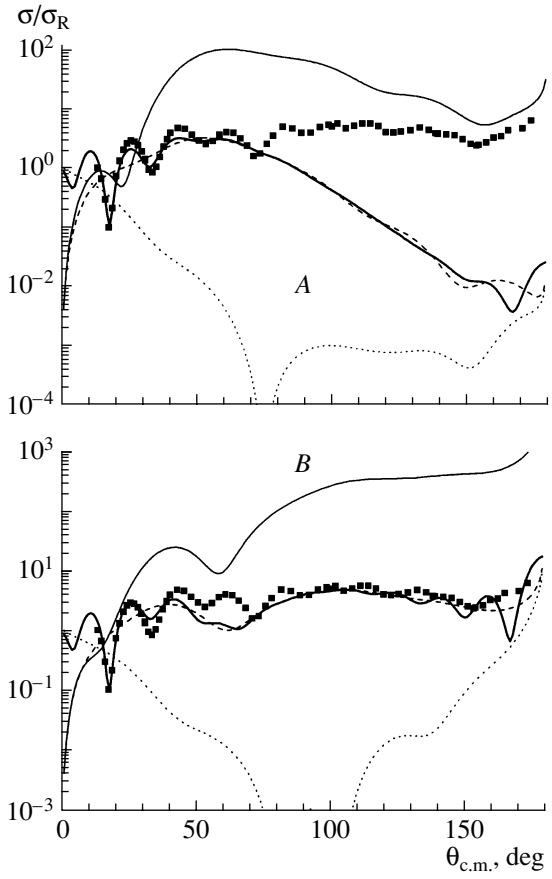

Fig. 3. As in Fig. 2, but for an energy of 50 MeV.

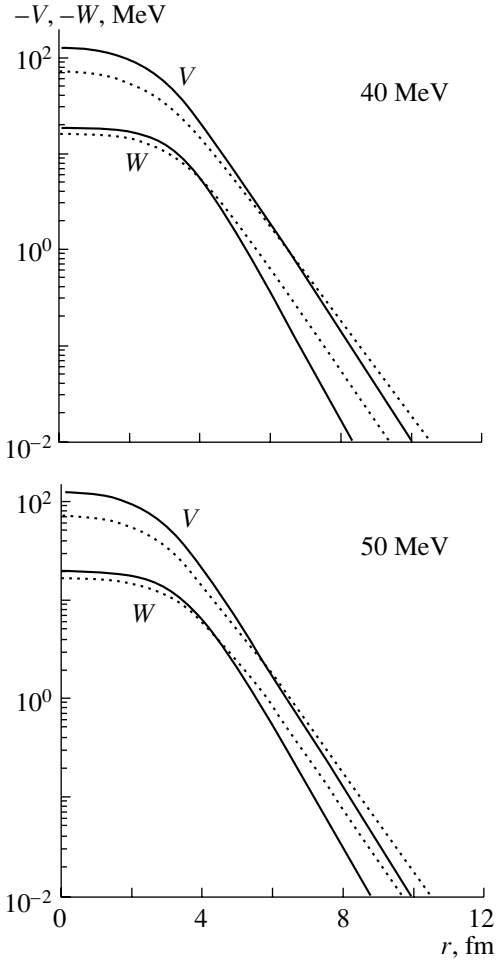

Fig. 4. Radial dependences of the optical potentials A (dotted curves) and B (solid curves) from Table 1 found by fitting the computed differential cross sections to the experimental elastic scattering data at energies of 40 and 50 MeV.

a monotonic decrease in the cross sections toward backward angles. In this sense, the potential A is of the rainbow type, while the potential B is not. It should be noted that the computed curves for the potential A are very similar to the experimental angular distributions for the elastic scattering of ^{3}He from ^{11}B nuclei at close energies. The already noted fact that the experimental angular distributions for the scattering of α particles and ^{3}He, nevertheless, differ greatly in shape suggests that the contribution of the heavy ^{8}Li stripping from the ^{11}B nucleus at backward angles for the ^{3}He scattering is much less significant than that of the ^{7}Li stripping for the scattering of α particles. This is not surprising, since the binding energy for ^{7}Li in the ^{11}B nucleus is relatively low, $\varepsilon_b = 8.67$ MeV, while for ^{8}Li it is much higher, 27.21 MeV; therefore, the amplitude of the $^3\mathrm{He} + {}^8\mathrm{Li}$ configuration in the surface region of the nucleus must be small.

The potential scattering and the heavy stripping are known to be separated with increasing α-particle energy: the potential scattering undoubtedly dominates in the forward hemisphere, while the heavy stripping dominates in the range of backward angles. Unfortunately, there is no data on the scattering of α particles from ^{11}B at fairly high energies as yet. The nearest (in mass) nucleus for which data are available is ^{12}C. For example, a rainbow maximum is observed at an angle of 40° in the angular distribution measured at an α-particle energy of 104 MeV [25]. Since the differential cross sections near the rainbow maximum are described by the Airy function in the semiclassical approximation and since the position of the maximum depends on energy as $\theta \sim 1/E$ [26], one may expect a similar feature at our energies to manifest itself in the range 70°–80°, which is predicted by the calculations with the potential A.

Thus, the potential A seems physically more justified, although it does not allow the experimental cross sections at backward angles to be described.

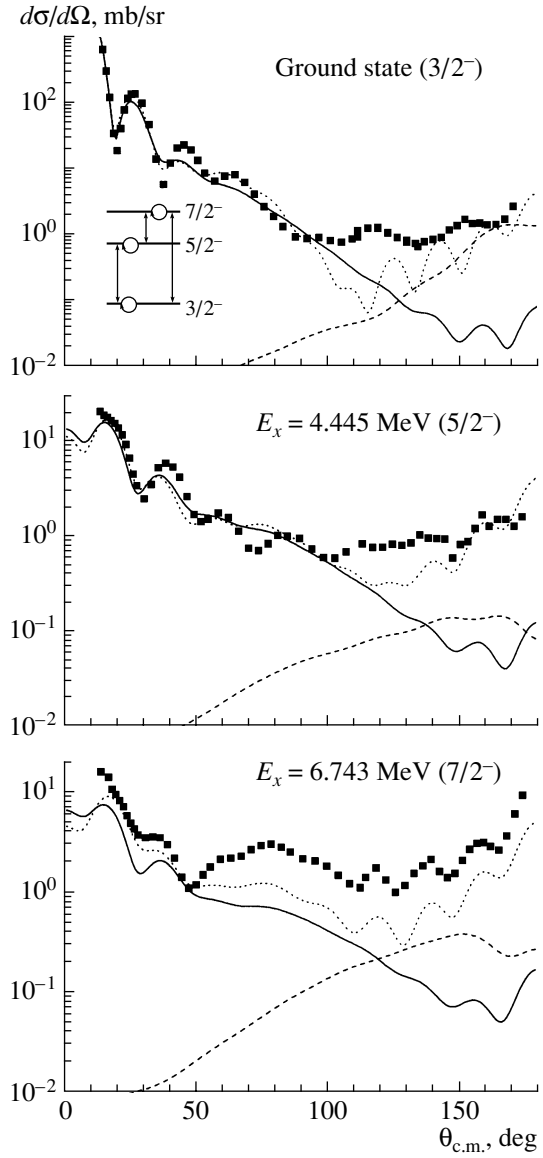

Fig. 5. Angular distributions for the elastic and inelastic scattering of α particles on ^{11}B nuclei with the transition to the $E_x = 4.445$ MeV $(5/2^-)$ and 6.743 MeV $(7/2^-)$ states measured in the present study at an energy of 40 MeV (points). The solid and dotted curves represent the calculations by the coupled-channel method with the potentials A and B, respectively, and with the deformation parameters $\beta_2 = -0.6$ and $\beta_4 = 0$. The coupling scheme used in the calculations is shown in the inset; the circumferences correspond to the reorientation matrix elements for the ground and excited states. The dashed curves represent the cross sections for elastic and inelastic transfer of the ^{7}Li cluster computed by the distorted-wave method with the spectroscopic amplitudes from Table 3.

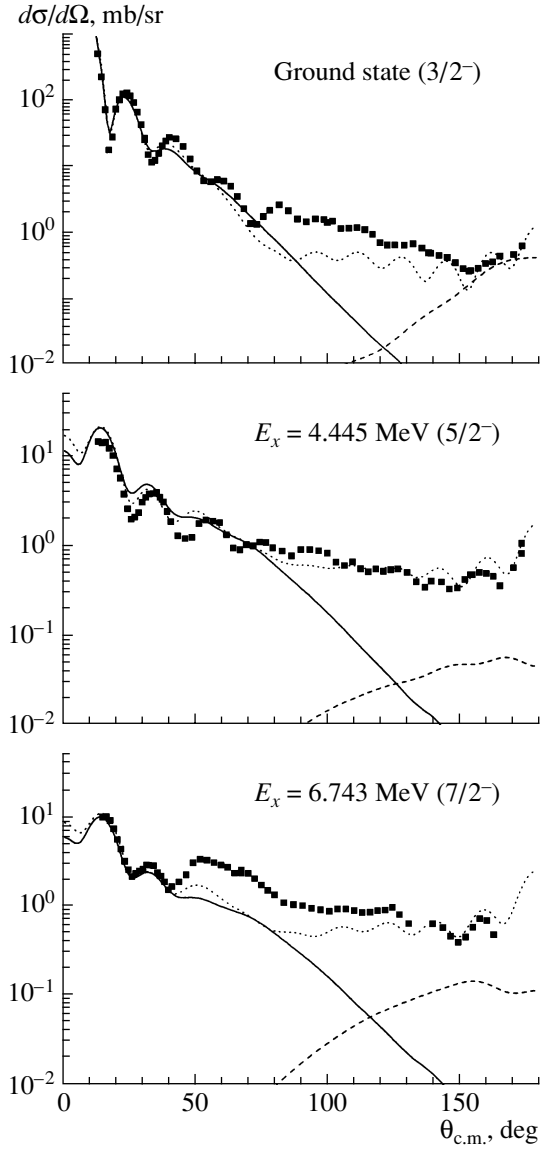

Fig. 6. As in Fig. 5, but for an energy of 50 MeV.

3.2. Description of the Scattering by the Coupled-Channel Method

The angular distributions of α particles for the members of the rotational band of the ^{11}B ground state ($E_x = 0.0$ $(3/2^-)$, 4.445 MeV $(5/2^-)$, and 6.743 MeV $(7/2^-)$) are shown in Figs. 5 and 6. In inelastic scattering, as in elastic scattering, the diffraction structure shows up in the entire angular range, and a rise in the cross sections is observed in the range of backward angles ($\theta > 130°$–$140°$). In analyzing the measured distributions by the coupled-channel method, we used the collective model in which the ^{11}B nucleus is represented as a symmetric rotor. In this model, the potential depends not only on the radius, but also on the angle (θ) between the radius vector and the symmetry axis associated with the nucleus. Taking into account only the quadrupole and hexadecapole deformations with the parameters β_2 and β_4, we now define the radii r_i in Eq. (1) for the

optical potential as

$$r_i(\theta) = r_i[1 + \beta_2 Y_2^0(\theta) + \beta_4 Y_4^0(\theta)], \qquad (4)$$

which makes the standard optical potential deformed.

In our calculations, we disregarded the mixing of the ground-state ($K = 3/2$) band and the band starting from the 2.125-MeV ($1/2^-$)($K = 1/2$) level. This is justified, because, first, the cross sections for the transitions to the $K = 1/2$ band levels are small, and, second, as the studies of the ^{3}He scattering from ^{11}B at energies 17.5 and 40 MeV [8] showed, the band mixing model does not improve the description of the experimental data and does not change significantly the deformation parameters extracted from the analysis, although it affects some of the above matrix elements.

The calculations were performed using the ECIS88 code [27]. The coupling scheme, including both the quadrupole ($L = 2$) and hexadecapole ($L = 4$) transitions in the ^{11}B nucleus, is shown in the inset in Fig. 5. Since the quadrupole moment of ^{11}B is large, the reorientation matrix elements whose values are proportional to the quadrupole moment were also included in the scheme. They correspond to the transitions from states i to the same states i; the contribution of only the quadrupole ($L = 2$) reorientation was taken into account. The starting potentials were taken from the optical-model analysis of the elastic scattering (Table 1). At the first stage, we assumed that $\beta_4 = 0$ and varied only the depths of the imaginary part of the potentials for a grid of both positive and negative quadrupole deformation parameters of the real part of the potentials A and B over the range from 0.3 to 0.9 to reconcile the computed and experimental cross sections. The parameters β_2 for the Coulomb and imaginary parts of the nuclear potential were chosen so that the deformation lengths were constant ($\beta_{2V} R_V = \beta_{2W} R_W = \beta_{2C} R_C$). The computed cross sections were fitted to the experimental ones simultaneously for three angular distributions. We sought the parameters that yielded the best agreement between the theoretical ($\sigma_t(\theta_i)$) and experimental ($\sigma_e(\theta_i)$) differential cross sections by minimizing

$$\chi^2/N = \frac{1}{N}\sum_{i=1}^{N}\left[\frac{\sigma_e(\theta_i) - \sigma_t(\theta_i)}{\Delta\sigma_e(\theta_i)}\right]^2,$$

where N is the total number of experimental points.

The χ^2/N values are plotted against β_2 in Fig. 7. The solid and dotted curves correspond to the negative and positive values of β_2, respectively. The filled and open squares indicate the calculations with the potentials A and B, respectively. We see that the χ^2/N values for the two potentials have minima in the range $\beta_2 = 0.5$–0.7 and that χ^2/N reach the lowest values for the negative sign (in the range $\beta_2 \geq 0.5$).

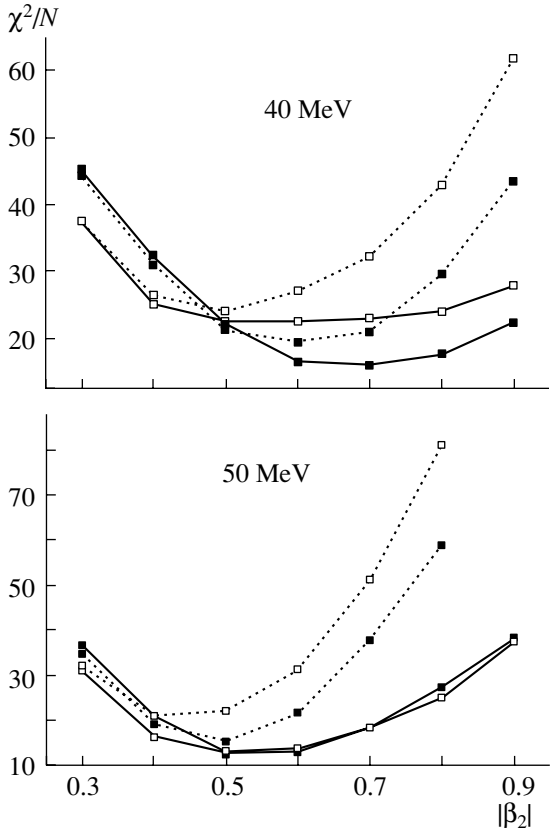

Fig. 7. χ^2 values divided by the number of points (N) versus β_2 at $\beta_4 = 0$ for energies 40 and 50 MeV. The solid and dotted curves were computed for $\beta_2 < 0$ and $\beta_2 > 0$, respectively. The calculations with the potentials A and B are indicated by the closed (■) and open (□) squares, respectively.

The subsequent calculations were performed for a grid of β_2 and β_4 at fixed parameters of the imaginary part W obtained at the first stage. For each given β_2, we varied the parameters β_4 over the range from -0.5 to $+0.5$. The χ^2/N values for positive and negative β_2 are shown in Fig. 8. For the two potentials, A and B, there are shallow minima at $\beta_2 = 0.5$–0.7 for both positive and negative values of this parameter. As previously, the calculations with negative β_2 are closer to the experimental points. The parameters β_4 that described best the experimental data for several fixed values of β_2 were related to β_2 almost linearly. For example, the approximate relation $\beta_4 = 1.18 + 2.16\beta_2$ holds for $E_\alpha = 50$ MeV (the potential A) and at negative β_2 (see the inset in Fig. 8). Thus, our analysis yields $\beta_2 = -0.6 \pm 0.15$ (irrespective of the chosen potential). The hexadecapole deformation parameter β_4 lies within the range from -0.1 to $+0.2$ and could not be determined with a better accuracy in our analysis. Therefore, the cross sections computed

Table 2. The deformation parameters (β_2) and the deformation lengths (δ_2) determined by analyzing the scattering of α particles, ^{3}He, and p using the coupled-channel method

a	E, MeV	Potential	$\langle r^2\rangle^{1/2}$, fm	R, fm	β_2	δ_2, fm	References
α	40	A	3.865	4.99	−0.6	−2.994	Our study
		B	3.551	4.58	−0.6	−2.748	Our study
	50	A	3.834	4.95	−0.6	−2.970	Our study
		B	3.525	4.55	−0.6	−2.730	Our study
^{3}He	17.5		3.166	4.09	−0.47	−1.920	[8]
	40.0		3.579	4.62	−0.53	−2.449	[8]
	74.0	C	3.348	4.32	−0.50	−2.161	[7]
		D	3.318	4.28	+0.43	+1.842	[7]
p	30		2.754	3.55	0.77*	2.737*	[3]

* The calculations were performed by the distorted-wave method; the sign of the deformation was not determined.

with $\beta_2 = -0.6$ and $\beta_4 = 0$ are assigned to the experimental angular distributions (Figs. 5 and 6). As in the case of elastic scattering, the calculations with the potential A reproduce well the experimental data in the forward hemisphere, but yield a smoother oscillatory structure. While reproducing well the behavior of the experimental cross sections in the entire angular range, the calculations with the potential B underestimate their values in the range of intermediate angles ($>70°$), particularly for the transition to the $7/2^-$ excited state at $E_x = 6.743$ MeV. Our analysis indicates that the reorientation effects for the excited states play no significant role. Only the inclusion of the matrix element responsible for the quadrupole scattering to the ground state leads to small changes in the intermediate angular range. This is in agreement with the results of a similar analysis in [28, 29], where the scattering from ^{9}Be with a deformation similar to that of ^{11}B was investigated.

In Table 2, our quadrupole deformation parameters β_2 and deformation lengths $\delta_2 = \beta_2 R$ are compared with those obtained by analyzing the scattering of ^{3}He at energies of 17.5, 40, and 74 MeV [7, 8] and protons at energy 30 MeV [3]. In our calculations of the deformation lengths, we used the mean radius of the actual potential related to the root-mean-square radius $\langle r^2\rangle^{1/2}$ by $R = \sqrt{5/3}\langle r^2\rangle^{1/2}$. Our values of δ_2 exceed those inferred from the ^{3}He scattering by 20–30%, which is within the errors of our analysis. The electromagnetic deformation parameter can be determined from the equality between the nuclear and electromagnetic deformation lengths, $\beta_2 R = \beta_{2C} R_C$. At the mean square of the Coulomb radius $\langle r^2\rangle = 5.0$ fm^2 [13] and the corresponding charge radius $R_C = 2.89$ fm, $\beta_{2C} = 0.99$.

Using the expression for the internal quadrupole moment (Q_0)

$$Q_0 = \frac{3Z}{\sqrt{5\pi}}\beta_{2C}R_C^2, \qquad (5)$$

we obtain $Q_0 = -31.29$ fm^2.

The reduced probability for the quadrupole transition defined by [13]

$$B(E2; I_i \to I_f) = \frac{5}{16\pi}e^2Q_0^2\langle I + iK20|I_fK\rangle^2 \quad (6)$$

is $B(E2; 5/2 \to 3/2) = 33.4\ e^2$ fm^4; this is in reasonable agreement with $B(E2) = 21.3 \pm 2.0\ e^2$ fm^4 inferred from the electron scattering [30], given the accuracy of the analysis itself and the possible error in the absolute value of the cross sections for the measured angular distributions.

The negative sign of the deformation obtained from our analysis and in the study of the ^{3}He scattering [8] is consistent with the theoretical calculations by the Hartree–Fock method for a self-consistent potential [31, 32]. Our calculations show that the total binding energy is at a minimum only for the deformation corresponding to an oblate nucleus ($Q_0 < 0$). On the other hand, since the sign of the internal quadrupole moment is negative, the static quadrupole moment Q defined by [13]

$$Q = \frac{3K^2 - I(I+1)}{(I+1)(2I+3)}Q_0, \qquad (7)$$

which is valid for an axially symmetric deformation, must also be negative. However, it follows from the

hyperfine structure of the ^{11}B atomic spectrum [33] that $Q > 0$.

This contradiction can probably be explained by the fact that our rotational model is not quite adequate when applied to the ^{11}B nucleus. Indeed, it can explain neither the location of the $7/2^-$ level nor the intensities of the transitions inside the rotational band $3/2^- - 5/2^- - 7/2^-$ [32]. It should be added that the enhancement of the transitions in ^{11}B could be associated not only with the axially symmetric deformation in the shape of an ellipsoid of revolution, but also with the cluster isolation effects, which are known to play a major role in light nuclei.

3.3. Allowance for the Transfer Mechanism of the Heavy Cluster

At backward angles, the cross sections for the transfer of a cluster ($C = A - a$) in the $A(a, A)a$ reaction can significantly exceed those for purely potential scattering. The optical model predicts that the latter, as the studies of the scattering of ^{3}He and α on light nuclei at energies of 40–70 MeV [7, 8, 21, 22] show, are no more than 0.1 mb sr^{-1}, while the cluster-transfer cross sections can reach 1–10 mb sr^{-1}. For the scattering of α particles on ^{11}B, the increase in the contribution of the transfer of the heavy ^{7}Li cluster in the ^{11}B(α, ^{11}B)α reaction is attributable to the low energy of ^{11}B dissociation into ^{7}Li and an α particle and the significant spectroscopic amplitudes of the $^7\mathrm{Li} + \alpha$ configuration for the ^{11}B nucleus. However, allowance for this mechanism is complicated by the fact that, in comparison with the transfer of light d, ^{3}He, t, and α clusters, the transfer of a heavy cluster is possible not only in the ground state, but also in the excited states for which the spectroscopic amplitudes are known with an insufficient accuracy.

The differential cross sections for the transfer mechanism were computed by the distorted-wave method with an accurate allowance for the finite interaction range using the DWUCK5 code [34]. In our calculations of distortions, we used the potentials A from Table 1. The cluster ($^7\mathrm{Li} + \alpha$) wave functions of the bound ^{11}B nuclear states were computed with the Woods–Saxon potential whose geometric parameters were $r_0 = 1.25$ fm and $a = 0.65$ fm. The potential depth was chosen to obtain the needed binding energy of the clusters. The number of nodes of the wave functions (N) was defined in the approximation of a harmonic oscillator by

$$2N + L = \sum_{i=1}^{7}(2n_i + l_i) - 3, \qquad (8)$$

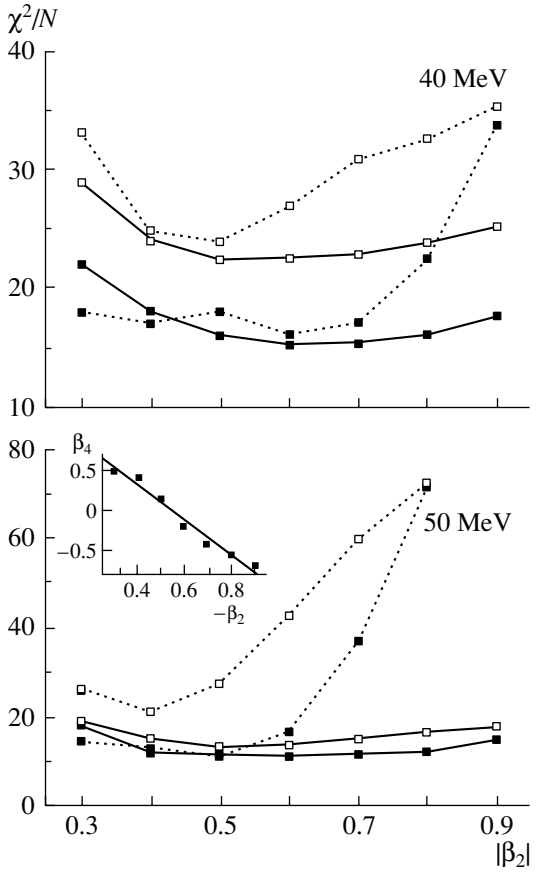

Fig. 8. As in Fig. 7, but with the parameters β_4 found from the best fit. The values of β_2 and β_4 that were obtained by minimizing χ^2/N are shown in the inset.

where L is the orbital angular momentum of the relative motion of the clusters, and n_i and l_i are the corresponding quantum numbers for the individual nucleons comprising ^{7}Li in the ^{11}B nucleus. We took into account the transfer of the ^{7}Li cluster in the ground ($3/2^-$) and two excited states with energies $E_x = 0.478$ MeV ($1/2^-$) and 4.652 MeV ($7/2^-$).

The spectroscopic amplitudes for the ground ($3/2^-$) and excited states with energies 4.445 MeV ($5/2^-$) and 6.743 MeV ($7/2^-$) for the $^{11}\mathrm{B} \to {}^7\mathrm{Li} + \alpha$ system were computed in terms of the translation-invariant shell model [35] using the DESNA code [36] and wave functions [37]. The results are presented in Table 3.

The computed angular distributions for the ^{7}Li cluster pickup mechanism are indicated in Figs. 5 and 6 by the dashed curves. The total scattering cross sections in which this mechanism would be included must be determined by a coherent addition of the scattering and cluster transfer amplitudes. However, due to the difficulties in describing the transfer of the heavy cluster noted above, we did not attempt to do

Table 3. The spectroscopic amplitudes (S_x) for the $^{11}B \to {}^{7}Li + \alpha$ system used in our calculations of the elastic and inelastic cluster transfer by the distorted-wave method

$E_x(^{11}B)$, MeV	J^π	$E_x(^{7}Li)$, MeV	J^π	E_b, MeV	nL_J	S_x
0	$3/2^-$	0	$3/2^-$	8.665	$3S_{3/2}$	−0.638
					$2D_{3/2}$	−0.422
		0.478	$1/2^-$	9.142	$2D_{3/2}$	−0.422
		4.652	$7/2^-$	13.294	$2D_{3/2}$	0.362
					$1G_{3/2}$	0.429
4.445	$5/2^-$	0	$3/2^-$	4.219	$2D_{5/2}$	−0.049
					$1G_{5/2}$	−0.192
		0.478	$1/2^-$	4.697	$2D_{5/2}$	0.092
		4.652	$7/2^-$	8.849	$2D_{5/2}$	−0.314
					$1G_{5/2}$	−0.507
6.743	$7/2^-$	0	$3/2^-$	1.921	$2D_{7/2}$	0.104
					$1G_{7/2}$	0.124
		0.478	$1/2^-$	2.399	$1G_{7/2}$	0.146
		4.652	$7/2^-$	6.551	$3S_{7/2}$	0.390
					$2D_{7/2}$	0.785
					$1G_{7/2}$	0.589

this summation and consider these calculations only as a means for rough estimates.

For the ground state, the cluster-transfer mechanism reproduces the absolute value of the experimental cross sections at backward angles, while, for the excited states, the theoretical cross sections exhaust only 30–50% of the experimental ones. The existing difference most likely results both from an incomplete description of the transfer process, in which the possible contribution from other excited states of the ^{7}Li nucleus was disregarded, and from insufficiently accurate knowledge of the spectroscopic amplitudes.

4. CONCLUSIONS

We measured the differential cross sections for elastic and inelastic scattering of α particles on ^{11}B nuclei in the entire range of angles at energies of 40 and 50 MeV.

Two potentials were found from our optical-model analysis of the elastic scattering. The first potential was obtained by fitting the computed cross sections to the experimental data in the forward hemisphere. In this case, the theoretical angular distributions have a rainbow shape with a broad maximum at angles 70°–80° followed by an exponential decrease, which agrees with the shape of the distribution for the elastic scattering of ^{3}He at close energies. The second potential was found from a fit over the entire angular range, and no nuclear rainbow effects manifest themselves in the corresponding distributions.

The two potentials were used to analyze the angular distributions for the member of the ground-state rotational band ($E_x = 0.0$ ($J^\pi = 3/2^-$), 4.445 MeV ($5/2^-$), and 6.743 MeV ($7/2^-$)) by the coupled-channel method within the collective model in which the ^{11}B nucleus was represented as a symmetric rotor. Irrespective of the chosen potential, the calculations yield approximately identical quadrupole deformation parameters, $\beta_2 = -0.6 \pm 0.15$, and provide direct evidence for the negative sign of the deformation. The hexadecapole-deformation parameter β_4 lies within the range from −0.1 to +0.2. In our analysis, it could not be determined with a better accuracy.

The internal quadrupole moment Q_0 and the reduced transition probabilities $B(E2)$ computed with the above parameters β_2 are in reasonable agreement with the electron-scattering data. The negative sign of the deformation is consistent with the results obtained from the scattering of ^{3}He at energies of 17.5 and 40 MeV [8] and with the theoretical calculations with a self-consistent potential using the Hartree–Fock method, but is in conflict with the analysis of the

hyperfine structure of the ^{11}B [33] atomic spectrum. This most likely suggests that the rotational model used in our analysis have certain limitations when applied to light nuclei in which the cluster effects could play a major role.

Our calculations by the distorted-wave method show that the rise in the cross sections observed in backward-angle scattering is attributable to the transfer mechanism of the heavy ^{7}Li cluster in the ^{11}B(α, ^{11}B)α reaction, which is indistinguishable from the scattering in the experiment.

ACKNOWLEDGMENTS

We are grateful to I.M. Pavlichenkov and A.T. Rudchik for helpful discussions of our results.

REFERENCES

1. B. Geoffrion, N. Marty, H. Morlet, *et al.*, Nucl. Phys. A **116**, 209 (1968).
2. A. J. Houdayer, T. Y. Li, and S. K. Mark, Can. J. Phys. **48**, 765 (1970).
3. J. F. Cavaignac, S. Jang, and D. H. Worledge, Nucl. Phys. A **243**, 349 (1975).
4. E. Fabrici, S. Micheletti, M. Pignanelli, *et al.*, Phys. Rev. C **21**, 844 (1980).
5. G. D. Alkhazov, S. L. Belostotskiĭ, A. A. Vorob'ev, *et al.*, Yad. Fiz. **42**, 8 (1985) [Sov. J. Nucl. Phys. **42**, 4 (1985)].
6. A. J. Buffa and M. K. Brussel, Nucl. Phys. A **195**, 545 (1972).
7. O. Aspelund, D. Ingham, A. Djaloeis, *et al.*, Nucl. Phys. A **231**, 115 (1974).
8. M. A. M. Shahabuddin, C. J. Webb, and V. R. W. Edwards, Nucl. Phys. A **284**, 83 (1977).
9. R. Görgen, F. Hintenberger, R. Jahn, *et al.*, Nucl. Phys. A **320**, 296 (1979).
10. A. E. Denisov, R. P. Kolalis, V. S. Sadkovskiĭ, and G. A. Feofilov, Yad. Fiz. **24**, 249 (1976) [Sov. J. Nucl. Phys. **24**, 129 (1976)].
11. N. S. Zelenskaya, V. M. Lebedev, and T. A. Yushchenko, Yad. Fiz. **28**, 90 (1978) [Sov. J. Nucl. Phys. **28**, 44 (1978)].
12. H. Abele, H. J. Hauser, A. Körber, *et al.*, Z. Phys. A **326**, 373 (1987).
13. A. Bohr and B. R. Mottelson, *Nuclear Structure* (Benjamin, New York, 1975; Mir, Moscow, 1977).
14. P. D. Kunz and E. Rost, Phys. Lett. B **53B**, 9 (1974).
15. O. Aspelund, D. Ingham, A. Djaloeis, *et al.*, Phys. Lett. B **50B**, 441 (1974).
16. A. M. Blekhman, N. Burtebaev, A. Duĭsebaev, and B. A. Duĭsebaev, Preprint No. 13-98, IYaF NYaTs RK (Institute of Nuclear Physics, National Nuclear Centre, Republick of Kazakhstan, Almaty, 1998).
17. F. Perey, SPI-GENOA an Optical Model Search Code (unpublished).
18. B. S. Nilsson, SPI-GENOA an Optical Model Search Code, Niels Bohr Institute Computer Program Library (1975).
19. S. A. Goncharov, private communication.
20. K. A. Gridnev and A. A. Ogloblin, Fiz. Élem. Chastits At. Yadra **6**, 393 (1975) [Sov. J. Part. Nucl. **6**, 158 (1975)].
21. N. Burterbaev, A. D. Duisebaev, G. N. Ivanov, and S. B. Sakuta, Yad. Fiz. **58**, 596 (1995) [Phys. At. Nucl. **58**, 540 (1995)].
22. N. Burterbaev, A. Duisebaev, B. A. Duisebaev, *et al.*, Yad. Fiz. **59**, 33 (1996) [Phys. At. Nucl. **59**, 29 (1996)].
23. M. Nolte, H. Machner, and J. Bojowald, Phys. Rev. C **36**, 1312 (1987).
24. R. C. Fuller, Phys. Rev. C **12**, 1561 (1975).
25. G. Hauser, R. Lohken, H. Rebel, *et al.*, Nucl. Phys. A **128**, 81 (1969).
26. J. Knoll and R. Schaeffer, Ann. Phys. (N.Y.) **97**, 307 (1976).
27. J. Raynal, Computer Code ECIS88 (unpublished).
28. R. J. Peterson, Nucl. Phys. A **377**, 41 (1982).
29. S. Roy, J. M. Chatterjee, H. Majumdar, *et al.*, Phys. Rev. C **52**, 1524 (1995).
30. P. T. Kan, G. A. Peterson, D. V. Webb, *et al.*, Phys. Rev. C **11**, 323 (1975).
31. F. Brut and S. Jang, Phys. Rev. C **14**, 1638 (1976).
32. M.-C. Bouten and M. Bouten, Z. Phys. A **280**, 45 (1977).
33. R. K. Nesbet, Phys. Rev. Lett. **24**, 1155 (1970).
34. P. D. Kunz, Computer Program DWUCK5 (unpublished).
35. Yu. F. Smirnov and Yu. M. Tchuvilsky, Phys. Rev. C **15**, 84 (1977).
36. A. T. Rudchik and Yu. M. Tchuvilsky, Preprint No. 82-12, KIYaI (Kiev Institute for Nuclear Research, Kiev, 1982).
37. A. N. Boyarkina, *Structure of the 1p-Shell Nuclei* (Mosk. Gos. Univ., Moscow, 1973) [in Russian].

Translated by V. Astakhov

Physics of Atomic Nuclei, Vol. 68, No. 8, 2005, pp. 1314–1351. Translated from Yadernaya Fizika, Vol. 68, No. 8, 2005, pp. 1368–1406.

NUCLEI
Theory

Dynamical Collective Model: Even–Even Nuclei[1)]

V. E. Mitroshin*

Kharkov National University, Kharkov, Ukraine

Received November 3, 2003

Abstract—A unified approach to describing the properties of spherical, transition, and deformed even–even nuclei (without invoking the concept of static nuclear deformation), a "dynamical collective model," is set out in retrospective. We present the results of calculations for a wide range of nuclei and, on this basis, reveal a number of experiments that are of fundamental importance in developing the theory further.

1. INTRODUCTION

Among the multitude of problems facing nuclear physics, one of the most important problems is to develop a model of the atomic nucleus that could reliably, within a reasonable accuracy, describe any of the properties of the first two or three states with any spin and parity, i.e., the structure of the states near the yrast band, for a given atomic number and nuclear charge. This problem is of fundamental importance not only because the insolubility of many questions in astrophysics and particle and solid-state physics rests precisely on this "nuclear factor," but also because the spectroscopy of low-lying nuclear states, perhaps as no other field of physics, provides a wealth of information on the spectral properties of multiparticle systems. Thus, we can refine to details the methods for solving multiparticle problems, the methods that have been successfully used and are being used in other fields of natural science.

However, despite the long history of development of nuclear spectroscopy, our views of the structure of atomic nuclei are still in such an "infant age" that, without comprehensive experimental information on the properties of excited states in a specific nucleus, we are often unable not only to predict, but even to describe the level spectrum for this nucleus, not to mention such subtle characteristics as the probability of its β decay. For two neighboring isotopes of the

*e-mail: mitroshin@univer.kharkov.ua

1) *From the Editorial Board*. The review by V.E. Mitroshin sets forth the main ideas and results of an original approach (the dynamical collective model, DCM) in the theory of low-lying nuclear excitations that he has developed for about thirty years. This approach is similar in original formulation to the quasiparticle–phonon model by V.G. Solov'ev and his disciples. Just as the latter, DCM uses the "pairing + multipole forces" Hamiltonian, but it is significantly advanced compared to Solov'ev's model primarily in that it allows for the Pauli exclusion principle in the microscopic construction of phonons, the main objects of both approaches. The choice of the form of multipole forces with surface form factors similar to those suggested by N.I. Pyatov, S.A. Fayans, and F.A. Gareyev also seems felicitous. DCM purports to give a unified description of both spherical nuclei, with the collective quadrupole oscillations making a dominant contribution to their dynamics, and deformed nuclei with a well-defined rotational spectrum. In addition, the so-called transition nuclei, traditionally difficult objects for the nuclear theory, can also be described in terms of DCM. In this respect, DCM can be likened to the interacting-boson model, but it is a microscopic approach of a deeper level: in DCM, bosons (phonons) are built from fermions. In the presented approach, for example, the properties of low-lying states in the Sm isotopes of spherical, transition, and deformed nuclei can be satisfactorily described without resorting to the concept of deformation and, accordingly, without introducing rotational degrees of freedom. This result seems very instructive: the rotational (or quasirotational) spectrum is not always direct evidence of deformation—certain additional conditions are required. In DCM, such a spectrum arises from the Pauli exclusion principle: as the j level is filled, the purely vibrational spectrum is distorted and transforms into a rotational spectrum in the limit. This has led the author to the far-reaching conclusion about the fundamental absence of deformation in the ground (and the first excited) states of nuclei. An attempt is made to substantiate this conclusion mathematically. It seems to us that this "extremist" conclusion is erroneous, which necessitated this comment. Without going into mathematical details, we note that the proof is apparently inapplicable to systems with spontaneously broken symmetry, to which the deformed nuclei belong (see, e.g., the well-known monograph by O. Bohr and B. Mottelson, vol. 2). The so-called Goldstone excitation mode starting "from zero" must necessarily exist in these systems. In a deformed nucleus, this is the rotational branch of excitations to which, according to the Goldstone theorem, all low-lying excitations belong. However, in our view, this assertion of the author, which seems erroneous to us, does not abolish the positive content of the approach developed by him, in which an important step has been taken in constructing a microscopic theory of low-lying nuclear excitations, particularly in the transition region between spherical and deformed nuclei.

1063-7788/05/6808-1314$26.00

same nucleus, our views of their structure often differ radically.

Henri Poincaré, a prominent thinker of the 19th century, emphasized that "science is built from facts as a house from bricks; but a simple collection of facts is as far from science as a pile of stones from a house." In this sense, we have to do with a pile of "bricks" and nothing else, although some of the "bricks" have been polished to a high gloss.

But is the problem of describing the structure of the states near the yrast band soluble at all? May it be that the oppressive variety of models each of which is applicable only to a narrow range of phenomena and nuclei is attributable precisely to the fundamental insolubility of even this narrow problem?

In Section 2, we look at the obstacles, achievements, and prospects that exist on the way to solving the problem of describing the structure of the states near the yrast band through a prism of history. We emphasize that we give an overview of not the models in the nuclear theory and their applications, but the historically conditioned reasons for our chosen approach under the name "dynamical collective model" (DCM). This is a figurative name. The mathematical essence can be expressed by the words "the method of an ordered basis in the nuclear theory." In Section 3, we describe the implementation of this program in terms of the "pairing + multipole–multipole interaction" scheme. The reader will find here not only the theory, but also an analysis of the experiments used as the basis for it. In Section 4, we present the results of our calculations for a number of spherical, transition, and deformed even–even nuclei. The results presented here allow the questions whose solution will play a key role in developing the theory further to be posed for an experiment.

2. INTERNAL PROBLEMS OF NUCLEAR SPECTROSCOPY

2.1. When studying the structure of atomic nuclei, we run into two main difficulties. On the one hand, we do not know the detailed nature of the nuclear forces, and it becomes increasingly clear that they can be fairly complex. On the other hand, even if we knew these forces, as in the case of an atom, how could we tackle the many-body problem that the problem of describing the properties of nuclei is? In such a situation, based on an experiment, each researcher initially identifies particular processes as the main ones and subsequently solves this simplified problem. This is how a model of the atomic nucleus arises, which in its essence no longer purports to describe the entire variety of phenomena in nuclear spectroscopy.

We emphasize that, in this paper, we will talk about models and only about models, because, paraphrasing Hertz's words about Maxwell's theory, the nuclear theory is Schrödinger's equation. Honestly, we are not quite sure of this either, since the studies of the past twenty years have shown an important role of nonnucleon degrees of freedom in nuclei and relativistic effects. However, even if we were sure that the "nuclear theory is Schrödinger's equation," we would still be unable to solve it exactly. We always solve it approximately. Whether we make these approximations once we have passed to a more convenient unitarily equivalent representation (the method of K-harmonics etc.), where we subsequently separate out the principal components of the wave function based on an experiment or on what is called physical considerations or we separate out the principal components based on an (even macroscopic) analogy, is not so important if the adequacy of the description of experimental data serves as a criterion of truth. Whether we construct the perturbation theory for Schrödinger's equation proper or for its resolvent (the method of Green's functions), these are all different ways of expressing the same thing and we have no grounds to call one of the approaches a theory and the other approaches models. Which models should be preferred is a different question. However, all criteria, alas, are subjective here as well: each researcher applies his own, often unconscious, evaluation system even in the concept of satisfactory agreement, all but one criterion—the completeness of the experimental data described by the model.

The historically formed path of cognizing any complex phenomenon, which consists in decomposing it into simple components (elementary excitation modes), studying them individually, and attempting to reproduce the original complex phenomenon in its interrelationship, is reflected surprisingly accurately in the development of models in any of the natural sciences. Nuclear spectroscopy also developed in this way, where the main events occurred at the turn of the 1950s. It was then that two central concepts were crystallized from an analysis of a vast collection of experimental data, the concepts of single-particle and collective degrees of freedom, which reflected the common property that was inherent in the dynamics of most nuclei and that depended weakly on the detailed nature of the nuclear forces. It would hardly be an exaggeration to say that these concepts will remain at the basis of the baggage of ideas of nuclear spectroscopy for a long time. It is through the prism of these concepts that we will look at the prospects for solving the main problem.

2.2. Let H_{mod} denote the model Hamiltonian through which we hope to describe the properties of atomic nuclei and let us assume that we are

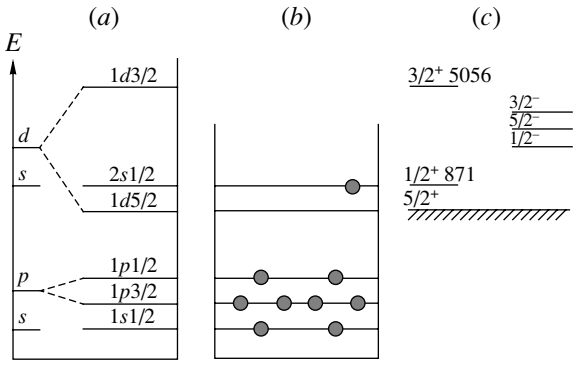

Fig. 1. (*a*) Single-particle state diagram. (*b*) The diagram for the filling of single-particle states with neutrons for the first excited ^{17}O state. (*c*) A fragment of the experimental diagram of excited ^{17}O states (the energy is in keV).

interested only in the discrete spectrum of $H_{\rm mod}$ and its eigenvectors. Methodologically, all approaches to finding the eigenvectors of $H_{\rm mod}$ and its eigenvalues are identical and are reduced to expanding the desired wave function of the nth state $|\psi^{(n)}\rangle$ in terms of a complete orthonormal set $\{|\varphi_\nu\rangle\}_1^\infty$ of functions of the required class:

$$|\psi^{(n)}\rangle = \sum r_\nu^{(n)}|\varphi_\nu\rangle. \qquad (1)$$

The expansion coefficients $\{r_\nu^{(n)}\}$ and the eigenvalues $E^{(n)}$ can be determined by solving the standard conditional-extremum problem:

$$\delta\{\langle\psi^{(n)}|H_{\rm mod}|\psi^{(n)}\rangle - E^{(n)}[\langle\psi^{(n)}|\psi^{(n)}\rangle - 1]\} = 0, \qquad (2)$$

where the requirement that eigenvectors (1) be orthonormal acts as the condition.

For any specific realization of (2), we have to restrict ourselves to a finite number of expansion terms. Therefore, the question about the convergence of expansion (1) and about the rate of its convergence immediately arises.

First of all, we emphasize that expansion (1) converges always. This directly follows from the fact that, since the binding energy of the nuclei is finite, the corresponding Hamiltonian $H_{\rm mod}$ must be limited below by a linear operator. In turn, this implies that, if we are interested only in a finite number of the first N eigenvalues, then, whatever the basis of vectors $\{|\varphi_\nu\rangle\}_1^\infty$ we choose, for any prespecified accuracy ε, we will find a finite number $N_\varepsilon \geq N$ of vectors $\{|\varphi_\nu\rangle\}_1^{N_\varepsilon}$ in the description, for example, of the eigenvalues at which the first N solutions of problem (2) in this finite-dimensional space will not differ from the exact solution by more than ε. As a result, the problem of finding the first N eigenvalues and eigenvectors is reduced to the trivial problem of diagonalizing the matrix

$$[\langle\varphi_\nu|H_{\rm mod}|\varphi_\mu\rangle]_{\mu,\nu=1,\ldots,N_\varepsilon}$$

of dimension N_ε. However, first, although N_ε is finite, it can be very large (the problem of diagonalizing large-dimension matrices); second, we must be able to efficiently calculate the matrix elements $\langle\varphi_\nu|H_{\rm mod}|\varphi_\mu\rangle$ (the problem of choosing a convenient basis); and, third, we do not know a priori precisely which of the vectors $|\varphi_\nu\rangle$ enter into our finite-dimensional space (whether the first hundred vectors or only ten starting from the hundred thousandth vector).

Whereas the first two problems are, as it were, technical ones, it is on the third problem that the development of any nuclear model rests, be it the translationally invariant shell model [1], the theory of finite Fermi systems [2], the method of hyperspherical functions [3], the quasiparticle–phonon model [4], or any other model. In fact, we wish to show this and to outline a possible way out of this impasse.

2.3. For convenience, we begin with the formal aspect of the question. Let H_0 be an arbitrary linear operator limited below whose domain of definition coincides with the domain of definition of $H_{\rm mod}$. For the sake of convenience, we assume that the eigenvectors of H_0 form a complete orthonormal system. Let us now rewrite $H_{\rm mod}$ as

$$H_{\rm mod} = H_0 + (H_{\rm mod} - H_0) = H_0 + H_{\rm int}. \qquad (3)$$

Now, the objective of the theory is to study how $H_{\rm int}$, figuratively speaking, "intermixes" the various eigenvectors of H_0. Fairly few constraints were imposed on the choice of H_0; it can also be chosen in such a way (perhaps randomly) that the effect of $H_{\rm int}$ for some of the eigenvectors of H_0 can be ignored; i.e., these eigenvectors are "almost" the eigenvectors of $H_{\rm mod}$.

Analysis of the experimental data (the theory gave no grounds for this) suggested that, to the first approximation, a nucleus could be treated as a system of noninteracting fermions that, according to the Pauli exclusion principle, move independently in the self-consistent "average" field generated by them. The analogy with an atom played a prominent role in the birth of this idea, but this analogy has hindered the perception of the ideas of the single-particle shell model (SSM) for a long time. However, the experimental data accumulated by the 1950s convincingly demonstrated that the ground states of several odd nuclei with the number of nucleons equal to the magic number $\pm$ 1 strikingly resemble the inert atom $\pm$ 1, but with the reversed pattern of spin–orbit coupling.

Figure 1*a* shows a fragment of the single-particle state diagram that was suggested to explain the magic numbers and related patterns. In the SSM

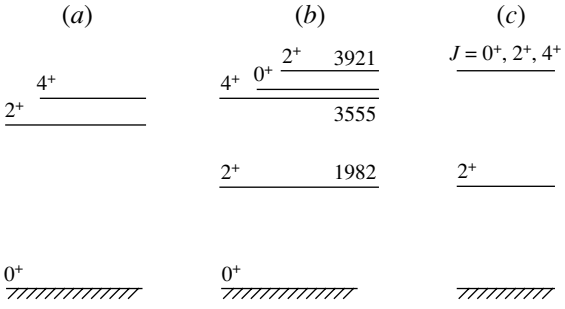

Fig. 2. (*a*) Level spectrum for the two-particle configuration $[1d_{5/2}]^2_{J=0,2,4}$. (*b*) A fragment of the experimental spectrum of excited ^{18}O states (the energy is in keV). (*c*) The spectrum of excited states for a harmonic oscillator.

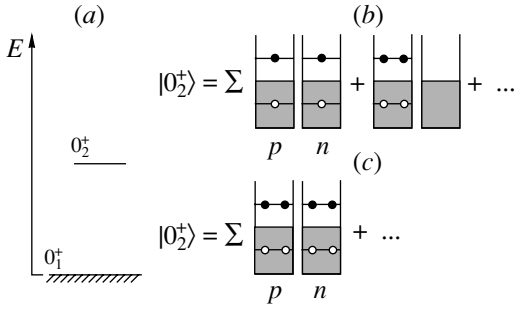

Fig. 3. (*a*) Fragment of the experimental spectrum of excited ^{16}O states. (*b*) Schematic view of the expected components of the wave function for the excited 0_2^+ state. (*c*) Schematic view of the components of the realistic wave function for the excited 0_2^+ state.

ideology, the wave functions of the ground states of the "magic number ± 1" nuclei represent Slater's determinant with the single-particle states packed most densely with nucleons up to the last j^π level, where the odd nucleon the spin and parity of whose state correspond to the experimental data is located. This is illustrated by Fig. 1*b*, which shows a diagram for the filling of single-particle ^{17}O nuclear states with neutrons. It turned out that some of the experimentally observed excited states (Fig. 1*c*) could be easily understood from an analysis of the lowest (in energy) transitions of nucleons to free single-particle states. The correctness of the identification of these states precisely as single-particle ones was soon confirmed in single-nucleon exchange reactions. Moreover, the magnetic moments of the ground states of the "magic number ± 1" nuclei and the probabilities of β transitions between such nuclei showed good agreement with SSM predictions.

This was the real triumph of the physical idea, since a tool for not only qualitative but also quantitative analysis of experimental data fell into the hands of researchers. It would not be an exaggeration to say that most of the theoretical works have been devoted to an increasingly thorough development of the ideas that underlie the shell model for 50 years. Now, it may even seem strange how long it has forced its way. Is this because it is hard to realize the idea that the SSM is just a luckily guessed H_0? Luckily means that, for some of the nuclei, the wave functions of the ground and several excited states contained one well-defined component. However, as soon as this idea had been realized, an attempt was made to extend it to all nuclei and to the entire spectrum of low-lying states.

As an example, let us consider ^{18}O, a fragment of whose excitation spectrum is shown in Fig. 2*b*. Following their ideology, the SSM proponents believed that the spectrum of low-lying ^{18}O states was nothing more than the split (through H_{int}) multiplet of $[1d_{5/2}]^2_{J=0,2,4}$ states formed by the last two nucleons. They were going to determine H_{int} from the multiplet splitting by performing similar calculations for many other nuclei. However, the level spectrum obtained in this way (Fig. 2*a*) was in poor agreement with the experimental data, while the experimental value of $B(E2; 2_1^+ \to 0_1^+)$ was a factor of 5 higher than its calculated value. In other words, the experimental data showed that adding only two nucleons leads to a strong polarization of the magic core and that the wave function even for the ground states of such and more complex nuclei should be sought in the form of expansion (1) in terms of the eigenvectors of H_0, admissible by the laws of conservation of total angular momentum and parity, and with a fairly low excitation energy.

This is how the multiparticle shell model (MSM) arose. However, in the 1960s, it did not attract attention, because no suitable computers were available and there were difficulties in classifying the multifermion states. The fruits of this direction of research began to mature relatively recently [5]. At the same time, it has emerged that there are no a priori criteria that would allow one to establish precisely which of the vectors of H_0 give the main, say, 90%, contribution to the formation of the spectrum of low-lying states. Let us illustrate this by describing the 0_2^+ state of ^{16}O as an example; a fragment of its spectrum is shown in Fig. 3*a*. It would be natural to assume (and therein lies the MSM ideology) that the spectrum of low-lying states with given spin and parity must be formed from the vectors of H_0 with the lowest excitation energy. Moving upward over the H_0 spectrum, we will see how rapidly our problem converges.

For ^{16}O, the "two particles + two holes" configurations are the lowest states in the H_0 spectrum with the 0^+ angular momentum (Fig. 3*b*). One would think that precisely these configurations must give

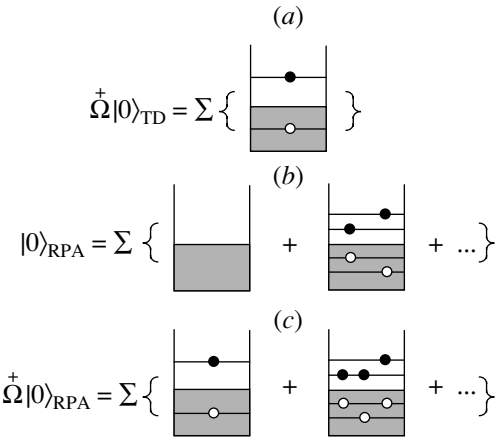

Fig. 4. Schematic view of the wave functions for (*a*) the single-phonon state in the Tamm–Dankov approximation, (*b*) the ground state in the random phase approximation, and (*c*) the single-phonon state in the random phase approximation.

the main contribution to the formation of the first excited 0^+ states of ^{16}O. What a surprise it was when it emerged that that the principal components of the excited 0_2^+ state were the vectors of the α-particle type "four particles + four holes," while the other, simpler, configurations yielded only small corrections (see, e.g., [6] and references therein). However, the question then arises as to whether we will encounter an even more pathological situation in other nuclei?

2.4. We have run a few steps forward; let us return to the 1960s, when each new experiment required an immediate explanation, and, therefore, each day gave birth to new ideas. Thus, for example, scrutiny of the ^{18}O spectrum revealed that it remarkably resembled the level spectrum of a weakly split harmonic oscillator (Fig. 2*c*). The systematics of experimental data showed that a similar picture is also observed in many other nuclei, and the idea that we have to deal with the surface oscillations of an incompressible liquid drop arose. Of course, this idea was not born out of nothing. The liquid-drop models of the nucleus have long and successfully been used to analyze the nuclear masses, the fission processes, etc. However, the creators of the generalized collective model (GCM) took a further step [7] by noting that, if the drop is statically deformed, then another degree of freedom, the rotation of the nucleus as a whole, appears in the nucleus. The almost purely rotational level spectra detected for many nuclei stimulated an intensive and comprehensive analysis of the ideas that underlie GCM. The separation of nuclei into spherical and deformed ones arose precisely at this time, and the no-man's land of transition nuclei lies between them.

The most striking thing in the history of the making and development of the rotational model is that its zeroth approximation worked excellently. Only subsequently did it emerge that "the more accurately you calculate, the worse result you obtain." For now, the very possibility of analyzing experimental data, as it were, on the fingers and conveniently systematizing them has led to the fact that the concept of statically deformed nuclei has become one of the main concepts of nuclear spectroscopy. Is this the reason why it took almost thirty years to return to the idea of unity of the dynamics in atomic nuclei and arbitrariness of the separation of nuclei into spherical and deformed ones following Sheline [8] and Sakai [9]? We will return to these fundamentally important questions below.

As regards the nature of the vibrational states, phonons, it was established by the mid-1960s that they are correlated particle–hole excitations with the corresponding spin and parity. This is shown in Fig. 4, which schematically displays the wave function for a phonon in the Tamm–Dankov approximation (Fig. 4*a*), the wave function for the ground state of an even–even nucleus in the random phase approximation (Fig. 4*b*), and the wave function for the single-phonon state in the random-phase approximation (Fig. 4*c*).

At that time, it seemed obvious that the switchover from the particle–hole MSM representation to the phonon representation would allow the observed spectrum of low-lying states for even–even nuclei to be easily constructed from various phonon modes and their degrees. It should be emphasized that this idea has not yet lost its appeal, reviving in various versions of the interacting boson model [10].

The hope for the fruitfulness of this approach is based on the simple consideration that, when phonons are formed, a fairly large fraction of the forces acting between the nucleons must go into the phonon dynamics; therefore, the residual forces that already act between the phonons, in a sense, are too weak to ensure good convergence of the expansions of the wave function in terms of multiphonon states. These hopes strengthened even more after the phenomenon of superfluidity was discovered in atomic nuclei and after yet another dynamical concept, a quasiparticle as an elementary excitation mode in compound nuclei, was shaped. However, the main thing was that, based on the concepts of a phonon and a quasiparticle, we managed to figure out a number of phenomena of nuclear physics that had not been explained until then. The impression from these results was so strong that, by the early 1970s, few doubted that the excitation spectra of both even–even and odd nuclei from the spherical mass region could be easily constructed from quasiparticles and quasiparticle-based phonons. At the same time, for deformed nuclei, it was suggested doing the same, but only in the corresponding deformed average field.

It seemed that the "bricks" from which the building of the theory of atomic nucleus could be easily erected had been found; it remained only to "count" them, and this is not so interesting....

Is this the reason why many prominent researchers have abandoned nuclear physics and turned to the construction of "bricks" in other fields of natural science? Is this the reason why many of the then published books contained the phrase "theory of atomic nucleus" in their titles, emphasizing the completeness of the problem? Is this the time from which interest in studying the structure of atomic nuclei has waned?

Forty years has elapsed in the development of this direction of research. What have we now? The "bricks" that have been polished to a high gloss and that we have inherited are simply unsuitable for constructing the theory of atomic nucleus. Why?

2.5. First, the concept of a phonon that we have inherited most often makes no sense—as soon as we depart from a magic nucleus by several nucleons, the energy of the quadrupole phonon becomes imaginary. Initially, this was considered as a point of phase transition from the spherical shape of the nucleus to a deformed shape. However, it was noted back in 1964 [11] that the reason lies in the overly rough approximations that were made in developing this concept, and a new approach to the problem was formulated. However, the first calculations yielded another negative result [12]: the energy of the 2_1^+ state stabilized rapidly at 500 keV almost in all nuclei without "wishing" to drop below this level. As was established subsequently [13, 14], the fact that the effect of collective degrees of freedom on the superfluid properties of the nucleus was disregarded is responsible for the failure. This effect is twofold. On the one hand, the presence of unpaired quasiparticles destroys the superfluid properties of the nucleus due to the blocking effect; on the other hand, the phonon exchange between the nucleons gives rise to an additional pairing field.

As a result, the quasiparticle energy decreases with increasing collectivity of the nucleus, causing the phonon energy to decrease, while the blurring of the Fermi surface characteristic of pairing increases. A proper realization of this idea was delayed for many years, and certain progress in describing the basic characteristics of spherical, transition, and deformed nuclei has been made in this direction only recently [14, 15]. The ^{112,122}Sn spectra calculated in the single-phonon approximation in comparison with the experimental spectra (Fig. 5) and the calculated and experimental dependences of the various characteristics of the Sm isotopes on the number of neutrons (Fig. 6) can serve as an illustration of the aforesaid. These questions are discussed in detail in Subsections 3.2–3.5. Here, these results are presented only to compare the concept of a phonon in the past (phonons are formed from quasiparticles, but exist as foreign bodies with respect to them) with the concept of a phonon at present (the mutual effect of the collective and single-particle degrees of freedom on one another is taken into account). As we see from our comparison with the experimental data, the latter can be used as the basis for describing spherical, transition, and deformed nuclei. What do these concepts have in common? Essentially, only the name.

2.6. Second, the presence of an odd quasiparticle can affect significantly the structure of the collective modes. This effect attributable to the Pauli exclusion principle manifests itself most clearly for odd nuclei in the $(j-1)$ anomaly and in the coexistence of the superfluid and normal phases in the spectra of odd nuclei.

The $(j-1)$ anomaly has been studied thoroughly [16, 17] and consists in the following. Let an odd quasiparticle be in a single-particle state with an angular momentum $j \geq 5/2$. Let us excite a quadrupole phonon. If the total angular momentum J of the excited state is $J = j-1$, then strong attraction arises between the odd quasiparticle and the quasiparticles that form the phonon, while repulsion arises in different (in spin) states. As a result, the phonon has a different structure not only depending on the position of the odd quasiparticle, but also in different (in total angular momentum) states. Occasionally, this change in the structure is so large that the $(j-1)$ anomaly becomes the ground state of the nucleus; i.e., the multiquasiparticle state proves to be energetically more favorable than the single-quasiparticle state.

This is observed in the rhodium isotopes, but it is most pronounced in the europium isotopes, where the spectrum of low-lying states has two $5/2^+$ states and one $7/2^+$ state. In light isotopes with $A \leq 151$, $5/2^+$ originating from the single-quasiparticle $2d_{5/2}$ state is the ground state, while the $(j-1)$ anomaly based on $1g_{7/2}$ is an excited state, as the single-quasiparticle $7/2^+$ state. However, the $5/2_1^+$ and $5/2_2^+$ states in the ^{153}Eu isotope change places (Fig. 7*a*); the $(j-1)$ anomaly becomes the ground state. Indeed, the g factor of the $(j-1)$ anomaly is almost the same [17] as that of the single-particle state on which it is formed, and, hence, $\mu(j-1) \cong (j-1)g(j)$. That is why a sharp decrease in the magnetic moment of the ground $5/2^+$ state is observed in the ^{153}Eu isotope (Fig. 7*b*), since $g(1g_{7/2}) \ll g(2d_{5/2})$. On the other hand, the root-mean-square

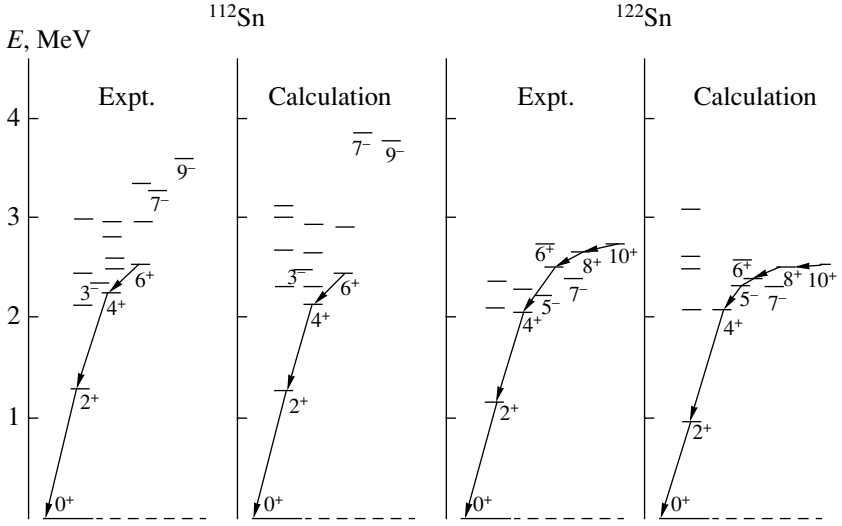

Fig. 5. Spin-expanded fragments of the calculated spectra for single-phonon ^{112,122}Sn states of various multipolarity in comparison with the experimental spectra.

charge radius of the $(j-1)$ anomaly is larger than the charge radius of the state on which it is formed due to the presence of a phonon; that is why a sharp increase in the charge radius of europium relative to the samarium isotope with the same number of neutrons is observed (Fig. 7*c*). If we take into account the previously discussed effect of the collective modes of motion on the quasiparticle ones, then we will immediately reach the conclusion that there are no universal bricks in odd nuclei; in each nucleus, specific concepts of dynamical variables whose quanta realize the spectrum are needed for each spin and parity.

The problem under discussion manifests itself even more clearly in the coexistence of the superfluid and normal phases in atomic nuclei.

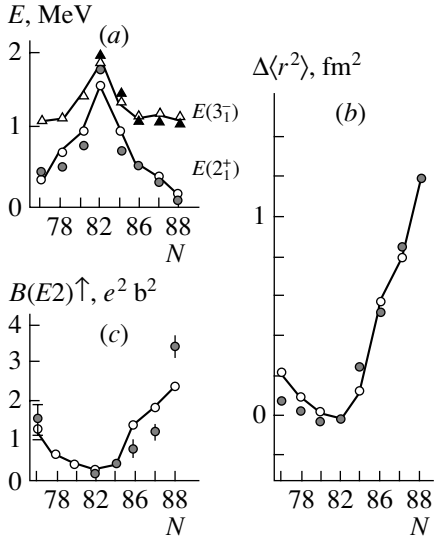

Fig. 6. (*a*) Energies of the 2_1^+ and 3_1^- states calculated for the samarium isotopes in the single-phonon approximation (open symbols) and their experimental values (closed symbols); variations in the charge radius of the isotope with $A = 144$ (*b*); $B(E2; 0_1^+ \to 2_1^+)$ (*c*).

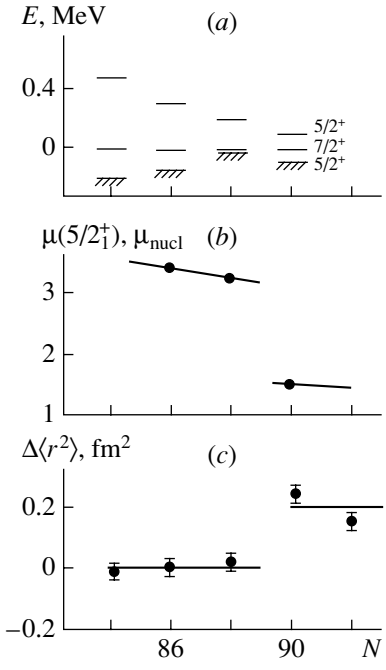

Fig. 7. (*a*) Fragments of the spectra of low-lying states for the Eu isotopes relative to the $7/2_1^+$ state. (*b*) The magnetic moment of the ground $5/2_1^+$ state. (*c*) Variations in the root-mean-square charge radius of the Eu isotopes relative to the Sm isotopes with the same number of neutrons.

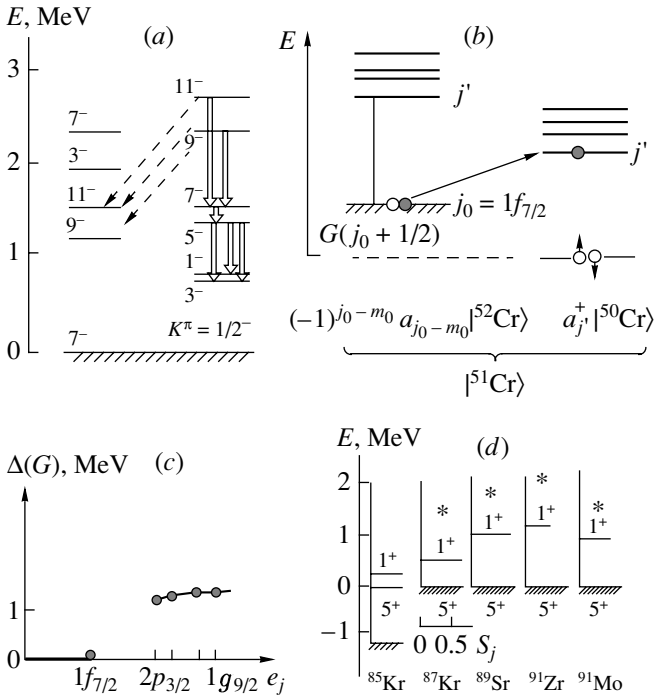

Fig. 8. (*a*) Fragment of the diagram of excited ^{51}Cr states with the highlighted $K^\pi = 1/2^-$ band. The spins are doubled. (*b*) Schematic view of the superfluidity mechanism at low excitation energies. (*c*) Neutron pairing gap in ^{51}Cr versus position of the odd neutron. (*d*) Spectra of the first excited $J^\pi = 5/2^+$ and $1/2^+$ states (the spins are doubled) for several isotopes and their spectroscopic factors S_j (the length of the horizontal line; the scale is specified in the figure); the asterisks indicate the values of $E(2_1^+)$ for the even core $(A-1)$.

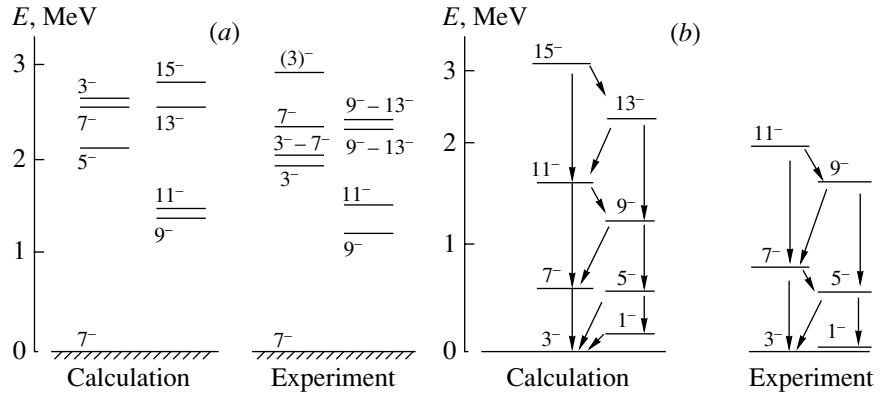

Fig. 9. Calculated and experimental spectra of the "nonrotational" (*a*) and "rotational" (*b*) ^{51}Cr states. The spins are doubled.

The history of this question began from the discovery of low-lying states with seemingly different equilibrium shapes in several nuclei. The ^{51}Cr isotope can serve as one of the most dramatic examples of such a nucleus. In addition to the typically vibrational states, a band of states that was identified [18] as the rotational $K^\pi = 1/2^-$ band based on the Nilsson 1/2[321] level was detected in its excitation spectrum (Fig. 8*a*). The zeroth approximation of the rotational model described excellently the properties of this band, while the fact that the γ transitions to states that did not belong to the band were hindered seemed to be convincing evidence for shape isomerism in this nucleus. However, analysis [19] of the accumulated data showed that most of the radiative transitions between states of different equilibrium shapes are not explicitly forbidden; the following alternative [20] to the description of shape isomers then appeared.

First of all, note that the values of $B(E2)$ between the band states are close to those of $B(E2; 2_1^+ \to$

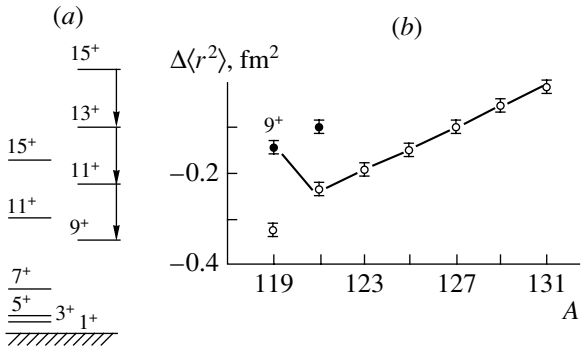

Fig. 10. (a) Fragment of the spectra of excited ^{119}Cs states. (b) Charge radius of the cesium isotopes versus mass number. The solid line combines the data for the ground nuclear states. The spins are doubled.

0_1^+) in the ^{50}Cr isotope. However, for ^{51}Cr to be similar to ^{50}Cr, the odd neutron from the $1f_{7/2}$ shell must be removed to a state from the overlying shell. The $1f_{7/2}$-state blocking effect then vanishes, strong pairing arises between the remaining neutrons, and the core becomes similar to the strongly collective ^{50}Cr isotope (Fig. 8b). The increase in the energy of the odd neutron is largely offset by the pairing energy, while the coupling of the odd neutron with the strongly collective ^{50}Cr states can produce a band similar to the experimental one (see below). However, when the odd neutron is in the $1f_{7/2}$ state or in any other hole-type state for the "magic number -1" nuclei, the blocking effect destroys the neutron superfluid properties, and the core becomes similar to the weakly collective ^{52}Cr nucleus. Figure 8c, in which the pairing gap is plotted against the position of the odd neutron, explains the aforesaid. As a result, the ^{51}Cr excitation spectrum breaks up into a sum of the spectra of the "hole + ^{52}Cr" and "quasiparticle + ^{50}Cr" systems that are virtually uncoupled. The results on the ^{84}Kr(d, p)^{85}Kr reaction [21], where states with $J^\pi = 5/2^+$ and $1/2^+$ and with large spectroscopic amplitudes were found, provide a good illustration to the hypothesis under discussion. These data are presented in Fig. 8d taken from the same paper in comparison with those for the nuclei with $N = 51$. The figure shows that the states are identical in nature, and the clear correlation of the energy of the $1/2^+$ states with $E(2_1^+)$ of the even $A-1$ core (asterisks) is indicative of a direct relationship to the collective motion.

Table 1. Transition probabilities between the "nonrotational" ^{51}Cr states (in Weisskopf units)

J_i^π	J_f^π	$B(E2; J_i \to J_f)$		$B(M1; J_i \to J_f)$	
		calc.	expt.	calc.	expt.
$9/2^-$	$7/2^-$	16.2	12^{+6}_{-3}	0.11	$0.24^{+0.10}_{-0.06}$
$11/2^-$	$7/2^-$	14.6	6^{+4}_{-2}	–	
	$9/2^-$	7.5	<25	0.31	$0.3^{+0.5}_{-0.13}$

Table 2. Transition probabilities between the "rotational" ^{51}Cr states (in $e^2\,\mathrm{b}^2 \times 10^{-3}$)

J_i^π	J_f^π	$B(E2; J_i \to J_f)$		
		calc.	rot. model	expt.
$1/2^-$	$3/2^-$	33	48	–
$5/2^-$	$3/2^-$	7	7	16^{+11}_{-6}
	$1/2^-$	22	24	24^{+14}_{-9}
$7/2$	$3/2^-$	33	31	32^{+17}_{-15}
	$5/2^-$	1	3	–
$9/2^-$	$5/2^-$	42	34	32^{+11}_{-8}
	$7/2^-$	2	2	–
$11/2^-$	$7/2^-$	51	36	≤ 51

The realization of this idea for the ^{51}Cr [20] and In [22] isotopes showed good agreement between the results of the calculations and the entire set of experimental data (see Fig. 9 and Tables 1, 2).

The situation with the bands of ($\Delta J = 1$)-type states detected in several antimony, iodine, and cesium isotopes is identical. These are hole-type excitations in the strongly collective tellurium, xenon, and barium isotopes, respectively [20]. In ^{119}Cs, this hole $9/2^+$ state even becomes the ground state of the nucleus with large root-mean-square deformation; as a result, a jump in the charge radius is observed (Fig. 10).

It should be emphasized that the attempt [23] to describe both the vibrational and rotational ^{115}In levels in terms of the "one particle + two holes + ^{116}Sn" scheme was made the earliest. In general, it was successful, but the transition probabilities between the states of the band calculated without introducing effective charges proved to be a factor of 2 or 3 lower than their observed values. Clearly, the reason is that the states of the cadmium core forming the rotational band do not fit into the "two holes + ^{116}Sn" space. These examples give an excellent illustration of the previously advanced idea that not the first (in order of increasing energy) thousand vectors, but only, for example, one hundred, but starting from the hundred thousandth vector, can play a major role in forming the low-lying and even ground nuclear states.

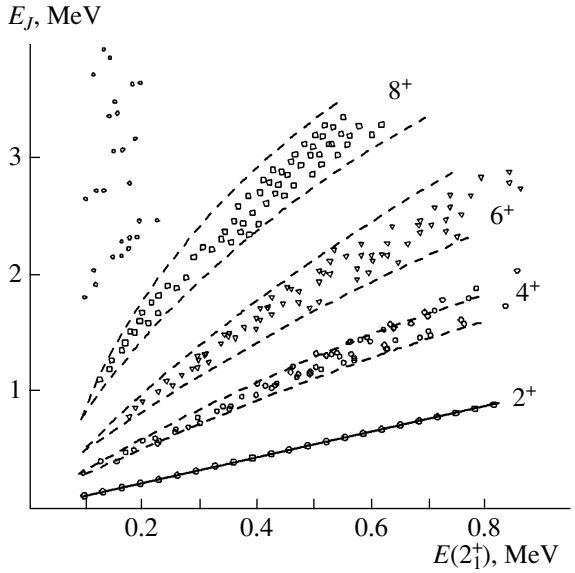

Fig. 11. Level systematics [25] for the yrast bands of nuclei with developed collectivity versus $E(2_1^+)$.

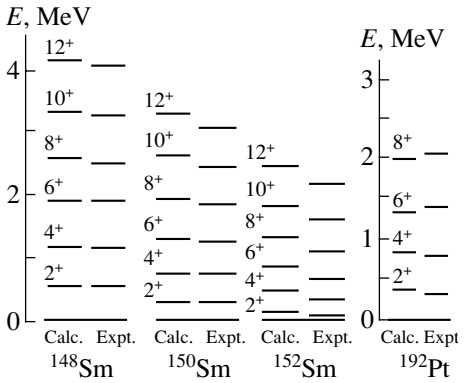

Fig. 12. Spectra of the yrast bands calculated in the harmonic DCM approximation for several nuclei in comparison with the experimental data.

2.7. Third, if one quasiparticle affects the phonon structure so strongly, then the question arises as to whether the effect of the phonons on one another is just as strong. Here is the line of reasoning that allows the answer to be guessed qualitatively.

Let us consider an N-phonon state. Being a fermion structure, each phonon blocks any of the available single-particle states for a certain time, thereby reducing the fraction of the phase volume for the other phonons. Therefore, the fraction of the phase volume for each phonon in the N-phonon state decreases proportionally to $N-1$. However, the phonon frequency ω then increases proportionally to $N-1$ with the coefficient $4g$ that depends on the structure of the Fermi surface and the quantum numbers of the N-phonon state: $\omega_N = \omega + 4g(N-1)$. Consequently, the total energy of the N-phonon state is $E_N = N\omega_N$; for the states aligned by the total angular momentum $R = 2N$, it takes the form of the standard formula $E_R = fR + gR(R+1)$ with $f = \omega/2 - 3g$. The phonon structure and the transition probabilities in the band change in accordance with the change in ω_N:

$$B(E2; R \to R-2) = NB(E2; \omega_N \to 0)$$
$$= \frac{R/2}{1+2g(R-2)/\omega} B(E2; 2_1^+ \to 0_1^+).$$

We see from the definition of the coefficient f that even the small contribution from the Pauli exclusion principle, $g \sim 10$ keV, will lead to the fact that the spectrum of the yrast band for soft nuclei will differ little from the rotational one, as will the $E2$-transition probabilities in the band. These ideas were first set forth in 1974 [24]; it emerged that the coefficient g depends weakly on the structure of the Fermi surface and, hence, on $\omega = E(2_1^+)$. Consequently, the dependence of E_R on $E(2_1^+)$ must be nearly linear [24].

This is demonstrated by Fig. 11, where the level systematics [25] for the yrast bands of nuclei is plotted against $E(2_1^+)$. This is how a simple and universal mechanism that leads to the rotational excitation spectra for soft nuclei with all their characteristic features was found without resorting to the concept of static deformation. However, the implementation of this program on the microscopic level was hindered by the fact that the concept of a phonon that would be acceptable for any mass region did not exist at that time. Therefore, to get a weighty argument for the chosen path, an attempt was made in 1977 [25] to find a classical analog of the Pauli exclusion principle in the liquid-drop model. It proved to be the surface tension coefficient, which increases with nuclear excitation; this coefficient directly demonstrates the extent to which Hooke's law is violated in nuclei:

$$\sigma_N = \sigma_1[1 + 2\bar{\gamma}(N-1)].$$

In this case, the frequency of a phonon in the N-phonon state is $\omega_N = \omega[1+2\gamma(N-1)]^{1/2}$ with $\gamma = \bar{\gamma}(1+\omega_C^2/\omega^2)$, where ω_C is the Coulomb frequency. We thus see that, although $\bar{\gamma}$ can be very small, γ is large in soft nuclei, because ω is small. A systematic analysis of the experimental data [25] showed good agreement with this hypothesis; therefore, the affirmative answer to the question about the universal role of the Pauli exclusion principle was beyond doubt.

Now that the concept of a phonon, the brick from which we can attempt to erect the building of spherical, transition, and deformed nuclei, has been developed, we can return to the role of the Pauli exclusion principle in forming the multiphonon states on the microscopic level. This is done in Sections 3.6

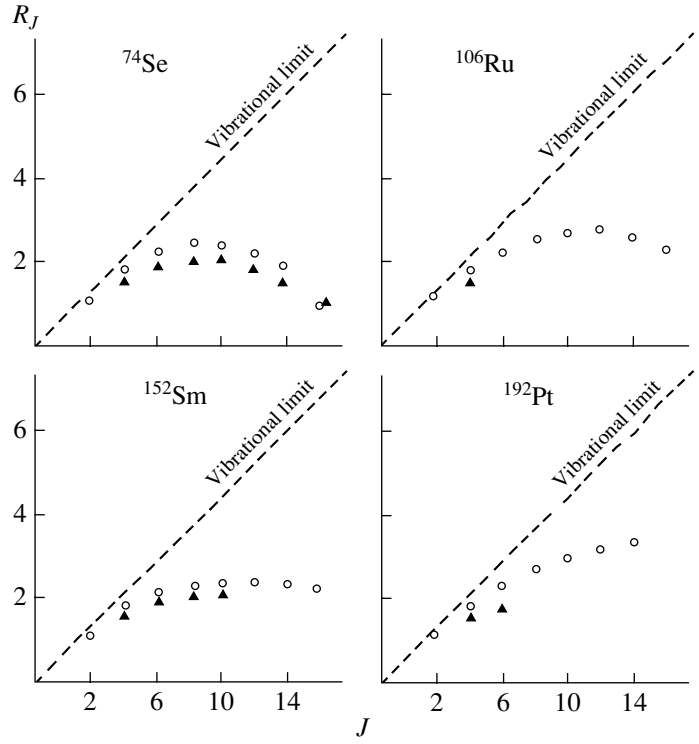

Fig. 13. Ratios $R_J = B(E2; J \to J-2)/B(E2; 2_1^+ \to 0_1^+)$ calculated in the harmonic DCM approximation (circles) and their experimental values (triangles) in the yrast band.

and 3.7, while here we present some of the results to immediately describe the prospects.

Figure 12 shows fragments of the calculated (in the harmonic approximation) and experimental spectra of the yrast bands for several isotopes. As we see from comparison, all of the characteristic features in the spectra of the bands when passing from spherical to deformed nuclei can be reproduced. The experimentally observed behavior of $B(E2)$ over the band is reproduced remarkably closely, irrespective of how strongly the nucleus is deformed, as illustrated by Fig. 13.

However, the main thing demonstrated by these results is that a dynamical variable whose quanta would realize the nuclear spectrum cannot be found in even–even nuclei: the phonons are different in different states.

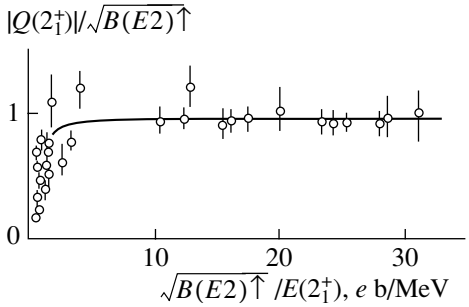

Fig. 14. $|Q(2_1^+)|/\sqrt{B(E2)\uparrow}$ systematics versus $\sqrt{B(E2)\uparrow}/E(2_1^+)$.

2.8. The zeroth (harmonic) approximation H_0 that we constructed reproduces many characteristic features in the spectra of actual nuclei. But will this success be destroyed after applying the anharmonic corrections, i.e., after including the residual interaction that mixes the modes with different numbers of phonons? After all, the sad experience of many preceding approaches points precisely to this.

Indeed, let σ_{N+1} mean the amplitude of the admixture of the $(N+1)$-phonon component to the N-phonon component attributable to $H_{\rm int}$. Then,

$$\sigma_{N+1} = \langle N+1|H_{\rm int}|N\rangle/[E_{N+1} - E_N] \sim N q_N [B(E2; N+1 \to N)]^{1/2}/\omega_{N+1}, \quad (4)$$

where ω_N is the frequency of a phonon in the N-phonon state, and q_N is a quantity proportional to the intrinsic quadrupole moment of one phonon in the N-phonon state. If we choose the random phase approximation for which

$$\omega_N = \text{const} = E(2_1^+), \quad q_N = \text{const},$$
$$B(E2; N+1 \to N) = (N+1)B(E2; 2_1^+ \to 0_1^+)$$

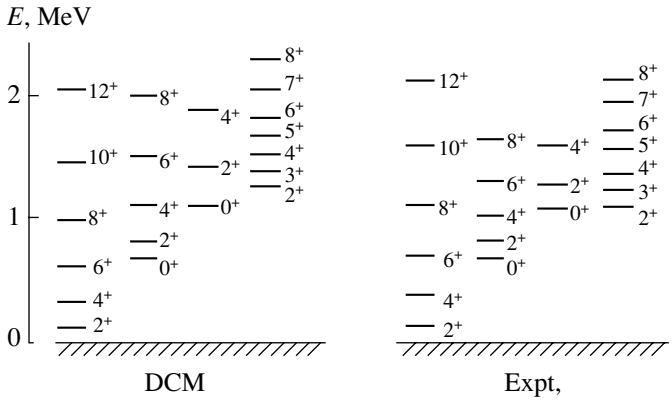

Fig. 15. Calculated (in DCM) and experimental spectra of excited ^{152}Sm states.

as H_0, then we will obtain

$$\sigma_{N+1} \sim \text{const} \cdot N^{3/2}[B(E2; 2_1^+ \to 0_1^+)]^{1/2}/E(2_1^+). \quad (5)$$

It can thus be seen that, in addition to the poor convergence due to the factor $N^{3/2}$, we also come up against the great sensitivity of the problem to the collectivity of the nucleus: when passing from spherical to deformed nuclei, the factor at $N^{3/2}$ increases by a factor of 30 or more. It thus follows, in particular, that the random phase approach has no prospects as the zeroth approximation.

Let us now look at the quadrupole moment of the 2_1^+ state. If we remain within perturbation theory and assume that $Q(2_1^+)$ is attributable to the admixture of a two-phonon component to the single-phonon component σ_2, then

$$Q(2_1^+) = \text{const} \cdot \sigma_2(1 - \sigma_2^2)^{1/2}[B(E2; 2_1^+ \to 0_1^+)]^{1/2}. \quad (6)$$

It thus follows that $y = |Q(2_1^+)|/\sqrt{B(E2)\uparrow}$ must be a nearly linear function of $x = \sqrt{B(E2)\uparrow}/E(2_1^+)$. The systematics of available experimental data presented in Fig. 14 shows that y depends on x, if at all, only at very low values of x and reaches rapidly the rotational limit.

Thus, something suppresses the mixing of the basis wave vectors with increasing collectivity of the nucleus. As follows from (4), only q_N can be such a quantity. One mechanism of q_N suppression with increasing collectivity of the nucleus was found in 1979 [26]; it is associated with the zero nuclear shape oscillations. By increasingly blurring the boundary of the nucleus with its growing collectivity, the zero oscillations or, figuratively speaking, vacuum fluctuations cause the particle–hole interaction in the scattering channels to be suppressed without affecting the interaction channels responsible for the phonon formation. Another mechanism that must clearly take place is associated with the Pauli exclusion principle; but the Pauli exclusion principle plays the most important role in destroying the strong dependence of the expansions in terms of phonon vectors on the number of phonons. As we saw above, allowing for the Pauli exclusion principle in the formation of phonon vectors leads not only to a nearly linear dependence of ω_N on the number of phonons N, but also to a weak dependence of $B(E2; N+1 \to N)$ on N. Moreover, the maximum number of phonons that can be excited in a nucleus turns out to be finite, and this solves the problem of convergence. A detailed discussion of these questions can be found in Sections 3.7 and 3.8, while here we finish the discussion with one typical (in terms of the accuracy of description) result of our complete calculation of the spectrum for the classically deformed ^{152}Sm nucleus (Fig. 15). What determines such spectra, rotation? No, the reason lies in the statistics, the Pauli exclusion principle, and the zero shape oscillations.

Below, we summarize our preliminary results of the discussion of the theoretical status of the previously formulated problem.

In the MSM ideology, the difficulties stem from the fact that we have no a priori criteria that would allow us to estimate whether we actually grasped in main features the part of the state space in which the nuclear dynamics is realized at low excitation energies. Transferring part of the interaction to the definition of new dynamical variables (and thus seemingly circumventing the difficulties) also proves to have no prospects. As we have tried to show, the way in which the quanta proper are redefined so as to fully take into account the mutual effect of the collective and single-particles degrees of freedom on one another turns out to be better. Formally, this is reduced to the problem of defining the phonons and the quasiparticle as the extremals of the complete Hamiltonian rather than a part of it and with allowance made for the

Pauli exclusion principle. To clarify the reasons, let us consider the mathematical essence of the problem.

2.9. Let us return to the original formulation of the problem.

1. We always solve the eigenvalue equation $H_{\text{mod}}|\psi^{(n)}\rangle = E^{(n)}|\psi^{(n)}\rangle$ in two steps. First, we divide H_{mod} into two parts: $H_{\text{mod}} = H_0 + (H_{\text{mod}} - H_0) = H_0 + H_{\text{int}}$, where the zeroth approximation H_0, we will now speak strictly, must satisfy two conditions:

(1) The eigenvectors $\{|\varphi_\nu\rangle\}_1^\infty$ of the linear self-adjoint operator H_0 limited from below form a complete orthonormal system in the space of quadratically summable functions of A-nucleon variables and are antisymmetric relative to the permutations of nucleon coordinates.

(2) The operators H_0 and H_{mod} must be commensurable; i.e., such real constants α, $\beta > 0$ that the following two inequalities are valid on any vector $|\psi\rangle$ from the domain of definition of H_{mod} must exist:

$$||(H_0 - H_{\text{mod}})\psi|| < \alpha\{||H_0\psi|| + ||\psi||\},$$
$$||(H_0 - H_{\text{mod}})\psi|| < \beta\{||H_{\text{mod}}\psi|| + ||\psi||\}.$$

If these conditions are satisfied, then the solution of the eigenvalue problem is sought in the form of an expansion, $|\psi^{(n)}\rangle = \sum_{\nu=1}^\infty r_\nu^{(n)}|\varphi_\nu\rangle$, provided that $\sum_{\nu=1}^\infty r_\nu^{(n)} r_\nu^{(m)} = \delta_{n,m}$. However, for any specific realization, we have to restrict ourselves to a finite number N of expansion terms: $|\psi_N^{(n)}\rangle = \sum_{\nu=1}^N r_\nu^{(n)}(N)|\varphi_\nu\rangle$, provided that $\sum_{\nu=1}^N r_\nu^{(n)}(N) \times r_\nu^{(m)}(N) = \delta_{n,m}$. By the convergence of the approximate solution $|\psi_N^{(n)}\rangle$ to the exact one $|\psi^{(n)}\rangle$, we mean the satisfaction of the Cauchy condition: $\lim\limits_{N\to\infty} ||\psi_N^{(n)} - \psi_{N+k(N)}^{(n)}|| = 0$ at any natural (even N-dependent) k.

We will call the expansion of the kth state in terms of basis vectors a k-ordered expansion if, for $\nu > k$,

$$|r_\nu^{(k)}| \geq |r_{\nu+1}^{(k)}|. \qquad (7)$$

In view of the well-known Neumann theorem [27], condition 1 can be easily satisfied for a wide choice of zeroth approximations. Condition 2 is necessary for $\lim\limits_{N\to\infty} ||\psi_N^{(n)} - \psi_{N+k(N)}^{(n)}|| = 0$, but checking whether it is satisfied is a difficult and not always solvable problem. Therefore, we assume condition 2 to be satisfied.

2. Let us now assume that we have such a Hamiltonian $H_0(\omega)$ dependent on the parameter(s) ω that conditions 1 and 2 are satisfied at any ω. We can then use the representation $H_{\text{mod}} = H_0 + (H_{\text{mod}} - H_0) = H_0 + H_{\text{int}}$ at each ω precisely because the eigenvectors of $H_0(\omega)$ are complete. Next, let $\{E^{(k)}(N,\omega)\}_{k=1,N}$ be the eigenvalue spectrum for H_{mod} obtained in the N-dimensional approximation.

Each eigenvalue of $E^{(k)}(N,\omega)$ depends on both the dimension N of the chosen subspace and the parameter ω. The ω dependence stems from the fact that the chosen subspace is finite-dimensional. The exact solution cannot depend on ω precisely because the system of eigenvectors of $H_0(\omega)$ is complete.

There can be two types of dependence of $E^{(k)}(N,\omega)$ on N. If the first eigenvectors of $H_0(\omega)$ are k-ordered, then, as the dimension increases, we will have a picture similar to curve *1* in Fig. 16; i.e., the kth eigenvalue decreases uniformly. Since H_{mod} is limited from below, $E^{(k)}(N,\omega)$ necessarily has a limit the attainment of which can be easily estimated from the condition $|E^{(k)}(N,\omega) - E^{(k)}(N+k,\omega)| < \varepsilon$, where ε is the prespecified accuracy of the calculation. If, however, the chosen basis is not k-ordered, then the N dependence of $E^{(k)}(N,\omega)$ can be similar to curve *2* in Fig. 16. In this case, the estimate of $|E^{(k)}(N,\omega) - E^{(k)}(N+k,\omega)| < \varepsilon$ gives no guarantees that we "grasped" in main features the part of the state space where the nuclear dynamics develops—we could be on one of the plateaus of curve *2* (Fig. 16). We tried to demonstrate this in previous sections. Finding a basis that is ordered relative to the first three to five vectors with given spin and parity means guessing the physics of the phenomenon. The dynamical collective model is a possible procedure for constructing an ordered basis or, more specifically, finding such a zeroth approximation H_0 from the specified initial model Hamiltonian H_{mod} that the following expansion would hold:

$$H_{\text{mod}} = H_0 + i\lambda[H_0 T - T H_0], \qquad (8)$$

where T is a self-adjoint operator whose domain of definition coincides with the domain of definition of H_{mod}, and λ is a real parameter.

To construct H_0 of interest, note that only the nondiagonal matrix elements of the residual interaction H_{int} in the space $\{|\varphi_n\rangle\}$ of eigenvectors of H_0 are nonzero and $\langle\varphi_n|H_{\text{mod}}|\varphi_n\rangle = \langle\varphi_n|H_0|\varphi_n\rangle \equiv \varepsilon_n$. Consequently, if we wish to solve the problem in the space of quasiparticle and phonon vectors, then their expansion amplitudes should be sought by minimizing the complete Hamiltonian H_{mod} rather than a separate part of it. This is a necessary but not sufficient condition for the existence of expansion (8).

3. Let us assume that N is chosen to be so large that the condition $|E^{(k)}(N,\omega) - E^{(k)}(N+k,\omega)| < \varepsilon$, $k \leq 5$ is satisfied for the first five eigenvalues. Let us now consider the dependences of $E^{(k)}(N,\omega)$ on ω.

They reach a minimum at a certain value of ω. Note that this minimum can be at different ω for different eigenvalues. Having these ω dependences of the eigenvalues before their eyes, nuclear physicists will begin to talk about intruder states and clustering and will undoubtedly be right if the basis is ordered for the solutions under consideration (in this case, the minima are indistinct). At the same time, the presence of well-defined minima is evidence that the space of states is incomplete.

4. The situation where we calculate the dependence of the total energy of a nucleus on the deformation parameter is identical. The presence of well-defined minima is evidence that the space of states is incomplete when the law of conservation of total angular momentum is violated.

I realize that this assertion demolishes the current ideas in nuclear physics and cannot but provoke criticism and a prejudiced attitude toward the foregoing. For most of the researchers who grew in the spirit of conceptual ideas of the 20th century, the question of whether the deformed nuclei are deformed may sound seditious, if not absurd. But who are the judges? Mathematics and experiment. And mathematics has said its word. For the lovers of computer graphics, I propose to carry out a numerical experiment: compute the total energy as a function of the deformation parameter by gradually increasing the number of oscillatory shells involved in the computation. As the number of oscillatory shells (there must be more than eight such shells for oxygen) increases, the dependence of the ground-state energy on the deformation parameter will become increasingly flat, gradually reaching a plateau, while the minimum will become progressively less distinct, being gradually lost in the unstable haze of computational errors.

Moreover, in my study of 1978 [28], I showed for odd nuclei that, in the limit of large oscillation amplitudes, the vibrational and rotational models become unitarily equivalent if the centrifugal and Coriolis (with $K = 1/2$) terms are included in the definition of the deformed average field. Note that this is also required by Eq. (8). In other words, deformed nuclei are a language that is convenient and clear, but severely narrows down the horizons. However, few physicists have paid attention to this work, probably because it is too mathematical.

Finally, if we could exactly solve Schrödinger's multiparticle equation $H_{\rm mod}|\Psi\rangle = E|\Psi\rangle$, then the question of whether the deformed nuclei are deformed even would not arise. We would calculate the level spectrum, the transition probabilities, etc., from the given charge and atomic number (this is done in Section 4) and would make sure that the choice of a two-particle component of the forces is correct. At the same time, we would attribute the small discrepancies

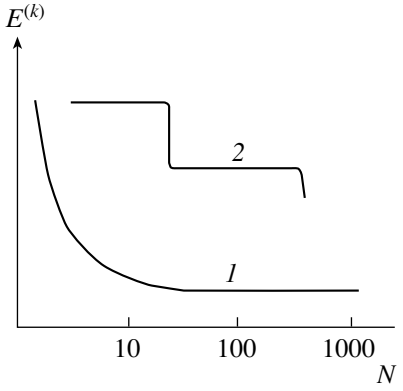

Fig. 16. Schematic dependence of the energy of the kth state on the number (on a logarithmic scale) of included basis vectors for the k-ordered (*1*) and unordered (*2*) bases.

with the experimental data that would remain, for example, to the disregarded three-particle forces, relativistic effects, etc. The density distribution of the material in the ground state of an even–even nucleus and, in general, in any other state with a total angular momentum of 0^+ would necessarily be spherically symmetric. The physics would be different. However, we are unable to directly solve Schrödinger's multiparticle equation. Hence, we must choose a zeroth approximation whose basis vectors would be ordered relative to the first three to five states. We have already seen what is obtained.

3. THE DYNAMICAL COLLECTIVE MODEL

We emphasize that the name we chose reflects not the specifically chosen (paring + multipole–multipole interaction) Hamiltonian, but the method of its analysis described in Section 2.9. In translation into the language of perturbation theory, we obtain a list of diagrams that play a crucial role in forming the spectrum of low-lying states. Once this list has been established, we can also perform calculations with realistic forces.

3.1. The Hamiltonian

The complete Hamiltonian is assumed to be

$$H_{\rm mod} = H_0 + H_G + H_Q, \qquad (9)$$

where H_0 describes the independent motion of the nucleons in an average field $V(r)$, H_G is the pairing Hamiltonian, and H_Q is the multipole–multipole interaction. In the representation of the secondary quantization, they are

$$H_0 = \sum_{jm}(e_j - \nu)a^+_{jm}a_{jm},$$

$$H_G = -\frac{G}{4}\sum_{jm,in}(-1)^{j-m+i-n}a^+_{jm}a^+_{j-m}a_{in}a_{i-n},$$

$$H_Q = -\frac{1}{2}\sum_{\lambda,\mu}\frac{\chi^{(\lambda)}}{2\lambda+1}Q^+_{\lambda\mu}Q_{\lambda\mu},$$

$$Q^+_{\lambda\mu} = \sum_{j_1,j_2} f^{(\lambda)}_{12}[a^+_1 a_2]_{\lambda\mu}, \quad f^{(\lambda)}_{12} = \langle j_1||f^{(\lambda)}Y_\lambda||j_2\rangle,$$

$$[a^+_1 a_2]_{\lambda\mu} = \sum_{m_1 m_2} C^{\lambda\mu}_{j_1 m_1 j_2 m_2} a^+_{j_1 m_1} a_{j_2 m_2}.$$

Here, $a^+_{j_1m_1}(a_{j_1m_1})$ is the nucleon creation (annihilation) operator in a single-particle state with energy e_{j_1}, total angular momentum and its projection j_1m_1, and other quantum numbers; $f^{(\lambda)}(r)$ is a function of the angular momentum $\lambda = 2, 3, \ldots$ and the single-particle radius r; and $C^{\lambda\mu}_{injm}$ are the Clebsch–Gordan coefficients. We will talk about the parametrization of $f^{(\lambda)}(r)$ and the average field and about the choice of constants of the effective forces in the proper place. The symbol ν denotes the proton or neutron chemical potential, and the energy is reckoned from $E_0 = \nu_p N_p + \nu_n N_n$, where N_p and N_n are the numbers of protons and neutrons, respectively. In most cases, we omit the isospin symbol where it is not needed. The remaining notation is standard [4].

3.2. The Theory of Single-Phonon States

Although the method for constructing the single-phonon states of $H_{\rm mod}$ is based on the random-phase approximation, it has a number of significant distinctions, which forces us to give plenty of space for its description.

All begins from the standard passage in (9) from the representation of $a^+(a)$ particles to the representation of $\alpha^+(\alpha)$ quasiparticles through the Bogolyubov canonical transformation [4]. To terms proportional to the pairs of operators $\alpha\alpha$ and $\alpha^+\alpha^+$ with zero total angular momentum, the expression for $H_0 + H_G$ then takes the form

$$\tilde{H}_0 = H_0 + H_G = \sum_1 (2j_1+1)(e_{j_1}-\nu)$$
$$\times [v^2_{j_1} + (u^2_{j_1} - v^2_{j_1})\widehat{\eta}_{j_1}] - (1/G)[(G/2)$$
$$\times \sum_1 (2j_1+1)u_{j_1}v_{j_1}(1-2\widehat{\eta}_{j_1})]^2$$
$$-(G/2)\sum_1 (2j_1+1)v^4_{j_1}(1-2\widehat{\eta}_{j_1}).$$

Here, $\widehat{\eta}_j = (2j+1)^{-1}\sum_m \alpha^+_{jm}\alpha_{jm}$, and u_j and v_j are the Bogolyubov transformation coefficients. Accordingly, H_Q takes the form

$$H_Q = H_{22} + H_{04} + H_{\rm sc} + H_{13},$$

$$H_{22} = -\frac{1}{4}\sum_{\lambda\mu}\frac{\chi^{(\lambda)}}{2\lambda+1}\sum_{1234} q^{(\lambda)}_{12}q^{(\lambda)}_{34}A^+_{12}(\lambda\mu)A_{34}(\lambda\mu),$$

$$H_{04} = -\frac{1}{8}\sum_{\lambda\mu}\frac{\chi^{(\lambda)}}{2\lambda+1}\sum_{1234} q^{(\lambda)}_{12}q^{(\lambda)}_{34}$$
$$\times [(-1)^{\lambda-\mu}A^+_{12}(\lambda\mu)A^+_{34}(\lambda-\mu) + \text{h.c.}],$$

$$H_{\rm sc} = -\frac{1}{2}\sum_{\lambda\mu}\frac{\chi^{(\lambda)}}{2\lambda+1}\sum_{1234} p^{(\lambda)}_{12}p^{(\lambda)}_{34}N^+_{12}(\lambda\mu)N_{34}(\lambda\mu),$$

$$H_{13} = -\frac{1}{2}\sum_{\lambda\mu}\frac{\chi^{(\lambda)}}{2\lambda+1}\sum_{1234} p^{(\lambda)}_{12}q^{(\lambda)}_{34}$$
$$\times N_{12}(\lambda-\mu)[A^+_{34}(\lambda\mu) + (-1)^{\lambda-\mu}A_{34}(\lambda-\mu)].$$

In these expressions,

$$q^{(\lambda)}_{12} = f^{(\lambda)}_{12}(u_1v_2 + v_1u_2),$$
$$p^{(\lambda)}_{12} = f^{(\lambda)}_{12}(u_1u_2 - v_1v_2),$$

$$A^+_{12}(\lambda\mu) = \sum_{m_1m_2} C^{\lambda\mu}_{j_1m_1j_2m_2}\alpha^+_{j_1m_1}\alpha^+_{j_2m_2},$$

$$N_{12}(\lambda\mu) = \sum_{m_1m_2}(-1)^{j_2+m_2}C^{\lambda\mu}_{j_1m_1j_2m_2}\alpha^+_{j_1m_1}\alpha_{j_2-m_2}.$$

At the first stage, we solve the problem in the harmonic approximation, i.e., disregard the role of H_{13}—it has no nonzero diagonal matrix elements. However, even with such a simplified Hamiltonian as

$$\tilde{H}_{\rm mod} = \tilde{H}_0 + H_{22} + H_{04} + H_{\rm sc},$$

the problem cannot be solved exactly. The random phase approximation appears at this stage. It lies in the fact that, instead of the exact commutation relations for $A_{12}(\lambda\mu)$ and $A^+_{34}(\lambda\mu)$ of the form

$$[A_{12}(\lambda\mu), A^+_{34}(\lambda\mu)] = \delta_{(12)(34)} - \sum_{\lambda_2\mu_2} W^{\lambda_2\lambda}_{1234}N_{13}(\lambda_2\mu_2), \qquad (10)$$

where W is a geometric factor, whose exact form is not yet important to us, and

$$\delta_{(12)(34)} = \delta_{13}\delta_{24} - (-1)^{j_1+j_3+\lambda}\delta_{14}\delta_{23},$$

one uses an approximation in which the terms proportional to W are discarded. Hara [11] suggested substituting the right-hand side of Eq. (10) with its

vacuum mean value and, thus, working again with the boson commutation relations, but now in the form

$$[A_{12}(\lambda\mu), A^+_{34}(\lambda\mu)] = \delta_{(12)(34)}(1-\eta_1-\eta_2),$$

where

$$\eta_1 = \langle 0|\widehat{\eta}_1|0\rangle = (2j_1+1)^{-1}\sum_{m_1}\langle 0|\alpha^+_{j_1m_1}\alpha_{j_1m_1}|0\rangle.$$

Subsequently, the problem is solved as follows: Let $\Omega^{+(i)}_{\lambda\mu}$ denote the production operator of the ith phonon with angular momentum λ and its projection μ. The ground state $|0\rangle$ is defined as a vacuum of phonons: $\Omega^{(i)}_{\lambda\mu}|0\rangle = 0$. The solution for $\Omega^{+(i)}_{\lambda\mu}$ is sought in the form of an expansion,

$$\Omega^{+(i)}_{\lambda\mu} = \frac{1}{2}\sum_{12}\{r^{(i\lambda)}_{12}A^+_{12}(\lambda\mu) - (-1)^{\lambda-\mu}s^{(i\lambda)}_{12}A_{12}(\lambda-\mu)\}, \quad (11)$$

where r and s are the sought expansion amplitudes. Requiring that the phonon operators satisfy the boson commutation relations

$$\langle 0|[\Omega^{(i)}_{\lambda\mu}, \Omega^{+(k)}_{\sigma\nu}]_{(-)}|0\rangle = \delta_{ik}\delta_{\lambda\sigma}\delta_{\mu\nu},$$

where $[K,L]_{(-)} = KL - LK$, we find that the expansion that is the inverse of (10) is

$$A^+_{12}(\lambda\mu) = (1-\eta_1-\eta_2)\sum_i\{r^{(i\lambda)}_{12}\Omega^{+(i)}_{\lambda\mu} + (-1)^{\lambda-\mu}s^{(i\lambda)}_{12}\Omega^{(i)}_{\lambda-\mu}\},$$

provided that the norm of the vectors is equal to unity:

$$\langle 0|\Omega^{(i)}_{\lambda\mu}\Omega^{+(i)}_{\lambda\mu}|0\rangle = \frac{1}{2}\sum_{12}\{[r^{(i\lambda)}_{12}]^2 - [s^{(i\lambda)}_{12}]^2\}\times(1-\eta_1-\eta_2) = 1.$$

It remains to determine the expansion amplitudes $\{r\}$ and $\{s\}$ by solving the equation

$$\delta\{\langle 0|\Omega^{(i)}_{\lambda\mu}[\tilde{H}_{\rm mod}, \Omega^{+(i)}_{\lambda\mu}]_{(-)}|0\rangle - \omega^{(i)}_\lambda[\langle 0|\Omega^{+(i)}_{\lambda\mu}\Omega^{(i)}_{\lambda\mu}|0\rangle - 1]\} = 0.$$

Before doing this, let us make several technical remarks. The expression for $\tilde{H}_0$ contains a term with the square of the operator

$$\widehat{\Delta} = \frac{G}{2}\sum_1(2j_1+1)u_1v_1(1-2\widehat{\eta}_1).$$

When calculating the commutator $[\tilde{H}_{\rm mod}, \Omega^{+(i)}_{\lambda\mu}]_{(-)}$ of this term, we then obtain

$$-\frac{1}{G}[\widehat{\Delta}^2, \Omega^{+(i)}_{\lambda\mu}]_{(-)} = -\frac{1}{G}[\widehat{\Delta}, [\widehat{\Delta}, \Omega^{+(i)}_{\lambda\mu}]]_{(-)} - \frac{2}{G}[\widehat{\Delta}, \Omega^{+(i)}_{\lambda\mu}]_{(-)}\widehat{\Delta}.$$

However,

$$-\frac{1}{G}[\widehat{\Delta}, [\widehat{\Delta}, \Omega^{+(i)}_{\lambda\mu}]]_{(-)} \quad (12)$$
$$= -\frac{G}{4}\sum_{12}(1-\eta_1-\eta_2)(u_1v_1+v_2u_2)^2\times\{[r^{(i\lambda)}_{12}]^2 - [s^{(i\lambda)}_{12}]^2\},$$

and since $u_jv_j \le 0.5$, it follows from the normalization condition that the contribution of (12) at any admissible u, v, r, and s does not exceed $G/2$ (for intermediate mass and heavy nuclei, it is negligible). $H_{\rm sc}$, which requires calculating commutators of the form $[N_{12}, A_{34}]_{(-)}$ constitutes the greatest inconvenience. However, this can be avoided by reducing $H_{\rm sc}$ to a normal form relative to the vacuum of phonons:

$$H_{\rm sc} = \frac{1}{2}\sum_{\Lambda\lambda\mu}\frac{\chi^{(\lambda)}}{2\lambda+1}\sum_{1234}p^{(\lambda)}_{12}p^{(\lambda)}_{34}(-1)^{j_3-j_4+\lambda}\times(2\Lambda+1)\begin{Bmatrix} j_1 & j_4 & \lambda \\ j_3 & j_2 & \Lambda\end{Bmatrix}A^+_{13}(\Lambda\mu)A_{42}(\Lambda\mu).$$

We can now perform all calculations by using the expansion of $A^+_{13}(\Lambda\mu)$, $A_{42}(\Lambda\mu)$ in terms of the phonon operators. As a result, we obtain the following equation for the r and s amplitudes:

$$[\varepsilon_1+\varepsilon_2-\omega^{(i)}_\lambda]r^{(i\lambda)}_{12} = \frac{\chi^{(\lambda)}}{2(2\lambda+1)}q^{(\lambda)}_{12}\times\sum_{34}q^{(\lambda)}_{34}(1-\eta_3-\eta_4)(r^{(i\lambda)}_{34}+s^{(i\lambda)}_{34}) - \chi^{(\lambda)}\sum_{34}p^{(\lambda)}_{14}p^{(\lambda)}_{32}(1-\eta_3-\eta_4)r^{(i\lambda)}_{34}\begin{Bmatrix} j_1 & j_4 & \lambda \\ j_3 & j_2 & \lambda\end{Bmatrix},$$

$$[\varepsilon_1+\varepsilon_2+\omega^{(i)}_\lambda]s^{(i\lambda)}_{12} = \frac{\chi^{(\lambda)}}{2(2\lambda+1)}q^{(\lambda)}_{12}\times\sum_{34}q^{(\lambda)}_{34}(1-\eta_3-\eta_4)(r^{(i\lambda)}_{34}+s^{(i\lambda)}_{34}) - \chi^{(\lambda)}\sum_{34}p^{(\lambda)}_{14}p^{(\lambda)}_{32}(1-\eta_3-\eta_4)s^{(i\lambda)}_{34}\begin{Bmatrix} j_1 & j_4 & \lambda \\ j_3 & j_2 & \lambda\end{Bmatrix},$$

where $\varepsilon_j = (e_j-\nu)(u_j^2-v_j^2) + 2u_jv_j\langle 0|\widehat{\Delta}|0\rangle + Gv_j^4$ is the quasiparticle energy. These equations formally differ from the standard equations [4] in that they include $H_{\rm sc}$, the exchange (with respect to H_{22}) interaction, and the blocking effect, the factors $(1-\eta_1-\eta_2)$, in both the pairing and multipole interaction

channels. As our calculations show, the contribution of H_{sc} to all of the calculated characteristics is 10%.

It remains to derive equations for the u and v coefficients and the η numbers. In general, the Bogolyubov transformation coefficients are sought by minimizing $\langle 0|\tilde{H}_0|0\rangle$. In this case, however, as we noted above, the important contribution from the multipole attractive forces is lost: it may turn out to be advantageous for the system to have a blurred Fermi surface, since in this case the contribution of the multipole attractive forces to the ground-state energy increases greatly. In other words, the total energy $\langle 0|\Omega^{(i)}\tilde{H}_{\rm mod}\Omega^{+(i)}|0\rangle$ in each of the phonon states must be minimized in u, v. Using the Heisenberg equation, the orthonormality of the phonon vectors, and the fact that $\omega_\lambda^{(i)}$ does not depend explicitly on u, v, we find that the problem is reduced to minimizing $\tilde{H}_{\rm mod}$ in the ground state, provided that $u_j^2 + v_j^2 = 1$ for any j, i.e.,

$$\delta\{\langle 0|\tilde{H}_{\rm mod}|0\rangle - \mu_j(u_j^2 + v_j^2 - 1)\} = 0.$$

The Lagrange factor μ_j in this equation can be easily eliminated by applying a linear operator of the form $\mathrm{curl}_j = 1/2(u_j\partial/\partial v_j - v_j\partial/\partial u_j)$ to the expression in the braces. Thus, the u and v coefficients must satisfy an equation of the following form for each j:

$$\mathrm{curl}_j\langle 0|\tilde{H}_{\rm mod}|0\rangle = 0.$$

Calculating curl_j of $\langle 0|\tilde{H}_0|0\rangle$ involves no difficulty. The situation with the contribution from $\langle 0|H_{22} + H_{04}|0\rangle$ proportional to $\left[\sum_{12}(1-\eta_1-\eta_2)q_{12}^{(\lambda)}s_{12}^{(i\lambda)}\right]^2$ is different. Using the equation for the s amplitudes, we obtain

$$\mathrm{curl}_3(q_{12}^{(\lambda)}s_{12}^{(i\lambda)}) = 2s_{12}^{(i\lambda)}\mathrm{curl}_3(q_{12}^{(\lambda)}) + \frac{\chi^{(\lambda)}}{2(2\lambda+1)}q_{12}^{(\lambda)}q_{12}^{(\lambda)}\mathrm{curl}_3\left[\frac{\sum\cdots}{\varepsilon_1+\varepsilon_2+\omega}\right]. \quad (13)$$

A numerical analysis in the constant pairing approximation by varying the constant of pairing forces shows that the contribution from the second term in (13) to the distributions of the u and v amplitudes is several percent of the first term, while the contribution from H_{sc} is negligible. As a result, we find that the distributions of the u and v numbers, with a good accuracy, satisfy the system of equations

$$(2j+1)(1-2\eta_j)[(e_j-\nu)u_jv_j - 1/2(u_j^2-v_j^2)\langle 0|\widehat{\Delta}|0\rangle] = 1/2\sum_i(u_jv_i - v_ju_i)(1-\eta_j-\eta_i)\Delta_{ji}, \quad (14)$$

where

$$\Delta_{ji} = 2\sum_{n\lambda}\frac{\chi^{(\lambda)}}{2(2\lambda+1)}f_{ji}^{(\lambda)}s_{ji}^{(n\lambda)} \times \sum_{kl}q_{kl}^{(\lambda)}(1-\eta_k-\eta_l)s_{kl}^{(n\lambda)},$$

and the position of the chemical potential is determined by the condition for the conservation of the number of particles on average:

$$N = \sum_j(2j+1)\{v_j^2 + (u_j^2 - v_j^2)\eta_j\}.$$

The left-hand side of Eq. (14) (if it were equal to zero) is the standard equation for superfluidity with the pairing gap $\Delta(G) = \langle 0|\widehat{\Delta}|0\rangle$ renormalized due to the presence of quasiparticles in each single-particle $(2j+1)\eta_j$ state. The right-hand side of Eq. (14) is the additional pairing field that arises from the exchange of phonons of different multipolarity between the nucleons. The role of this field is extremely important, since Eq. (14) can have a solution corresponding to a blurred Fermi surface even for $G \to 0$.

This is illustrated by Fig. 17*a*, which schematically shows the dependence of uv on the constant of pairing forces at $\chi = 0$ and at χ exceeding a critical value of χ^*, which is determined by the specific Fermi surface. In the past [14], this served as the basis for calling the phenomenon under discussion "anomalous superfluidity." To demonstrate the effect of the Δ_{ji} terms on the blurring of the Fermi surface additional to $\Delta(G)$, Fig. 17*b* shows the change in the numbers of nucleons Δn_j in single-particle states of the ^{152}Sm nucleus caused by the inclusion of the Δ_{ji} terms. As a result, we come up against a situation that is paradoxical at first glance. On the one hand, as the collectivity of the nucleus grows, as we will see below, the η numbers increase, and, as a result of the corresponding decrease in $\Delta(G)$, the quasiparticle energies decrease. On the other hand, the blurring of the Fermi surface does not decrease, but progressively increases due to the increasing role of the Δ_{ji} terms. The decrease in the quasiparticle energies with growing collectivity of the nucleus directly follows from the decrease in the even–odd mass difference in strongly collective nuclei and can be observed by a sharp increase in the density of states in nuclei at low excitation energies. This is demonstrated by Fig. 17*c*, which shows the experimental level density in $^{144-152}$Sm as a function of the excitation energy. In plotting this dependence, we discarded the states belonging to the yrast band and followed only the energy starting from which the density increased sharply (after all, we do not yet know the nature of most states). The position of the first noncollective solution

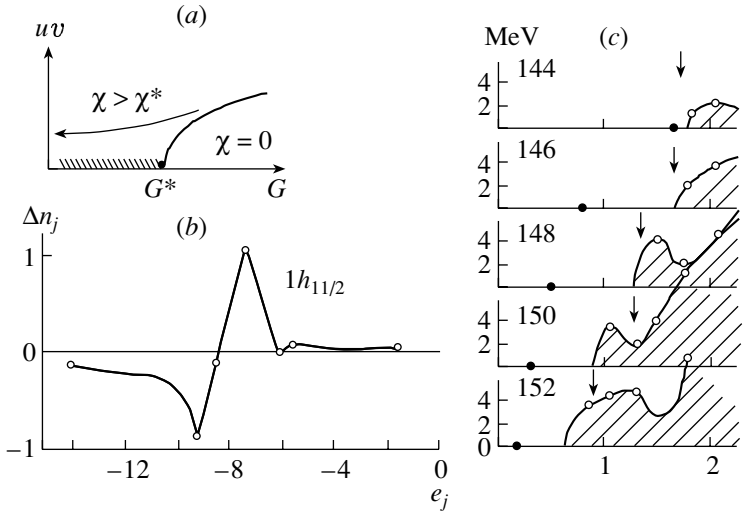

Fig. 17. (a) Schematic dependence of uv on the constant of pairing forces at zero constant of multipole forces, $\chi = 0$, and at a constant exceeding a critical value $\chi > \chi^*$. (*b*) The change in the occupation numbers of single-particle ^{152}Sm states by nucleons caused by the inclusion of the multipole forces. (*c*) The experimental level density of the excited states of samarium isotopes as a function of the excitation energy. The arrows indicate the positions of the first calculated noncollective state; the closed circles indicate the position of the collective state.

we calculated is indicated by the arrow in each of these figures. The observed correlation is so clear that the affirmative answer to the question of the decrease in the quasiparticle energy with growing collectivity of the nucleus is beyond doubt.

We see that both the decrease in the quasiparticle energies with growing collectivity of the nucleus and the increasing blurring of the Fermi surface are the two most important dynamical effects whose neglect is responsible for the failures of the previous attempts to describe even–even nuclei.

Let us now proceed to calculate the η numbers. An exact expression cannot be derived for them; we always have to restrict ourselves to an approximation. The zeroth approximation

$$\eta_j = \sum_{ni\lambda} (2\lambda+1)/(2j+1)[s_{ij}^{(n\lambda)}]^2,$$

on which the authors of [4] relied for $\omega \to 0$, has asymptotic behavior of the form $\eta|_{\omega\to 0} \sim 1/[\omega/c]$, where c is a constant. However, by definition, the η numbers cannot exceed $1/2$. The linear approximation [12, 14, 26]

$$\eta_j = \sum_{ni\lambda} (2\lambda+1)/(2j+1)[s_{ij}^{(n\lambda)}]^2(1-\eta_i-\eta_j)$$

with the asymptotic behavior $\eta|_{\omega\to 0} \sim 1/2[1 - \omega/(2c)]$ also has a low accuracy in strongly collective nuclei ($\sim$80%), which can easily be estimated by calculating, for example, the total angular momentum of the single-particle state. To find a more adequate approximation, let us consider the set of "quasiparticle + N phonons" vectors

$$|JM\rangle = [D_j]^{-1/2}\alpha_j^+ \otimes \{\Omega_\lambda^{+(i)}\}^N|0\rangle$$

with the normalization $D_j = (1-\eta_j)$. As a result, we obtain

$$\eta_j = (2j+1)^{-1}\sum_m \langle 0|\alpha_{jm}^+\alpha_{jm}|0\rangle$$
$$= (2j+1)^{-1}\sum_{m,J_i,M} \langle 0|\alpha_{jm}^+|J_iM\rangle\langle J_iM|\alpha_{jm}|0\rangle$$
$$= \sum_{n,i,\lambda}(2\lambda+1)/(2j+1)[s_{ij}^{(n\lambda)}]^2$$
$$\times (1-\eta_i-\eta_j)^2/(1-\eta_i)$$

with the asymptotic behavior $\eta|_{\omega\to 0} \sim 1/2\{1 - [\omega/c]^{1/2}/2\}$. As our numerical calculations show, when summing over n and λ both in Eq. (14) and in others, we may restrict ourselves to the first three or four solutions with the angular momenta $\lambda = 2, 3$; the contribution from the remaining solutions to the distributions of the u, v, and η numbers and the contribution from the states of higher multipolarity are negligible at the computational accuracy (0.1%) in spherical, transition, and deformed nuclei. The fact that the calculated values of the total angular momentum for any of the phonon states do not differ from the exact value by more than 0.2% is particularly attractive.

In the described scheme of our calculations, the nonunitarity of the Bogolyubov canonical transfor-

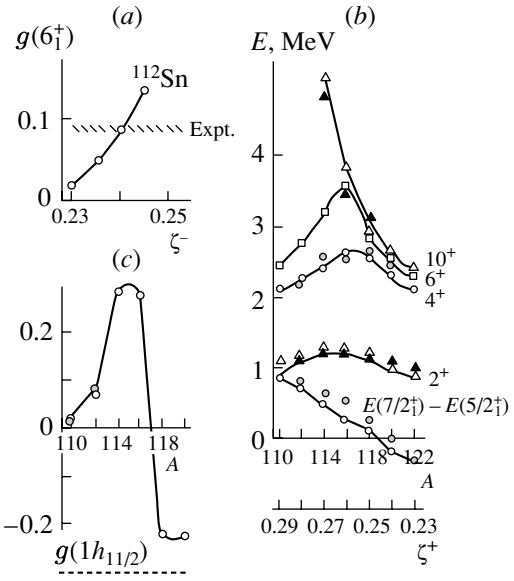

Fig. 18. (a) Calculated values of $g(6_1^+)$ for ^{112}Sn versus neutron constant ζ^- of spin–orbit forces in comparison with the experimental data. (b) Calculated (open symbols) and experimental (closed symbols) energies of the 2_1^+, 4_1^+, 6_1^+, and 10_1^+ states in the tin isotopes and energy difference of the $7/2_1^+$ and $5/2_1^+$ states in the corresponding Sb isotopes versus mass number. The scale of variations in the proton constant of spin–orbit forces corresponding to these mass numbers is shown below. (c) Calculated (open symbols) and experimental (closed symbols) values of $g(6_1^+)$ versus mass number.

mation, as a result of which the total number of nucleons is not an exact quantum number, introduces the largest uncertainty; their number is conserved only on average. To apply a correction for this, we used the standard projection method [4] and obtained the following renormalization for the constant of pair forces:

$$G \to G\left\{1 + \left[\sum_j (2j+1)[\eta_j (u_j^2 - v_j^2)^2 + (1+2\eta_j)2u_j^2 v_j^2]\right]^{-1}\right\}.$$

A curious feature has been found: if, as is customary, the renormalization is made in the $\eta = 0$ approximation, then its value changes greatly from nucleus to nucleus. In contrast, the renormalization is almost constant, slightly more than 12%, in the approximation for the u, v, and η numbers under consideration.

We calculated the probabilities of electromagnetic transitions and the magnetic moments of the states in a standard way. As regards the charge radius of the nucleus in the ground state (a vacuum of phonons), the expression

$$Z\langle R^2\rangle = \sum_j (2j+1)\langle j|r^2|j\rangle[v_j^2 + (u_j^2 - v_j^2)\eta_j]$$

does not include the anharmonic corrections attributable to H_{13}, which we have not yet calculated. To obtain an upper limit for the role of H_{13}, we renormalized the single-particle operator $\widehat{r}^2$ to $1 + [5/(4\pi)]\beta^2$, where the root-mean-square deformation can be expressed in terms of the normalization factor Y_2 of the phonon amplitudes r and s as follows: $\beta^2 = 25/[2E(2_1^+)Y_2]$.

3.3. Parametrization

Describing the parametrization, we will naturally also present a number of results that underlie it.

The average field. The parameters of the average field $V(r)$ taken in the form of the Woods–Saxon potential differ little from the standard parameters [4]. The depth is defined as

$$V_0^\pm = 52[1 \pm 0.647(N-Z)/A] \text{ MeV},$$

where (+) and (−) refer to the protons and neutrons, respectively. We chose the half-decay radius $r_0 = 1.28$ fm and the diffusivity $a = 0.69$ fm (of course, not uniquely) from the description of the absolute values of the charge radii for the ^{116}Sn and ^{144}Sm nuclei. The most uncertain characteristics of the average field are the constants of spin–orbit forces $\zeta^\pm$:

$$V_{ls}^\pm = \zeta^\pm[1 + 2(N-Z)/A]V_0^\pm/2.$$

In a sense, they have been reliably determined only for the magic nuclei. Are they constant in the entire mass region or do they change significantly? The boson model of spin–orbit forces gives no answer to this question. There is only evidence that, to within the isotopic factor, the sum of the proton and neutron constants is constant throughout the mass region, i.e.,

$$1/2(V_0^+\zeta^+ + V_0^-\zeta^-) \approx \text{const}. \qquad (15)$$

On the other hand, there are direct experimental data showing that ζ^+ changes significantly even within the same isotopic chain. The case in point is the $7/2_1^+$ and $5/2_1^+$ states of the Sb isotopes, which are identified as single-particle ones and which change significantly their relative positions as the atomic number increases. Thus, we have every reason to consider the constants $\zeta^\pm$ as free parameters chosen from the condition for the best description of the spectroscopic information. We began with this, but soon made sure that (15) with const ~ 14 MeV is valid even based on a cursory analysis of the properties of the Sn and Hg isotopes.

This was an unexpected result of our work: our Hamiltonian is approximate, and we solve the problem approximately; as a result, we arrive at pure relativity! Below, we will return to the discussion of this problem, and now we only emphasize that, in view of (15), one free parameter remains in the model.

The pairing interaction. From the wide range of various parametrizations of the pairing interaction that we analyzed, the following parametrization proved to be the most satisfactory:

$$G = (19.5/A)[1 \pm 0.51(N-Z)/A].$$

The multipole interaction. We chose the parametrization of the multipole forces by following the reasonable ideology of the liquid-drop model, in which the function $f^{(\lambda)}(r) = r\partial V(r)/\partial r$ does not depend on the multipolarity. The constants of forces then do not depend on the multipolarity either:

$$1/\chi_{\pm} = \int_0^{\infty} r\frac{dV^{\pm}}{dr}\frac{d\rho^{\pm}}{dr}dr.$$

Here, $\rho^{\pm}$ is the single-particle proton (+) or neutron (−) density calculated at $\eta = 0$. As regards the pn interaction, $\chi_{np} = \chi_{pn} = \sqrt{\chi_+\chi_-}$. Including the Coulomb interaction proved to be important for properly describing the experimental data as a whole. For potentials with a fairly sharp edge, $\chi \approx \text{const}/A^{4/3}$.

Choosing a basis of single-particle states. Four oscillatory shells both for protons and for neutrons were involved in our calculations. When varying the constants of spin–orbit forces in the chain of isotopes, we made sure that the same single-particle states were involved in the calculations. The dimension of the basis was determined from the description of the $E2$ transitions in the Sn isotopes.

3.4. Results of the Calculations in the Single-Phonon Approximation

First of all, recall that any of the results presented here were obtained by choosing the proton (or neutron) constant of spin–orbit forces, since sum (15) proved to be constant throughout the mass region and equal to 13.9 MeV. This sum was fixed by analyzing the properties of the Sb and Sn isotopes. More specifically, having determined ζ^+ from the description of the relative positions of the $7/2_1^+$ and $5/2_1^+$ states in the ^{113}Sb isotope, we find the constant ζ^- from the description of the g factor for the 6_1^+ state of ^{112}Sn. This is demonstrated by Fig. 18a, where $g(6_1^+)$ is plotted against ζ^-. Such a sharp dependence of the g factor on ζ^- is attributable to different degrees of mixing of the two-quasiparticle configurations $[1g_{7/2}, 2d_{5/2}]_{6^+}$ and $[1g_{7/2}]^2_{6^+}$ with significantly different magnetic moments.

Once sum (15) has been fixed, one parameter, for example, ζ^+, which can be determined from the description of all the available spectroscopic information on the nucleus in question, remains in the model.

Can the characteristic changes in the excitation spectra of the nuclei in the chain of isotopes be reproduced by choosing one parameter? Figure 18*b* for the 2_1^+, 4_1^+, 6_1^+, and 10_1^+ states of the tin isotopes answers this question. How the relative positions of the $7/2_1^+$ and $5/2_1^+$ states in the corresponding Sb nuclei are described in this case is shown in the lower part of Fig. 18*b* together with its scale of the ζ^+ variations. The behavior of $g(6_1^+)$ as a function of the mass number proved to be curious (Fig. 18*c*). We see that, in agreement with the experimental data, $g(6_1^+)$ increases rapidly as we pass from ^{110}Sn to ^{112}Sn, reaching its maximum in ^{114}Sn. However, it has the opposite sign even in ^{118}Sn $g(6_1^+)$, which is attributable to the leading role of the $[1h_{11/2}]^2_{6^+}$ configuration in forming the 6_1^+ state. However, as yet, there are no experimental data for $g(6_1^+)$ in the ^{114}Sn and ^{118}Sn isotopes.

A series of other known data is given in Tables 3 and 4 together with the results of our calculations.

Whereas Fig. 18 characterizes the general trend, Fig. 5, which was discussed above, shows the degree of detail to which the excitation spectra of the best studied isotopes can be described in the single-phonon approximation.

We also performed similar calculations for many other chains of isotopes from the region of $A \sim 100$,

Table 3. Values of $g(J_i^{\pi})$ calculated in the single-phonon approximation for some of the states of the ^{A}Sn isotopes in comparison with its experimental values

A	J_i^{π}	Calc.	Expt.
110	6_1^+	+0.028	+0.012(5)
112	6_1^+	+0.091	+0.089(6)
114	7_1^-	−0.047	−0.081
116	5_1^-	−0.049	−0.045
	10_1^+	−0.263	−0.231(2)
118	5_1^-	−0.080	−0.065(5)
	7_1^-	−0.065	−0.098
120	5_1^-	−0.081	−0.061(5)

Table 4. Results of our calculations in the single-phonon approximation

A	$E(2_1^+)$, MeV		$B(E2)\uparrow$, e^2 b^2		$g(2_1^+)$		$\Delta\langle r^2\rangle_{A,A'}$, fm^2	
	calc.	expt.	calc.	expt.	calc.	expt.	calc.	expt.
				Sn				
110	1.024	1.212	0.24		0.13		−0.278	−0.417
112	1.207	1.257	0.21	0.24(2)	0.14		−0.164	−0.269
114	1.373	1.300	0.18	0.23(5)	0.15		−0.040	−0.136
116	1.422	1.294	0.16	0.21(1)	0.12		0	
118	1.350	1.230	0.17	0.21(1)	0.09		+0.064	+0.128
120	1.038	1.171	0.22	0.20(1)	0.03		+0.199	+0.241
122	0.983	1.141	0.21	0.19(1)	0.00		+0.254	+0.342
				Ba				
130	0.450	0.386	0.88	0.60(20)	0.37	0.35(3)	−0.074	−0.086
132	0.523	0.465	0.80	0.86(6)	0.38	0.34(3)	−0.049	−0.068
134	0.679	0.605	0.79	0.68(20)	0.53	0.43(5)	−0.017	−0.053
136	0.883	0.819	0.66	0.40(1)	0.57	0.34(5)	0.014	−0.041
138	1.556	1.436	0.40	0.23(1)	0.80		0	0
140	0.817	0.602	0.81		0.34		+0.315	+0.281
				Hg				
186	0.367	0.405	0.95	1.37(23)	0.63		−0.522	−0.464
190	0.366	0.416	1.13	–	0.49		−0.314	−0.319
196	0.347	0.426	0.99	1.15(5)	0.49		−0.067	−0.081
198	0.394	0.412	0.86	0.99(1)	0.57	0.56(9)	0	0

150, and 200 (see Fig. 6 and Table 4). As we see, the single-phonon approximation satisfactorily reproduces the properties of the basic characteristics of the nuclei in long isotopic chains.

There arises the question of whether we have the right to draw any conclusions from the comparison of the results of our calculations in the harmonic approximation with the experimental data. For the tin isotopes, this comparison is quite legitimate, since the smallness of the quadrupole moment of the 2_1^+ states is indicative of a minor role of H_{13}. However, this cannot be said, for example, about the samarium isotopes. Why do we speak about a satisfactory description in this case as well? The point is that our numerous studies of odd nuclei have shown that H_{13} affects rather weakly the description of the relative positions of the yrast states, the probabilities of transitions between them, etc. Therefore, our calculated characteristics in the harmonic approximation also closely correspond to the calculated values of the same characteristics after including H_{13}.

Although the results obtained appear to be successful, we found a number of systematic discrepancies with the experimental data. These primarily include (i) an overestimated $B(E2; 2_1^+ \to 0_1^+)$ compared to its experimental values in nuclei with a magic number of neutrons, and (ii) an underestimated high-spin multiplet splitting compared to its experimental value.

Collectively, these discrepancies stem from the fact that the range of the multipole–multipole interaction is too small; as a result, the diagonal and off-diagonal pair matrix elements are comparable in magnitude. If the magnitude of the forces is chosen from the description of the high-spin multiplet splitting, then we will always obtain overestimated values of $B(E2)$ due to the overly strong mixing of the configurations. In this respect, the multipole–multipole approximation to the effective forces in nuclei may be considered to be "doomed." However, the experience in recognizing the "main diagrams" gained in this

way is a necessary prerequisite for further progress in a future study with realistic nuclear forces. Therefore, below, we also rely on the multipole–multipole approximation when constructing the multiphonon states and when applying the anharmonic corrections.

3.5. The Theory of Multiphonon States

Let, as above, $\Omega^{+(i)}_{\lambda\mu}$ denote the production operator of the ith phonon with angular momentum λ and its projection μ. Consider a two-phonon wave function (to save space, we omit the letter i) with angular momentum R and projection M:

$$|[\lambda]^2_R\rangle = [K_{2\lambda R}]^{-1/2}\sum_{\mu\nu} C^{RM}_{\lambda\mu\lambda\nu}\Omega^+_{\lambda\mu}\Omega^+_{\lambda\nu}|0\rangle,$$

where $K_{2\lambda R}$ is the normalization factor determined from the condition $\langle[\lambda]^2_R||[\lambda]^2_R\rangle = 1$:

$$K_{2\lambda R} = 2 + P^R_{\lambda\lambda},$$

$$P^R_{\lambda_1\lambda_2} = -(2\lambda_1+1)(2\lambda_2+1)\sum_{1234}\begin{Bmatrix} j_1 & j_2 & \lambda_1\\ j_3 & j_4 & \lambda_2\\ \lambda_1 & \lambda_2 & R\end{Bmatrix}$$
$$\times\left[r^{(\lambda_1)}_{12}r^{(\lambda_2)}_{34}r^{(\lambda_1)}_{13}r^{(\lambda_2)}_{24} - s^{(\lambda_1)}_{12}s^{(\lambda_2)}_{34}s^{(\lambda_1)}_{13}s^{(\lambda_2)}_{24}\right]$$
$$\times(1-\eta_1-\eta_3)(1-\eta_2-\eta_4).$$

Here, the amplitudes r and s depend on the number of phonons N and on the total angular momentum R; we do not write out these quantum numbers in order not to overload the expression, but this should be kept in mind.

Now, note that we will obtain the same result if we assume that the phonon operators satisfy the boson commutation relations, while we apply the Pauli corrections by introducing a special antisymmetrization operator P whose action on the two-phonon vector $|[\lambda]^2_R\rangle$ is defined in such a way that the following identity holds:

$$\langle[\lambda]^2_R|(1+P)|[\lambda]^2_R\rangle = 1.$$

As a result, we find that

$$P[A^+_{12}(\lambda)A^+_{34}(\lambda)]_R$$
$$= -\sum_{\lambda_1\lambda_2}(2+1)[(2\lambda_1+1)(2\lambda_2+1)]^{1/2}$$
$$\times\left([A^+_{13}(\lambda_1)A^+_{24}(\lambda_2)]_R\begin{Bmatrix} j_1 & j_2 & \lambda\\ j_3 & j_4 & \lambda\\ \lambda_1 & \lambda_2 & R\end{Bmatrix}\right.$$
$$\left. + (-1)^{j_3-j_4-\lambda}[A^+_{14}(\lambda_1)A^+_{23}(\lambda_2)]_R\begin{Bmatrix} j_1 & j_2 & \lambda\\ j_4 & j_3 & \lambda\\ \lambda_1 & \lambda_2 & R\end{Bmatrix}\right).$$

We defined $P[A_{12}(\lambda)A_{34}(\lambda)]_R$ in a similar way. As yet, we have made no approximations, and, formally, the essence of the method suggested in [24] is to restrict the analysis to the contribution from the two-phonon components when allowing for the Pauli corrections. The norm of the N-phonon state is then found to be

$$K_{N\lambda J} = N!\left\{1 + (N-1)/2\sum_R \Gamma^2_{NJR}P^R_{\lambda\lambda}\right\},$$

where Γ_{NJR} is the weight of the two-phonon component with angular momentum R in the N-phonon state with the set of quantum numbers N and J calculated in a standard way via the genealogical coefficient [29].

We can verify that this approximation is highly accurate by considering various limiting situations. For example, let us choose a spin-forbidden multiquasiparticle configuration $\{j\}^N_J$. If we attempt to represent it as an $N/2$-phonon configuration, then we will find $K_{N/2,\lambda J} = 0$. Another example: if a phonon is assumed to be formed at one single-particle j level, then we will easily obtain the maximum number of phonons that can be excited in such a system, which is determined by the condition for the norm of the vector being equal to zero. As a result, the maximum angular momentum $J_{\max} = 2N_{\max}$ that the $\{j\}^{N_{\max}}_J$ configuration can have is almost always equal to its exact value. In other words, the two-phonon approximation used to allow for the Pauli corrections reflects the actual situation quite adequately, while the entire procedure of calculations can be unified by introducing the operator P.

It remains to present the variational equation that defines the structure of one phonon in the N-phonon state with the set of quantum numbers J and N:

$$\delta\{\langle[\lambda]^1_\lambda|\tilde{H}_0 + H_{qq}|[\lambda]^1_\lambda\rangle + [(N-1)/2]$$
$$\times\sum_R\Gamma^2_{NJR}\langle[\lambda]^2_R|H_{qq}P|[\lambda]^2_R\rangle$$
$$-\omega_{\lambda NJ}(\langle[\lambda]^1_\lambda|[\lambda]^1_\lambda\rangle - 1)\} = 0, \quad E_{\lambda NJ} = N\omega_{\lambda NJ},$$

where $H_{qq} = H_{22} + H_{04} + H_{\rm sc}$. After variations in the r and s amplitudes, we find that

$$(2\lambda+1)^{-1}\{S^{(\lambda)}_p(\chi_{pp}F^{(\lambda)}_p + \chi_{pn}F^{(\lambda)}_n)$$
$$+ S^{(\lambda)}_n(\chi_{nn}F^{(\lambda)}_n + \chi_{np}F^{(\lambda)}_p)\}$$
$$+ D^{(\lambda)}_p + D^{(\lambda)}_n = F^{(\lambda)}_p + F^{(\lambda)}_n.$$

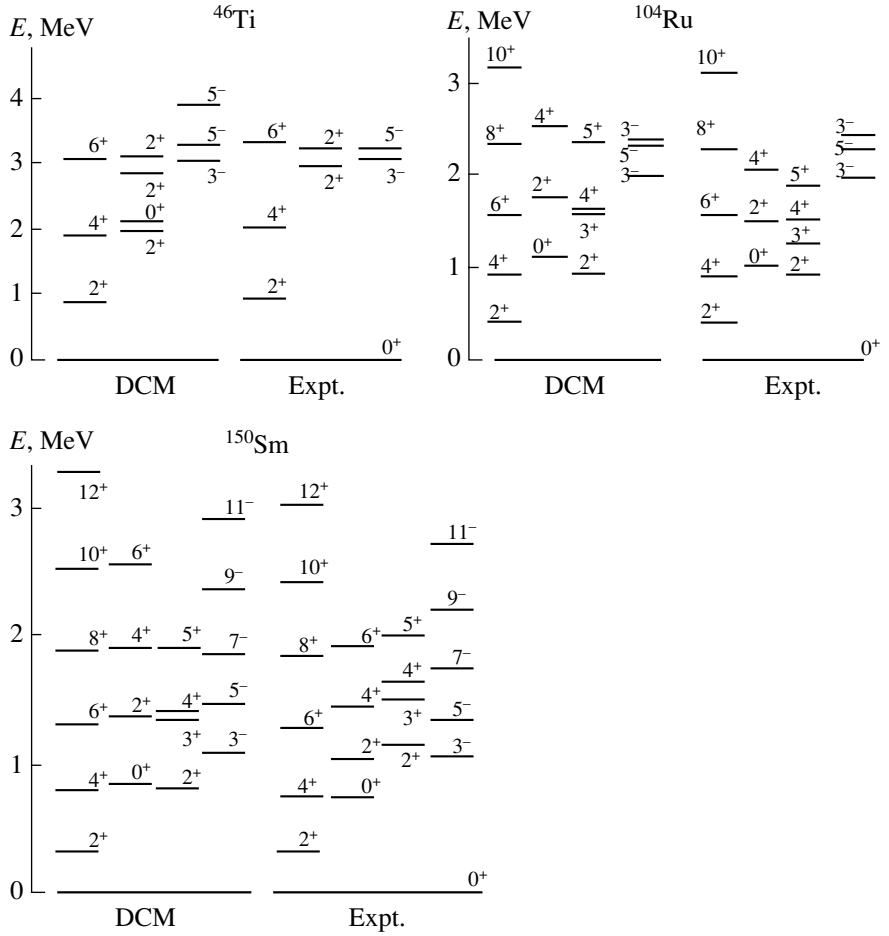

Fig. 19. Spectra of multiphonon states for several nuclei calculated in the harmonic DCM approximation in comparison with the experimental excitation spectra.

Here (the isospin symbol $\tau = p,\ n$ in the formulas given below indicates that the summation is over the corresponding single-particle states),

$$S_\tau^{(\lambda)} = \sum_{1\tau 2\tau} q_{1\tau 2\tau}^{(\lambda)} [(\varepsilon_{1_\tau} + \varepsilon_{2_\tau})/([\varepsilon_{1_\tau} + \varepsilon_{2_\tau}]^2 - \omega_{\lambda NJ}^2)](1 - \eta_{1_\tau} - \eta_{2_\tau}),$$

$$F_\tau^{(\lambda)} = \sum_{1\tau 2\tau} q_{1\tau 2\tau}^{(\lambda)} (r_{1\tau 2\tau}^{(\lambda)} + s_{1\tau 2\tau}^{(\lambda)})(1 - \eta_{1_\tau} - \eta_{2_\tau}),$$

$$r_{1_p 2_p}^{(\lambda)} = \frac{q_{1_p 2_p}^{(\lambda)}}{2(2\lambda+1)(\varepsilon_{1_p} + \varepsilon_{2_p} - \omega_{\lambda NJ})} \times (\chi_{pp} F_p^{(\lambda)} + \chi_{pn} F_n^{(\lambda)}) - [(\varepsilon_{1_p} + \varepsilon_{2_p} - \omega_{\lambda NJ}) \times (1 - \eta_{1_p} - \eta_{2_p})]^{-1} \frac{\partial M}{\partial r_{1_p 2_p}^{(\lambda)}},$$

$$s_{1_p 2_p}^{(\lambda)} = \frac{q_{1_p 2_p}^{(\lambda)}}{2(2\lambda+1)(\varepsilon_{1_p} + \varepsilon_{2_p} + \omega_{\lambda NJ})} \times (\chi_{pp} F_p^{(\lambda)} + \chi_{pn} F_n(\lambda)) - [(\varepsilon_{1_p} + \varepsilon_{2_p} + \omega_{\lambda NJ}) \times (1 - \eta_{1_p} - \eta_{2_p})]^{-1} \frac{\partial M}{\partial s_{1_p 2_p}^{(\lambda)}},$$

$$D_p^{(\lambda)} = \sum_{12} q_{1_p 2_p}^{(\lambda)} \left[(\varepsilon_{1_p} + \varepsilon_{2_p} - \omega_{\lambda NJ})^{-1} \frac{\partial M}{\partial r_{1_p 2_p}^{(\lambda)}} + (\varepsilon_{1_p} + \varepsilon_{2_p} + \omega_{\lambda NJ})^{-1} \frac{\partial M}{\partial s_{1_p 2_p}^{(\lambda)}} \right],$$

$$M = \frac{N-1}{2} \sum_R \Gamma_{NJR}^2 \langle [\lambda_1 \lambda_2]_R^2 | H_{qq} P | [\lambda_1 \lambda_2]_R^2 \rangle,$$

$$\langle [\lambda_1 \lambda_2]_R^2 | H_{qq} P | [\lambda_1 \lambda_2]_R^2 \rangle = -\left\{ \chi_{pp} \left(F_p^{(\lambda_1)} Q_{\lambda_1 \lambda_2}^{Rp} + F_p^{(\lambda_2)} Q_{\lambda_2 \lambda_1}^{Rp} \right) + \chi_{pn} \left(F_n^{(\lambda_1)} Q_{\lambda_1 \lambda_2}^{Rn} + F_n^{(\lambda_2)} Q_{\lambda_2 \lambda_1}^{Rn} \right) \right\} + \left\{ \chi_{nn} \left(F_n^{(\lambda_1)} Q_{\lambda_1 \lambda_2}^{Rn} + F_n^{(\lambda_2)} Q_{\lambda_2 \lambda_1}^{Rn} \right) \right.$$

$$+ \chi_{np}\left(F_p^{(\lambda_1)}Q^{Rp}_{\lambda_1\lambda_2} + F_p^{(\lambda_2)}Q^{Rp}_{\lambda_2\lambda_1}\right)\Big\},$$

where

$$Q^{R\tau}_{\lambda_1\lambda_2} = -(2\lambda_1+1)(2\lambda_2+1)\sum_{1234}\begin{Bmatrix} j_1 & j_2 & \lambda_1 \\ j_3 & j_4 & \lambda_2 \\ \lambda_1 & \lambda_2 & R\end{Bmatrix}$$
$$\times\Big[q_{13}^{(\lambda_1)}\Big\{r_{12}^{(\lambda_1)}r_{24}^{(\lambda_2)}r_{34}^{(\lambda_2)} + s_{12}^{(\lambda_1)}s_{24}^{(\lambda_2)}s_{34}^{(\lambda_2)}\Big\}$$
$$+ q_{24}^{(\lambda_1)}\Big\{r_{12}^{(\lambda_1)}r_{13}^{(\lambda_2)}r_{34}^{(\lambda_2)} + s_{12}^{(\lambda_1)}s_{13}^{(\lambda_2)}s_{34}^{(\lambda_2)}\Big\}\Big]$$
$$\times(1-\eta_1-\eta_3)(1-\eta_2-\eta_4).$$

The expressions for the neutron amplitudes r and s derived from these relations by substituting the index n for p appear similar. Next, to save space, in all expressions, we do not specify that the amplitudes r and s and, hence, S, F, and Q depend on the set of quantum numbers that characterize the N-phonon state. We emphasize that the solution of the equations has a meaning only for a positively defined vector norm. The values of the quantum numbers at which the vector norm is zero imply a break of the band of collective states. However, it does not follow from this that a state with an even larger angular momentum cannot be excited in the system. This requires considering the band of states in a noncollective state of large multipolarity.

3.6. Results of the Calculations of Multiphonon States

The parametrization was discussed in detail in Section 3.3. Here, we merely recall that there is only one free parameter in the approach under consideration, the proton or neutron constant of spin–orbit forces.

The spectra of the bands of ground nuclear states and the transition probabilities in them calculated in the harmonic approximation are shown in Figs. 12 and 13. Figure 19 shows the total spectra of collective states for several nuclei calculated in the harmonic approximation in comparison with the experimental data.

We see that, after allowing for the Pauli exclusion principle in the formation of multiphonon states, we can reproduce not only the structure of the yrast bands of nuclei and the characteristic changes in them when passing from spherical to deformed nuclei, but also many characteristic features observed in the total spectra.

However, the role of the Pauli exclusion principle manifests itself most clearly in the existence of a critical number of phonons $N_{\max}$ and the corresponding angular momentum $J_{\max} = 2N_{\max}$.

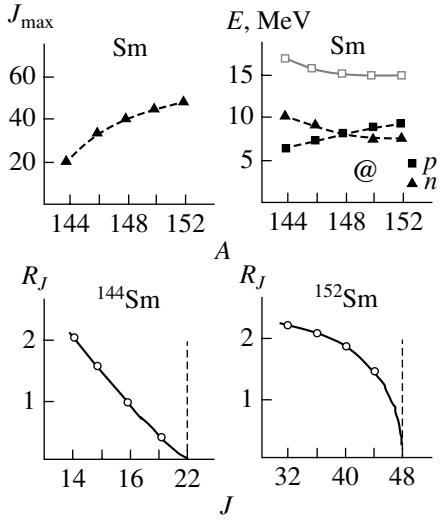

Fig. 20. Calculated (closed triangles) critical angular momenta, excitation energies corresponding to these angular momenta (open squares), and proton (closed squares) and neutron (closed triangles) separation energies versus mass number of the samarium isotopes. Two typical patterns of behavior of $R_J = B(E2; J \to J-2)/B(E2; 2_1^+ \to 0_1^+)$ near the critical angular momentum (the value is indicated by the dashed line) are shown in the lower part of the figure.

The calculated values of $J_{\max}$ and $E_{\max}$ for the samarium isotopes are shown in Fig. 20 together with the experimental data on the nucleon separation energies in these nuclei. The clear correlation of $E_{\max}$ with the neutron separation energy S_n is not random; it is repeated from calculation to calculation. This suggests that $E_{\max}$ is precisely the energy at which the nucleus is easily deexcited by emitting a neutron with an orbital angular momentum $l = 2$ (the Coulomb barrier is a hindrance to protons).

The behavior of $B(E2)$ near $J_{\max}$ is shown in the lower part of Fig. 20 to demonstrate two typically encountered situations. The last situation is observed in the experiment for ^{74}Se at $J^\pi = 16^+$ (see Section 4.1). It remains to apply the anharmonic corrections to complete our analysis of the "pairing + multipole–multipole" interaction scheme.

3.7. The Theory of Anharmonic Corrections

The Hamiltonian of the multipole attractive forces H_Q consists of two main parts: $H_{qq} = H_{22} + H_{04} + H_{\rm sc}$ and H_{13}. The first part is responsible for the formation of phonon vectors, while the second part is responsible for their mixing. Naturally, the constants of forces in the first and second parts are identical. However, it follows from our analysis of the experimental data, in particular, from the analysis of $Q(2_1^+)$, as we saw, that as the collectivity of the nucleus grows, i.e.,

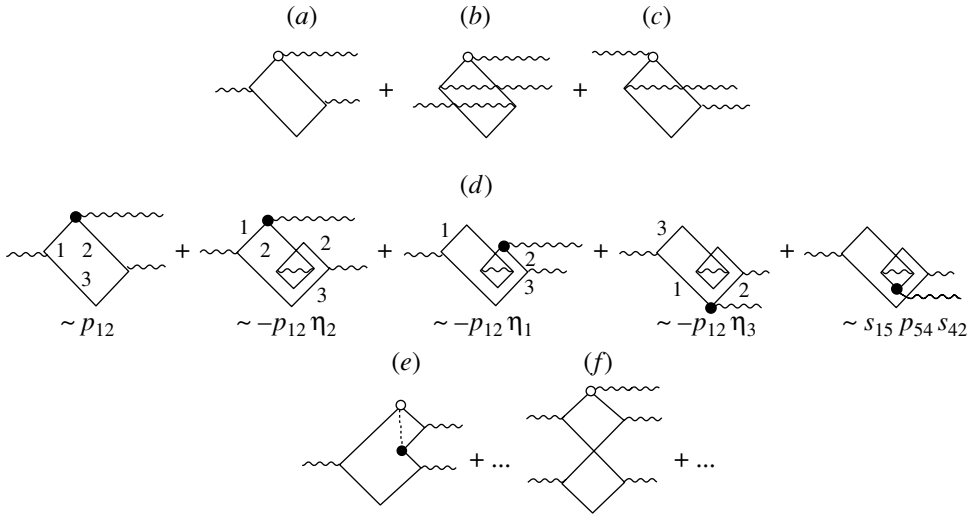

Fig. 21. Diagram representation of the anharmonic corrections in a channel with the number of phonons changed by one. The corresponding terms of the matrix element $G^{(\lambda)}_{123}$ are shown under each diagram of Fig. 21*d*. The solid and wavy lines represent the quasiparticles and phonons, respectively.

as the contribution from H_{qq} increases, the corresponding contribution from H_{13} must decrease. This characteristic relationship between the contributions was first established in 1979 [26] by analyzing the properties of odd nuclei; the cause (zero shape oscillations) was also established at this time. Therefore, turning to even–even nuclei, we knew where to seek the answer.

Formally, our problem is to calculate matrix elements of the form $\langle[\lambda]^{N_1}_{J_1}|H_{13}(1+P)|[\lambda]^{N_2}_{J_2}\rangle$ and diagonalize the matrix constructed as a result. There is no need to describe a detailed derivation of the formulas for these matrix elements; except the separation of the corrections related to the zero oscillations, a standard technique is used here. We will discuss this point using the calculation of the matrix element $\langle\Omega_{\lambda\mu}N_{ji}(\Lambda M)\Omega^+_{\lambda\mu}\rangle$ to which many of the calculations are eventually reduced as an example.

The standard procedure for calculating this matrix element is based on the tacit assumption that the commutator $\Omega_{\lambda\mu}$ with $\Omega^+_{\lambda\mu}$ is identically equal to a Kronecker delta, and the contribution of the second term in the expression

$$\langle\Omega_{\lambda\mu}N_{ji}\Omega_{\lambda\mu}\rangle = \langle\Omega_{\lambda\mu}[N_{ji},\Omega^+_{\lambda\mu}]_{(-)}\rangle + \langle\Omega_{\lambda\mu}\Omega^+_{\lambda\mu}N_{ji}\rangle \tag{16}$$

is then equal to zero at $\Lambda \neq 0$. However, for any microscopic definition of the phonon, only the vacuum mean of the commutator rather than its exact expression, which also contains terms proportional to N_{kl}, can be equal to a Kronecker delta. Hence, the contribution of the second term in (16) is proportional to $\langle N_{kl}(\Lambda M)N_{ji}(\Lambda' M')\rangle$. The latter can be easily calculated by reducing it to a normal (relative to the phonon vacuum) form and using the expansion of the quasiparticle pairs $\alpha^+_i\alpha^+_j$ and $\alpha_k\alpha_l$ in terms of the phonon operators. As a result, we obtain

$$\begin{aligned}\langle\Omega_{\lambda\mu}\Omega^+_{\lambda\mu}N_{kl}(LM)\rangle &\sim \langle\alpha^+_i\alpha_j\alpha^+_k\alpha_l\rangle \sim \eta_j\delta_{kj}\delta_{il}\\ &- \langle\alpha^+_i\alpha^+_j\alpha_k\alpha_l\rangle \sim \eta_j\delta_{kj}\delta_{il}\\ &- \sum_{n\Lambda} s^{(n\Lambda)}_{ik}s^{(n\Lambda)}_{jl}(1-\eta_i-\eta_k)(1-\eta_j-\eta_l).\end{aligned}$$

These corrections in (16) play a crucial role in strongly collective nuclei. It remains to give the final expressions for the matrix elements.

The matrix elements with $\Delta N = 1$.

$$\begin{aligned}\langle[\lambda]^{N-1}_J|H_{13}|[\lambda]^N_J\rangle &= (N-1)\left[\frac{K_{N,J,\ldots}}{K_{N-1,J,\ldots}}\right]^{1/2}\\ &\times\Gamma^{N,J,\ldots}_{N-1,J,\ldots}\{[\chi_{pp}F^{(N\lambda J)}_p + \chi_{pn}F^{(N\lambda J)}_n]L^p_{N\lambda J}\\ &+ [\chi_{nn}F^{(N\lambda J)}_n + \chi_{np}F^{(N\lambda J)}_p]L^n_{N\lambda J}\\ &+ [\chi_{pp}F^{(N-1\lambda J)}_p + \chi_{pn}F^{(N-1\lambda J)}_n]M^p_{N\lambda J}\\ &+ [\chi_{nn}F^{(N-1\lambda J)}_n + \chi_{np}F^{(N-1\lambda J)}_p]M^n_{N\lambda J}\}.\end{aligned}$$

In these expressions, the ellipses stand for the entire set of quantum numbers that characterize the N-phonon state. Further, we have

$$\begin{aligned}L^\tau_{N\lambda J} &= -\frac{1}{2}\sum_{123}(-1)^{j_1+j_3+\lambda}\left\{\begin{array}{ccc}\lambda & \lambda & \lambda\\ j_1 & j_2 & j_3\end{array}\right\}\\ &\times G^{(\lambda)}_{123}[r^{(N\lambda J)}_{23}r^{(N-1\lambda J)}_{13} + (-1)^\lambda s^{(N\lambda J)}_{13}s^{(N-1\lambda J)}_{23}],\end{aligned}$$

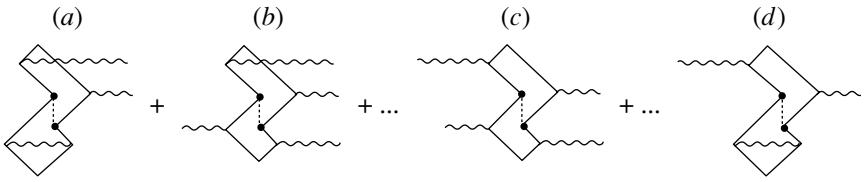

Fig. 22. Diagram representation of the anharmonic corrections in a channel with the number of phonons changed by two (*a*, *b*) and in a channel without any change in the number of phonons (*c*, *d*) attributable to the pairing interaction. The solid and wavy lines represent the quasiparticles and phonons, respectively.

$$M^{\tau}_{N\lambda J} = -\frac{1}{2}\sum_{123}(-1)^{j_1+j_3+\lambda}\left\{\begin{array}{ccc}\lambda & \lambda & \lambda\\ j_1 & j_2 & j_3\end{array}\right\} \times G^{(\lambda)}_{123}r^{(N\lambda J)}_{23}s^{(N\lambda J)}_{13},$$

$$G^{(\lambda)}_{123} = p^{(\lambda)}_{12}(1-\eta_1-\eta_2-\eta_3) + \sum_{45\Lambda}(-1)^{j_4+j_5+\lambda}(2\Lambda+1)\left\{\begin{array}{ccc}j_4 & j_5 & \lambda\\ j_1 & j_2 & \Lambda\end{array}\right\} \times s^{(0\Lambda 0)}_{15}p^{(\lambda)}_{54}s^{(0\Lambda 0)}_{42}(1-\eta_1-\eta_5)(1-\eta_4-\eta_2).$$

In these expressions, we specified all those quantum numbers on which the amplitudes r and s depend. The weighting factors $\Gamma^{N,J,\ldots}_{N-1,J,\ldots}$ can be calculated inductively,

$$\Gamma^{N,J,\ldots}_{N-1,J,\ldots} = \sum\Gamma^{N-1,J_{N-1},\ldots}_{N-2,J_{N-2},\ldots} \times G^{N,J_N,\ldots}_{N-1,J_{N-1},\ldots}[\lambda]G^{N-1,J_{N-1},\ldots}_{N-2,J_{N-2},\ldots}[\lambda],$$

from the known single-phonon fractional-parentage coefficients [29] $G^{N,J_N,\ldots}_{N-1,J_{N-1},\ldots}[\lambda]$ with the initial condition $\Gamma^{2,J_2}_{1,\lambda} = \delta_{\lambda,J_2}$; the summation is over all intermediate quantum numbers.

Similarly, we also determined the weighting factors encountered below

$$\Gamma^{N,J,\ldots}_{N-3,J,\ldots} = \sum\Gamma^{N-1,J_{N-1},\ldots}_{N-4,J_{N-4},\ldots} \times G^{N,J_N,\ldots}_{N-1,J_{N-1},\ldots}[\lambda]G^{N-3,J_{N-3},\ldots}_{N-4,J_{N-4},\ldots}[\lambda]$$

and the coefficients $D^{\cdots}_{\cdots}[R]$ whose determination differs from that of $\Gamma^{N,J,\ldots}_{N-1,J,\ldots}$ only by the initial condition

$$D^{3,J,\ldots}_{2,R,\ldots}[R] = [(2\lambda+1)(2R+1)]^{1/2} \times \left\{\begin{array}{ccc}\lambda & \lambda & R\\ \lambda & J & \lambda\end{array}\right\} G^{3,J,\ldots}_{2,R,\ldots}[\lambda].$$

The matrix elements proportional to $F\cdot L$ and $F\cdot M$ correspond to the diagrams shown in Figs. 21*a*, 21*b*, and 21*c*, respectively. The open circle corresponds to the matrix element $G^{(\lambda)}_{123}$ that includes the renormalization of the matrix element $p^{(\lambda)}_{12}$ attributable to the vacuum fluctuations. In the language of the diagrams shown in Fig. 21*a*, allowance for the vacuum fluctuations implies allowance for the set of diagrams shown in Fig. 21*d*. A similar expansion in terms of vacuum contributions should be kept in mind for any diagram where the open circle is encountered.

In addition to the above matrix elements responsible for the processes with the change in the number of phonons by one, there are two more purely Pauli matrix elements:

$$\langle[\lambda]^{N-1}_J|H_{13}P|[\lambda]^N_J\rangle = N(N-1)\left[\frac{K_{N-1,J,\ldots}}{K_{N,J,\ldots}}\right]^{1/2} \times \Gamma^{N,J,\ldots}_{N-1,J,\ldots}\{\chi_{pp}R^p_{N\lambda J}+\chi_{nn}R^n_{N\lambda J}\} + N(N-1)(N-2)\left[\frac{K_{N-1,J,\ldots}}{K_{N,J,\ldots}}\right]^{1/2} \times \sum_{R=0,2,4}D^{N,J,\ldots}_{N-1,J,\ldots}[R]\{[\chi_{pp}F^p_{N\lambda J}+\chi_{pn}F^n_{N\lambda J}] \times T^p_{N\lambda J}[R]+[\chi_{nn}F^n_{N\lambda J}+\chi_{np}F^p_{N\lambda J}]T^n_{N\lambda J}[R]\},$$

$$R^{\tau}_{N\lambda J} = -\sum_{1,\ldots,5}(2\lambda+1)^2 \times \left\{\begin{array}{ccc}\lambda & \lambda & \lambda\\ j_1 & j_2 & j_5\end{array}\right\}\left\{\begin{array}{ccc}j_2 & j_3 & \lambda\\ j_5 & j_4 & \lambda\\ \lambda & \lambda & \lambda\end{array}\right\} q^{(\lambda)}_{34}G^{(\lambda)}_{125} \times [r^{(N\lambda J)}_{32}r^{(N\lambda J)}_{45}r^{(N-1\lambda J)}_{51} + s^{(N\lambda J)}_{32}s^{(N\lambda J)}_{45}s^{(N-1\lambda J)}_{51}](1-\eta_3-\eta_4),$$

$$T^{\tau}_{N\lambda J}[R] = -\sum_{1,\ldots,5}(2\lambda+1)^2 \times \left\{\begin{array}{ccc}\lambda & \lambda & \lambda\\ j_1 & j_2 & j_5\end{array}\right\}\left\{\begin{array}{ccc}j_2 & j_3 & \lambda\\ j_5 & j_4 & \lambda\\ \lambda & \lambda & R\end{array}\right\} G^{(\lambda)}_{125}$$

$$\times [r_{32}^{(N\lambda J)} r_{54}^{(N\lambda J)} r_{51}^{(N-1\lambda J)} r_{34}^{(N-1\lambda J)} + s_{32}^{(N\lambda J)} s_{54}^{(N\lambda J)} s_{51}^{(N-1\lambda J)} s_{34}^{(N-1\lambda J)}](1-\eta_3-\eta_4).$$

The matrix elements proportional to R and $F\cdot T$ correspond to the diagrams shown in Figs. 21*e* and 21*f* and to similar diagrams obtained by reversing the phonon lines. In general, the diagrams in Fig. 21*e* are suppressed with respect to those in Fig. 21*f* due to the absence of a coherently enhanced factor F. For this reason, we also disregarded other similar Pauli diagrams arising from $H_{13}P$. We emphasize that the role of the diagrams in Fig. 21*f* becomes significant at $N \sim N_{\max}/2$.

The matrix elements with $\Delta N = 2$. In the standard random phase approximation, the matrix elements with $\Delta N = 2$ are identically equal to zero. However, numerical simulations of the various types of matrices to which the multipole interaction can lead and analysis of their spectra have led us to conclude that these matrix elements are largely responsible for the formation of the spectra with a low-lying gamma band. ^{166}Er serves as a typical example of such a nucleus.

Not all of the matrix elements with $\Delta N = 2$ are equal to zero in our approach, but they are all purely Pauli ones. Therefore, they are a factor of 2 or 3 smaller than the value required to describe the ^{166}Er-type spectra. As our analysis indicates, neglecting the role of the pairing interaction could be mainly responsible for the observed "deficit." We established this by analyzing the diagrams with $\Delta N = 0$ shown in Fig. 22*c* and similar diagrams obtained by symmetrically reversing the phonon lines.

The contribution of the diagrams in Figs. 22*a* and 22*b* from the pairing interaction is large at zero total angular momentum of the isolated phonon pair and for a certain structure of the Fermi surface. However, it thus follows that the diagrams shown in Fig. 22*d* also play an important role in forming the phonon vectors in strongly collective nuclei; including them means going far outside the scope of Hara's approximation that we took as the basis.

The contribution of the pairing Hamiltonian to the energy functional of the single-phonon state is found to be

$$\langle 0|\Omega_\lambda^{(i)}[H_G, \Omega_\lambda^{+(i)}]_{(-)}|0\rangle = H_G^{(1)} + H_G^{(2)} + H_G^{(3)} + H_G^{(4)},$$

where

$$H_G^{(1)} = -\sum_\tau (G_\tau/2) \sum_{1\tau 2\tau} [\{r_{1\tau 2\tau}^{(i)}\}^2 - \{s_{1\tau 2\tau}^{(i)}\}^2](\eta_{1\tau}+\eta_{2\tau}),$$

$$H_G^{(2)} = -\sum_\tau [2\lambda+1]^{1/2}(G_\tau/2) \times \sum_{1\tau 2\tau} [u_{1\tau}^2 v_{2\tau}^2 + v_{1\tau}^2 u_{2\tau}^2] r_{1\tau 2\tau}^{(i\lambda)} s_{1\tau 2\tau}^{(i\lambda)} \times (1-2\eta_{1\tau})(1-2\eta_{2\tau}),$$

$$H_G^{(3)} = -\sum_\tau G_\tau \sum_{\substack{1\tau 2\tau 3\tau 4\tau \\ k\Lambda}} [r_{1\tau 2\tau}^{(i\lambda)} r_{3\tau 4\tau}^{(i\lambda)} - s_{1\tau 2\tau}^{(i\lambda)} s_{3\tau 4\tau}^{(i\lambda)}] \times s_{1\tau 4\tau}^{(k\Lambda)} s_{2\tau 3\tau}^{(k\Lambda)} (2\Lambda+1) \begin{Bmatrix} j_{3\tau} & j_{4\tau} & \lambda \\ j_{1\tau} & j_{2\tau} & \Lambda \end{Bmatrix} \times (1-\eta_{1\tau}-\eta_{4\tau})(1-\eta_{2\tau}-\eta_{3\tau}),$$

$$H_G^{(4)} = -\sum_\tau G_\tau \frac{\sqrt{2\lambda+1}}{2} \sum_{\substack{1\tau 2\tau 3\tau 4\tau \\ k\Lambda}} (u_{1\tau}^2 v_{2\tau}^2 + v_{1\tau}^2 u_{2\tau}^2) \times [r_{1\tau 3\tau}^{(i\lambda)} s_{4\tau 2\tau}^{(i\lambda)} + r_{4\tau 2\tau}^{(i\lambda)} s_{1\tau 3\tau}^{(i\lambda)}] s_{1\tau 2\tau}^{(k\Lambda)} s_{3\tau 4\tau}^{(k\Lambda)} (2\Lambda+1) \times \begin{Bmatrix} j_{2\tau} & j_{4\tau} & \lambda \\ j_{3\tau} & j_{1\tau} & \Lambda \end{Bmatrix} (1-\eta_{1\tau}-\eta_{2\tau})(1-\eta_{3\tau}-\eta_{4\tau}).$$

$H_G^{(1)}$ gives the largest contribution to the energy of the single-phonon 2_1^+ state: it is easy to see (after variations in the r_{ji} and s_{ji} amplitudes) that the effect of $H_G^{(1)}$ reduces to an effective decrease in the energy of each single-quasiparticle state by $\varepsilon_j \to \varepsilon_j - \eta_j G/2$, which causes the energy of the single-phonon state to decrease by about 50 keV for the nuclei from the samarium region. This means that the correction to the energy of the single-phonon state can reach 30%. In general, however, the situation becomes radically more complicated.

Our accumulated experience in modeling the spectra of matrices suggested a way out; we must choose suitable objects for comparison, i.e., choose nuclear isotopes in whose excitation spectra the base of the gamma band lies at a higher excitation energy than the base of the beta band. In such nuclei, the diagrams in Fig. 22 discussed above will not play a significant role in forming the spectrum.

We will most likely have to devote more than one paper to the diagrams in Fig. 22.

The matrix elements with $\Delta N = 3$. The contribution from the Pauli corrections to the matrix elements with $\Delta N = 3$ can be disregarded, since their relative importance is more than a factor of 3 smaller than that for the processes with $\Delta N = 1$. Then,

$$\langle [\lambda]_J^{N-3}|H_{13}|[\lambda]_J^N\rangle = N(N-1)\left[\frac{K_{N-2,J,\ldots}^2}{K_{N-3,J,\ldots}K_{N,J,\ldots}}\right]^{1/2} \Gamma_{N-3,J,\ldots}^{N,J,\ldots}$$

Table 5. Experimental and calculated (in DCM and IBM) values of $B(E2; J_i \to J_f)$ for ^{74}Se (in $e^2\,\mathrm{b}^2 \times 10^{-3}$)

J_i	J_f	Expt.	DCM	IBM	J_i	J_f	Expt.	DCM	IBM
2_1	0_1	74^{+4}_{-4}	74	74	0_2	2_1	152^{+11}_{-11}	141	148
4_1	2_1	102^{+15}_{-11}	130	137	3_1	2_1	$9.3^{+5.6}_{-3.7}$	21	3
6_1	4_1	117^{+19}_{-15}	162	179	3_1	2_2	19^{+15}_{-6}	63	50
8_1	6_1	122^{+28}_{-19}	180	196	3_1	4_1	55^{+33}_{-15}	36	31
10_1	8_1	152^{+50}_{-30}	187	192	4_2	4_1	26^{+15}_{-6}	40	33
12_1	10_1	134^{+37}_{-24}	185	166	4_2	2_1	0.6^{+4}_{-2}	2	1
14_1	12_1	92^{+28}_{-17}	170	126	4_2	2_2	50^{+28}_{-13}	83	104
16_1	14_1	< 70	162	68	5_1	3_1	83^{+50}_{-22}	90	91
2_2	0_1	$1.6^{+0.6}_{-0.4}$	5	2	5_1	4_1	3^{+2}_{-1}	16	2
2_2	2_1	89^{+35}_{-20}	65	78	7_1	5_1	105^{+48}_{-26}	129	120
2_2	0_2	< 148	26	48	9_1	7_1	75^{+39}_{-26}	143	120

$$\times [[\chi_{pp}F_p^{(N\lambda J)} + \chi_{pn}F_n^{(N\lambda J)}]N_{N\lambda J}^p$$
$$+ [\chi_{nn}F_n^{(N\lambda J)} + \chi_{np}F_p^{(N\lambda J)}]N_{N\lambda J}^n],$$

$$N_{N\lambda J}^{\tau} = -\frac{\sqrt{2\lambda+1}}{2}\sum_{1\,2\,3}(-1)^{j_1+j_3+\lambda}$$
$$\times \begin{Bmatrix} \lambda & \lambda & \lambda \\ j_1 & j_2 & j_3 \end{Bmatrix} G_{123}^{(\lambda)} r_{23}^{(N\lambda J)} s_{13}^{(N\lambda J)}.$$

The matrix elements with $\Delta N = 4.6$. If we were consistent in our approximations, then we should also forget the matrix elements of this type at the current stage.

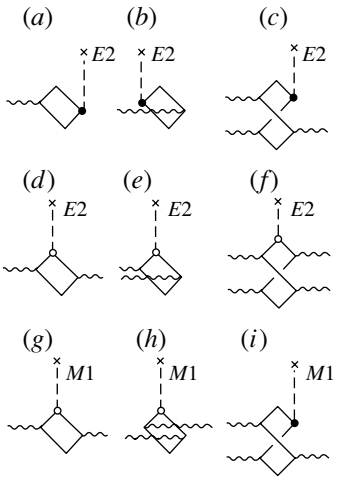

Fig. 23. Diagram representation of the processes that were taken into account in our calculations of the electromagnetic moments.

3.8. The Electric and Magnetic Moments

We performed our calculations in the approximation of the main diagrams shown in Figs. 23*a*–23*c* and 23*g*–23*i*.

Although the nontrivial role of the pairing interaction that we found narrowed the validity range of our approach, this range remains wide enough. It includes spherical, transition, and deformed nuclei, but of a certain type. More specifically, if the β and γ bands were formed in the nuclear spectrum, then we have the right to touch only on those nuclei for which $E_\beta < E_\gamma$.

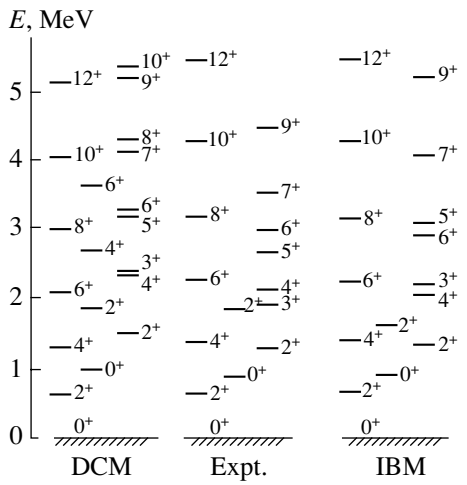

Fig. 24. Calculated (in DCM and IBM) and experimental ^{74}Se excitation spectra.

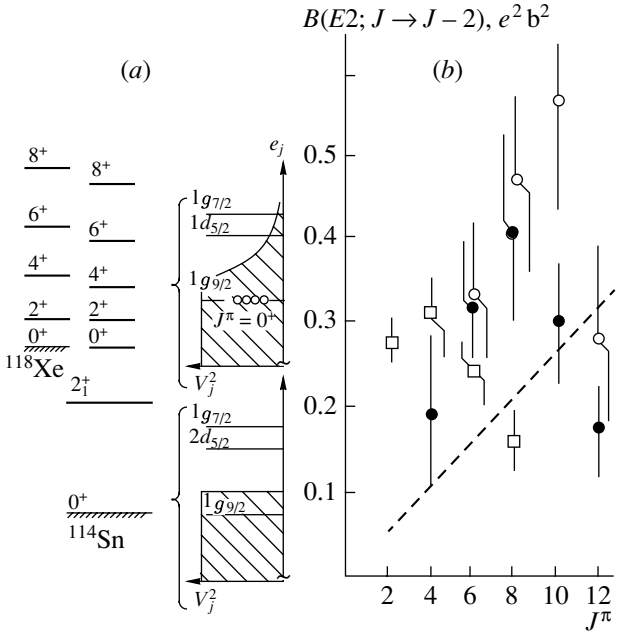

Fig. 25. (a) Band of intruder ^{114}Sn states in comparison with the yrast band of ^{118}Xe and schematic view of the wave function for the ground, 0_1^+, and intruder, 0_2^+, states. (b) The probabilities of $E2$ transitions between the intruder states of the ^{112,114}Sn isotopes (the open and closed circles, respectively) and the corresponding data for ^{118}Xe (squares). The dashed straight line represents the vibrational limit.

4. RESULTS OF THE CALCULATIONS: β-SOFT NUCLEI

First of all, recall that there is only one parameter to describe the spectra in DCM, the proton or neutron constant of spin–orbit forces.

In the calculations of the $M1$ angular momenta, the spin g factor is taken to be 0.8 of its value for a free nucleon according to our previous studies of the properties of odd nuclei. In the calculations of the $E2$ angular momenta, the effective charge of the neutron was chosen from the description of $B(E2; 2_1^+ \to 0_1^+)$, but, in all cases, it did not exceed five times the effective charge of the neutron associated with the nuclear recoil, i.e., $5Z/A^2 \sim 2 \times 10^{-3}$. This suggests that we have almost exhausted the space of single-particle states in which the dynamics of the described states is realized. In the calculations of the $E1$ transitions, we took into account only the nuclear recoil.

The nuclear isotopes that we chose for our analysis were determined, first, by the availability of fairly comprehensive information on their properties; second, these must include spherical, transition, and deformed nuclei from different mass regions; third, and most importantly, the experimental information must be "live" for any arising questions to be resolved in communication with experimenters.

We emphasize that we also performed approximate calculations for many other nuclei. The accuracy of describing the experimental spectra achieved in the calculations differs only slightly from those presented below, but the scarcity and uncertainty of other experimental spectroscopic information forces us to abandon the presentation of this material, although some of the model-independent results are presented below.

4.1. The ^{74}Se Isotope

The ^{74}Se nucleus belongs to typically transition nuclei. The presence of the low-lying 0_2^+ state in its spectrum maintained constant interest in this nucleus. Recently, the $E2$-transition probabilities have been measured [30] for most of the observed collective states in this isotope. Therefore, this nucleus can serve as a kind of a testing ground for various theoretical approaches. Figure 24 and Table 5 present the level spectra and the $E2$-transition probabilities calculated in terms of DCM [31] and the interacting-boson model (IBM) [30] in comparison with the experimental data. In this case, $Q(2_1^+)_{\mathrm{DCM}} = -0.31\ e$ b, while the experimental value is $Q(2_1^+)_{\mathrm{expt}} = -0.36(7)\ e$ b. Further, note that the $0_2^+ \to 2_1^+$ transition is highly accelerated; therefore, it seems impossible to talk about the coexistence of the shapes in the selenium isotopes. Another curious fact is that $B(E2)$ falls sharply at $J^\pi = 16^+$. In DCM, the fall just begins to show up and occurs at $J^\pi = 18^+$. The discrepancy stems from the fact that the limiting number of phonons obtained from our DCM calculations is nine rather than eight, as follows from the direct interpretation of the data on $B(E2)$. As regards the picture as a whole, the quality of describing the experimental data is approximately the same in both DCM and IBM, although DCM has only one free parameter to describe the level spectrum, while IBM has six such parameters.

4.2. The ^{112,114}Sn Isotopes

The even ^{112,114}Sn isotopes are known for the clear manifestation of the so-called intruder states in their excitation spectra along with the vibrational and non-collective modes. The energy spectrum of these states closely resembles the main band of states of nuclei with four particles or four holes for the closed $Z = 50$ shell and the same number of neutrons. Thus, for example, a band of states similar to the main ^{118}Xe band is observed in the ^{114}Sn isotope, as demonstrated by Fig. 25a. This figure also schematically shows the

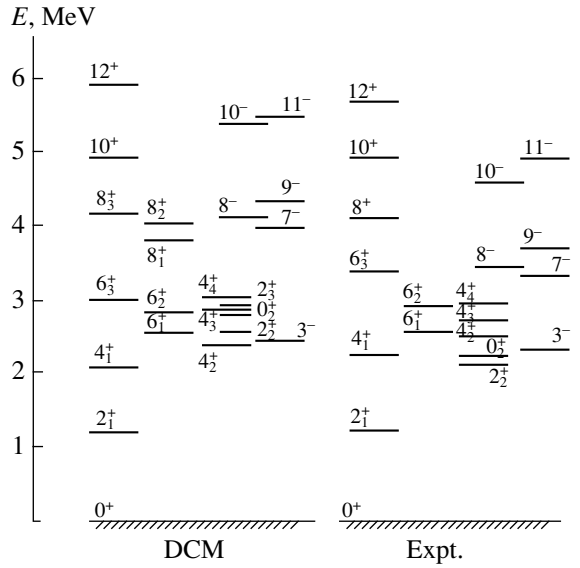

Fig. 26. Calculated (in DCM) and experimental spectra of excited ^{112}Sn states.

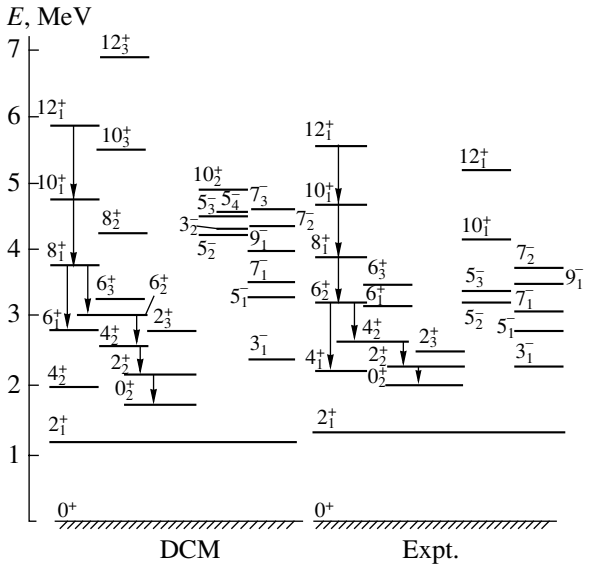

Fig. 27. Calculated (in DCM) and experimental spectra of excited ^{114}Sn states.

structures of the ground 0^+_1 state and the intruder 0^+_2 state of type "$4h + \mathrm{Xe}$." These ideas have long been discussed in the literature, and we have already touched on them in Section 2. However, in most of the papers, the conclusions are drawn only from the analysis of data on level energetics, while the natural aspiration of experimenters for the novelty of the results obtained does not allow them to notice obvious conflicts of this hypothesis with other experimental facts. The simplest of them are the acceleration of certain γ transitions between states of different natures and the intense population of some of the intruder states in single-nucleon exchange reactions. In other words, the foundation of energetics is too shaky to assert the coexistence of the shapes in the nuclear spectrum. In DCM, the "$4h + \mathrm{Xe}$" states can be easily taken into account. This requires finding a local extremum of the complete Hamiltonian on the described configuration and including this configuration in the computational scheme. It is easy to estimate the energy at which this configuration (with four holes in the lower shell) is, $\sim$10 MeV, given the emerging proton superfluidity and with the collectivity increased by a factor of 4. It is hard to imagine another mechanism that would reduce the energy of this configuration to 2 MeV. An uncertainty in describing the chemical potential of only 10 keV will lead to an error in describing the level energy of $\sim$1 MeV. Most importantly, the standard DCM methods have not been exhausted.

For the two ^{112,114}Sn isotopes, the lifetimes for most of the intruder states have been measured recently [32, 33]. The values of $B(E2; J \to J-2)$ for the intruder states of the ^{112,114}Sn isotopes calculated from the measured level lifetimes are shown (the open and closed circles, respectively) in Fig. 25*b* together with the available data on the $E2$-transition probabilities in the main band of ^{118}Xe states (squares). We see from this figure that the $B(E2)$ scale for the intruder states does not correspond to the data for xenon (unless the discrepancy by a factor of 2 is assumed to be negligible). Moreover, the observed acceleration of certain γ transitions between states of different natures contradicts this apparently consistent picture. For example, $B(E2; 6^+_3 \to 4^+_1) \sim B(E2; 2^+_1 \to 0^+_1)$ in ^{112}Sn, while $B(E2; 0^+_2 \to 2^+_1) \sim B(E2; 2^+_1 \to 0^+_2)$ in ^{114}Sn. Note that the latter ratio is typical of the deexcitation of the two-phonon 0^+_2 states in spherical nuclei.

A careful analysis of the experimental data shows that the large values of $B(E2)$ for the intruder states could result from the absolutization of the processing of the measurements. To elucidate this, let us turn to the experimental ^{112}Sn spectrum shown in Fig. 26. The probability $B(E2; 6^+_3 \to 4^+_4)$ calculated from the measured branching and lifetime is 0.324(97) e^2 b^2, which is a factor of 8 higher than $B(E2; 2^+_1 \to 0^+_1)$. The derived value does not include the possible deexcitation of $6^+_3 \to 6^+_1$ with energy 865.1 keV, which differs only slightly from the observed γ transition with energy 865.2 keV identified as the $12^+_1 \to 10^+_1$ transition. Similarly, if the lifetime of the 8^+ state is assumed to be entirely determined by only one $8^+ \to 6^+_3$ transition, then $B(E2; 8^+ \to 6^+_3) = 0.461(138)\ e^2$ b^2. However, this value does not include the possible deexcitation with the transitions

Table 6. Calculated transition energies E_γ (in MeV), $B(E2)$ (in $e^2\,\mathrm{b}^2 \times 10^{-3}$), $B(E1)$ (in $\mathrm{fm}^2 \times 10^{-4}$), $B(M1)$ (in μ_{nucl}^2), and lifetimes T (in ps) of the ^{112}Sn states in comparison with the experimental data

J_i^π	J_f^π	E_γ		$B(E2), B(E1), B(M1)$	T	
		calc.	expt.	calc.	calc.	expt.
				$B(E2)$		
2_1^+	0_1^+	1.22	1.26	41.0	0.63	0.6(2)
4_1^+	2_1^+	0.88	0.99	44.0	1.96	$2.5^{+2.5}_{-1.5}$
4_2^+	2_1^+	1.15	1.26	23.0	1.12	0.6(2)
4_3^+	2_1^+	1.64	1.53	2.7	3.62	1.2(4)
4_4^+	2_1^+	1.85	1.69	0.9	6.61	>2
6_1^+	4_1^+	0.51	0.30	2.0	16×10^3	20×10^3
6_2^+	4_1^+	0.75	0.68	3.0	188	
6_3^+	4_1^+	0.99	1.17	64.0	0.58	1.5(5)
8_1^+	6_1^+	1.16		26.0	1.50	
8_2^+	6_3^+	0.91		8.0	16.4	
8_3^+	6_1^+	1.57	1.53	14.0	0.7	1.3(4)
10_1^+	8_1^+	1.16		8.0	5.0	
	8_2^+	0.87		17.0	9.7	
	8_3^+	0.75	0.74	128.0	2.9	0.6(2)
12_1^+	10_1^+	1.00	0.87	164.0	1.0	0.7(3)
11_1^-	9_1^-	1.19	1.24	28.0	1.0	0.7(3)
				$B(E1)$		
3_1^-	2_1^+	1.20	1.10	3.2	1.5	0.65(25)
7_1^-	6_1^+	1.36	0.81	0.6	20	> 3.5
				$B(M1)$		
6_2^+	6_1^+	0.24	0.38	0.24	4.2	$1.2^{+1.3}_{-0.5}$
8_1^-	7_1^-	0.22	0.08	0.18	720	850
9_1^-	8_1^-	0.10	0.26	0.10	31	> 1

Table 7. Components of the wave functions for some of the ^{112}Sn states

$$|2_1^+\rangle = 0.95|[2_1]_2^1\rangle + 0.25|[2_1]_2^2\rangle + \dots$$
$$|4_1^+\rangle = 0.72|[2_1]_4^2\rangle + 0.26|[2_1]_4^3\rangle + 0.53|[4_1]_4^1\rangle$$
$$-0.12|[4_2]_4^1\rangle - 0.21|[4_3]_4^1\rangle - \dots$$
$$|6_3^+\rangle = 0.70|[2_1]_6^3\rangle + 0.31|[2_1]_6^4\rangle$$
$$- 0.28|[6_1]_6^1\rangle - 0.29|[6_2]_6^1\rangle$$
$$+ 0.24|[2_1]_2^1[4_1]_4^1\rangle - 0.18|[2_1]_2^1[4_2]_4^1\rangle$$
$$- 0.24|[2_1]_2^1[4_5]_4^1\rangle - \dots$$
$$|8_3^+\rangle = 0.55|[2_1]_8^4\rangle + 0.26|[2_1]_8^5\rangle$$
$$- 0.32|[2_1]_4^2[4_1]_4^1\rangle - 0.21|[2_1]_4^2[4_2]_4^1\rangle$$
$$- 0.17|[2_1]_4^2[4_3]_4^1\rangle - 0.35|[2_1]_4^2[4_5]_4^1\rangle$$
$$+ 0.53|[2_1]_2^1[6_1]_6^1\rangle + \dots$$
$$|10_1^+\rangle = 0.53|[2_1]_{10}^5\rangle + 0.23|[2_1]_{10}^6\rangle$$
$$+ 0.33|[2_1]_6^3[4_1]_4^1\rangle - 0.33|[2_1]_6^3[4_5]_4^1\rangle$$
$$- 0.22|[2_1]_6^3[4_3]_4^1\rangle + 0.58|[2_1]_4^2[6_1]_6^1\rangle + \dots$$

$8^+ \to 6_2^+$ with $E_\gamma = 1151.3$ keV and $8^+ \to 6_1^+$ with $E_\gamma = 1528.8$ keV. The latter cannot be distinguished in the observed γ spectrum from the γ transitions with energies $E_\gamma = 1151.9$ and 1527.2 keV identified as $10^- \to 8^-$ and $4_3^+ \to 2_1^+$, respectively. However, the lower limit for $B(E2; 8^+ \to 6_3^+)$ is estimated to be 0.129 e^2 b^2, but it already fits quite well into the vibrational views of the ^{112}Sn spectrum. Similarly, the short lifetime of the 10^+ state is probably attributable to the deexcitation to the 8^+ states that have not been identified in the spectrum, but are genetically related to the $6_{1,2}^+$ states. The transition probability can be low, but the high transition energy ensures the short lifetime of the intruder 10^+ state.

But why does the spectrum of intruder states resemble the main band of xenon rather than tin? This can be understood if it is considered that the energy of the two-phonon mode in the tin isotopes is close to the energy of the two-quasiparticle state; in these cases, a strong coupling arises between the collective and noncollective degrees of freedom [34, 35], which leads to noticeable distortions in the level spectrum. The results of the implementation [32, 33] of this

Table 8. Calculated energies E_γ (in MeV), $B(E2)$ (in $e^2\,\mathrm{b}^2 \times 10^{-3}$), $B(E1)$ (in $e\,\mathrm{fm}^2 \times 10^{-4}$), and lifetimes T (in ps) of the ^{114}Sn states in comparison with the experimental data

J_i^π	J_f^π	E_γ		$B(E2), B(E1)$	T	
		calc.	expt.	calc.	calc.	expt.
				$B(E2)$		
2_1^+	0_1^+	1.14	1.30	46.0	0.48	0.45(15)
4_1^+	2_1^+	0.80	0.89	80.0	1.73	>2.0
4_2^+	2_1^+	1.40	1.31	4.0	5.3	2.0^{+2}_{-1}
4_3^+	2_1^+	1.87	1.47	3.0	4.0	1.8(7)
6_1^+	4_1^+	0.84	1.00	111.0	0.74	$3.1^{+0.9}_{-0.5}$
	4_2^+	0.24	0.57	22.0	3.6	$1.4^{+0.6}_{-0.4}$
8_1^+	6_1^+	0.97	0.68	138	1.47	0.90(25)
10_1^+	8_1^+	1.01	0.80	170	0.84	$0.7^{+0.3}_{-0.2}$
12_1^+	10_1^+	1.09	0.88	185		
				$B(E1)$		
3_1^-	2_1^+	1.20	0.98	4.2	1.6	$2.5^{+1.5}_{-1.0}$

program in terms of DCM are presented in Fig. 26 and Table 6. Comparison with the experimental data indicates that DCM reproduces all characteristic features of the spectrum, while the calculated total lifetimes of the levels, including all ways of their deexcitation, are in good agreement with the experimental data. To illustrate how complex the dynamics of the observed phenomenon is, Table 7 presents the component composition of the wave functions for some of the ^{112}Sn states. Recall that $|[\lambda_i]^N_J[\lambda_j]^M_L\rangle$ means that the vector has a component composed of N phonon vectors $[\lambda_i]$ with total angular momentum J and M phonon vectors $[\lambda_j]$ with total angular momentum L. The index on the multipolarity denotes the solution number in the harmonic approximation. The weight of the collective components changes sharply twice, at $J^\pi = 4^+$ and 8^+. This double resonance is responsible for the observed deviations in the spectrum from the vibrational pattern.

We also performed similar calculations for ^{114}Sn. The results are presented in Fig. 27 and Table 8. As we see, the agreement with the experimental data is also quite satisfactory here.

Two facts have engaged our attention. First, the low-lying 0_2^+ state appeared in the ^{114}Sn spectrum, which is at a fairly high excitation energy in ^{112}Sn. This is because there is a strong competition in the ^{112}Sn isotope between the diagrams with $\Delta N = 1$ and $\Delta N = 3$; therefore, the position of the 0_2^+ state is highly sensitive to the chosen constant of spin–orbit forces; in heavier isotopes, there is no such sensitivity to the choice of parametrization. Second, the calculated positions of the noncollective 6_i^+ states and the genetically related 8_i^+ states rose sharply when passing to ^{114}Sn. Hence, the lifetimes of the intruder states in this isotope are determined to a larger degree by the transitions in the band. Since $B(E2; 2_1^+ \to 0_1^+)_{112}$ is almost equal to $B(E2; 2_1^+ \to 0_1^+)_{114}$, the values of $B(E2)$ for ^{114}Sn calculated from the measured lifetimes of the intruder states are lower than those of $B(E2)$ for ^{112}Sn. This conclusion, which can be reached without any calculations using DCM, is based only on the hypothesis about the vibrational nature of the intruder states. It was completely confirmed by the experimental results, as demonstrated by Fig. 25*b*, although the experimental error is so large that any model can actually fit into the error limits.

4.3. The ^{150,152,154}Sm Isotopes

This is the best-studied chain of isotopes that contains spherical, transition, and deformed nuclei. Figure 28 shows the calculated (in DCM [36]) and experimental spectra of these nuclei in comparison with two more well-known theoretical approaches: the six-boson expansion of the fermion operators by Tamura *et al.* [37] (TKB) and the adiabatic approximation by Kumar and Baranger [38] (KB).

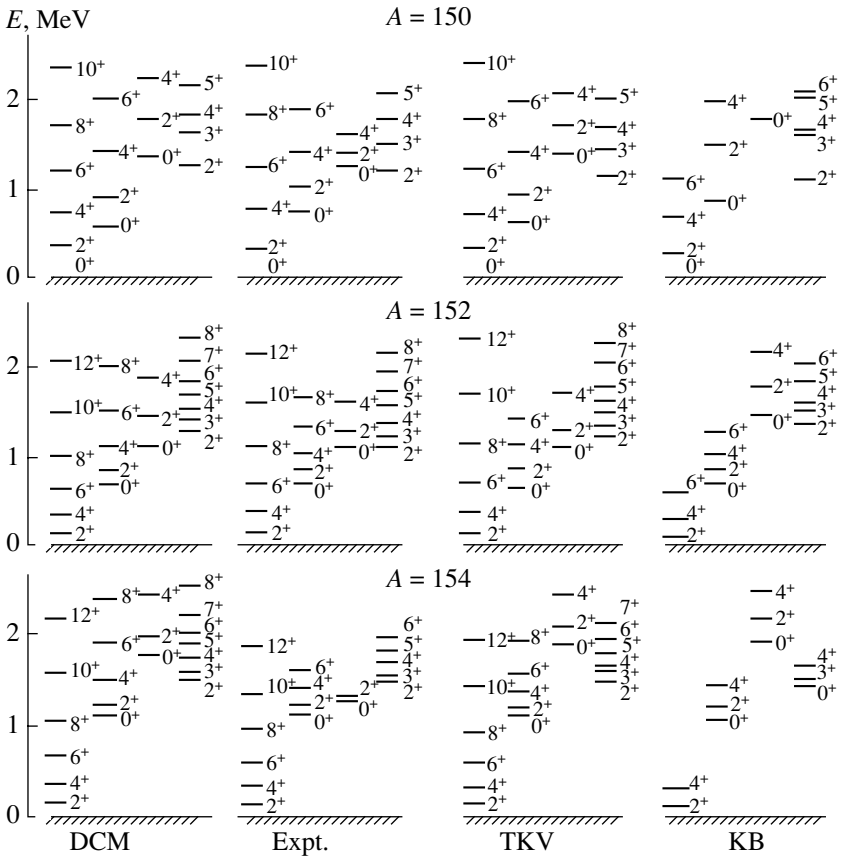

Fig. 28. Spectra of excited ^{150,152,154}Sm states calculated in DCM, TKV, and KB in comparison with the experimental data.

First of all, the remarkable similarity between the DCM and TKB results is immediately apparent, although these two approaches differ significantly in formulation (see below for a discussion). However, the main thing is that DCM with the chosen neutron ζ^- constant of spin–orbit forces, which varies within a very narrow range in these isotopes, from 0.290 to 0.305, allows the passage from the vibrational pattern of the spectrum to its rotational pattern to be described without introducing rotational degrees of freedom.

Analysis of the results of our calculations revealed two phenomena that deserve rapt attention.

First, the spectra of the samarium isotopes become similar at fairly high angular momenta and excitation energies, as do the transition probabilities. This is demonstrated by Fig. 29*a*, in which the ratio $\Delta E(J)_{152}/\Delta E(J)_{150}$, where $\Delta E(J) = E(J) - E(J-2)$, and the ratio of the calculated values of $B(E2; J \to J-2)$ for these isotopes are plotted against the spin of the yrast state. As we see, these ratios tend to unity as the angular momentum increases. However, the most striking thing is that the wave functions also become similar, for example,

$$|12_1^+\rangle_{150} = 0.72|[2_1]_{12}^{6.1}\rangle - 0.59|[2_1]_{12}^{7.1}\rangle - 0.26|[2_1]_{12}^{8.2}\rangle + \ldots,$$

$$|12_1^+\rangle_{152} = 0.58|[2_1]_{12}^{6.1}\rangle - 0.63|[2_1]_{12}^{7.1}\rangle - 0.36|[2_1]_{12}^{8.2}\rangle + \ldots.$$

At the same time, at low angular momenta, even the principal components differ:

$$|2_1^+\rangle_{150} = 0.82|[2_1]_2^{1.1}\rangle - 0.41|[2_1]_2^{2.1}\rangle - 0.23|[2_1]_2^{4.2}\rangle + \ldots,$$

$$|2_1^+\rangle_{152} = 0.39|[2_1]_2^{3.1}\rangle - 0.33|[2_1]_2^{2.1}\rangle - 0.34|[2_1]_2^{4.2}\rangle + \ldots.$$

Recall that, for example, $|[2_1]_{12}^{8.2}\rangle$ denotes the second eight-phonon doublet—the first with a total angular momentum of 12. The presented results suggest that the nucleus loses its individuality and resembles a heated liquid drop at a fairly large number of excited quasiparticles. Is this characteristic of all nuclei, given the correction for their phase volume? To answer this question, we note that, as our calculations show, the spectra become similar at $J \sim A/10$; if the hypothesis is valid, then the energy intervals in

Table 9. Experimental and calculated values of $B(E2; J_i \to J_f)$ (in e^2 b^2) for the samarium isotopes

J_i	J_f	Expt.	DCM	TKV	KB
		^{150}Sm			
2_1	0_1	270(10)	290	280	230
4_1	2_1	530(60)	530	510	430
6_1	4_1		860	640	560
0_2	2_1	260(30)	490	420	330
2_2	0_1	3.6(1.4)	15	20	3
	2_1	43(20)	176	181	2
	4_1	166(98)	205	77	90
	0_2	560(310)	270	190	140
4_2	2_2		500	350	300
2_3	0_1	8.8(2.0)	12	20	10
	2_1	39(14)	71	24	125
	4_1	19(10)	90	87	34
		^{152}Sm			
2_1	0_1	670(20)	700	670	650
4_1	2_1	1020(10)	990	980	990
6_1	4_1	1180(30)	1090	1090	1190
8_1	6_1	1390(140)	1160	1110	–
10_1	8_1	1550(150)	1180	–	–
0_2	2_1	176(11)	42	120	200
2_2	0_1	4.6(0.3)	2	7	3
	2_1	26(3)	5	25	28
	4_1	98(18)	24	70	137
4_2	2_1	5.3(3.5)	1	5	0
	4_1	37(23)	11	16	27
	6_1	100(57)	39	47	–
2_3	0_1	16(1)	36	50	22
	2_1	42(4)	67	53	51
	4_1	4.2(0.3)	10	6	3
4_3	2_1	3.5(0.2)	12	26	8
	4_1	37(1)	74	76	49
		^{154}Sm			
2_1	0_1	922(40)	880	880	940
4_1	2_1	1210(70)	1230	1250	1400
6_1	4_1	1410(60)	1350	1350	–
8_1	6_1	1570(100)	1420	1380	–
10_1	8_1	1600(150)	1410	–	–
0_2	2_1		9	54	235
2_2	0_1	6.0(1.4)	1	1	13
	2_1	12(3)	5	25	28
	4_1	98(18)	1	10	54
2_3	0_1	13(3)	35	21	33
	2_1	20(4)	68	47	47
	4_1	0.8(0.3)	12	0	10

Table 10. Experimental and calculated values of $|\delta| = T(M1)/T(E2)$ for the transitions with $\Delta J = 0$ in ^{152}Sm

J_i	J_i	Expt.	DCM
2_2	2_1	$13^{+\infty}_{-7.9}$	36.0
2_3	2_1	-27^{+11}_{-56}	25.0
4_2	4_1	6^{+4}_{-2}	4.1
4_3	4_1	-6^{+2}_{-19}	9.8

the yrast band corresponding to these spins must be described well by the liquid-drop parametrization

$$\Delta E|_{J\sim A/10} \sim \text{const}/\sqrt{A}.$$

The systematics of experimental data for the nuclei from the region $A = 100-180$, shown in Fig. 29*b*, confirms the aforesaid. Here, not the description itself, but the fact that the microscopic calculations lead to this is striking.

Second, let us look carefully at the spectrum of the γ band in ^{152}Sm. This is a typical rotational band. However, if we look at the calculated values of $B(E2)$ in it, then it comprises, as it were, two nested bands with odd and even spins. Thus, for example, for this isotope, $B(E2; 5^+_\gamma \to 4^+_\gamma) = 0.040\ e^2$ b^2, while $B(E2; 5^+_\gamma \to 3^+_\gamma) = 0.55\ e^2$ b^2. At the same time, the ratio of the values considered in the rotational model differs little from unity. Perhaps our results follow from the neglect of the role of the diagrams with $\Delta N = 2$, but what does the experiment say? It turns out that virtually no transitions with $\Delta J = 1$ in the γ band are observed in the experimental γ spectra if the base of the γ band is at a higher energy than the base of the β band (note that the $M1$ component must also be present in the $5^+_\gamma \to 4^+_\gamma$ transition, although, as our calculations show, it is insignificant). In those cases where these transitions are observed, the uncertainty in the experimental information is so large that no conclusions can be reached. As an example, let us consider ^{152}Sm. The transition with $E_\gamma = 148.01$ keV identified precisely as the $3^+_\gamma \to 2^+_\gamma$ deexcitation is observed in the γ-ray spectrum. However, at least three ways of placing this γ transition can be found in the ^{152}Sm level diagram. The most interesting placement corresponds to the possible deexcitation of the $(1^+, 2^+)$ state with $E = 2294.1$ keV to the state with $E = 2146$ keV whose spin is uncertain. In turn, this state can be deexcited via the observed γ transition with $E_\gamma = 616.05$ keV to the 2^- state with $E = 1529.8$ keV and the observed γ transition with $E_\gamma = 852.8$ keV to the 2^+ state with $E = 1292.8$ keV. All these states have rich branchings, including the direct deexcitation to the base of

Table 11. Calculated and experimental ratios $R = B(E2; J_i \to J_{f1})/B(E2; J_i \to J_{f2})$ for ^{152}Sm

J_i	J_{f1}	J_{f2}	DCM	TKB	KB	IBM [43]	Expt. [46]	Expt. [43]
2_2	0_2	0_1	66	69	236	890		107
	0_2	2_1	45	3		18		20
	4_1	2_1	5		5	2	3	4
4_2	2_1	4_1	0.1	0.3	0.01	0.01	0.1	0.1
	2_2	4_1	65	39	41	18	41	37
2_3	2_1	0_1	2	1	2	1	2	2
	2_1	4_1	8	9	20	1	12	9
	0_2	0_1	0.2	0.4	1	0.7	–	0.02
	2_2	2_1	0.1	2.6	1	31	1	3
	0_2	2_2	0.1	0.3	0.02	0.02	–	0.005

the γ band. This means that the γ transition with $E_\gamma = 148.01$ keV under discussion will also be seen in the spectrum of the coincidences with the γ deexcitation of the base of the γ band. Most sadly, the described situation is typical of the accumulated experimental information (we will turn to this isotope below).

However, let us return to DCM and the description of the transition probabilities. Table 9 gives the available experimental data on the $E2$-transition probabilities in ^{150,152,154}Sm and the results of the calculations by various authors. Before we turn to a comparison, let us make several general remarks. The experimental data for the absolute values of $B(E2)$ obtained by various authors often differ markedly even at small errors. On the other hand, the theoretical models cannot purport to describe weak transitions, since a small admixture in the wave function uncontrollable by the theory can affect significantly the calculated values of $B(E2)$ without affecting the description of other nuclear characteristics. If all of this is kept in mind, then a comparison shows that both DCM and TKB describe the observational data equally successfully and are similar. However, there are appreciable discrepancies with the experimental data. They all concern the transitions with $\Delta J = 1$ in the γ band, but this has already been discussed above.

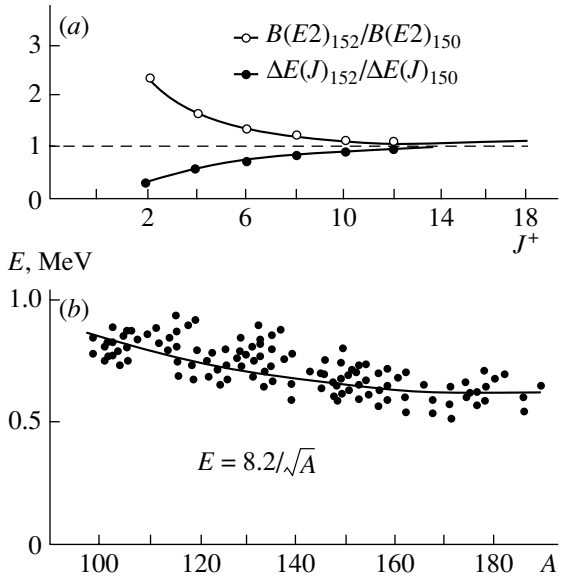

Fig. 29. (a) Calculated (in DCM) ratios $\Delta E(J)_{152}/\Delta E(J)_{150}$ of the energy intervals $\Delta E(J) = E(J) - E(J-2)$ in the yrast band and ratios $B(E2; J \to J-2)$. (b) Systematics of the intervals $\Delta E(J) = E(J) - E(J-2)$ at $J \sim A/10$ and the hydrodynamic limit.

One curious feature has been revealed for the ratios of the interband $E2$ transitions: the ratio $B(E2; J_\gamma \to J_g - 1)/B(E2; J_\gamma \to J_g + 1)$ for the odd spins of the γ band and the ratio $B(E2; J_\gamma \to J_g)/B(E2; J_\gamma \to J_g - 2)$ for the even spins depend only slightly on the structure of the wave function (except the first two states), reflecting the geometry rather than the dynamics to a larger degree. This is demonstrated by Fig. 30, which shows the various experimental ratios of the interband $E2$-transition probabilities for nuclei from a wide mass region (dots) and the expected values from the calculations (shaded zones) without any detailed fitting to the excitation spectra of a large group of nuclei.

A few words should be said about the $M1$ angular momenta. As with the $E2$ transitions, the $M1$ transitions were calculated in the approximation of the main diagrams. It emerged that, in view of the peculiarity of the geometry, the values of $B(M1)$ for transitions

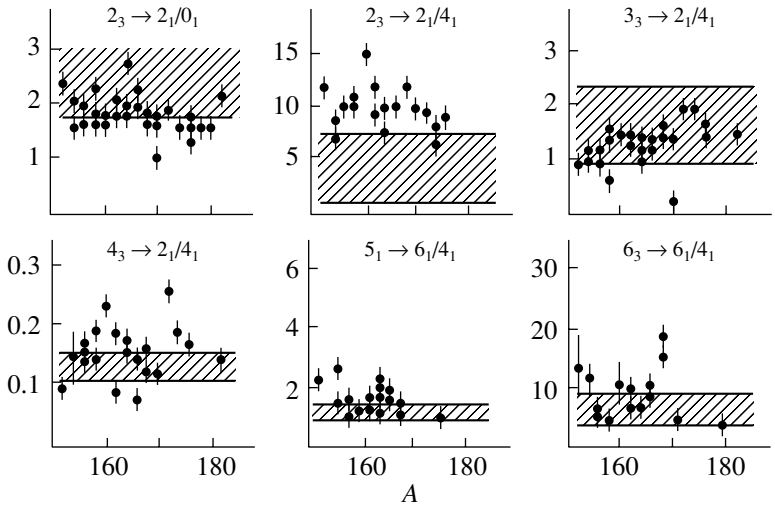

Fig. 30. Systematics of the ratios of the probabilities of $E2$ transitions from γ-band levels to states of the main band (dots) and expected values in DCM (shaded zones). $5_1 \to 6_1/4_1$ denotes $B(E2; 5_\gamma \to 6_g)/B(E2; 5_\gamma \to 4_g)$.

with the spin changed by one prove to be less than $10^{-3}\ \mu^2_{\rm nucl}$, and an accurate allowance for the Pauli corrections becomes important for these transitions. Since the experimental data on the $M1$ transitions contain a significant uncertainty, we did not venture to undertake this large work. At the same time, for transitions without any change in the spin, the calculated probabilities prove to be significant, and their comparison with the experimental data is quite legitimate. Some of the results of this kind are presented in Table 10 for ^{152}Sm. As we see, the agreement with the experimental data is quite satisfactory.

As regards the description of the g factors for excited states, curious features have been found here. First, as the magic number of neutrons is approached, the g factor of the 2^+_1 state decreases in accordance with the experimental data (Fig. 31) rather than increasing, as is commonly the case. This is because $[1g_{7/2}]^2$, the proton configuration with a low $M1$ angular momentum, becomes the main component in the wave function of the 2^+_1 state. Second, as the angular momentum of the excited state of the band increases, the g factor also decreases, although slowly. This is demonstrated by Fig. 31, which presents the results of our calculations in comparison with the experimental data. The reason again lies in the fact that, at high angular momenta, the phonons in all samarium isotopes become similar and weakly collective and have a small g factor.

As regards the description of the quadrupole moments, our calculations in DCM describe excellently the experimental data as a function of the mass number (Fig. 31). It turned out that, as the angular momentum of the excited state of the yrast band increases, the quadrupole moment of the state decreases in absolute value. This is a purely Pauli effect: as the angular momentum increases, the phonons become progressively less collective. In weakly collective nuclei, the quadrupole moment usually initially increases with angular momentum. At the same time, in any version of the boson model and in any version of the rotational model, the quadrupole moment of the states of the yrast band increases with angular momentum up to $J \sim J_{\max}/2$. The following exper-

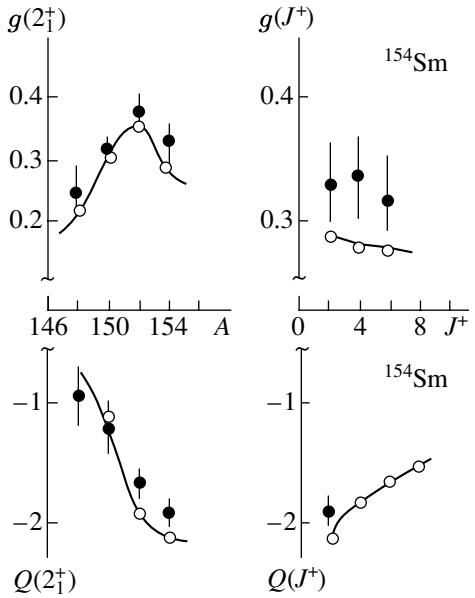

Fig. 31. Calculated (in DCM) dependences of the g factors and quadrupole moments on the mass number and on the spin of the excited state. The closed circles represent the experimental data.

iment then suggests itself to answer the question about the existence of rotational degrees of freedom in nuclei at low angular momenta and excitation energies: measuring $Q(4_1^+)/Q(2_1^+)$ in a particular strongly collective nucleus with a high accuracy. If this ratio is less than unity, then it will no longer be pertinent to talk about deformation.

The samarium isotopes were studied in [39] and in the interacting boson model. However, these eight-parameter calculations yielded results that were in poorer agreement with the experimental data than those presented above. As regards the ^{152}Sm isotope, it has aroused heightened interest in recent years [40–45]. It was noticed that the states near the 0_2^+ level remarkably resemble the level spectrum of a weakly split harmonic oscillator, while some of the newly measured [43] γ-transition probabilities differed significantly from previous results. The idea that we have to deal with the existence of a spherical shape in a deformed nucleus arose, and various kinds of calculations were performed [42–45], in particular, in terms of IBM [43]. The experimentally observed fact that the $2_3^+ \to 0_2^+$ transition is greatly hindered, which is obtained in the IBM calculations in a very narrow range of parameters of the Hamiltonian, attracted particular attention; however, the level spectrum for the β band at these parameters is described poorly. Table 11 presents some of the ratios of the $E2$-transition probabilities calculated using DCM, TKB, KB, and IBM [43] in comparison with the experimental data. The comparison shows that both DCM and TKB describe much better the experimental situation as a whole, including the fact that the $2_3^+ \to 0_2^+$ transition is hindered relative to other transitions, although they exceed the experimental value by more than an order of magnitude (remaining less than the single-particle estimate in magnitude). However, as we have already noted above, the theory cannot purport to describe such weak transitions in principle. Therefore, we have no reason to attach crucial importance of the information to the $2_3^+ \to 0_2^+$ transition with respect to other data. (The work [46] was the main source of experimental data on the samarium isotopes.)

5. CONCLUSIONS

The basic research by V.G. Solov'ev and his disciples on the quasiparticle–phonon model has shown that many phenomena in nuclear spectroscopy can be described in terms of this model both at low excitation energies and in the continuum spectral range. The relative simplicity of the model allowed the level of its underlying approximations to deepen step by step. As a result, we arrived at the dynamical collective model. The basis vectors in DCM, quasiparticles and phonons, are constructed for each specific spin–parity and the numbers of phonons, and quasiparticles by minimizing the total Hamiltonian in phonon and quasiparticle amplitudes on these vectors rather than a particular part of it and, naturally, by taking into account the Pauli exclusion principle. We construct an ordered basis. Therein lies the first fundamental difference between DCM and many other similar (in many respects) models. The second fundamental difference between DCM and the existing approaches lies in allowance for the vacuum fluctuations to renormalize the effective forces. As a result, it proved to be possible to uniformly describe the states near the yrast band in a wide mass region of spherical, transition, and deformed nuclei by varying only the constant of spin–orbit forces without invoking the concept of static nuclear deformation.

Our calculations revealed a number of model-independent phenomena and the relativistic nature of the spin–orbit forces and raised questions of fundamental importance in developing the theory further for an experiment.

And in closing, we formulated the ideas set out in this paper back in 1975 [47]. However, it took fifteen years to approach the calculations of specific even–even nuclei. And we are still halfway. This is depressing. However, if we look at the active studies [48] of complex atoms in atomic and molecular physics, then we will see that researchers in these fields have just embarked on studying the role of the diagrams that have been analyzed in detail in nuclear physics since the mid-1970s. This is encouraging.

ACKNOWLEDGMENTS

Many researchers have helped me in implementing the program over many years at different stages of this work. I am grateful to all of them.

REFERENCES

1. V. G. Neudatchin and Yu. F. Smirnov, *Nucleon Associations in Light Nuclei* (Nauka, Moscow, 1968) [in Russian].
2. A. B. Migdal, *Theory of Finite Fermi Systems and Applications to Atomic Nuclei* (Nauka, Moscow, 1983; Interscience, New York, 1967).
3. G. F. Filippov, V. I. Ovcharenko, and Yu. F. Smirnov, *Microscopical Theory of Collective Excitations of Atomic Nuclei* (Naukova Dumka, Kiev, 1981) [in Russian].
4. V. G. Solov'ev, *Theory of Atomic Nuclei* (Énergoatomizdat, Moscow, 1989; Institute of Physics, Bristol, 1992).
5. A. Poves and A. Zuber, Phys. Rep. **70**, 236 (1981).

6. V. Yu. Gonchar, Yad. Fiz. **43**, 1409 (1986) [Sov. J. Nucl. Phys. **43**, 907 (1986)].
7. A. Bohr and B. R. Mottelson, *Nuclear Structure* (Benjamin, New York, 1975; Mir, Moscow, 1977), Vols. 1, 2.
8. R. K. Sheline, Rev. Mod. Phys. **32**, 1 (1960).
9. M. Sakai, Nucl. Phys. A **104**, 301 (1967).
10. S. T. Belyaev and V. G. Zelenevskiĭ, Zh. Éksp. Teor. Fiz. **42**, 1590 (1962) [Sov. Phys. JETP **15**, 1104 (1962)]; A. Arima and F. Iachello, Ann. Phys. (N.Y.) **99**, 253 (1976); R. V. Dzholos *et al.*, Fiz. Élem. Chastits At. Yadra **16**, 280 (1985) [Sov. J. Part. Nucl. **16**, 121 (1985)].
11. K. Hara, Prog. Theor. Phys. **32**, 88 (1964).
12. K. Ikeda *et al.*, Prog. Theor. Phys. **33**, 22 (1965).
13. R. V. Jolos and W. Rybarska, Preprint No. E4-5578, OIYaI (Joint Institute for Nuclear Research, Dubna, 1971).
14. V. E. Mitroshin, Preprint No. 206, LIYaF (Leningrad Institute of Nuclear Physics, Gatchina, 1976).
15. G. B. Krygin, V. E. Mitroshin, and I. G. Fisenko, in *Proceedings of 38th Conference on Nuclear Spectroscopy and Nuclear Structure, Baku, 1988*, p. 207.
16. A. Kuriyama *et al.*, Prog. Theor. Phys. **45**, 784 (1971); **47**, 498 (1972).
17. V. E. Mitroshin, Preprint No. 74, LIYaF (Leningrad Institute of Nuclear Physics, Gatchina, 1973); Izv. Akad. Nauk SSSR, Ser. Fiz. **38**, 2070 (1974); **39**, 93 (1975).
18. J. Kasagi and H. Ohnuma, J. Phys. Soc. Jpn. **45**, 1099 (1978).
19. Yu. P. Gangrinskiĭ, Fiz. Élem. Chastits At. Yadra **9**, 344 (1978) [Sov. J. Nucl. Phys. **9** (1978)].
20. V. E. Mitroshin, Preprint No. 563, LIYaF (Leningrad Institute of Nuclear Physics, Gatchina, 1980).
21. C. P. Browne *et al.*, Phys. Rev. C **9**, 1831 (1974).
22. O. D. Kovrigin and V. E. Mitroshin, Izv. Akad. Nauk SSSR, Ser. Fiz. **47**, 2231 (1983).
23. S. M. Abecasis *et al.*, Phys. Rev. C **9**, 2320 (1974).
24. V. E. Mitroshin, Preprint No. 98, LIYaF (Leningrad Institute of Nuclear Physics, Gatchina, 1974); Izv. Akad. Nauk SSSR, Ser. Fiz. **40**, 126 (1976).
25. V. S. Zvonov and V. E. Mitroshin, Preprint No. 353, LIYaF (Leningrad Institute of Nuclear Physics, Gatchina, 1977); Izv. Akad. Nauk SSSR, Ser. Fiz. **42**, 2 (1978).
26. K. I. Erokhina and V. E. Mitroshin, Preprint No. 469, LIYaF (Leningrad Institute of Nuclear Physics, Gatchina, 1979); Izv. Akad. Nauk SSSR, Ser. Fiz. **45**, 37 (1981).
27. T. Kato, *Perturbation Theory for Linear Operators* (Springer-Verlag, Berlin, 1976; Mir, Moscow, 1972).
28. V. E. Mitroshin, Preprint No. 441, LIYaF (Leningrad Institute of Nuclear Physics, Gatchina, 1978); Izv. Akad. Nauk SSSR, Ser. Fiz. **44**, 986 (1980).
29. B. F. Beĭman, *Lectures on Applications of the Group Theory in Nuclear Spectroscopy* (Fizmatgiz, Moscow, 1961) [in Russian].
30. J. Adam *et al.*, Z. Phys. A **332**, 143 (1989).
31. G. B. Krygin and V. E. Mitroshin, in *Proceedings of 41st Conference on Nuclear Spectroscopy and Nuclear Structure, Leningrad, 1991*, p. 147.
32. I. N. Vishnevskiĭ *et al.*, Ukr. Fiz. Zh. **36**, 982 (1991).
33. I. N. Vishnevskiĭ *et al.*, Ukr. Fiz. Zh. **36**, 1132 (1991).
34. A. I. Vdovin and Ch. Stoyanov, Izv. Akad. Nauk SSSR, Ser. Fiz. **38**, 2598 (1974).
35. V. E. Mitroshin, Izv. Akad. Nauk SSSR, Ser. Fiz. **38**, 811 (1974).
36. G. B. Krygin and V. E. Mitroshin, in *Proceedings of 41st Conference on Nuclear Spectroscopy and Nuclear Structure, Leningrad, 1991*, p. 149.
37. T. Tamura *et al.*, Phys. Rev. C **20**, 307 (1979).
38. K. Kumar and M. Baranger, Nucl. Phys. A **110**, 529 (1968); **231**, 189 (1974).
39. M. M. King Yen *et al.*, Phys. Rev. C **29**, 688 (1984).
40. R. F. Casten *et al.*, Phys. Rev. C **57**, R1553 (1998).
41. F. Ichello, N. V. Zamfir, and R. F. Casten, Phys. Rev. Lett. **81**, 1191 (1998).
42. R. F. Casten, D. Kusnezov, and N. V. Zamfir, Phys. Rev. Lett. **82**, 5000 (1999).
43. N. V. Zamfir *et al.*, Phys. Rev. C **60**, 054312 (1999).
44. J. Jolie, P. Cejnar, and J. Dobes, Phys. Rev. C **60**, 061303 (1999).
45. Jing-ye Zhang *et al.*, Phys. Rev. C **60**, 061304 (1999).
46. R. B. Begzhanov, V. M. Belen'kiĭ, I. I. Zalyubovskiĭ, and A. V. Kuznichenko, *Handbook on Nuclear Physics* (Fan, Tashkent, 1989), Vol. 1 [in Russian]; L. K. Peker, Nucl. Data Sheets **58**, 93 (1989).
47. V. E. Mitroshin, Preprint No. 152, LIYaF (Leningrad Institute of Nuclear Physics, Gatchina, 1975).
48. V. A. Dzyuba *et al.*, Zh. Éksp. Teor. Fiz. **114**, 1636 (1998) [JETP **87**, 885 (1998)].

Translated by V. Astakhov

Physics of Atomic Nuclei, Vol. 68, No. 8, 2005, pp. 1352–1371. Translated from Yadernaya Fizika, Vol. 68, No. 8, 2005, pp. 1407–1426.

NUCLEI
Theory

Employing a Spheroidal Global Potential to Estimate the Quadrupole Deformation of Nuclei

B. S. Ishkhanov and V. N. Orlin

Institute of Nuclear Physics, Moscow State University, Vorob'evy gory, Moscow, 119899 Russia

Received May 11, 2004

Abstract—A spheroidal global shell potential is constructed on the basis of the optical model whose global parameters are extracted from experimental data on nucleon–nucleus scattering. This potential is used to estimate the quadrupole deformation of a large number of light, intermediate, and heavy nuclei in the mass-number range $10 \lesssim A \lesssim 240$. The results are compared with the results of similar calculations for the Nilsson potential and with the estimates of the quadrupole deformation that follow from data on the static quadrupole moments of the nuclei considered in the present study. © *2005 Pleiades Publishing, Inc.*

1. INTRODUCTION

A microscopic description of nuclear shapes is usually based on one of two approaches, that which involves calculating a mean self-consistent field of the Skyrme–Hartree–Fock type (see, for example, [1–3]) or that which involves introducing an anisotropic shell-model potential and finding an equilibrium nuclear deformation by minimizing the sum of single-particle nucleon energies $E_{\text{s.p.}}$ (see, for example, [4, 5]).

It seems that the first of these methods is more justified. However, calculations of a mean self-consistent field yield results that depend strongly on the choice of parameters of the nuclear Hamiltonian, to say nothing of the intricacy of the underlying mathematical procedure itself. In view of this, rather simple calculations of a quadrupole nuclear deformation δ on the basis of the single-particle shell model are still appealing.

Calculations in which an oscillating term $\delta E_{\text{s.p.}}$ [6–9] is isolated in the sum of single-particle energies $E_{\text{s.p.}}$ belong to the same type. This oscillating term is treated as a shell correction to the macroscopic energy E_{macro} of the nucleus being considered, and it can be calculated, for example, by the semiempirical Weizsäcker mass formula. As a result, one minimizes the improved total energy $E_{\text{tot}} = E_{\text{macro}} + \delta E_{\text{s.p.}}$ of the nucleus rather than the single-particle energy $E_{\text{s.p.}}$. This relaxes significantly the requirements on the choice of anisotropic shell potential used in the calculations, because, in the case under consideration, it determines only those of the forces stabilizing the shape of a nucleus that are due to inhomogeneities in the single-particle spectrum [7, 10, 11].

With the aid of such calculations, it proved to be possible to explain the observed quadrupole deformations ($\delta \sim 0.2$–0.3) of the ground states of actinides and rare-earth elements [10, 12], to reveal the origin of isomeric states of strongly deformed ($\delta \sim 0.6$) actinide nuclei, and to describe some of those features of their fission that could not be reproduced within the macroscopic liquid-drop model without taking into account microscopic shell effects [11, 13].

However, it is illegitimate to apply this approach to describing the equilibrium shapes of light and medium-mass nuclei ($A < 100$), since details of the behavior of the single-particle-level scheme play an important role in this mass-number region. Moreover, the replacement of the single-particle energy by the total energy, $E_{\text{s.p.}} \to E_{\text{tot}}$, does not guarantee a correct inclusion of the residual-force effect on the nuclear-deformation process. In particular, this replacement does not take into account the effect of pairing forces, which, as is well known, render closed spherical shells more stable.

The effect of pairing interaction on the quadrupole deformation of medium-mass and heavy nuclei was considered in [14], where, in calculating the sum of $E_{\text{s.p.}}$, the single-particle energies in the Nilsson potential [4] were replaced by quasiparticle energies. These calculations revealed that pairing forces lead to a decrease in the equilibrium deformation of nuclei and facilitate an earlier transition to the spherical shape as one approaches filled shells.

In order to describe quadrupole deformations of nuclei, a method that combines both main approaches was chosen in [15]: a specific anisotropic shell potential, the Nilsson potential [4], was used in the calculations, while the equilibrium nuclear

1063-7788/05/6808-1352$26.00

deformation was found from the condition requiring that the shape of equipotential surfaces be matched with the shape of the nucleon-density distribution rather than from the condition requiring that the sum of the single-particle energies $E_{\text{s.p.}}$ be minimal. It was additionally assumed that, for modest variations in the nuclear shape, single-particle orbitals associated with spherical magic numbers of nucleons always remained filled, undergoing adiabatic deformations. This made it possible to describe satisfactorily the quadrupole deformation of the majority of β-stable nuclei in the mass-number region $A > 16$. That it was impossible in the course of such calculations to discriminate between isomer and stationary shapes of the nuclear surface was a serious drawback of the method.

In the present study, we attempt to construct a realistic spheroidal shell potential that has global parameters (in the following, we refer to it as a spheroidal global potential) and which would make it possible to reproduce correctly deformation forces by minimizing the energy $E_{\text{s.p.}}$ without resort to the replacement of the single-particle energy by the total energy, $E_{\text{s.p.}} \to E_{\text{tot}}$. In constructing such a potential, we rely on the spherical optical Woods–Saxon potential involving global parameters that was described in [16]. The spheroidal global potential (SGP) introduced here differs by a number of important special features from the deformed Woods–Saxon potential that was used previously in [17] to estimate the equilibrium quadrupole and hexadecapole deformations of rare-earth and transuranic elements. Namely, a unified set of parameters for the spheroidal global potential over the entire mass-number range is used here in contrast to [17]. In addition, we consider arbitrary elliptic deformations of an axisymmetric nucleus (not only quadrupole and hexadecapole deformations) and take into account the dependence of the nuclear-surface diffuseness on angular variables (this is of particular importance in describing the deformations of light nuclei, whose radii are commensurate with the size of the surface-diffuseness region).

With the aid of the global potential obtained in the way outlined above, we calculate the quadrupole-deformation parameters δ for 90 nuclei in the mass-number range $10 \lesssim A \lesssim 240$. In order to reveal the effect of residual forces, we compare two versions of the calculation of equilibrium deformations—specifically, we fix the quantum numbers K and π (K is the spin projection onto the nuclear-symmetry axis, while π is the parity of the ground state of a nucleus) in the first and do not do this in the second version. Simultaneously, we perform calculations with the Nilsson potential [4].

2. SPHEROIDAL GLOBAL POTENTIAL

In order to construct the spheroidal global potential, we will consider only the real part of the optical potential from [16]. This real part involves a nuclear, a spin–orbit, and a Coulomb component,

$$\begin{aligned}\mathrm{Re}[V_{\text{opt}}(r,\varepsilon)] &= -U_1(\varepsilon) f_1(r) \\ &+ 4U_2 \frac{1}{r}\frac{df_2(r)}{dr}\mathbf{l}\cdot\mathbf{s} + V_{\text{Coul}}(r),\end{aligned} \tag{1}$$

where r is the radial component of spherical coordinates (r,θ,φ) of the scattered nucleon in the body reference frame, ε is its energy, $U_1(\varepsilon)$ is the depth of the nuclear potential, U_2 is the amplitude of spin–orbit forces, and

$$f_i(r) = \frac{1}{1+\exp[(r-R_i)/a_i]} \tag{2}$$

are the radial Woods–Saxon form factors for the nuclear and spin–orbit interactions ($R_i = r_i A^{1/3}$, $i = 1,2$). The Coulomb potential is taken in the form

$$V_{\text{Coul}}(r) = \begin{cases} 0.5(qZe^2/R_{\text{Coul}})[3-(r/R_{\text{Coul}})^2] & \text{for } r \le R_{\text{Coul}} \\ qZe^2/r & \text{for } r > R_{\text{Coul}}, \end{cases} \tag{3}$$

where $q = 0,1$ is the nucleon charge number; Z is the charge number of the target nucleus; and $R_{\text{Coul}} = 1.149A^{1/3} + 1.788A^{-1/3} - 1.163/A$ [fm] is its Coulomb radius, $A = Z + N$ being its mass number.

On the basis of an analysis of data on (n,n) and (p,p) reactions, the following global parameters for the optical model were chosen in [16] for the mass-number region $16 \le A \le 208$:

$$\begin{aligned}U_1(\varepsilon) &= 54.19 - 0.33\varepsilon + 0.4\frac{qZ}{A^{1/3}} \\ &- (-1)^q \frac{N-Z}{A}(22.7 - 0.19\varepsilon)\ [\text{MeV}],\end{aligned} \tag{4}$$

$r_1 = 1.198$ fm, $a_1 = 0.663$ fm, $U_2 = 6.2$ MeV, $r_2 = 1.01$ fm, and $a_2 = 0.75$ fm.

The sought spheroidal global potential must include, in just the same way as the input isotropic potential (1), three components:

$$V_{\rm SGP}(r,\theta) = \hat{V}_{\rm nucl}(r,\theta) + \hat{V}_{\rm spin-orb}(r,\theta) + \hat{V}_{\rm Coul}(r,\theta). \quad (5)$$

Let us consider each of these components individually.

2.1. Nuclear Potential

The radial dependence of the nuclear component of the potential in (1) is tightly correlated with the radial nuclear-matter-density distribution that is obtained in experiments that study fast-electron scattering (this is suggested by a close similarity of the corresponding radial form factors). In a deformed nucleus, the geometric form factor of the nuclear potential must depend not only on radial but also on angular variables. If the thickness of the diffuse layer of the nuclear surface is much smaller than the radius of the nucleus being considered, the variation in the shape of the mean nuclear field in response to a surface deformation can be taken into account by replacing the isotropic form factor $f_1(r) = \{1 + \exp[(r - R_1)/a_1]\}^{-1}$ by its anisotropic counterpart,

$$\hat{f}_1(r,\theta,\varphi) = \{1 + \exp[(r - \hat{R}_1(\theta,\varphi))/\hat{a}_1(\theta,\varphi)]\}^{-1}, \quad (6)$$

the condition that the gradient of the potential at the nuclear surface is constant being respected [9]:

$$(\mathrm{grad}\hat{f}_1)^2_{r=\hat{R}_1(\theta,\varphi)} = (\mathrm{grad}f_1)^2_{r=R_1} = \frac{1}{16a_1^2}. \quad (7)$$

From Eqs. (7), we find that the quantity $\hat{a}_1(\theta,\varphi)$, which characterizes the diffuseness of the nuclear surface, has the form

$$\hat{a}_1(\theta,\varphi) = a_1\left[1 + (\mathrm{grad}\hat{R}_1)^2_{r=\hat{R}_1(\theta,\varphi)}\right]^{1/2}. \quad (8)$$

The function $\hat{R}_1(\theta,\varphi)$ describes the equipotential surface (by convention, it can be referred to as the nuclear surface) at which the nuclear potential takes the value of $-0.5U_1(\varepsilon)$. We will assume that, in a deformed nucleus, this surface has the form of a spheroid and denote by c_1 and d_1 its semiaxes in, respectively, the direction of the symmetry axis z of the nucleus and the direction orthogonal to it; that is,

$$\hat{R}_1(\theta) = \left[\frac{\cos^2\theta}{c_1^2} + \frac{\sin^2\theta}{d_1^2}\right]^{-1/2}. \quad (9)$$

In view of the condition that the volume of the nucleus remains unchanged, $c_1 d_1^2 = R_1^3$, this relation can be recast into the form

$$\hat{R}_1(\theta) = R_1(1-\eta_1)^{1/6}(1-\eta_1\cos^2\theta)^{-1/2}, \quad (10)$$

where $\eta_1 = (c_1^2 - d_1^2)/c_1^2$ is a parameter that characterizes the nuclear deformation.

From relations (8) and (10), we find that, in a spheroidal nucleus, the nuclear-surface-diffuseness parameter is given by

$$\hat{a}_1(\theta) = a_1\left[1 + \eta_1^2\frac{\sin^2\theta\cos^2\theta}{(1-\eta_1\cos^2\theta)^2}\right]^{1/2}. \quad (11)$$

Many features of a nucleus, including its ground-state deformation [7, 10], are determined by the behavior of single-particle levels near the Fermi surface. Bearing this in mind, we equate the energy ε, on which the optical potential (1) depends, to the average Fermi energy $\bar{\varepsilon}_{\rm F} \approx -8$ MeV. For the nuclear component of the spheroidal global potential, this ultimately yields

$$\hat{V}_{\rm nucl}(r,\theta) = -\hat{U}_1\{1 + \exp[(r - \hat{R}_1(\theta))/\hat{a}_1(\theta)]\}^{-1}, \quad (12)$$

where

$$\hat{U}_1 = 56.83 + 0.4\frac{qZ}{A^{1/3}} - 24.22(-1)^q\frac{N-Z}{A} \quad [\mathrm{MeV}] \quad (13)$$

is the depth of the nuclear potential and the quantities $\hat{R}_1(\theta)$ and $\hat{a}_1(\theta)$ are given by (10) and (11).

In the following, we will have to match the deformations of the various terms of the global potential (5). This can be done by introducing a unified quadrupole-deformation parameter δ_0 for all three terms of the potential—in general, it does not coincide with the quadrupole-nuclear-deformation parameter δ (see Section 3). In the case of the nuclear potential, the parameter δ_0 is related to the parameter η_1, which was introduced above, by the relation

$$\delta_0 = \frac{3}{4}\frac{\int_0^\pi \mathcal{I}(\theta)(3\cos^2\theta - 1)\sin\theta d\theta}{\int_0^\pi \mathcal{I}(\theta)\sin\theta d\theta}, \quad (14)$$

where

$$\mathcal{I}(\theta) \equiv \int_0^\infty \hat{f}_1(r,\theta)r^4 dr \approx \frac{1}{5}\hat{R}_1^5(\theta) + \frac{2}{3}\pi^2\hat{R}_1^3(\theta)\hat{a}_1^2(\theta) + \frac{7}{15}\pi^4\hat{R}_1(\theta)\hat{a}_1^4(\theta). \quad (15)$$

(The error made in approximating the quantity $\mathcal{I}(\theta)$ does not exceed $24\hat{a}_1^5(\theta)\exp\{-\hat{R}_1(\theta)/\hat{a}_1(\theta)\}$.)

2.2. Spin–Orbit Potential

In infinite uniform nuclear matter, the mean nuclear field cannot depend on the spin of a moving nucleon [18]. In a finite nucleus, there arises a spin–orbit interaction that has the form $\text{const}\cdot[\text{grad}f\times\mathbf{p}]\cdot\mathbf{s}$, where $\text{grad}f$ is the gradient of the form factor of the mean nuclear field, $\mathbf{p}=-i\hbar\nabla$ is the nucleon momentum, and $\mathbf{s}$ is the nucleon spin. It can be seen from formula (1) that, in the isotropic optical model [16], this interaction can be described by the potential

$$V_{\text{spin–orb}}(r)=-2i\hbar U_2[\text{grad}f_2\times\nabla]\mathbf{s} + \text{h.c.}=4U_2\frac{1}{r}\frac{df_2(r)}{dr}\mathbf{l}\cdot\mathbf{s}. \quad (16)$$

For a spheroidal nucleus, the spin–orbit potential (16) reduces to the form

$$\hat{V}_{\text{spin–orb}}(\mathbf{r})=-2i\hbar U_2[\text{grad}\hat{f}_2\times\nabla]\mathbf{s}+\text{h.c.}, \quad (17)$$

where $\hat{f}_2(r,\theta)=\{1+\exp[(r-\hat{R}_2(\theta))/\hat{a}_2(\theta)]\}^{-1}$ is the form factor of the spheroidal mean field generating the spin–orbit interaction. This form factor can be constructed in the same way as the spheroidal form factor $\hat{f}_1(r,\theta)$—that is, with the aid of formulas (10) and (11), where the parameters $R_1=r_1A^{1/3}$, a_1, and η_1 are replaced by the parameters $R_2=r_2A^{1/3}$, a_2, and η_2, respectively. (Similar substitutions must be made in formulas (14) and (15) in employing them to describe the relation between the deformation parameters η_2 and δ_0.)

Calculating the right-hand side of the equality in (17) in the system of local spherical coordinates, we obtain

$$\hat{V}_{\text{spin–orb}}(\mathbf{r})=4U_2\left\{\frac{1}{r}\frac{d\hat{f}_2(r,\theta)}{dr}\mathbf{l}\cdot\mathbf{s} - i\hbar\frac{d\hat{f}_2(r,\theta)}{d\theta}\left[(s_x\cos\varphi+s_y\sin\varphi+s_z\cot\theta)\times\frac{1}{r^2}\frac{d}{d\varphi}+(s_x\sin\varphi-s_y\cos\varphi)\frac{1}{r}\frac{d}{dr}\right]\right\}. \quad (18)$$

Owing to terms involving the factors $s_x\cos\varphi$, $s_y\sin\varphi$, $s_x\sin\varphi$, and $s_y\cos\varphi$, the potential (18) can mix single-particle states for which $\Delta\Omega=\pm2$ (Ω is the projection of the total nucleon angular momentum onto the symmetry axis of the nucleus). However, the matrix elements of the operator $\hat{V}_{\text{spin–orb}}(r,\theta)$ that correspond to such transitions are smaller than the matrix elements for $\Delta\Omega=0$ by a factor of about δ_0. For this reason, we disregard these terms and approximate the spin–orbit term in the spheroidal global potential by the expression

$$\hat{V}_{\text{spin–orb}}(r,\theta)=4U_2\left[\frac{1}{r}\frac{d\hat{f}_2(r,\theta)}{dr}\mathbf{l}\cdot\mathbf{s}+\frac{1}{r^2}\frac{d\hat{f}_2(r,\theta)}{d\theta}\cot\theta\, l_zs_z\right]. \quad (19)$$

2.3. Coulomb Potential

Formula (3) describes the Coulomb interaction generated by a uniformly charged sphere of radius R_{Coul}. We generalize this expression to the case where the sphere is deformed to become a uniformly charged spheroid of the same volume.

The surface of such a spheroid is described by the function [compare with Eq. (10)]

$$R(\theta)=R_{\text{Coul}}(1-\eta)^{1/6}(1-\eta\cos^2\theta)^{-1/2}, \quad (20)$$

where $\eta=(c^2-d^2)/c^2$ is the deformation parameter and c and d are the semiaxes of the spheroid in, respectively, the direction along the symmetry axis z of the spheroid and the direction orthogonal to it.

The parameter η is related to the spheroid-quadrupole-deformation parameter $\delta_0=\dfrac{3}{2}\dfrac{c^2-d^2}{c^2+2d^2}$ by the equation

$$\eta=\frac{2\delta_0}{1+4\delta_0/3}. \quad (21)$$

The Coulomb component of the spheroidal global potential can be calculated by the formula

$$\hat{V}_{\text{Coul}}(r,\theta)=\frac{3}{2}\frac{qZe^2}{R^3_{\text{Coul}}}\times\int_0^{\pi}\sin\theta'd\theta'\int_0^{R(\theta')}\frac{(r')^2dr'}{\sqrt{r^2+(r')^2-2rr'\cos\beta}}, \quad (22)$$

where β is the angle between the radius vectors $\mathbf{r}$ and $\mathbf{r}'$.

By using the expansion

$$\frac{1}{\sqrt{r^2+(r')^2-2rr'\cos\beta}}=\sum_{\lambda=0}^{\infty}k_\lambda(r,r')P_\lambda(\cos\beta), \quad (23)$$

$$k_\lambda(r,r')=\begin{cases}r^\lambda/(r')^{\lambda+1} & \text{at } r\le r',\\ (r')^\lambda/r^{\lambda+1} & \text{at } r>r',\end{cases} \quad (24)$$

which follows from the form of the generating function for Legendre polynomials, and the addition theorem for spherical harmonics, we can recast expression (22) into the form

$$\hat{V}_{\rm Coul}(r,\theta) = \frac{3}{2}\frac{qZe^2}{R_{\rm Coul}^3} \times \sum_{\lambda=0}^{\infty} P_\lambda(\cos\theta)\int_0^\pi P_\lambda(\cos\theta')K_\lambda(r,\theta')\sin\theta' d\theta', \quad (25)$$

where

$$K_\lambda(r,\theta) = \int_0^{R(\theta)} k_\lambda(r,r')(r')^2 dr'. \quad (26)$$

The function $K_\lambda(r,\theta)$ can readily be expanded in powers of the parameter η by considering individually the case of $r \le R_{\rm Coul}$ and the case of $r > R_{\rm Coul}$. Upon substituting the series found in this way into formula (25) and performing integration with respect to the variable θ', we have

$$\hat{V}_{\rm Coul}(r,\theta) = \begin{cases} \dfrac{3}{2}\dfrac{qZe^2}{R_{\rm Coul}}\left[\left(1-\dfrac{r^2}{3R_{\rm Coul}^2}\right) + \sum\limits_{n=1}^{\infty}\left(\alpha_n + \beta_n\dfrac{r^2}{R_{\rm Coul}^2}P_2(\cos\theta)\right)\eta^n\right] & \text{at } r \le R_{\rm Coul}, \\ qZe^2\left[\dfrac{1}{r} + \sum\limits_{n=1}^{\infty}\sum\limits_{l=0}^{n}\gamma_{nl}\dfrac{R_{\rm Coul}^{2l}}{r^{2l+1}}P_{2l}(\cos\theta)\eta^n\right] & \text{at } r > R_{\rm Coul}, \end{cases} \quad (27)$$

where the coefficients α_n, β_n, and γ_{nl} are given by

$$\alpha_n = \sum_{k=0}^{n}\frac{(-1)^k\Gamma_k(1/3)}{(2n-2k+1)k!}, \quad (28)$$

$$\beta_n = \frac{2}{(2n+1)(2n+3)},$$

$$\gamma_{nl} = \frac{3}{(2l+3)!!} \times \sum_{k=l}^{n}\frac{(-1)^{n-k}\Gamma_{n-k}\left(\dfrac{2l+3}{6}\right)(2l+2k+1)!!}{2^{2l+k}(n-k)!k!} \times \sum_{m=0}^{l}\frac{(-1)^m(4l-2m)!}{m!(2l-m)!(2l-2m)!(2l-2m+2k+1)}.$$

[Here, $\Gamma_j(x) = x(x-1)\ldots(x-j+1)$ at $j = 1,2,\ldots$; $\Gamma_0(x) = 1$.]

The infinite series in (27) converge in the region $|\eta| < 1$. This ensures the description of the Coulomb component of the spheroidal global potential at quadrupole deformations in the range $-0.3 < \delta_0 < 1.5$ [see (21)]. For oblate nuclei ($\delta_0 < 0$), it is more reasonable to expand the potential $\hat{V}_{\rm Coul}(r,\theta)$ in the parameter $\xi = (c^2-d^2)/d^2 = 2\delta_0/(1-2\delta_0/3)$ rather than in the parameter $\eta = (c^2-d^2)/c^2$, the general form of the expansion in (27) remaining unchanged if we replace the parameter η by the parameter ξ and the coefficients α_n, β_n, and γ_{nl} by the coefficients

$$\alpha'_n = \sum_{k=0}^{n}\frac{(-2)^k k!\Gamma_{n-k}(2/3)}{(2k+1)!!(n-k)!}, \quad \beta'_n = -\frac{(-2)^n n!}{(2n+3)!!}, \quad (29)$$

$$\gamma'_{nl} = \frac{3}{(2l+3)!!}\sum_{k=l}^{n}\frac{(-1)^k\Gamma_{n-k}\left(\dfrac{2l+3}{3}\right)(2l+2k+1)!!}{2^{2l}(n-k)!}\sum_{m=0}^{l}\frac{(-1)^m(4l-2m)!(2l-2m+1)!!}{m!(2l-m)!(2l-2m+1)!(2l-2m+2k+1)!!}.$$

The resulting series converge in the region $-0.75 < \delta_0 < 0.375$ ($|\xi| < 1$).

3. APPLICATION OF THE SPHEROIDAL GLOBAL POTENTIAL TO CALCULATING THE QUADRUPOLE DEFORMATION OF NUCLEI

3.1. Calculation of Single-Particle States for the Spheroidal Global Potential

A complete description of the eigenstates of the anisotropic single-particle Hamiltonian

$$H(\delta_0) = T + V_{\rm SGP}(\delta_0), \qquad (30)$$

where $T = -\frac{\hbar^2}{2m}\Delta$ is the nucleon (proton or neutron) kinetic energy, is an involved mathematical problem. However, it is not necessary to solve it completely, because, in estimating the equilibrium deformation of a nucleus, we can restrict ourselves to calculating only filled (in the ground state) single-particle orbitals. This simplifies the analysis significantly since such single-particle states are localized in a bounded region of a space; therefore, they can be approximated by a finite set of bound orthonormalized functions.

In order to diagonalize the Hamiltonian in (30), we used the truncated oscillator basis $\{|\mathcal{N}lj\Omega\rangle\}$, $\mathcal{N} \leq \mathcal{N}_0$ (where $|\mathcal{N}lj\Omega\rangle$ is the spherical-oscillator wave function characterized by the orbital angular momentum l, the total angular momentum j, the projection Ω of the total angular momentum onto the z axis, and the number of excited quanta $\mathcal{N}$). The quantum energy $\hbar\omega_0 = 41A^{-1/3}$ MeV was chosen in such a way that the experimental value of the root-mean-square nucleon radius [4] would be faithfully reproduced as the oscillator states are filled.

In diagonalizing the energy matrix $\langle\mathcal{N}'l'j'\Omega|H(\delta_0)|\mathcal{N}lj\Omega\rangle$, we took into account the conservation of the parity $\pi = (-1)^{\mathcal{N}'} = (-1)^{\mathcal{N}}$ and of the total-angular-momentum projection Ω. The maximum oscillator number $\mathcal{N}_0$ at which the basis was truncated was determined by the condition $\mathcal{N}_0 = \mathcal{N}_{\rm val} + 6$, where $\mathcal{N}_{\rm val}$ is the oscillator number of the valence shell of the nucleus being considered. Thus, the calculation of bound states in the valence shell was performed by using the basis that included, in addition to this shell, three oscillator shells of the same parity. In fact, we took into account seven oscillator shells for extremely light nuclei ($A \sim 10$) and 11 and 12 shells (for protons and neutrons, respectively) for very heavy nuclei ($A \sim 240$).

The basis that we chose ensures quite a reliable description of bound states in the spheroidal global potential for the potential-deformation parameter taking values in the range $-0.5 \leq \delta_0 \leq 0.5$. This is illustrated in Fig. 1*a*, where the results of the calculation of the $1p$ and $1d2s$ neutron levels for the ^{25}Mg nucleus and the nuclei neighboring it ($\mathcal{N}_{\rm val} = 2$) are given at the $\mathcal{N}_0$ values of (dotted curves) 4, (dashed curves) 6, and (solid curves) 8.

In expansion of the Coulomb potential $\hat{V}_{\rm Coul}(r,\theta)$ in powers of the parameter η (ξ) [see Eq. (27)], we took into account powers up to ten inclusively.

3.2. Estimating Equilibrium Nuclear Deformations

The eigenenergies $\varepsilon_i(\delta_0)$ and eigenstates $|\varphi_i(\delta_0)\rangle$ of the Hamiltonian in (30) that were found individually for protons and for neutrons were used to calculate the single-particle energy of the ground state of a nucleus,

$$E_{\rm s.p.}(\delta_0) = \sum_{i=1}^{A} \varepsilon_i(\delta_0), \qquad (31)$$

and its deformation

$$\delta(\delta_0) = \frac{3}{4}\sum_{i=1}^{A}\langle 2z^2 - x^2 - y^2\rangle_i \Big/ \sum_{i=1}^{A}\langle r^2\rangle_i. \qquad (32)$$

Here, the sum $\sum_{i=1}^{A}$ is taken over all filled proton and neutron states, $\{x, y, z\}$ are the nucleon coordinates in the body reference frame, $r^2 = x^2 + y^2 + z^2$, and the symbol $\langle\ldots\rangle_i$ means averaging over the state $|\varphi_i(\delta_0)\rangle$.

The equilibrium nuclear deformation δ was determined by minimizing the function $E_{\rm s.p.}(\delta_0)$, the respective minimum being sought (with a rather small step in the potential deformation parameter δ_0) in the interval $-0.5 \leq \delta_0 \leq 0.5$.

The above procedure does not take into account the effect of pairing and of other residual forces on the nuclear shape, which are responsible, in particular, for an earlier transition to the spherical shape as nucleon configurations approach filled shells. An investigation of the spectroscopic features of low-lying nuclear states shows that the effect of residual forces often violates a natural order in the filling of single-particle levels of the mean nuclear field. This can affect substantially the equilibrium deformation of a nucleus, especially in odd and odd–odd nuclei. In order to take into account this effect to some extent, we used, along with the computational scheme described above, yet another version of calculations of the equilibrium deformation, that where the proton and neutron ground-state configurations, which determine the order of summation in (31), are determined with allowance for the requirement that the experimental values of the parity π and of the spin J of the nucleus be reproduced (it was assumed that, in the ground state, the spin J is equal to its projection $K = \sum_{i=1}^{A}\Omega_i$ onto the symmetry axis of the nucleus). It will be shown below (see Section 4) that, upon fixing the quantum

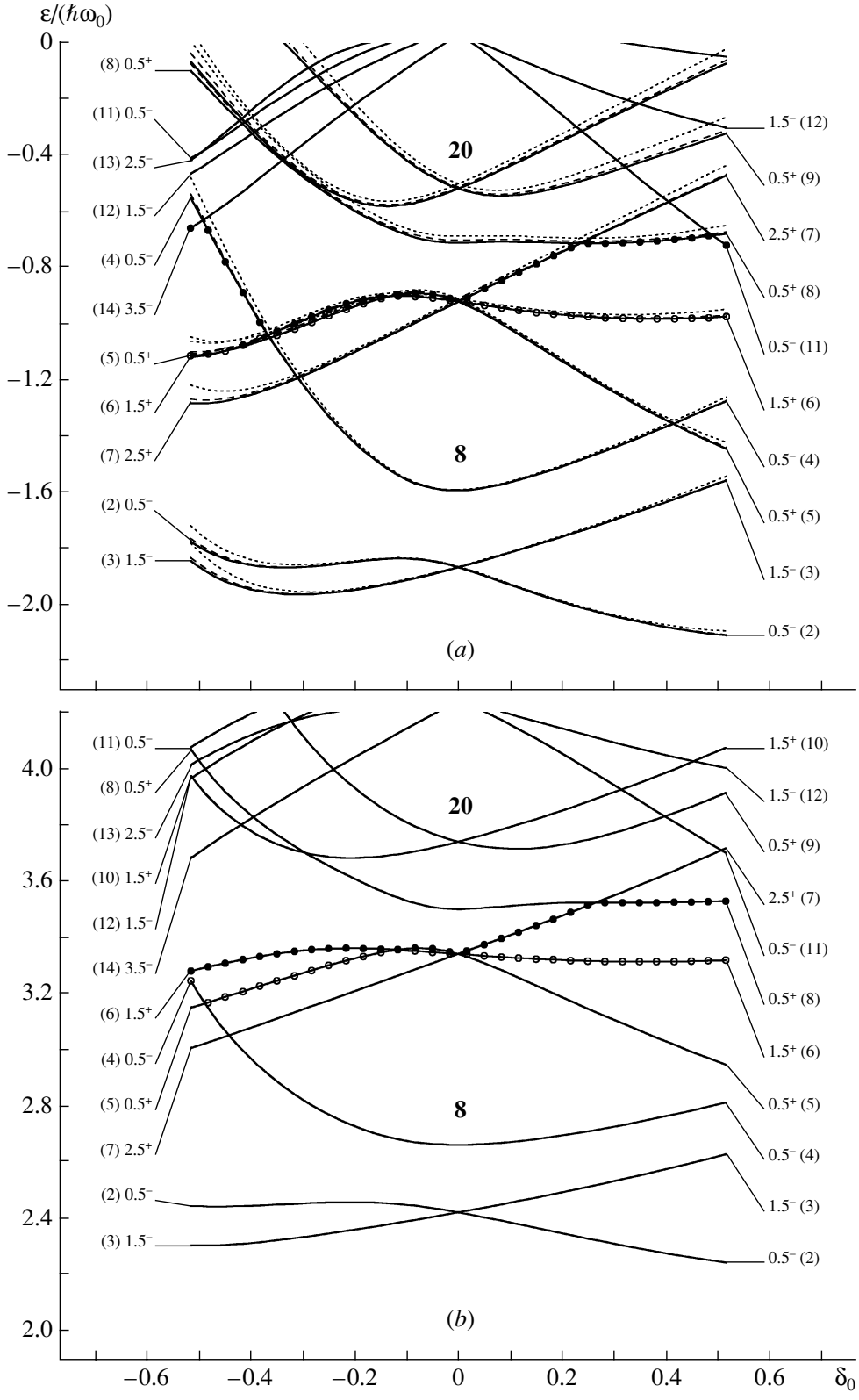

Fig. 1. Neutron-level scheme for the ^{25}Mg nucleus and for nuclei neighboring it: (*a*) results of the calculations based on the spherical global potential with $\mathcal{N}_0 =$ (solid curves) 8, (dashed curves) 6, and (dotted curves) 4 oscillator quanta and (*b*) results of the calculation with the aid of the Nilsson potential. The closed and open circles show the position of the Fermi surface for, respectively, the $N = 13, 14$ and the $N = 11, 12$ nuclei. The energies are normalized to the quantity $\hbar\omega_0 = 41A^{-1/3}$ MeV.

numbers π and K, the theoretical results for nuclei of nonzero angular momentum in the ground state appear to be significantly closer to their experimental counterparts.

3.3. Alternative Calculations with the Nilsson Potential

A universal set of parameters for all nuclei is used in the spheroidal global potential (see Section 2). This inevitably affects estimates of the equilibrium deformation for individual nuclei. Because of this, we deemed it reasonable to perform calculations described in Subsection 3.2 not only for the spheroidal global potential but also for the spheroidal Nilsson potential [4], whose parameters are varied in going over from one principal shell to another (this enables one to describe better the features of the ground states of beta-stable nuclei).

Since the procedure for finding eigenstates for the Nilsson potential is described in detail elsewhere [4, 9], we do not dwell on it here. We only indicate how one can introduce the quadrupole-deformation parameter δ_0 for the Nilsson potential. In the oscillator Nilsson potential, equipotential surfaces are to a good approximation spheroids whose semiaxes are proportional to ω_z^{-1} and ω_x^{-1} (where ω_z and $\omega_x = \omega_y$ are the frequencies of oscillations in the potential, respectively, in the direction of the nuclear-symmetry axis z and in the direction orthogonal to it). From the condition requiring that the potential shape be matched with the nucleon distribution, it follows that $\sum_{i=1}^{A}\langle x^2\rangle_i = \sum_{i=1}^{A}\langle y^2\rangle_i \propto \omega_x^{-2}$ and $\sum_{i=1}^{A}\langle z^2\rangle_i \propto \omega_z^{-2}$. Substituting these relations into (32), we find that the quadrupole-deformation parameter for the Nilsson potential can be represented in the form

$$\delta_0 = \frac{6\delta_{osc} - \delta_{osc}^2}{2\delta_{osc}^2 - 4\delta_{osc} + 6}, \tag{33}$$

where

$$\delta_{osc} = 3\frac{\omega_x - \omega_z}{2\omega_x + \omega_z} \tag{34}$$

is a standard parameter that characterizes the anisotropy of the Nilsson potential [9].

3.4. Estimating Nuclear Deformations on the Basis of Measured Static Quadrupole Moments

The results of our calculations were compared with the estimates of the quadrupole-deformation parameter δ that follow from data reported in [19] for static electric quadrupole moments.

The parameter δ is related to the intrinsic electric quadrupole moment Q_0 by the equation

$$\delta = \frac{3}{4}\frac{Q_0}{Z\langle r^2\rangle}, \tag{35}$$

where $\langle r^2\rangle$ is the mean-square radius of the charge distribution in a nucleus.

The static quadrupole moment Q measured in the laboratory frame does not coincide with Q_0 because of the precession of the angular momentum about the symmetry axis of a nucleus. If the nuclear state being considered belongs to the rotational band, we have the equality

$$Q = \frac{3K^2 - J(J+1)}{(J+1)(2J+3)}Q_0, \tag{36}$$

where J is the angular momentum of the state and K is its projection onto the symmetry axis of the nucleus.

Taking into account the conditions of applicability of this formula, we used only those data from [19] on the static quadrupole moments Q that satisfy the conditions $Q \gtrsim Q_{\text{s.p.}}$ and $Q_0 \gtrsim 3Q_{\text{s.p.}}$ ($Q_{\text{s.p.}} \approx \langle r^2\rangle$ is the single-particle quadrupole moment). We also restricted ourselves to considering the ground states of odd and odd–odd nuclei (here, it was assumed that $K = J$) and the first excited 2^+ states of even–even nuclei [for which, the value of $K = 0$ was substituted into formula (36)]. In all, we thereby chose 90 nuclei (see table).

The mean-square radius of the charge distribution in a nucleus was estimated on the basis of the relations

$$\langle r^2\rangle = \begin{cases} \dfrac{3}{5}R_0^2\dfrac{1 + (10\pi^2/3)(a_0/R_0)^2}{1 + \pi^2(a_0/R_0)^2} & \text{for } A \le 100, \\ \dfrac{3}{5}(1.2A^{1/3})^2 & \text{for } A > 100, \end{cases} \tag{37}$$

which take into account the effect of the surface diffuseness in light nuclei (the parameters appearing in the radial form factor of the charge distribution, $R_0 = 1.07A^{1/3}$ fm and $a_0 = 0.55$ fm, were extracted from data on fast-electron scattering).

4. DISCUSSION OF THE RESULTS

The main results of our calculations are given in the table. In the first column of this table, we list nuclei for which we estimated the quadrupole-deformation parameter δ. The second and third columns display, respectively, the excitation energies E_{exc} and the spin–parities J^π of nuclear states for which the static quadrupole moment Q was measured in [19]. The values of Q and their measurement errors dQ are quoted in, respectively, the fourth and the fifth column. The quadrupole-deformation parameters δ calculated on the basis of the Q values are presented in the sixth column. The seventh and eighth columns show the deformation parameters obtained by minimizing the sum of single-particle

Quadrupole deformation of nuclei [the second and third columns present, respectively, the excitation energies E_{exc} and spin–parities J^π of nuclear states for which the static quadrupole moment Q was measured in [19]; the fourth and fifth columns give, respectively, the values of Q and their measurement errors dQ; the sixth column displays the quadrupole-deformation parameters δ calculated on the basis of the Q values; the seventh and eighth columns show the deformation parameters obtained by minimizing the sum of single-particle energies in the spheroidal global potential, respectively, with and without fixing the quantum numbers K^π of the nuclear ground state, while the ninth and tenth columns present their counterparts for the Nilsson oscillator potential; if two theoretical values of δ are given, the second corresponds to a shallower energy minimum (an asterisk indicates that there is a considerable loss in energy)]

Nucleus	E_{exc}, MeV	J^π	Q, fm^2	dQ, fm^2	Estimates of the parameter δ				
					on the basis of Q	on the basis of the SG potential		on the basis of the Nilsson potential	
						with K^π	without K^π	with K^π	without K^π
^{11}B	0.00	$3/2^-$	4.07	0.03	0.498	0.276	−0.328	0.250	−0.377
^{12}C	4.44	2^+	6.00	3.00	−0.411	−0.358	−0.358	−0.380	−0.380
^{21}Ne	0.00	$3/2^+$	10.30	0.80	0.463	0.431	0.431	0.451	0.451
^{23}Na	0.00	$3/2^+$	10.40	0.40	0.407	0.429	0.429	0.446	0.446
^{25}Na	0.00	$5/2^+$	−10.00	5.00	−0.210	0.225	0.398	−0.319	−0.319
						−0.273	−0.273	0.385	0.444
^{23}Mg	0.00	$3/2^+$	125.20	5.10	4.489	0.429	0.429	0.446	0.446
^{24}Mg	1.37	2^+	−17.30	1.10	0.425	0.429	0.429	0.444	0.444
^{25}Mg	0.00	$5/2^+$	19.94	0.20	0.384	0.376	0.427	0.385	0.443
^{26}Mg	1.81	2^+	−14.00	4.30	0.331	0.401	0.401	−0.348	−0.348
^{27}Al	0.00	$5/2^+$	14.50	0.50	0.249	0.201	−0.341	−0.351	−0.351
^{28}Si	1.78	2^+	16.70	1.20	−0.326	−0.346	−0.346	−0.376	−0.376
^{32}Si	1.94	2^+	−14.50	2.00	0.265	−0.207	−0.207	−0.220	−0.220
						0.104	0.104	0.111	0.111
^{32}S	2.23	2^+	−14.80	2.10	0.237	0.202	0.202	0.015	0.015
^{33}S	0.00	$3/2^+$	−7.40	1.40	−0.167	−0.118	0.158	−0.081	−0.081
^{36}Ar	1.97	2^+	11.00	6.00	−0.148	−0.161	−0.161	−0.148	−0.148
^{44}Ca	1.16	2^+	−14.00	7.00	0.153	0.117	0.117	0.120	0.120
^{46}Ti	0.89	2^+	−21.00	6.00	0.204	0.240	0.240	0.247	0.247
^{50}V	0.00	6^+	21.00	4.00	0.085	0.162	0.250	0.161	0.280
^{50}Cr	0.78	2^+	−36.00	7.00	0.307	0.247	0.247	0.275	0.275
^{54}Cr	0.83	2^+	−21.00	8.00	0.172	0.235	0.235	0.245	0.245
^{51}Mn	0.00	$5/2^-$	42.00	7.00	0.272	0.243	0.243	0.249	0.249
^{55}Mn	0.00	$5/2^-$	32.00	2.00	0.199	0.233	0.233	0.242	0.242
^{56}Fe	0.85	2^+	−21.00	8.00	0.156	0.201	0.201	0.217	0.217
^{59}Co	0.00	$7/2^-$	39.50	3.00	0.168	0.191	0.241	0.183	0.248
^{58}Ni	1.45	2^+	−10.00	6.00	0.068	0.278	0.278	0.280	0.280
						0.111	0.111	0.444	0.444
^{64}Ni	1.35	2^+	40.00	20.00	−0.257	0.103	0.103	−0.284	−0.284
						−0.112	−0.112	0.345	0.345
^{70}Zn	1.35	2^+	−24.00	3.00	0.137	0.059	0.059	0.046	0.046

Table. (Contd.)

Nucleus	E_{exc}, MeV	J^π	Q, fm^2	dQ, fm^2	Estimates of the parameter δ				
					on the basis of Q	on the basis of the SG potential		on the basis of the Nilsson potential	
						with K^π	without K^π	with K^π	without K^π
^{75}As	0.00	$3/2^-$	30.70	5.00	0.220	0.141	0.141	−0.214	−0.214
^{74}Se	0.64	2^+	−36.00	7.00	0.176	0.069	0.069	−0.210	−0.210
^{77}Kr	0.00	$5/2^+$	94.00	10.00	0.341	0.066	0.066	−0.246	−0.246
						0.310*	0.290*	0.315*	0.295*
^{81}Kr	0.00	$7/2^+$	64.00	7.00	0.173	0.115	0.142	0.121	−0.275
^{83}Kr	0.00	$9/2^+$	26.00	3.00	0.059	0.113	0.140	0.119	−0.278
^{79}Sr	0.00	$3/2^-$	72.60	6.20	0.439	−0.088	−0.063	−0.233	−0.053
						0.380*	0.361*	0.385	0.358*
^{83}Sr	0.00	$7/2^+$	78.10	6.70	0.197	−0.075	0.101	−0.088	−0.088
						0.073	−0.102	0.085	0.085
^{85}Sr	0.00	$9/2^+$	28.90	2.90	0.062	0.071	0.099	0.083	0.083
^{99}Sr	0.00	$3/2^+$	84.00	8.00	0.450	−0.148	−0.148	0.374	0.394
						0.354	0.354	−0.301	−0.307
^{91}Zr	0.00	$5/2^+$	−20.60	1.00	−0.061	−0.021	0.021	−0.017	−0.017
^{98}Mo	0.79	2^+	−26.00	9.00	0.089	0.195	0.195	−0.215	−0.215
^{100}Ru	0.54	2^+	−34.00	15.00	0.109	0.184	0.184	0.176	0.176
^{104}Ru	0.36	2^+	−63.00	19.00	0.197	0.147	0.147	−0.246	−0.246
^{108}Pd	0.43	2^+	−55.00	15.00	0.160	0.149	0.149	0.267	0.267
^{110}Cd	0.66	2^+	−39.00	8.00	0.108	0.144	0.144	0.239	0.239
^{115}In	0.00	$9/2^+$	75.50	12.00	0.104	0.063	0.063	0.248	0.268
^{109}Sn	0.00	$5/2^+$	31.00	10.00	0.066	0.107	0.107	0.110	0.110
^{121}Sb	0.00	$5/2^+$	−40.50	5.00	−0.079	−0.017	0.017	−0.175	−0.175
^{123}Sb	0.00	$7/2^+$	−49.00	5.00	−0.072	−0.055	−0.055	−0.142	−0.142
^{124}Sb	0.00	3^-	190.00	40.00	0.312	0.057	0.057	0.142	0.142
^{121}Xe	0.00	$5/2^+$	133.00	5.00	0.245	0.232	−0.187	−0.206	−0.206
^{135}Xe	0.00	$3/2^+$	21.40	0.70	0.065	0.092	0.092	0.052	0.075
^{137}Xe	0.00	$7/2^-$	−49.01	1.70	−0.064	−0.061	0.094	−0.050	−0.050
^{120}Cs	0.00	2^+	145.00	2.00	0.329	0.234	0.234	0.360	0.360
^{121}Cs	0.00	$3/2^+$	83.80	0.90	0.270	0.232	0.232	0.357	0.357
^{131}Cs	0.00	$5/2^+$	−62.00	5.00	−0.106	0.109	0.147	0.149	0.170
						−0.114	−0.142	−0.145	−0.145
^{132}Cs	0.00	2^-	50.00	2.00	0.107	0.141	0.141	0.144	0.144
^{130}Ba	0.36	2^+	−57.00	43.00	0.121	0.188	0.188	0.202	0.202
^{143}Pr	0.00	$7/2^+$	77.00	16.00	0.089	0.105	0.105	0.084	0.107
^{135}Nd	0.00	$9/2^-$	192.00	48.00	0.194	0.309	0.309	0.239	0.325

Table. (Contd.)

Nucleus	E_{exc}, MeV	J^π	Q, fm^2	dQ, fm^2	Estimates of the parameter δ				
					on the basis of Q	on the basis of the SG potential		on the basis of the Nilsson potential	
						with K^π	without K^π	with K^π	without K^π
^{144}Nd	0.70	2^+	−22.00	9.00	0.041	0.105	0.105	0.106	0.106
^{146}Nd	0.45	2^+	−78.00	9.00	0.142	0.141	0.141	0.448	0.448
^{148}Nd	0.30	2^+	−146.00	13.00	0.264	0.187	0.187	0.454	0.454
^{149}Nd	0.00	$5/2^-$	130.00	30.00	0.187	0.189	0.189	0.454	0.357
^{150}Nd	0.13	2^+	−200.00	50.00	0.359	0.225	0.225	0.332	0.332
^{154}Sm	0.08	2^+	−187.00	4.00	0.319	0.259	0.259	0.356	0.356
^{159}Eu	0.00	$5/2^+$	266.00	30.00	0.350	0.298	0.298	0.360	0.360
^{160}Gd	0.08	2^+	−208.00	4.00	0.335	0.296	0.296	0.358	0.358
^{152}Tb	0.00	2^-	34.00	13.00	0.056	0.218	0.218	0.413	0.385
^{153}Tb	0.00	$5/2^+$	108.00	14.00	0.141	0.221	0.221	0.360	0.360
^{157}Tb	0.00	$3/2^+$	140.10	8.00	0.321	0.259	0.259	0.330	0.330
^{163}Dy	0.00	$5/2^-$	265.00	2.00	0.327	0.297	0.297	0.322	0.322
^{153}Ho	0.00	$11/2^-$	−110.00	50.00	−0.082	−0.143	0.216	−0.117	−0.239
^{154}Ho	0.00	2^-	19.00	10.00	0.030	0.219	0.219	0.205	0.205
^{155}Ho	0.00	$5/2^+$	152.00	10.00	0.191	0.222	0.222	0.209	0.296
^{165}Ho	0.00	$7/2^-$	339.00	34.00	0.313	0.299	0.299	0.322	0.322
^{165}Er	0.00	$5/2^-$	271.00	3.00	0.322	0.295	0.268	0.321	0.321
^{170}Tm	0.00	1^+	72.00	5.00	0.295	0.296	0.296	0.303	0.322
^{173}Lu	0.00	$7/2^+$	356.00	4.00	0.300	0.264	0.264	0.298	0.327
^{178}Hf	0.09	2^+	−202.00	2.00	0.269	0.343	0.343	0.449	0.449
^{182}Ta	0.00	3^-	260.00	30.00	0.231	0.221	0.221	0.232	0.232
^{186}W	0.12	2^+	−160.00	30.00	0.202	0.181	0.181	0.174	0.174
^{190}Os	0.19	2^+	−115.00	13.00	0.139	0.175	0.175	0.167	0.167
^{189}Ir	0.00	$3/2^+$	87.80	1.00	0.150	0.174	0.174	−0.171	0.143
^{185}Pt	0.00	$9/2^+$	385.00	50.00	0.242	0.253	0.226	0.259	0.259
^{187}Pt	0.00	$3/2^-$	−100.10	7.00	−0.170	0.175	0.175	0.170	0.170
						−0.148	−0.148	−0.230	−0.250
^{185}Au	0.00	$5/2^-$	−110.10	10.00	−0.104	−0.146	0.224	0.265	0.265
^{186}Au	0.00	3^-	314.00	16.00	0.254	0.223	0.223	0.263	0.291
^{191}Au	0.00	$3/2^+$	71.60	2.10	0.119	−0.140	−0.140	0.136	0.136
						0.108	0.108	−0.142	−0.142
^{229}Ra	0.00	$5/2^+$	310.00	20.00	0.229	0.178	0.178	–	–
^{229}Th	0.00	$5/2^+$	430.00	90.00	0.310	0.206	0.174	–	–
^{235}U	0.00	$7/2^-$	457.00	161.00	0.243	0.246	0.246	–	–
^{241}Am	0.00	$5/2^-$	380.00	120.00	0.251	0.252	0.252	–	–

energies in the spheroidal global potential, respectively, with and without fixing the quantum numbers K^π in the ground states of the nuclei, while the ninth and tenth columns display their counterparts for the oscillator Nilsson potential. If two theoretical values of δ are given, the second corresponds to a shallower energy minimum (an asterisk indicates that there is a considerable loss in energy).

It can be seen from the table that the estimates of the nuclear quadrupole deformation that were obtained on the basis of the spheroidal global potential with fixed quantum numbers K^π describe fairly well experimental data in the stable-deformation regions (rare-earth elements, actinides, and $^{24-26}$Mg isotopes). These regions correspond to new (nonspherical) magic numbers and gaps that arise at $\delta_0 \neq 0$ in the single-particle spectrum of the deformed potential.

In the vicinity of such a gap, the oscillating component of the energy $E_{\text{s.p.}}$ (see Section 1)—it is proportional to the level density near the Fermi surface—attains a minimum value corresponding to the maximum of the binding energy of the nucleus being considered [6, 7, 10]. This explains, among other things, the behavior of the energy $E_{\text{s.p.}}(\delta_0)$ of the ^{165}Ho nucleus, this energy taking a minimum value at $\delta_0 \sim 0.25$ (see Fig. 2*a*). Indeed, it follows from the data in Figs. 3 and 4 that the proton and neutron Fermi surfaces of the ^{165}Ho nucleus lie near the energy gap at $\delta_0 \sim 0.3$ (compare with the weakly deformed ^{153}Ho isotope, whose neutron Fermi surface at $\delta_0 \sim 0.3$ lies in the region of concentration of single-particle levels). In the same way, one can explain the deformation of the $^{24-26}$Mg isotopes (see Fig. 1).

The proposed method leads to a much poorer description of the equilibrium deformations of vibrational nuclei ($A \sim 60-100$), in which the static deformation is commensurate with the amplitude of surface vibrations; the deformations of nuclei in the regions where there occurs a transition from the value of $\delta = 0$ to values of $\delta \neq 0$ (see, for example, the data for the Tb and Ho isotopes in the table); and the deformations of the set of light nuclei that can change shape sharply upon the addition or removal of one nucleon. In all of these cases, it is illegitimate to disregard the effect of residual forces. We will demonstrate this by considering the example of the ^{25}Na nucleus. According to experimental data, the ^{25}Na nucleus in the ground state has a negative deformation δ and the spin–parity of $J^\pi = 5/2^+$. It can be seen from Fig. 5 that, for the ^{25}Na nucleus, the correct spin–parity can be obtained only if the odd proton is in the seventh orbital, but, for $\delta < 0$, this orbital lies below the Fermi boundary; therefore, the required proton configuration in the ^{25}Na nucleus may arise only under the effect of residual forces.

As was mentioned above (see Subsection 3.2), the effect of residual forces can be partly taken into account if, in calculating the energy $E_{\text{s.p.}}$, one fixes the quantum numbers K^π of the ground state of the nucleus (by estimating them on the basis of spectroscopic data). A comparison of the data in the sixth and the seventh column of the table shows that, in this way, the agreement between the results of the calculations with the spheroidal global potential, on one hand, and the experimental estimates of the quadrupole-deformation parameter δ, on the other hand, is significantly improved for odd and odd–odd nuclei.

The effect of residual forces also manifests itself in that experimental data are compatible, in some cases, with the theoretical estimates of δ that do not correspond to the deepest minimum of the curve $E_{\text{s.p.}}(\delta_0)$ (see table). As a rule, the energy of such a minimum exceeds insignificantly (by less than 1 MeV) the energy of the absolute minimum of the function $E_{\text{s.p.}}(\delta_0)$; owing to this, residual forces can readily shift the position of the stable equilibrium.

This is not so only for the strongly deformed (according to data on static quadrupole moments) ^{77}Kr and ^{79}Sr nuclei, for which such a shift leads to an increase in the single-particle energy $E_{\text{s.p.}}$ by a few megaelectronvolts. This is corroborated by Fig. 6, where it can be seen that the minimum of the energy of the ^{77}Kr nucleus according to experimental data lies 4 to 5 MeV above the absolute minimum. This brings about the question of accuracy in determining the static quadrupole moments for soft vibrational nuclei such as ^{77}Kr and ^{79}Sr.

There is the reason to question the accuracy of the estimate of the ground-state quadrupole moment of the ^{23}Mg nucleus, since an improbably large value of $\delta \approx 4.5$ follows from this estimate. Moreover, a sharp jump of the experimental estimate of the parameter δ in going over from the ^{123}Sb to the ^{124}Sb nucleus (see table) is surprising.

It is interesting to trace the behavior of experimental and theoretical estimates of the deformation parameter for Tb and Ho isotopes. It can be seen from the table that, as one approaches the boundary of stable deformations, δ between 0.2 and 0.3, the experimental estimates increase more smoothly, which can be explained by the effect of pairing forces, stabilizing a spherical shape of nucleus. This can be observed, for example, in going over from the ^{153}Ho to the ^{154}Ho nucleus. For the ^{153}Ho nucleus, the dashed curve drawn in Fig. 7*a* according to the calculations of $E_{\text{s.p.}}(\delta_0)$ at fixed quantum numbers K^π exhibits three local minima: at $\delta_0 \sim -0.1$, 0.05, and 0.15, the

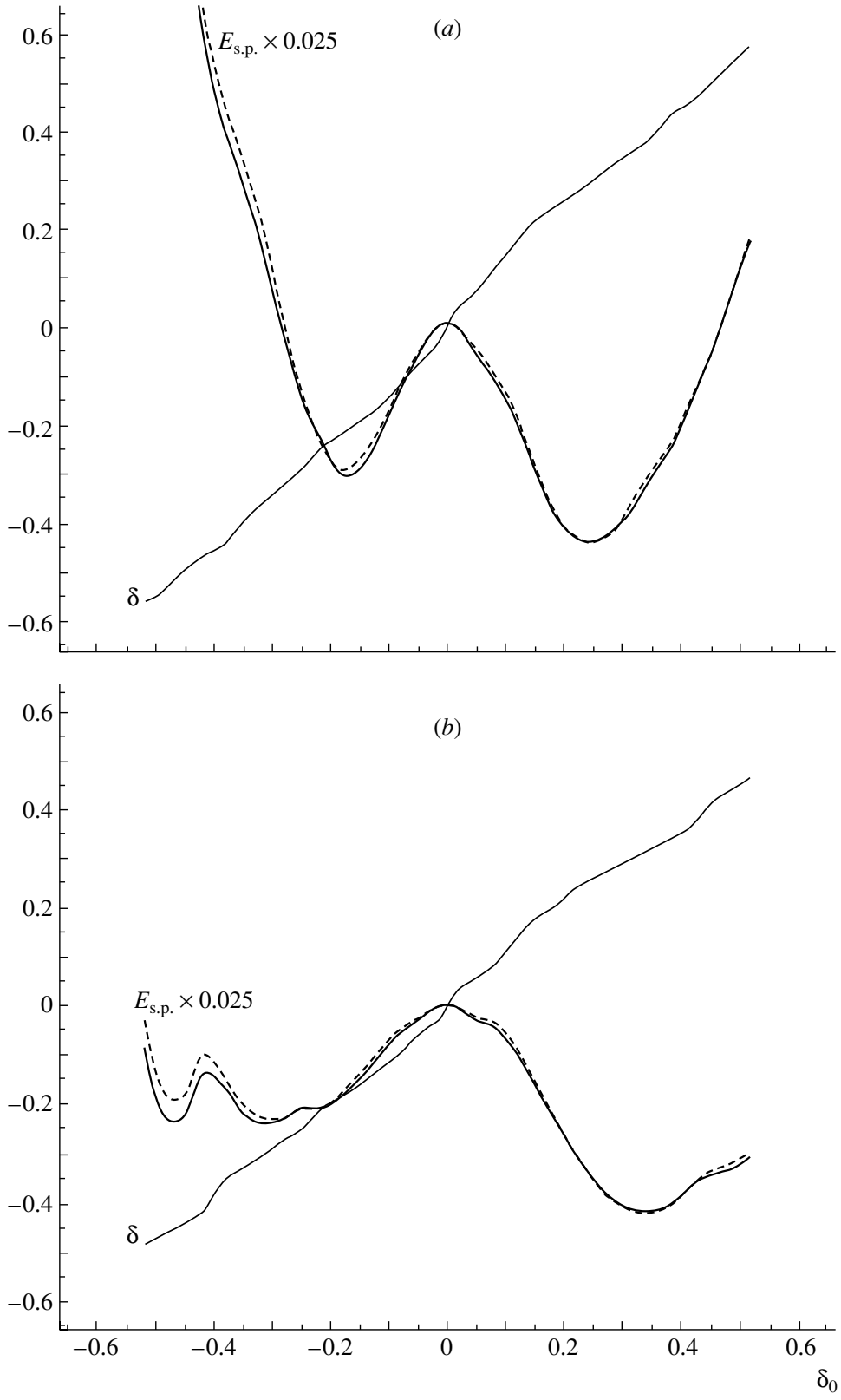

Fig. 2. Single-particle energy $E_{s.p.}$ (in MeV) and quadrupole deformation δ of the ^{165}Ho nucleus versus the parameter δ_0: (*a*) results of the calculations with the spheroidal global potential and (*b*) results of the calculation on the basis of the Nilsson potential. The results for $E_{s.p.}$ are given here for the calculations (dashed curve) with and (solid curve) without fixing the quantum numbers K^π of the ground state.

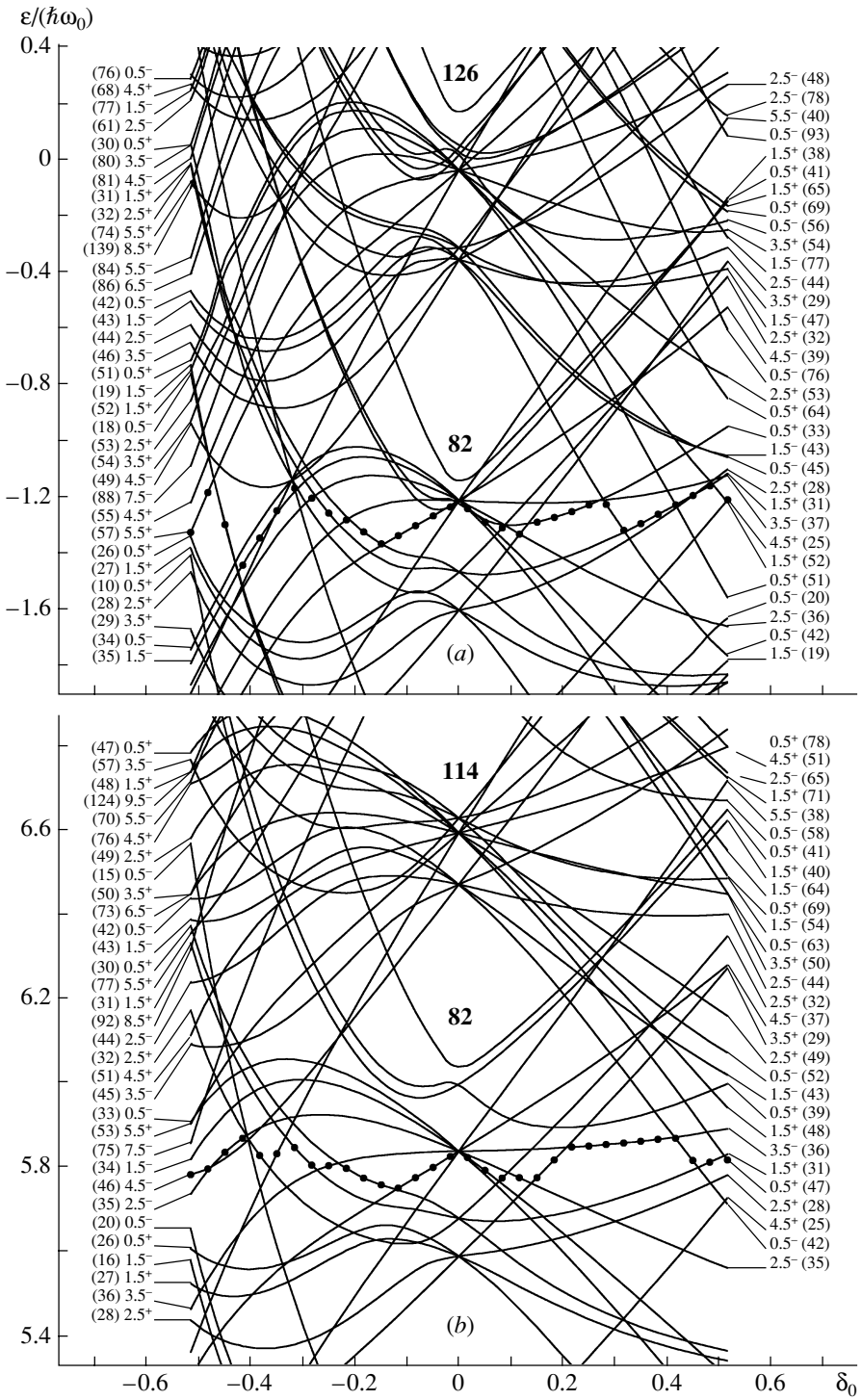

Fig. 3. Proton-level scheme for the ^{165}Ho nucleus and for nuclei neighboring it: (*a*) results of the calculations with the spheroidal global potential and (*b*) results of the calculations with the Nilsson potential. The points indicate the position of the Fermi surface for the ^{165}Ho nucleus.

first of these being the deepest. If we do not take into account the effect of residual forces, the third minimum becomes the deepest upon the addition of one neutron. However, the effect of residual forces results in that the second rather than the third minimum of the curve $E_{\text{s.p.}}(\delta_0)$ becomes the position of stable equilibrium.

A comparison of the results of the calculations performed by using the spheroidal global potential with those obtained on the basis of the Nilsson poten-

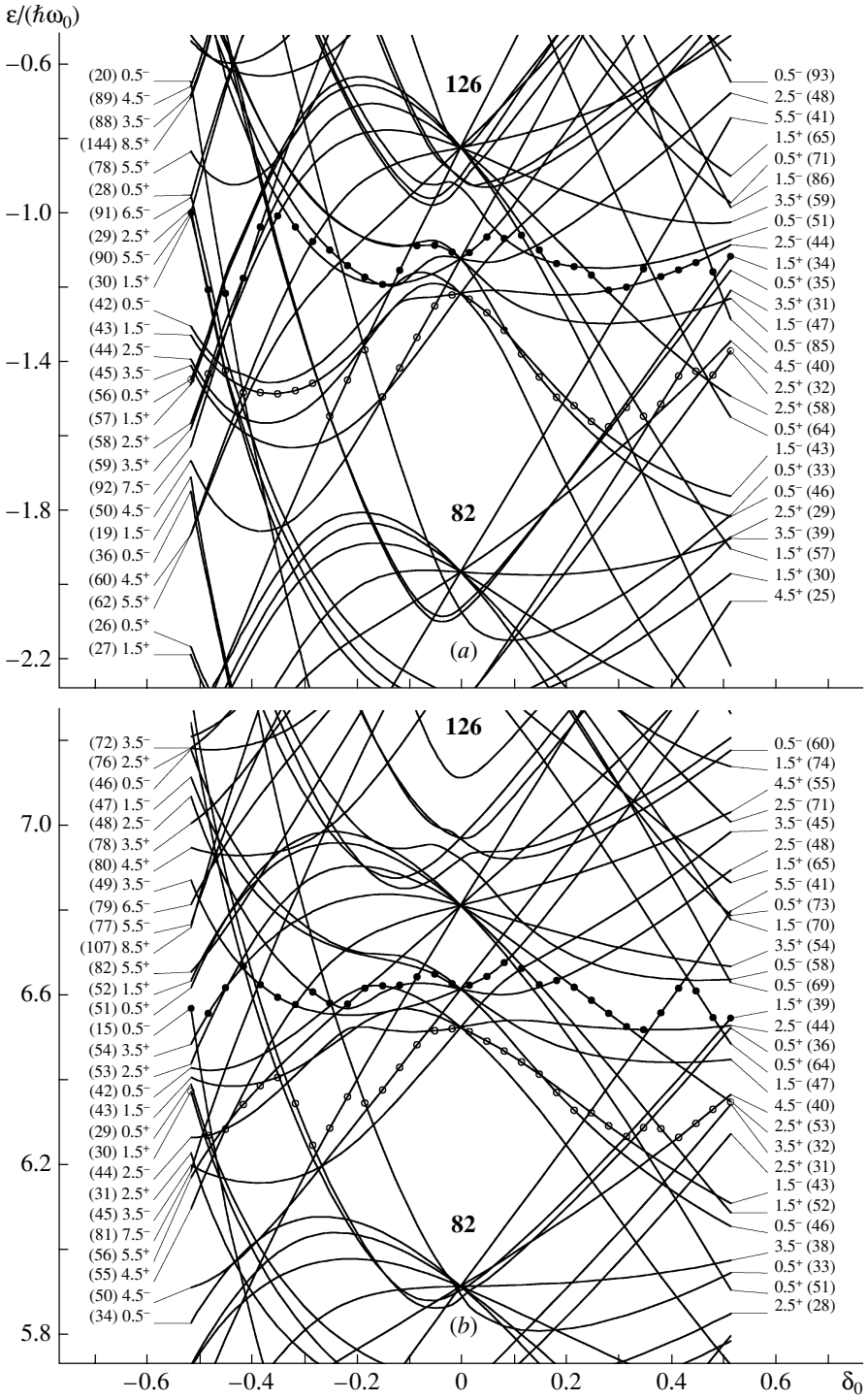

Fig. 4. Neutron-level scheme for the ^{165}Ho nucleus and for nuclei neighboring it: (*a*) results of the calculations with the spheroidal global potential and (*b*) results of the calculations with the Nilsson potential. The closed and open circles indicate the positions of the Fermi surface for, respectively, the ^{165}Ho and the ^{153}Ho nucleus.

tial shows that these results are close in many cases. However, the results of the calculations that employ the spheroidal global potential are by and large in better agreement with experimental data. Analyzing the variation of the energy $E_{\text{s.p.}}(\delta_0)$ in response to the deformation of the potential, we can see that the use of the Nilsson potential leads to underestimating forces hindering the increase in the nuclear deformation. This is especially so for heavy nuclei. For $A \gtrsim 200$ nuclei, one can see from Fig. 8*b* that, with increasing

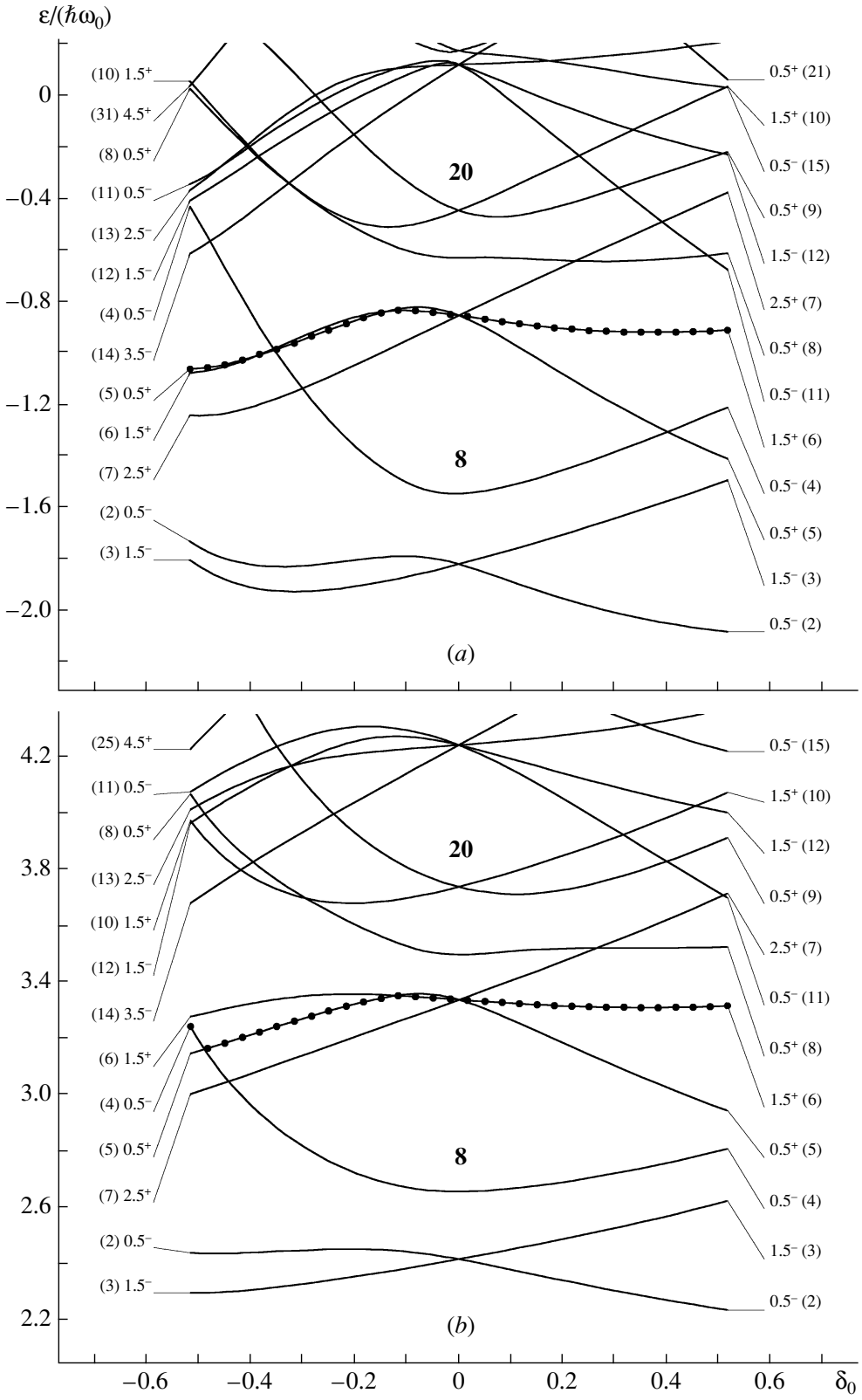

Fig. 5. Proton-level scheme for the ^{25}Na nucleus: (*a*) results of the calculations with the spheroidal global potential and (*b*) results of the calculations with the Nilsson potential. The closed circles indicate the position of the Fermi surface for the ^{25}Na nucleus.

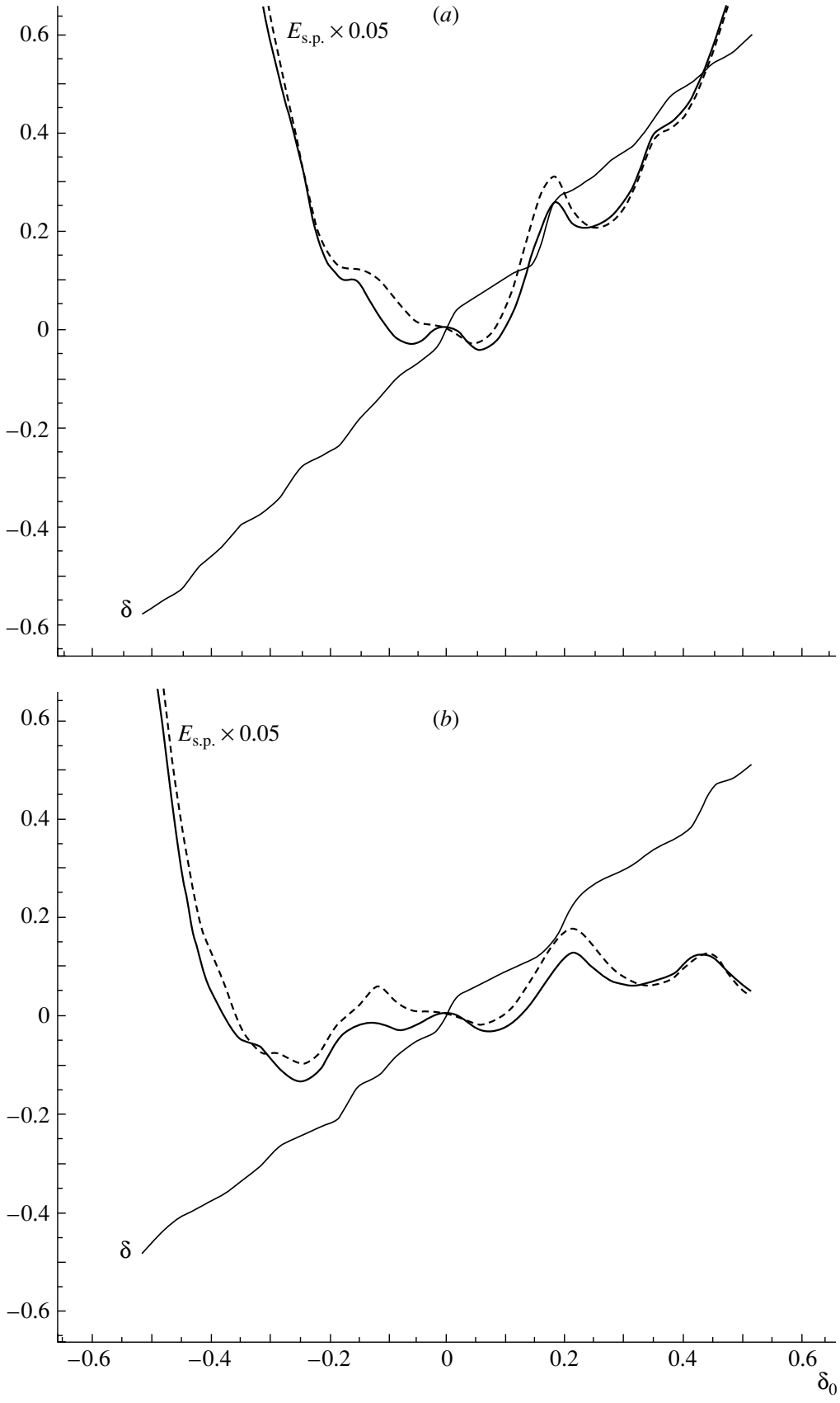

Fig. 6. As in Fig. 2, but for the ^{77}Kr nucleus.

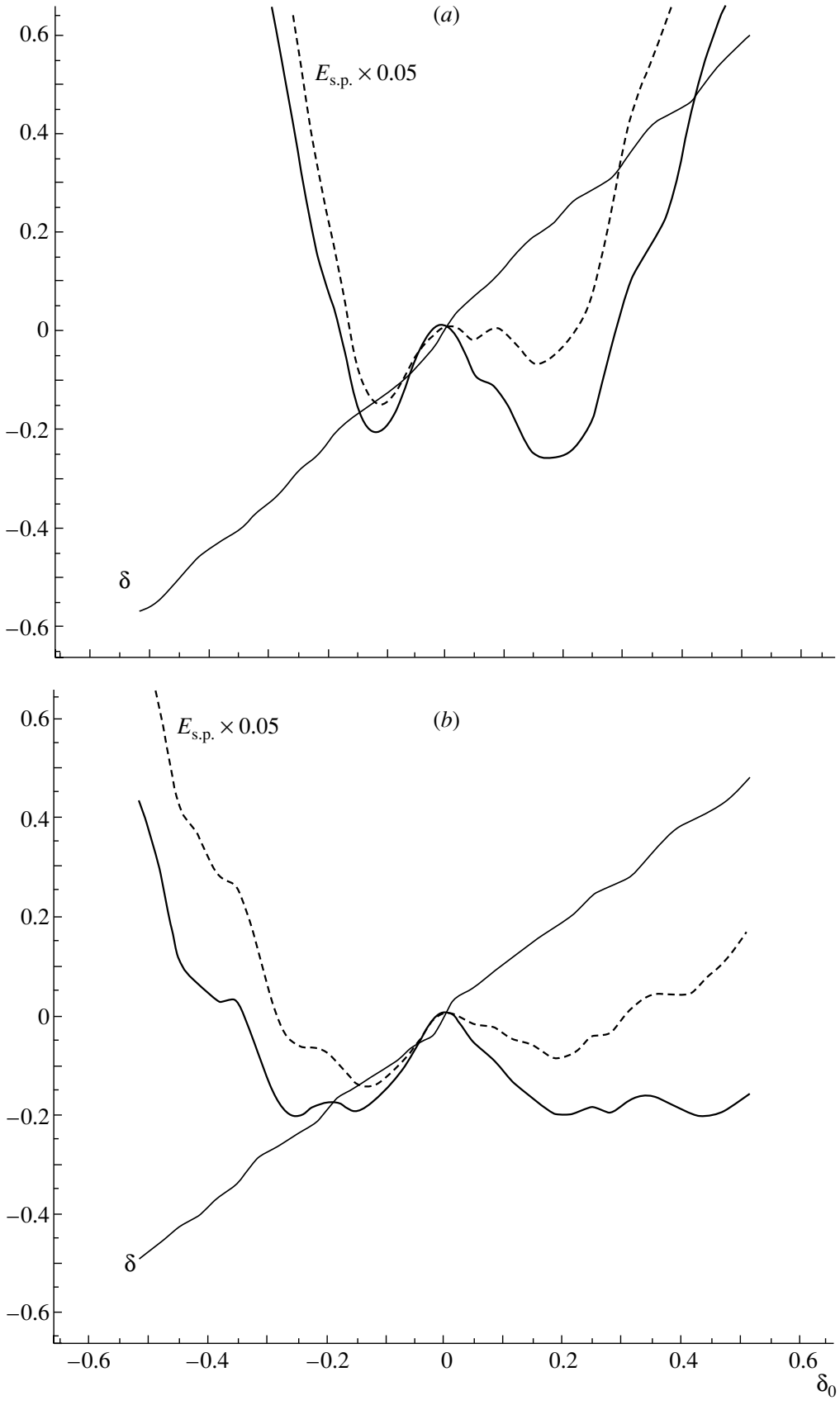

Fig. 7. As in Fig. 2, but for the ^{153}Ho nucleus.

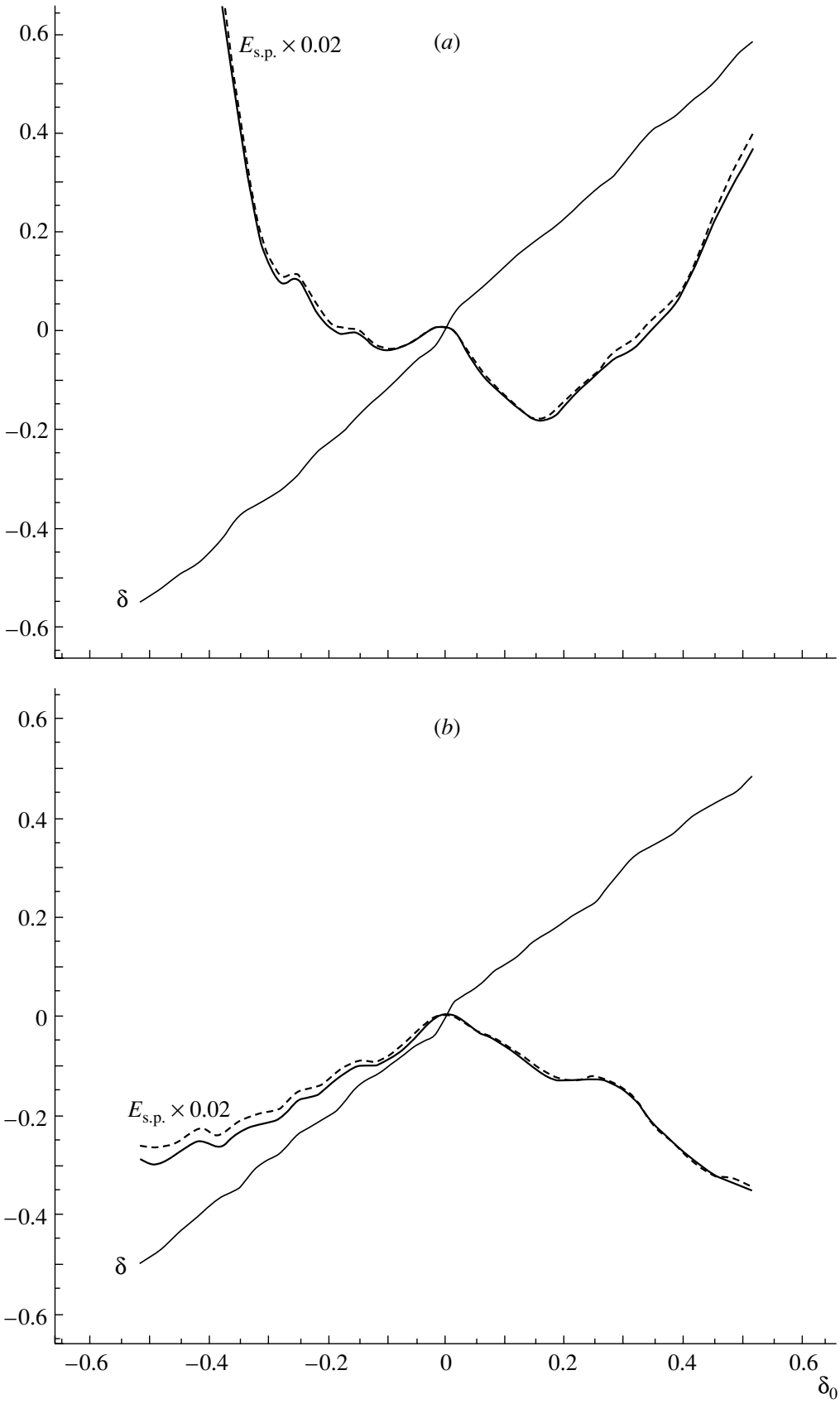

Fig. 8. As in Fig. 2, but for the ^{229}Ra nucleus.

$|\delta_0|$, the Nilsson curve $E_{\text{s.p.}}(\delta_0)$ descends so fast that the local minima in the region $-0.5 \leq \delta_0 \leq 0.5$ disappear (or are leveled out). For this reason, dashes appear in the ninth and tenth columns of the table beginning from the ^{229}Ra nucleus.

5. CONCLUSIONS

Our analysis has led to the following conclusions:

(i) The spheroidal global potential introduced in this study ensures a more adequate description of the equilibrium deformation of nuclei than that obtained on the basis of the Nilsson potential.

(ii) In order to describe correctly the quadrupole deformation of odd and odd–odd nuclei, it is desirable to fix the quantum numbers K^π of the ground state.

(iii) For nuclei that do not belong to the region of stable deformations, the possibility of obtaining a few (usually two) competitive values of the deformation parameter δ must be taken into account in general. The choice between them must be performed either by taking into account the effect of residual forces or by invoking additional experimental data.

ACKNOWLEDGMENTS

We are grateful to I.N. Boboshin (Center for Photonuclear Experimental Data, Institute of Nuclear Physics, Moscow State University) for the assistance in selecting the required experimental data.

This work was supported in part by the Council of the President of the Russian Federation for Support of Young Russian Scientists and Leading Scientific Schools (project no. 1619.2003.2).

REFERENCES

1. R. V. F. Jansens and T. L. Khoo, Annu. Rev. Nucl. Part. Sci. **41**, 321 (1991).
2. A. N. Andreyev *et al.*, Nature **405**, 430 (2000).
3. M. Bender *et al.*, Phys. Rev. C **60**, 034304 (1999).
4. S. G. Nilsson and K. Dan, Vidensk. Selsk. Mat. Fys. Medd. **29** (16) (1955); C. Gustafson *et al.*, Ark. Fys. **36**, 613 (1967).
5. S. Moshkovsky, *Nuclear Structure* (Inostrannaya Literatura, Moscow, 1959), p. 471 [in Russian].
6. V. M. Strutinsky, Nucl. Phys. A **95**, 420 (1967); **122**, 1 (1968).
7. M. Brack *et al.*, Rev. Mod. Phys. **44**, 320 (1972).
8. V. S. Ramamurthy and S. S. Kapoor, Phys. Lett. B **42B**, 389 (1972).
9. A. Bohr and B. R. Mottelson, *Nuclear Structure*, Vol. 2: *Nuclear Deformations* (Benjamin, New York, 1975; Mir, Moscow, 1977).
10. V. M. Strutinsky and A. G. Magner, Fiz. Élem. Chastits At. Yadra **7**, 356 (1976) [Sov. J. Part. Nucl. **7**, 138 (1976)].
11. V. Strutinsky, Nucl. Phys. A **502**, 67c (1989).
12. V. Strutinsky, *The Variety of Nuclear Shapes* (World Sci., Singapore, 1988).
13. Yu. Melnikov *et al.*, Nucl. Instrum. Methods Phys. Res. B **33**, 81 (1988).
14. D. A. Arsen'ev *et al.*, Izv. Akad. Nauk SSSR, Ser. Fiz. **32**, 866 (1968); D. A. Arseniev, A. Sobiczewski, and V. G. Soloviev, Nucl. Phys. A **126**, 15 (1969); **139**, 269 (1969).
15. B. S. Ishkhanov and V. N. Orlin, Yad. Fiz. **65**, 1858 (2002) [Phys. At. Nucl. **65**, 1809 (2002)].
16. J. Rapaport, Phys. Rep. **87**, 25 (1982).
17. F. A. Gareev, S. P. Ivanova, and V. V. Pashkevich, Yad. Fiz. **11**, 1200 (1970) [Sov. J. Nucl. Phys. **11**, 667 (1970)]; F. A. Gareev *et al.*, Nucl. Phys. A **171**, 134 (1971).
18. L. D. Landau and E. M. Lifshitz, *Quantum Mechanics: Non-Relativistic Theory* (Nauka, Moscow, 1989; Pergamon, Oxford, 1977), p. 319.
19. N. Stone, *Table of New Nuclear Moments*, Preprint 1997, A revision of the *Table of Nuclear Moments* by P. Raghavan, At. Data Nucl. Data Tables **42**, 189 (1989); http://www.nndc.bnl.gov/nndc/stone-moments

Translated by A. Isaakyan

Physics of Atomic Nuclei, Vol. 68, No. 8, 2005, pp. 1372–1380. Translated from Yadernaya Fizika, Vol. 68, No. 8, 2005, pp. 1427–1435.

NUCLEI
Theory

Coordinate Asymptotic Behavior of the Radial Three-Particle Wave Function for a Bound State Involving Two Charged Particles

L. D. Blokhintsev, M. K. Ubaidullaeva[1)], and R. Yarmukhamedov[1)]

Institute of Nuclear Physics, Moscow State University, Vorob'evy gory, Moscow, 119899 Russia

Received April 21, 2004; in final form, December 23, 2004

Abstract—The asymptotic expression for the radial component of the wave function for a three-particle bound state involving two charged particles is derived in an explicit form. This expression contains a three-particle asymptotic normalization factor $C(\varphi)$, where φ is a hyperangle in the six-dimensional space of intrinsic coordinates of the three-particle system. The resulting expressions are used to analyze the asymptotic behavior of the wave functions for the ^{9}Be nucleus that were calculated within the $\alpha+\alpha+n$ three-particle model for various forms of the αn potential. A comparison of the asymptotic expression derived here and the asymptotic expressions for model wave functions makes it possible to extract $C(\varphi)$ values, which turned out to be sensitive to the form of αn interaction. This permits deducing information about two-particle interaction from a comparison of the theoretical values of $C(\varphi)$ with their phenomenological counterparts found from an analysis of experimental differential cross sections for relevant nuclear reactions. © *2005 Pleiades Publishing, Inc.*

1. INTRODUCTION

In order to describe the structure of light nuclei, especially halo nuclei, various three-body approaches have been intensively developed since the early 1990s along with the microscopic multiparticle model [1–3]. These include the multicluster dynamical stochastic method [4–6], the method of hyperspherical functions [7, 8], and the Lagrange mesh method [9]. The main advantage of these approaches is that they make it possible to treat three-particle systems in a nearly model-independent way by applying mathematically correct methods. Wave functions were obtained for some light nuclei—in particular, ^{6}He, ^{6}Be, ^{6}Li, ^{9}Be, and ^{11}Li—on the basis of these approaches within the three-body model. These wave functions made it possible to explain not only static observables (energies of low-lying states; root-mean-square radii; and magnetic, quadrupole, and octupole moments) but also electromagnetic form factors and spectroscopic factors.

Within the approaches in question, the three-particle wave function for a bound system $a=(bcd)$ is expanded, as a rule, in one set of angular basis functions or another, whereupon an infinite-dimensional set of coupled integro-differential equations is obtained for the radial component of the three-particle wave function. In order to obtain numerical solutions, this set is truncated—that is, it is approximated by a finite-dimensional set of equations. Such an approximation can affect the calculated values of the three-particle wave function in the asymptotic region of configuration space, where the wave function decreases exponentially as the hyperradius R increases [10]. In view of this, it is of interest to study in detail the asymptotic behavior of the radial three-particle wave function. The importance of studying the asymptotic behavior is associated, first, with the problem of approximating infinite sets of equations for the radial components of three-particle wave functions by finite-rank sets and, second, with the problem of deducing information about the three-particle asymptotic normalization factor, which is a quantity of fundamental importance. In just the same way as the asymptotic normalization factor for the radial component of the wave function in the two-particle $((bc)+d)$ channel [11], it is an important feature of the three-particle bound (bcd) system, carrying information about two-particle interactions [12].

In [12], we studied in detail the genuinely three-particle asymptotic expression for the radial component of the wave function for the bound state $a=(bcd)$ in the case of short-range interaction between particles b, c, and d and showed that the resulting asymptotic formula involves a factor that can affect significantly the asymptotic values of the three-particle wave function for some specific directions in configuration space. By comparing the resulting asymptotic formula with the asymptotic behavior of the model three-particle wave function for the

[1)]Institute of Nuclear Physics, Uzbek Academy of Sciences, pos. Ulughbek, Tashkent, 702132 Uzbekistan.

^{6}He nucleus [4], we also obtained there information about the three-particle asymptotic normalization factor and revealed its sensitivity to the form of the αn potential.

The overwhelming majority of nuclear systems that can be described within three-body models (including nuclei of interest for nuclear astrophysics) contain two or three charged particles, whose Coulomb interaction changes the asymptotic behavior of the wave function for short-range potentials. In this connection, we analyze here the asymptotic behavior of the radial component of the wave function for the bound three-particle (bcd) system involving two charged particles. The results are used to extract the three-particle asymptotic normalization factor for the ^{9}Be nucleus by means of an analysis of the wave functions calculated within the $\alpha\alpha n$ three-particle model.

Hereafter, we will use the system of units where $\hbar = c = 1$.

2. COORDINATE ASYMPTOTIC BEHAVIOR OF THE RADIAL COMPONENT OF THE THREE-PARTICLE WAVE FUNCTION FOR A BOUND SYSTEM WITH ALLOWANCE FOR COULOMB INTERACTION

Let us consider the case of a bound three-particle system $a = (bcd)$ where two particles (for example, b and c particles) are charged, while the third particle (d) is not charged. The ^{9}Be nucleus in the $(\alpha\alpha n)$ three-body model is an important example of such systems. The Fourier transform of the wave function $\psi(\mathbf{r}, \boldsymbol{\rho})$ for the a system has the form

$$\psi(\mathbf{r}, \boldsymbol{\rho}) = \int \frac{d^3q}{(2\pi)^3}\frac{d^3p}{(2\pi)^3} e^{-i(\mathbf{r}\cdot\mathbf{q}+\boldsymbol{\rho}\cdot\mathbf{p})}\Psi(\mathbf{q}, \mathbf{p}), \quad (1)$$

where $\mathbf{r}$ is the relative coordinate of particles b and c, $\boldsymbol{\rho}$ is the coordinate of the third particle d with respect to the center of mass of the bc pair,

$$\mathbf{q} = \frac{m_c\mathbf{k}_b - m_b\mathbf{k}_c}{m_{bc}},$$

$$\mathbf{p} = \frac{m_{bc}\mathbf{k}_d - m_d(\mathbf{k}_b + \mathbf{k}_c)}{m_a}$$

are the Jacobi momenta corresponding to them, $\Psi(\mathbf{q}, \mathbf{p})$ is the three-particle wave function in the momentum representation, m_j ($\mathbf{k}_j$) is the mass (momentum) of particle j, and $m_{ij} = m_i + m_j$.

The function $\Psi(\mathbf{q}, \mathbf{p})$ is related to the noncovariant vertex function $W(\mathbf{q}, \mathbf{p})$ for the virtual decay

$$a \to b + c + d \quad (2)$$

by the equation [13]

$$\Psi(\mathbf{q}, \mathbf{p}) = -\frac{W(\mathbf{q}, \mathbf{p})}{L(q, p)}, \quad (3)$$

where $L(q,p) = \varepsilon(q,p) + \varepsilon_a$, $\varepsilon(q,p) = q^2/(2\mu_{bc}) + p^2/(2\mu_{(bc)d})$, $\mu_{bc} = m_b m_c/m_{bc}$, $\mu_{(bc)d} = m_d m_{bc}/m_a$, and ε_a is the binding energy of the a system with respect to the virtual process (2). It was indicated in [13] that, if there are bound states in the two-particle subsystems (bc), (cd), and (db), the vertex function $W(\mathbf{q}, \mathbf{p})$ has two-particle singularities at the points $E_{ij} = -\varepsilon_{ij}$, where E_{ij} is the relative kinetic energy of particles i and j and ε_{ij} is the binding energy of the bound two-particle subsystem (ij) with respect to the decay $(ij) \to i + j$. For the two-particle systems (bd) and (cd), where there is no Coulomb interaction, these singularities are poles, while, for the (bc) system, the singularity has the form of a power-law branch point [14]. It should also be noted that, according to [10, 15], the vertex function $W(\mathbf{q}, \mathbf{p})$ additionally has a three-particle singularity of the branch-point type at $\varepsilon(p,q) = -\varepsilon_a$ and that its singular part $W^{(s)}(\mathbf{q}, \mathbf{p})$ has the form [15]

$$W^{(s)}(\mathbf{q}, \mathbf{p}) = \Gamma(1 - \eta_{bc})\tilde{W}(\mathbf{q}, \mathbf{p})\left[\frac{\varepsilon(q,p) + \varepsilon_a}{4\varepsilon_a}\right]^{\eta_{bc}}, \quad (4)$$

where $\eta_{bc} = iz_b z_c e^2 \mu_{bc}/q$, $z_j e$ being the charge of particle j, and $\tilde{W}(\mathbf{q}, \mathbf{p})$ is the vertex-function component that is regular at the point $\varepsilon(q,p) = -\varepsilon_a$ and which coincides with the vertex function on the mass shell [15]—that is, with the vertex function $W(\mathbf{q}, \mathbf{p})$ whose arguments satisfy the relation $q^2/(2\mu_{bc}) + p^2/(2\mu_{(bc)d}) = -\varepsilon_a$.[2)]

According to [10], the asymptotic behavior of the three-particle wave function $\psi(\mathbf{r}, \boldsymbol{\rho})$ for $\rho \to \infty$ (or $r \to \infty$) is determined by the two-particle singularities of the vertex function $W(\mathbf{q}, \mathbf{p})$ at $E_{ij} = -\varepsilon_{ij}$ ($ij = bc, cd, bd$) and the three-particle singularity at $\varepsilon(q,p) = -\varepsilon_a$. For $\rho \to \infty$, the contribution to (1) from the singularities $E_{ij} = -\varepsilon_{ij}$ produces the cluster component of the asymptotic expression, this component being responsible for the formation of possible bound states in two-particle ij subsystems, while the contribution to (1) from the three-particle singularity at $\varepsilon(q,p) = -\varepsilon_a$ generates the genuinely three-particle asymptotic behavior of the wave function $\psi(\mathbf{r}, \boldsymbol{\rho})$. In the following, we consider the (bcd) bound three-particle system featuring no bound states in the

[2)] It should be noted that there are misprints in formulas (8)–(10) from [15]. In formula (8), the factor of 1/2 is omitted in the definition of $\tilde{\eta}_0$; moreover, the factors $e^{i\pi\tilde{\eta}_0}$ and $e^{i\pi\eta_a}$ should be removed from formulas (8)–(10).

two-particle subsystems. The $^9\mathrm{B} = (\alpha\alpha p)$ and $^9\mathrm{Be} = (\alpha\alpha n)$ nuclei exemplify such systems. For $\rho \to \infty$ or $r \to \infty$, the leading asymptotic expression for the wave function $\psi(\mathbf{r}, \boldsymbol{\rho})$ can then be determined by isolating the contribution from three-particle singularity at $\varepsilon(q,p) = -\varepsilon_a$ in the integral in Eq. (1).

Let us analyze expression (1) for $\rho \to \infty$. For this purpose, we introduce modified Jacobi variables [10], $\mathbf{x} = \mathbf{r}\sqrt{2\mu_{bc}}$, $\mathbf{y} = \boldsymbol{\rho}\sqrt{2\mu_{(bc)d}}$, $\mathbf{q}' = \mathbf{q}/\sqrt{2\mu_{bc}}$, and $\mathbf{p}' = \mathbf{p}/\sqrt{2\mu_{(bc)d}}$, and then construct the partial-wave expansions of the wave function $\psi(\mathbf{r}, \boldsymbol{\rho}) \equiv \psi(\mathbf{x}, \mathbf{y})$ and the vertex function $W(\mathbf{q}, \mathbf{p}) \equiv W(\mathbf{q}', \mathbf{p}')$ in the total set of orthonormalized functions $Y_{\lambda l L M_L}$, following the same line of reasoning as in [12]. As a result, the radial three-particle wave function $\psi_\nu(x,y)$ can be represented in the form [12]

$$\psi_\nu(x,y) = -i^{-\lambda-l}\frac{m^{3/2}}{2\pi^4}\int\limits_{-\infty}^{\infty} dq' q'^2 j_\lambda(q'x) \qquad (5)$$
$$\times \int\limits_{-\infty}^{\infty} dp' p'^2 j_l(p'x)\frac{W_\nu(q',p')}{q'^2 + p'^2 + \varepsilon_a},$$

where $m = m_b m_c m_d/m_a$, $\nu = \{\lambda l L s_{bc} S\}$, $\lambda\,(l)$ is the orbital angular momentum of the (bc) pair (d particle), $\mathbf{L} = \mathbf{l} + \boldsymbol{\lambda}$, $\mathbf{s}_{bc} = \mathbf{s}_b + \mathbf{s}_c$, $\mathbf{S} = \mathbf{s}_{bc} + \mathbf{s}_d$, $\mathbf{s}_j$ is the spin of the j particle, $j_l(z)$ is a spherical Bessel function, and $W_\nu(q',p')$ is the radial part of the vertex function. By using the representation of the spherical Bessel function $j_l(z)$ in the form (8.462 (1)) from [16],

$$j_l(z) = \frac{1}{2z}\left[e^{iz}\sum_{n=0}^{l}\frac{i^{-l+n-1}(l,n)}{(2z)^n}\right. \qquad (6)$$
$$\left. + e^{-iz}\sum_{n=0}^{l}\frac{(-i)^{-l+n-1}(l,n)}{(2z)^n}\right],$$

where $(l,n) = (l+n)!/(n!(l-n)!)$, and taking into account expression (4), we then recast formula (5) for $y \to \infty$ into the form

$$\psi_\nu(x,y) = (-1)^{\lambda+l}\frac{m^{3/2}}{2\pi^4 xy} \qquad (7)$$
$$\times \int\limits_{-\infty}^{\infty} dq' q' e^{iq'x} f_\lambda(q'x) I_\nu(q';y),$$

$$I_\nu(q';y) = \frac{\Gamma(1-\eta_{bc})}{4\varepsilon_a}\int\limits_{-\infty}^{\infty} dp' p' e^{ip'y} \qquad (8)$$
$$\times f_l(p'y)\tilde{W}_\nu(q',p')\left(\frac{q'^2 + p'^2 + \varepsilon_a}{4\varepsilon_a}\right)^{\eta_{bc}-1},$$

where $\eta_{bc} = iz_b z_c e^2 \mu_{bc}^{1/2}/(\sqrt{2}q')$, $\tilde{W}_\nu(q',p')$ is the radial component of the vertex function $W_\nu(q',p')$ regular at the point $q'^2 + p'^2 = -\varepsilon_a$, and

$$f_l(x) = \sum_{n=0}^{l}\frac{(l,n)}{(-2ix)^n}. \qquad (9)$$

By using in (5) the change of integration variables $q' \to -q'$ and $p' \to -p'$ and the relations

$$W_\nu(q,p) = (-1)^\lambda W_\nu(-q,p) = (-1)^l W_\nu(q,-p),$$

one can show that the two terms on the right-hand side of (6) make identical contributions to the right-hand side of (5).

For $y \to \infty$ ($\rho \to \infty$), we isolate in (8) the contribution of the singularity at $p'^2 + q'^2 + \varepsilon_a = 0$. This part of expression (8) can be obtained by displacing the integration contour to the upper half-plane and by isolating there the integral along the straight line going along the imagine axis from the point $p' = i\sqrt{q'^2 + \varepsilon_a}$ to $i\infty$. The contribution from the singularity at $p' = i\sqrt{q'^2 + \varepsilon_a}$ to (8) then assumes the form

$$I_\nu(q';y) \approx I_\nu^{(s)}(q';y) = i\pi\left(\frac{\sqrt{q'^2 + \varepsilon_a}}{2\varepsilon_a y}\right)^{\eta_{bc}} \qquad (10)$$
$$\times \tilde{W}_\nu(q', i\sqrt{q'^2 + \varepsilon_a}) f_l(i\sqrt{q'^2 + \varepsilon_a}) e^{-y\sqrt{q'^2 + \varepsilon_a}}.$$

In order to find the three-particle asymptotic behavior of the wave function $\psi_\nu(x,y)$ for $y \to \infty$ ($\rho \to \infty$), we must substitute expression (10) into (7) and, in the resulting expression, calculate the integral with respect to the variable q' by using the saddle-point technique [17]. The point $q' = q'_0 \equiv i\sqrt{\varepsilon_a}x/R$ is the saddle point in this case. As a result, the sought three-particle asymptotic expression for the wave function in the limit $y \to \infty$ takes the form

$$\psi_\nu(x,y) \approx \psi_\nu^{(\mathrm{as})}(R,\varphi) \qquad (11)$$
$$= C_\nu(\varphi)(2\sqrt{\varepsilon_a}R)^{-\eta} f_l(i\sqrt{\varepsilon_a}R\sin^2\varphi)$$
$$\times f_\lambda(i\sqrt{\varepsilon_a}R\cos^2\varphi)\frac{e^{-\sqrt{\varepsilon_a}R}}{R^{5/2}}, \quad y \to \infty,$$

where

$$\eta = \frac{z_b z_c e^2}{\cos\varphi}\left(\frac{\mu_{bc}}{2\varepsilon_a}\right)^{1/2}$$

and

$$C_\nu(\varphi) = (-1)^{\lambda+l+1}\frac{(m\sqrt{\varepsilon_a})^{3/2}}{\sqrt{2}\pi^{5/2}} \qquad (12)$$
$$\times W_\nu(i\sqrt{\varepsilon_a}\cos\varphi, i\sqrt{\varepsilon_a}\sin\varphi)$$

is the three-particle asymptotic normalization factor [12], in which $x = R\cos\varphi$ and $y = R\sin\varphi$. In deriving expressions (11) and (12), we considered that

the function $\tilde{W}_\nu(q'_0, i\sqrt{q'^2_0 + \varepsilon_a})$, which is regular at the point $q'^2 + p'^2 + \varepsilon_a = 0$, coincides with the vertex function on the mass shell, $W_\nu(i\sqrt{\varepsilon_a}\cos\varphi, i\sqrt{\varepsilon_a}\sin\varphi)$ [15, 18]. We note that the asymptotic formula (11) is valid for $x \to \infty$ ($r \to \infty$) as well, but that it is not applicable for those values of x and y (or r and ρ) at which $|q'_0|$ and $|p'_0|$ ($p'_0 = i\sqrt{\varepsilon_a}y/R$) are rather close to zero. In this case, the representations in Eqs. (8) and (9) cannot be used in determining the asymptotic behavior of the wave function $\psi_\nu(x, y)$ since the saddle point q'_0 (p'_0) approaches the singularities (poles) of the integrand at $q' = 0$ ($p' = 0$), which appear at $\lambda \neq 0$ ($l \neq 0$). The problem of deriving the asymptotic formula for this case requires a dedicated consideration. We emphasize that this comment also applies to the asymptotic formula (15) from [12], which was obtained for short-range two-particle potentials.

3. ANALYSIS OF THE MODEL THREE-PARTICLE WAVE FUNCTION FOR THE ^{9}Be NUCLEUS

On the basis of the results obtained in Section 2, we study here the asymptotic behavior of the $(\alpha\alpha n)$ three-particle wave function obtained in [5, 6] for the ground state of the ^{9}Be nucleus within the dynamical multicluster model of light nuclei [4]. In [5, 6, 19], this wave function was used to calculate a number of static features of the ground and low-lying excited states of the ^{9}Be nucleus. For the $\alpha\alpha$ interaction, use was made of the deep Buck–Friedrich–Wheatley $\alpha\alpha$ potential involving forbidden $0S$, $2S$, and $2D$ states [20], which describes well $\alpha\alpha$ phase shifts up to energies of about 40 MeV. For the αN interaction, two kinds of potentials were used: the Sack–Biedenharn–Breit potential and an improved αN potential that takes into account the exchange Majorana component both in the central and in the spin–orbit term [4].

In [19], static features of the ^{9}Be nucleus were studied on the basis of an improved version of the wave function [21] obtained within the dynamical multicluster model for two sets of potentials characterizing the αN and $\alpha\alpha$ interactions (M1 and M2 models). In the M1 model, the Ali–Bodmer potential [22], where the Pauli exclusion principle is taken into account via the presence of a repulsive core at short distances, was used for the $\alpha\alpha$ interaction. In the M2 model, an attractive potential involving forbidden states and also providing a good description of $\alpha\alpha$ phase shifts up to 40 MeV [23] was used to describe the $\alpha\alpha$ interaction. In both models, a potential involving the exchange Majorana component was used for the αn interaction. For the binding energy ε_a corresponding to the decay of the ^{9}Be nucleus through the $(\alpha + \alpha + n)$ three-particle channel, the values of $\varepsilon_a = 1.76$ and 2.86 MeV were obtained for the αN and $\alpha\alpha$ potentials in, respectively, the M1 and the M2 model [21]. We note that the experimental value of the binding energy, $\varepsilon_a^{\exp}$, is 1.57 MeV.

Since there are no two-particle bound subsystems for the ^{9}Be nucleus within the $(\alpha\alpha n)$ three-particle model, the leading asymptotic expression for the ^{9}Be three-particle wave function is determined by expression (11). Therefore, it is of interest, first, to assess the extent to which the ^{9}Be three-particle wave functions proposed in [5, 6, 21] have a correct asymptotic behavior and, second, to find out whether it is possible to deduce, from these wave functions, information about the value of the three-particle asymptotic normalization factor and its sensitivity to the form of the $\alpha\alpha$ potential.

Within the dynamical multicluster model, the radial component of the three-particle wave function for the ^{9}Be nucleus is represented as a finite series in two-dimensional Gaussian functions [5, 6] (below, we omit the index $s_{bc} = 0$); that is,

$$\psi_{\lambda lLS}(r, \rho) = r^\lambda \rho^l \sum_{i,j=1}^{n_i,n_j} C_{ij;\lambda lLS} \exp\{-a_i r^2 - b_j \rho^2\}, \tag{13}$$

where a_i, b_j, and $C_{ij;\nu}$ are variational parameters. The coefficients a_i, b_j, and $C_{ij;\nu}$ calculated for both the M1 and the M2 models and for each set of quantum numbers (λ, l, L, S) were placed at our disposal by Kukulin in a tabular form [21]. We perform our analysis for four components of the model wave function (13) that correspond to various quantum-number sets (λ, l, L, S) (three of them are dominant components, while the remaining one is a small component).

In order to deduce information about the three-particle asymptotic normalization factor, it is necessary first to establish the extent to which the model wave function (13) reproduces the asymptotic behavior of the three-particle wave function for $r \to \infty$ and $\rho \to \infty$. For this purpose, it is convenient to make use of the ratio [12]

$$R_{\lambda lLS}(\varphi, \rho) = \frac{\psi_{\lambda lLS}(r, \rho)}{\psi_\nu^{(\mathrm{as})}(R, \varphi)} C_\nu(\varphi), \tag{14}$$

where $\psi_\nu^{(\mathrm{as})}(R, \varphi)$ is given by (11). For $\rho \to \infty$ and $r \to \infty$, we vary the variables r and ρ in such a way as to ensure fulfillment of the equality $r/\rho = \mathrm{const}$, which is equivalent to the condition

$$\varphi = \arctan\left(\sqrt{\mu_{(bc)d}/\mu_{bc}}\,\rho/r\right) \tag{15}$$

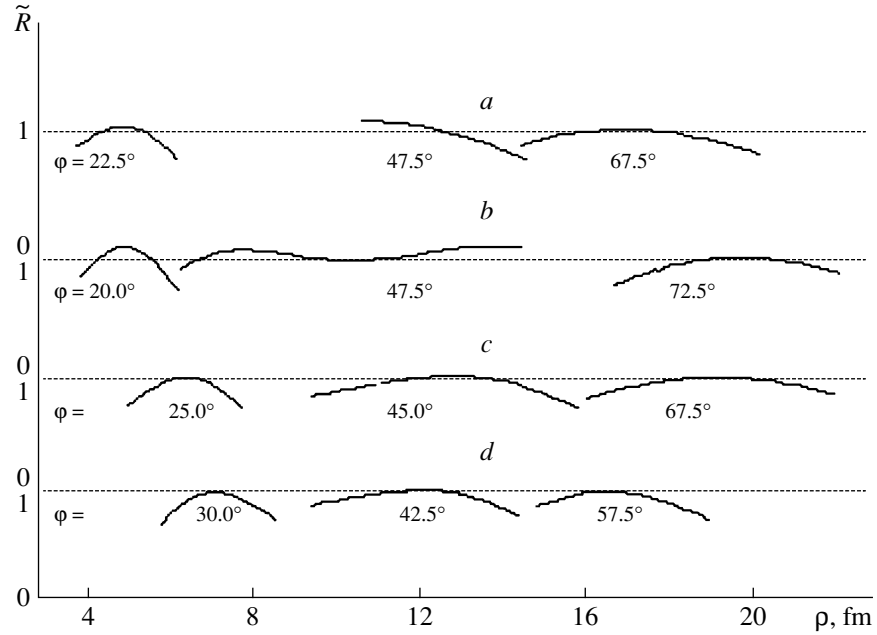

Fig. 1. Ratio $\tilde{R} = \psi_{\lambda l LS}(r,\rho)/\psi_{\nu}^{(\mathrm{as})}(\rho,\varphi)$ of the model radial ^{9}Be wave functions for the M1 model to the corresponding asymptotic expression (11) versus the variable ρ at a fixed value of the hyperangle φ for various sets of quantum numbers: (*a*) $(\lambda, l, L, S) = (0,1,1,1)$; (*b*) $(\lambda, l, L, S) = (2,1,1,1)$; (*c*) $(\lambda, l, L, S) = (2,1,2,1)$; and (*d*) $(\lambda, l, L, S) = (2,3,1,1)$.

$$= \arctan(2\rho/3r) = \mathrm{const}.$$

If the condition in (15) is valid, the values of the variables r and ρ must be chosen in such a way that they belong to the configuration-space region far off the points $q_0' = 0$ and $p_0' = 0$—that is, far off the hyperangle values of $\varphi = \pi/2$ and $\varphi = 0$, respectively, at which the asymptotic formula (11) is not applicable. The asymptotic region of the variables r and ρ that is considered in the present study is given by the inequalities $r \geq 3$ fm and $\rho \geq 3$ fm, the corresponding range of the hyperangle φ in configuration space being $20^\circ \leq \varphi \leq 72.5^\circ$.

We note that, if the model wave function $\psi_{\lambda l LS}(r,\rho)$ has a correct asymptotic behavior, the left-hand side of relation (14) for $\rho \to \infty$ and $\varphi = \mathrm{const}$ is independent of ρ and coincides with the three-particle asymptotic normalization factor:

$$R_{\lambda l LS}(\rho,\varphi) = C_\nu(\varphi). \qquad (16)$$

It is obvious that, at rather large values of r and ρ, the behavior of the wave function (13), which is a finite sum of Gaussian functions, inevitably deviates from the rigorous asymptotic form (11). If, nevertheless, the number of terms on the right-hand side of (11) is large, a situation is possible where, at large (but finite) values of r and ρ, this deviation is moderate. If one plots, on a graph, the ratio $\tilde{R} = \psi_{\lambda l LS}(r,\rho)/\psi_{\nu}^{(\mathrm{as})}(\rho,\varphi)$ versus ρ at fixed values of the hyperangle φ, the curves representing this dependence will feature a maximum (see Fig. 1). By a region where the wave function (13) has a "correct" asymptotic behavior (at $\varphi = \mathrm{const}$), we will imply the ρ interval that contains this maximum and within which the ratio $\tilde{R}$ differs from its value at the maximum by not more than 15%.

The results obtained by analyzing the asymptotic behavior of the model three-particle wave function (13) on the basis of the asymptotic formula (11) and relations (14) and (16) are given in Table 1 for some values of the hyperangle φ. The sets of quantum numbers (λ, l, L, S) and the relative weights P_k (in percent) for each component of the model wave function (13) are presented in the first column of this table. The P_k values quoted in Table 1 correspond to the potentials used in the M1 model. The P_k values corresponding to the M2 model differ insignificantly from the analogous P_k values in the M1 model. The third and the fourth column of Table 1 display three sets of variables r and ρ for each fixed value of the hyperangle φ. The r and ρ values presented in the first and the third row for each fixed value of the hyperangle φ correspond to the lower ($\{r_{\min}, \rho_{\min}\}$) and the upper ($\{r_{\max}, \rho_{\max}\}$) boundary of the interval that was defined above and in which the wave function (13) has a "correct" asymptotic behavior. In the second row, intermediate r and ρ values that approximately correspond to the maxima of the curves in Fig. 1 are given for each value of φ. The

Table 1. Three-particle asymptotic normalization factor $C(\varphi)$ versus the matching point $\{r, \rho\}$ for various sets of quantum numbers (λ, l, L, S) within the M1 and M2 models

(λ, l, L, S) $(P_k, \%)$	φ, deg	r, fm	ρ, fm	C_ν, fm$^{-7/4}$	
				M1	M2
1	2	3	4	5	6
(0, 1, 1, 1)	22.5	7.08	4.42	−158	−270
(40.78)		8.05	5.00	−181	−305
		9.01	5.60	−163	−296
	37.5	5.04	5.80	−232	−320
		6.43	7.40	−256	−360
		7.82	9.00	−223	−334
	47.5	4.77	7.80	−321	−408
		6.48	10.60	−361	−458
		7.70	12.60	−327	−450
	57.5	5.78	13.60	−885	−1020
		6.12	14.40	−898	−1090
		6.97	16.40	−796	−1130
	67.5	4.42	16.00	−4260	−4320
		4.70	17.00	−4340	−4670
		5.19	18.80	−3940	−4760
(2, 1, 1, 1)	20.0	7.69	4.20	−54.7	−99.8
(34.71)		8.79	4.80	−62.0	−115.0
		9.89	5.40	−57.2	−109.0
	45.0	4.13	6.20	−25.8	−48.1
		4.93	7.40	−28.1	−52.3
		5.73	8.60	−26.2	−47.3
	47.5	4.03	6.60	−24.0	−45.4
		4.77	7.80	−26.5	−50.1
		5.62	9.20	−24.9	−45.6
	72.5	3.91	18.60	−134.0	−263.0
		4.21	20.00	−138.0	−292.0
		4.58	21.80	−122.0	−280.0
(2, 1, 2, 1)	25.0	8.58	6.00	−45.3	−87.0
(21.31)		9.15	6.40	−46.7	−93.2
		10.01	7.00	−43.8	−93.4
	45.0	7.60	11.40	−27.0	−49.8
		8.27	12.40	−30.1	−54.1
		8.67	13.00	−30.1	−56.0
	67.5	4.97	18.00	−67.0	−112.0
		5.36	19.40	−64.2	−123.0
		5.52	20.00	−63.3	−125.0
(2, 3, 1, 1)	30.0	8.31	7.20	−1.42	−4.08
(1.67)		8.78	7.60	−1.37	−3.99
		9.24	8.00	−1.26	−3.70
	42.5	8.29	11.40	−1.92	−3.95
		9.02	12.40	−1.95	−3.99
		9.90	13.60	−1.73	−3.51
	57.5	7.14	16.80	−5.86	−14.5
		7.31	17.20	−5.70	−15.0
		7.56	17.80	−5.26	−16.1

Table 2. Ratio $R_{\lambda l} = f_{\lambda l}(r_{\min}, \rho_{\min})/f_{\lambda l}(r_{\max}, \rho_{\max})$ versus the hyperangle φ for various values of the orbital angular momenta (λ, l) and the binding energy ε_a of the ^{9}Be nucleus with respect to the $\alpha\alpha n$ channel

(λ, l)	ε_a, MeV	φ, deg	$r_{\min}$, fm	$r_{\max}$, fm	$\rho_{\min}$, fm	$\rho_{\max}$, fm	$R_{\lambda l}$
(0, 1)	1.76	42.5	4.81	7.57	6.6	10.4	1.19
	1.76	50.0	4.81	7.83	8.6	14.0	1.16
	2.86	42.5	4.66	8.00	6.4	11.0	1.22
	2.86	50.0	5.71	8.39	10.20	15.0	1.19
(2, 1)	1.76	32.5	4.60	9.21	4.40	8.80	2.60
	1.76	47.5	4.15	9.53	6.80	15.60	2.97
	2.86	32.5	6.28	8.79	6.00	8.40	1.45
	2.86	47.5	4.03	5.62	6.60	9.2	1.57
(2, 3)	1.76	42.5	6.99	9.90	9.6	13.6	2.32
	1.76	62.5	5.55	6.60	16.0	19.0	1.48
	2.86	42.5	6.55	10.62	9.0	14.6	2.76
	2.86	62.5	6.39	7.57	18.4	21.8	1.36

three-particle asymptotic normalization factor $C_\nu(\varphi)$ calculated on the basis of formulas (14) and (16) for the aforementioned three sets of r and ρ (treated as the points of matching) is given in the fifth and the sixth column of Table 1 for the potentials of the M1 and the M2 model, respectively.

From Table 1 and from the results that are not given there and which are associated with other values of the hyperangle φ, it follows that, in general, the interval Δ of ρ values ($\Delta = \rho_{\max} - \rho_{\min}$) within which the wave function (13) has a correct (to within 15%) asymptotic behavior becomes wider with increasing φ. This can also be seen from Fig. 1, where the calculated ratio $\tilde{R}_{\lambda l LS}(r, \rho) = \psi_{\lambda l LS}(r, \rho)/\psi^{(\mathrm{as})}_{\lambda l LS}(R, \varphi)$ is given as a function of ρ for various values of the hyperangle φ. In plotting the curves in Fig. 1, we employed the values of the three-particle asymptotic normalization factor $C_\nu(\varphi)$ from Table 1 that correspond to the M1 model (fifth column) and the set $\{r_{\min}, \rho_{\min}\}$ (the upper row of the values of $\{r, \rho\}$ for each value of φ). From Fig. 1, it can be seen that, with increasing φ, the region of a correct asymptotic behavior of the model wave function $\psi_{\lambda l LS}(r, \rho)$ (13) is shifted toward large values of ρ, its width Δ becoming larger. From the results of our calculations, it also follows that the width Δ depends on the form of the $\alpha\alpha$ potential used. By way of example, we indicate that, for the $(\lambda, l, L, S) = (2, 1, 1, 1)$ configuration at $\varphi = 47.5°$, $\Delta \approx 9$ fm for the M1 model and $\Delta \approx 3$ fm for the

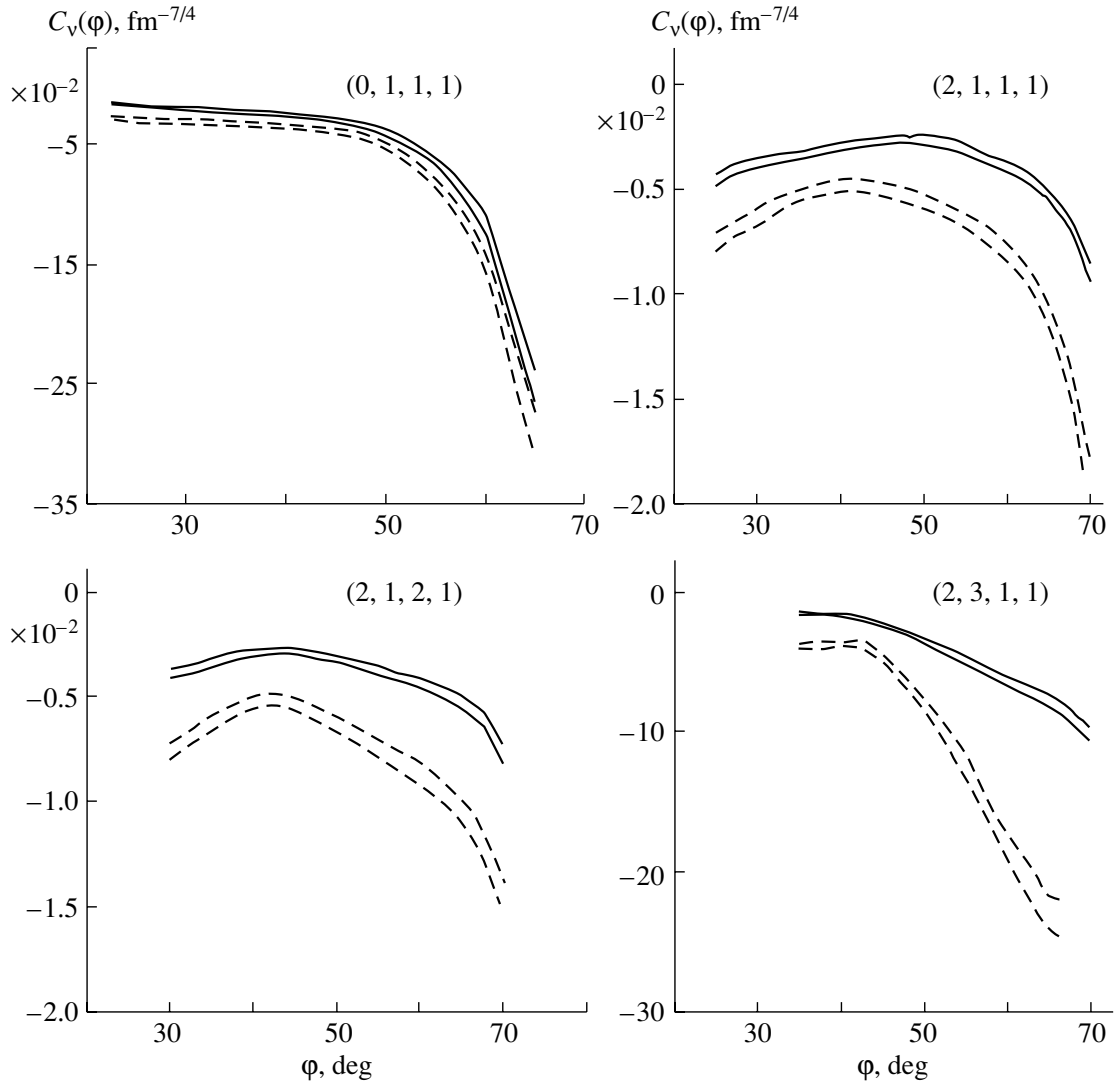

Fig. 2. Three-particle asymptotic normalization factor $C_\nu(\varphi)$ versus the hyperangle φ according to calculations with the ^{9}Be radial wave functions for various sets of quantum numbers (λ, l, L, S). The solid (dashed) curves correspond to the potentials of the M1 (M2) model.

M2 model. In all probability, this is because the ^{9}Be binding energy is less in the M1 than in the M2 model, with the result that the wave function (13) in the M1 model has a longer asymptotic tail in the variable ρ than the wave function in the M2 model. It should also be noted that, at $\lambda \neq 0$ and $l \neq 0$, the factors $f_{\lambda l}(r,\rho) = f_\lambda(i\sqrt{\varepsilon_a}R\cos^2\varphi) f_l(i\sqrt{\varepsilon_a}R\sin^2\varphi)$ affect significantly the absolute values of the asymptotic expression for the three-particle wave function. In Table 2, the calculated values of the ratio $R_{\lambda l} = f_{\lambda l}(r_{\min},\rho_{\min})/f_{\lambda l}(r_{\max},\rho_{\max})$ are given for the purpose of illustration for various values of the orbital angular momenta (λ, l) and the hyperangle φ. From this table, one can see that the effect of the factor $f_{\lambda l}(r,\rho)$ on the three-particle wave function is sizable and that this effect depends significantly on the orbital angular momenta (λ, l) and on the hyperangle φ.

It was indicated above that the asymptotic formula (11), which was derived in the present study, may become invalid at values of the hyperangle φ that are close to 0 or $\pi/2$. For this reason, we considered only the interval $22.5^\circ \leq \varphi \leq 70^\circ$ in determining the three-particle asymptotic normalization factor $C_\nu(\varphi)$ from a comparison of the model wave function (13) and the asymptotic formula (11). For all hyperangles from this interval, the condition $\Delta \geq 2$ fm holds.

Figure 2 shows the extracted values of $C_\nu(\varphi)$. The solid (dashed) curves in this figure correspond to the potentials of the M1 (M2) model. For either model, the upper and the lower curve represent, respectively, the maximum and the minimum values of $C_\nu(\varphi)$

within the interval Δ. From Fig. 2, one can draw the important conclusion that the extracted values of the three-particle asymptotic normalization factor $C_\nu(\varphi)$ are highly sensitive to the nuclear model used to determine the ^{9}Be wave function, actually to the form of the $\alpha\alpha$ potential, which is markedly different in the M1 and in the M2 model.

4. CONCLUSION

Here, we briefly list the basic results of this study.

An explicit asymptotic expression for the radial component of the three-particle wave function for an $a = (bcd)$ bound state in the limit at large values of the hyperradius ($R \to \infty$) has been obtained for the case of two charged particles. The asymptotic expression derived in the present study has been compared with the asymptotic expression for the ^{9}Be model ($\alpha\alpha n$) three-particle wave function [5, 6, 21] involving three dominant and one small component that correspond to various sets of quantum numbers (λ, l, L, S). The intervals of the Jacobi variables r and ρ within which the (λ, l, L, S) components have a correct asymptotic behavior within a preset accuracy have been determined. The effect of the centrifugal potentials, which are determined by the factor $f_{\lambda l}(R, \varphi)$, on the asymptotic values of the three-particle wave functions has been estimated, and it has been shown that this effect depends greatly on the direction in configuration space.

Information about the values of the three-particle asymptotic normalization factor $C_\nu(\varphi)$ over a wide range of the hyperangle φ has been obtained, and it has been found that they are highly sensitive to the form of the $\alpha\alpha$ potential. For this reason, it is of interest to obtain "experimental" information about the three-particle asymptotic normalization factor, for example, from data on the reaction $^9\mathrm{Be}(p, d)\alpha\alpha$ or $^9\mathrm{Be}(d, t)\alpha\alpha$ by continuing the experimental differential cross sections to the pole of the reaction amplitude corresponding to the pole mechanism of neutron transfer.[3)] This would make it possible to refine the form of potentials for the $\alpha\alpha$ and αn interactions by comparing the phenomenological values of $C_\nu(\varphi)$ with their theoretical counterparts obtained from the above analysis of the ^{9}Be wave functions calculated by using various forms of the $\alpha\alpha$ and αn potentials.

It should be noted that, in general, the values of the three-particle asymptotic normalization factor $C_{a\nu}(\varphi)$ that have been extracted from the present analysis may involve additional ambiguities that arise from the expected dependence of the model wave function in the asymptotic region on the numbers n_i and n_j of basis functions in expansion (13) (in our case, $n_i = n_j = 7$). An increase in n_i and n_j is expected to result in the expansion of the range Δ within which the model wave function (13) would have a correct asymptotic behavior and, hence, in the improvement of the accuracy to which one assesses the three-particle asymptotic normalization factor. In this connection, it would be of importance to construct a model wave function of the form in (13) but for greater values of the parameters n_i and n_j than in [5, 6, 21].

[3)] A similar method was successfully used in [24] to determine the three-particle asymptotic normalization factor for the $^3\mathrm{He} \to p + p + n$ vertex function from data on the reaction $^3\mathrm{He}(p, d)pp$.

ACKNOWLEDGMENTS

We are grateful to V.I. Kukulin for placing at our disposal an improved version of the wave functions for the ^{9}Be ground state.

This work was supported in part by the Foundation for Basic Research of the Uzbek Academy of Sciences (project no. 18-99) and by the Russian Foundation for Basic Research (project no. 04-02-16602).

REFERENCES

1. D. Baye, P. Descouvemont, and N. K. Timofejuk, Nucl. Phys. A **588**, 147 (1995).
2. N. K. Timofejuk, P. Descouvemont, and D. Baye, Nucl. Phys. A **600**, 1 (1996).
3. N. K. Timofejuk, Nucl. Phys. A **631**, 19 (1998).
4. V. I. Kukulin, V. N. Pomerantsev, Kh. D. Razikov, *et al.*, Nucl. Phys. A **586**, 151 (1995).
5. V. T. Voronchev, V. I. Kukulin, V. N. Pomerantsev, *et al.*, Yad. Fiz. **57**, 1964 (1994) [Phys. At. Nucl. **57**, 1890 (1994)].
6. V. T. Voronchev, V. I. Kukulin, V. N. Pomerantsev, and G. G. Ryzhikh, Few-Body Syst. **18**, 191 (1995).
7. M. V. Zhukov, B. V. Danilin, D. V. Fedorov, *et al.*, Phys. Rep. **231**, 151 (1993).
8. B. V. Danilin, I. J. Thompson, J. S. Vaagen, and M. V. Zhukov, Nucl. Phys. A **632**, 383 (1998).
9. D. Bay, M. Kruglansk, and M. Vincke, Nucl. Phys. A **573**, 431 (1994).
10. S. P. Merkur'ev and L. D. Faddeev, *Quantum Scattering Theory for Few-Body Systems* (Nauka, Moscow, 1985) [in Russian].
11. L. D. Blokhintsev, I. Borbely, and E. I. Dolinsky, Fiz. Élem. Chastits At. Yadra **8**, 1189 (1977) [Sov. J. Part. Nucl. **8**, 485 (1977)].
12. L. D. Blokhintsev, M. K. Ubaidullaeva, and R. Yarmukhamedov, Yad. Fiz. **62**, 1368 (1999) [Phys. At. Nucl. **62**, 1289 (1999)].
13. L. D. Blokhintsev and É. I. Dolinskiĭ, Yad. Fiz. **5**, 797 (1967) [Sov. J. Nucl. Phys. **5**, 565 (1967)].

14. É. I. Dolinskiĭ and A. M. Mukhamedzhanov, Yad. Fiz. **3**, 252 (1966) [Sov. J. Nucl. Phys. **3**, 180 (1966)].
15. A. M. Mukhamedzhanov, M. K. Ubaidullaeva, and R. Yarmukhamedov, Teor. Mat. Fiz. **94**, 448 (1993).
16. I. S. Gradshteĭn and I. M. Ryzhik, *Table of Integrals, Series, and Products* (Nauka, Moscow, 1971; Academic, New York, 1980).
17. M. V. Fedoryuk, *Saddle-Point Technique* (Nauka, Moscow, 1977) [in Russian].
18. L. D. Blokhintsev, S. N. Belolipetskiĭ, and R. Yarmukhamedov, in *Proceedings of the International Seminar "Microscopic Methods in the Theory of Few-Body Systems", Kalinin, 1988*, Part 1, p. 35.
19. M. A. Zhusupov, S. K. Sakhiev, and T. D. Kaipov, Izv. Akad. Nauk, Ser. Fiz. **60** (11), 123 (1996).
20. B. Buck, H. Friedrich, and C. Wheatley, Nucl. Phys. A **275**, 246 (1977).
21. V. I. Kukulin, private communication.
22. S. Ali and A. R. Bodmer, Nucl. Phys. **80**, 99 (1966).
23. V. G. Neudatchin, V. I. Kukulin, V. L. Korotkikh, and V. P. Korennoy, Phys. Lett. B **34B**, 581 (1971).
24. G. V. Avakov *et al.*, Yad. Fiz. **47**, 1508 (1988) [Sov. J. Nucl. Phys. **47**, 957 (1988)].

Translated by A. Isaakyan

Physics of Atomic Nuclei, Vol. 68, No. 8, 2005, pp. 1381–1394. Translated from Yadernaya Fizika, Vol. 68, No. 8, 2005, pp. 1436–1450.

NUCLEI
Theory

Quark Microscopic Picture for Vector and Pseudoscalar Mesons in the Nucleon and Their Quasielastic Knockout by High-Energy Electrons

I. T. Obukhovsky*, V. G. Neudatchin, L. L. Sviridova, and N. P. Yudin

Institute of Nuclear Physics, Moscow State University, Vorob'evy gory, Moscow, 119899 Russia

Received July 6, 2004

Abstract—A technique for projecting a multiquark wave function in the microscopic model of a $^3P_0$ scalar fluctuation onto the virtual-decay channels $N \to N + \rho$ and $N \to N + \pi$ is formulated (at a more general level for the latter than previously). The amplitude for the electromagnetic transition $\rho + \gamma_T^* \to \pi$ in electron-induced quasielastic rho-meson knockout followed by rho-meson conversion to a pion is considered. Theoretical results obtained in this way are contrasted against available experimental data, and reasonable agreement is found for cross-section values. This confirms a universal character of the $^3P_0$ model. The precision of relevant experiments is as yet insufficient for comparing the momentum distribution of the rho meson from the channel $N \to N + \rho$ with its theoretical counterpart. © *2005 Pleiades Publishing, Inc.*

1. INTRODUCTION

Much attention has been given in the literature to constructing a quark microscopic description of hadron degrees of freedom in the nucleon [1–5]. This approach is used to analyze the deep-inelastic scattering of leptons on nucleons and nuclei [6, 7], pion photo- [8] and electroproduction [9], and the decays of excited nucleon states to pions and rho mesons [10–12]. In principle, such a description may form a basis of a unified approach to studying a broad set of various meson–baryon components in the nucleon in terms of a minimum number of parameters that characterize vacuum polarization by the color charges of the nucleon quarks and the sizes of hadrons.

In [13, 14], it was indicated that quasielastic meson knockout induced by high-energy electrons provides a highly efficient tool for studying the quark microscopic picture of the structure of the nucleon and its meson cloud. In the laboratory frame, this process is described by two t-channel pole diagrams (of these, one is the z diagram) and is realized for pions at intermediate values of the squared virtual-photon mass Q^2, $1 \lesssim Q^2 \lesssim 3\,(\mathrm{GeV}/c)^2$. This makes it possible to extract, from experimental data directly, the momentum distributions of mesons M in individual decay channels $N \to B + M$; as a result, one can determine the corresponding wave functions and their normalization (spectroscopic factors). For a broader discussion on this issue, the interested reader is referred to the recent articles of our group [15–17] (for an overview, see [18]).

Since $Q^2 = 0$ (pion photoproduction), the contributions of the s- and t-channel pole diagrams are commensurate [8], so that the extracted information about the pole in the t channel is not so clear. At $Q^2 \approx 10$–$20\ (\mathrm{GeV}/c)^2$, meson electroproduction must be considered at the level of perturbative QCD and the corresponding diagram technique without indulging in the use of concepts of the physics of "soft" hadronic degrees of freedom (which is applicable in the region of intermediate energies) such as quasielastic meson knockout and momentum distributions in various channels.

In just the same way as in [15–17], we rely here on the model of a localized scalar $q\bar{q}$ fluctuation ($^3P_0$) in the QCD vacuum [1, 5]. Albeit being conceptually similar to other approaches to the issues being discussed, this model may differ from them in a number of important details. For example, the fluctuation considered here is color-singlet (in all probability, this is so precisely for knock-on mesons of intermediate energy in the range between 1 and 2 GeV, in which case the color-singlet channel of the primary interaction between the projectile electron and a virtual meson has time to be formed). On the contrary, the fluctuation has color in the string model advocated in [2, 10, 11], which corresponds to higher meson energies and in which the underlying physics presumes the scenario where an instantaneous electron impact

*e-mail: obukh@nucl-th.sinp.msu.ru

directly on a quark is followed by the hadronization of this quark. This issue of the physical pattern can be explored experimentally in meson electroproduction processes (see below) at various values of the final meson energy.

Within the model being discussed, our group calculated the momentum distributions of pions in the virtual-decay channels $N \to B + \pi$ [$B = N$, Δ, $N^*(3/2^-, 1/2^-)$, $N^{**}(1/2^+)$ (Roper)] [13, 15, 17] and the momentum distributions of kaons in the channels $N \to \Lambda + K, \Sigma + K$ [16, 17]. The formalism here is based on a specific rearrangement of quark coordinates between the nucleon (q^3) and the $q\bar{q}$ fluctuation, since the $^3P_0$ fluctuation is a scalar having the spin of $S = 1$, while the pion is an isovector of zero spin. Thus, the calculated momentum distributions provide, within the model being studied, a special multifaceted characterization of the synthesis of primary degrees of freedom (valence quarks of the nucleon, on one hand, and sea quarks and antiquarks, on the other hand) into various secondary soft meson–baryon degrees of freedom, both mesons and baryons being treated as composite particles. To some extent, this resembles the formation of cluster degrees of freedom in a nucleus [19]. Of course, this multichannel approach is highly sensitive to the structure of the fluctuation model used.

The above range of specific physics problems corresponds to the quasielastic knockout of pions [13, 15, 17] and kaons [16, 17], which involves longitudinal virtual photons (γ_L^*). The processes in question are diagonal in the quantum numbers of the knocked-on charged meson: $\pi^{*+} + \gamma_L^* \to \pi^+$ and $K^{*+} + \gamma_L^* \to K^+$ (although the possibility of the deexcitation of virtual states through the processes $\pi^* \to \pi$ and $K^* \to K$ without changes in their spin–isospin structure is also implied—see below).

The momentum distribution that we extracted in the pole approximation for pions in the channel $N \to N + \pi$ (in doing this, we used data in the region $1 \lesssim Q^2 \lesssim 3$ (GeV/c)^2 [20–22] as a basis) proved to be in reasonable agreement in shape with the results of the calculation within the model of a $^3P_0$ scalar fluctuation [15, 17]. As a good illustration of the validity of the pole approximation, we can indicate that the resulting shape of the momentum distribution is quite compatible with the cutoff-constant value of $\Lambda_\pi = 0.7$ GeV/c, which appears in the phenomenological theory of pion–nucleon coupling. This value was determined previously in [23] from data on pion electroproduction in the delta-resonance region. Further, it was briefly mentioned in [17] that the scalar-fluctuation constant g_s can be expressed in terms of the phenomenological pseudovector pion–nucleon coupling constant $f_{\pi NN}$, and this provides the possibility of analyzing the normalization of the momentum distribution in the channel $p \to n + \pi^+$ as well—that is, the possibility of supplementing our consideration with an analysis of the absolute value of the cross section for quasielastic pion knockout in the reaction $p(e, e'\pi^+)B$ involving spectator baryons B listed above.

We hope that, together with the predictions formulated in the present article for the momentum distributions of vector mesons, the momentum distributions (including their normalization) calculated for the channels $N \to B + \pi$ [15, 17] and $N \to Y + K$ [16] will give impetus to performing new exclusive coincidence experiments in the Jefferson Laboratory. In particular, the latest data from this laboratory [22, 24] on quasielastic pion and kaon knockout were analyzed in [17], and it was shown there that these data are in good agreement with our predictions in the range $1 \lesssim Q^2 \lesssim 2$ (GeV/c)^2 for pions. For kaons, the data in question made it possible to assess more accurately the degree to which strange fluctuations ($\bar{s}s$) in the nucleon are suppressed in relation to nonstrange fluctuations ($\bar{u}u$ and $\bar{d}d$).

The ensuing exposition is organized as follows. A formal scheme for projecting the nucleon wave function dressed with a $\bar{q}q$ scalar fluctuation onto the virtual-nucleon-decay channels $N \to B + \rho$ and $N \to B + \omega$, which involve vector mesons, is a key point of the present study. This scheme, which is based on the covariant model employing a scalar source of $\bar{q}q$ pairs [4, 17], is formulated in Section 2. By considering the example of pions and rho mesons, we discuss the important possibility of going over from the universal quark microscopic picture to the phenomenological theory of meson–nucleon coupling for various meson channels; as was indicated above, this makes it possible to express the known phenomenological parameters of coupling to the nucleon for pseudoscalar and vector mesons, such as $f_{\pi NN}$ and $f_{\rho NN}$, in terms of the scalar-fluctuation constant g_s. This in turn enables one to determine the constant g_s in terms of the known quantity $f_{\pi NN}$ and to relate parameters, such as $f_{\pi NN}$ and $f_{\rho NN}$, to one another through the microscopic picture, as well as to predict their values for various virtual-decay channels $N \to B + M$. In addition, we derive microscopic expressions for the vertex functions $F_{\pi NN}(\mathbf{k})$ and $F_{\rho NN}(\mathbf{k})$. As a result, we can write expressions for the momentum distributions of the above mesons, including the normalization of these distributions, and proceed to discuss the differential cross sections for quasielastic knockout (Section 3). In this discussion, we rely on experiments that study processes where quasielastic rho-meson knockout induced by high-energy electrons that involves transverse virtual

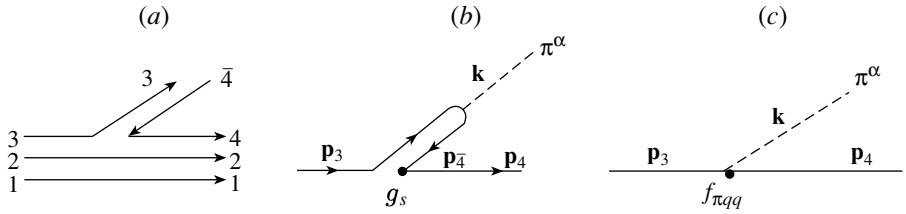

Fig. 1. Diagrams representing quark–pion coupling in (*a*, *b*) the model of a scalar $\bar{q}q$ fluctuation and (*c*) the Riska–Brown chiral model [12].

photons γ_T^* characterized by $Q^2 \sim 2$–3 $(\mathrm{GeV}/c)^2$ is followed by the spin-flip conversion of the virtual rho meson to a pion $(\rho + \gamma_T^* \to \pi)$ [9, 13, 14]. This corresponds to measuring the transverse differential cross section $d\sigma_T/dt$ for pion electroproduction via the process $p(e, e'\pi^+)n$ in quasielastic-knockout kinematics. The required electromagnetic meson form factors are discussed in Section 3 in connection with the problems arising in directly analyzing the differential cross sections for $p(e, e'\pi^+)B$ processes involving longitudinal and transverse virtual photons. Also, the question of what information can be deduced from the absolute values of these cross sections for refining the constant g_s is analyzed there. Finally, the possibility of further exploring the properties of $^3P_0$-fluctuations in various meson–baryon channels is considered in Section 4, which concludes our present study.

2. PROJECTING THE QUARK WAVE FUNCTION FOR THE NUCLEON ONTO BARYON–MESON CHANNELS INVOLVING VECTOR AND PSEUDOSCALAR MESONS AND CONNECTION WITH PHENOMENOLOGY

Since the mechanism of meson production (absorption) is essentially nonperturbative at low and intermediate energies, a detailed ab initio description is impossible here. In view of this, use is made of a phenomenological model of a $^3P_0$ scalar fluctuation [1, 4, 5, 17] in the form that satisfies the empirical Okubo–Zweig–Iizuka rule [25], according to which quark annihilation transitions must be suppressed in hadronic processes. A special role assigned to a color-singlet scalar (not vector) $q\bar{q}$ fluctuation complies well with the well-known suppression of vector annihilation transitions in meson-production and meson-decay processes, which is explained only within QCD, a theory where quarks interact with color vector gluons.

The physics content of the problem considered here corresponds to the following scheme: in the nucleon, the (1 2 3 4 $\bar{4}$) quark system fragments into the (1 2 4) and (3 $\bar{4}$) subsystems (Fig. 1), which can be formed in various excited states (this wide variety of information permits a profound verification of the model). For the $^3P_0$ scalar $q\bar{q}$ fluctuation of spin $S = 1$ and isospin $T = 0$ to be compatible with the production of an $S = 1, T = 1$ rho-meson state in the field of a baryon B (including the case of the $B = N$ diagonal transition), it is necessary to consider the redistribution of quarks between the original (1 2 3) and (4 $\bar{4}$) subsystems.[1)]

In addition to the fact that the model being considered possesses a "correct" algebraic structure, it presumes a specific prediction for the shape of the momentum distribution of mesons in the nucleon (or of meson–baryon form factors), and this is the point in which we are interested first of all. More specifically, the momentum distribution of mesons must replicate (with allowance for the motion of the common center of mass) the momentum distribution of constituent quarks in the nucleon. We show that this prediction can readily be tested in quasielastic-meson-knockout processes and present the corresponding estimates for pions and rho mesons.

Such predictions are quite general and are independent of a specific mechanism of the production of $q\bar{q}$ pairs—this may be the mechanism of rupturing color-flux tubes [2], the Schwinger mechanism of pair production in a classical external field (a color field in the present case [26]), or some other mechanism. It is the most convenient to use the universal formulation proposed in [4] and to represent the Hamiltonian for the production of $q\bar{q}$ pairs in the $^3P_0$ state in a covariant form by introducing interaction with a scalar source of these pairs:

$$H_s = g_s \int d^3x \bar{\psi}_q(x) Z \psi_q(x) \qquad (1)$$
$$= g_s \int d^3x [\bar{u}(x)u(x) + \bar{d}(x)d(x) + z\bar{s}(x)s(x)].$$

[1)] We note that, within the model being considered, only in the knockout of a scalar f_0 meson (whose internal structure is assumed to be $q\bar{q}$) via processes like $N(\pi, \pi f_0)N$ would the redistribution of quarks between the subsystems be unnecessary, with the result that the momentum distribution of f_0 mesons would feature a peak at zero momentum, this peak corresponding to projecting the $^3P_0$ fluctuation as such onto the f_0 meson. Obviously, there must be no such peak in the case of a color fluctuation [2, 10].

Here, $u(x)$, $d(x)$, and $s(x)$ are the Dirac fields of the triplet of constituent quarks (summation over the three color indices of quarks is also implied, but it is not indicated here to avoid encumbering the presentation).

The Hamiltonian in (1) is considered here as an effective operator that describes nonperturbative dynamics in terms of the creation and annihilation of $q\bar{q}$ pairs. In expression (1), $SU(3)_F$ symmetry is broken (if it is assumed that $z \neq 1$)[2)] because of the mass difference between the strange and nonstrange quarks; however, this distinction is of importance only for the strange sector [16, 17], which is not considered here.

In terms of the creation and annihilation operators $b^\dagger_{\mu\alpha}(\mathbf{p})$, $b_{\mu\alpha}(\mathbf{p})$, $d^\dagger_{\bar{\mu}\bar{\alpha}}(\mathbf{p})$, and $d_{\bar{\mu}\bar{\alpha}}(\mathbf{p})$ defined in Fock space,

$$\{b^\dagger_{\mathbf{p}'\mu'\alpha'}, b_{\mathbf{p}\mu\alpha}\} = \delta_{\mu\mu'}\delta_{\alpha\alpha'}\frac{E_q(\mathbf{p})}{m_q}(2\pi)^3\delta(\mathbf{p}-\mathbf{p}'), \tag{2}$$

$$b_{\mathbf{p}\mu\alpha}|0\rangle = 0, \text{ etc.},$$

the component H_s corresponding to the production of scalar $q\bar{q}$ pairs has the form

$$H_{\text{pair}} = g_s \sum_{\alpha\mu}\int \frac{d^3p}{(2\pi)^3}\frac{m_q}{E_p} \tag{3}$$
$$\times \int \frac{d^3p'}{(2\pi)^3}\frac{m_q}{E_{p'}}(2\pi)^3\delta(\mathbf{p}+\mathbf{p}')\bar{u}(\mathbf{p}\mu)$$
$$\times v(\mathbf{p}'\bar{\mu})b^\dagger_{\mu\alpha}(\mathbf{p})d^\dagger_{\bar{\mu}\bar{\alpha}}(\mathbf{p}'),$$

where $\alpha = u, d, s$ and $E_p(\mathbf{p}) = \sqrt{m_q^2+\mathbf{p}^2}$. Here, m_q is the constituent quark mass, $m_q \approx M_N/3 \approx m_\rho/2$ (or $m_q = m_s \approx m_\phi/2$ in the strange sector), and the Dirac bispinors are subjected to the standard normalization condition $\bar{u}(\mathbf{p}\mu)u(\mathbf{p}\mu') = \delta_{\mu\mu'}$.

The amplitudes for meson emission (absorption) in $N \to M + B$ and $M \to M_1 + M_2$ processes are defined as the matrix elements

$$\mathcal{M}_s(N \to M + B) = \langle M|\langle B|H_s|N\rangle, \tag{4}$$
$$\mathcal{M}_s(M \to M_1 + M_2) = \langle M_1|\langle M_2|H_s|M\rangle,$$

where the initial and the final state are basis vectors of hadronic states in the constituent quark model. In particular, we use the following expressions for the pion and the nucleon:

$$|\pi(\widetilde{\bar{q}q}), \alpha, \mathbf{k}\rangle = i\int \frac{d^3p_3}{(2\pi)^3}\frac{m_q}{E_q(\mathbf{p}_3)} \tag{5}$$
$$\times \int \frac{d^3p_{\bar{4}}}{(2\pi)^3}\frac{m_q}{E_q(\mathbf{p}_{\bar{4}})}(2\pi)^3\delta(\mathbf{k}-(\mathbf{p}_3+\mathbf{p}_{\bar{4}}))$$
$$\times \Phi_\pi(\boldsymbol{\varkappa}, \mathbf{k})\sum_{c\bar{c}}(\delta_{c\bar{c}}/\sqrt{3})\sum_{\mu_3\bar{\mu}_{\bar{4}}}(-1)^{1/2-\bar{\mu}_{\bar{4}}}$$
$$\times \left(\frac{1}{2}\mu_3\frac{1}{2}-\bar{\mu}_{\bar{4}}\middle|00\right)\sum_{t_3t_{\bar{4}}}(-1)^{1/2-\bar{t}_{\bar{4}}}$$
$$\times \left(\frac{1}{2}t_3\frac{1}{2}-\bar{t}_{\bar{4}}\middle|1\alpha\right)b^\dagger_{\mathbf{p}_3\mu_3t_3}d^\dagger_{\mathbf{p}_{\bar{4}}\bar{\mu}_{\bar{4}}\bar{t}_{\bar{4}}}|0\rangle$$

[here, $\delta_{c\bar{c}}/\sqrt{3}$ is the color component of the wave function, where, for the sake of simplicity, we have omitted the obvious indices 3 and $\bar{4}$ on the color projections of the quark and the antiquark and have not indicated them on the creation operators $b^\dagger$ and $d^\dagger$; in addition, we have used the following notation: α is the pion isospin projection (that is, the pion charge) and $\boldsymbol{\varkappa} = (\mathbf{p}_3 - \mathbf{p}_{\bar{4}})/2$];

$$|N(\widetilde{3q}), \mu, t, \mathbf{P}\rangle = \int \frac{d^3p_1}{(2\pi)^3}\frac{m_q}{E_q(\mathbf{p}_1)} \tag{6}$$
$$\times \int \frac{d^3p_2}{(2\pi)^3}\frac{m_q}{E_q(\mathbf{p}_2)}\int \frac{d^3p_3}{(2\pi)^3}\frac{m_q}{E_q(\mathbf{p}_3)}(2\pi)^3$$
$$\times \delta\left(\mathbf{P}-\sum_i \mathbf{p}_i\right)\Phi_N(\boldsymbol{\varkappa}_1, \boldsymbol{\varkappa}_2; \mathbf{P})$$
$$\times \sum_{\mu_i}\sum_{t_i}\left[2^{-1/2}\left(\frac{1}{2}\mu_1\frac{1}{2}\mu_2\middle|1\mu_{12}\right)\right.$$
$$\times \left(1\mu_{12}\frac{1}{2}\mu_3\middle|\frac{1}{2}\mu\right)\left(\frac{1}{2}t_1\frac{1}{2}t_2\middle|1t_{12}\right)\left(1t_{12}\frac{1}{2}t_3\middle|\frac{1}{2}t\right)$$
$$\left. + 2^{-1/2}\delta_{\mu_3\mu}\delta_{t_3t}\left(\frac{1}{2}\mu_1\frac{1}{2}\mu_2\middle|00\right)\left(\frac{1}{2}t_1\frac{1}{2}t_2\middle|00\right)\right]$$
$$\times b^\dagger_{p_1\mu_1t_1}b^\dagger_{p_2\mu_2t_2}b^\dagger_{p_3\mu_3t_3}\middle|0\rangle$$

[here, we have omitted the (obvious) color part, which is proportional to $\varepsilon_{c_1c_2c_3}$, and have introduced the following notation for the relative momenta of the quarks in the nucleon: $\boldsymbol{\varkappa}_1 = (\mathbf{p}_1 - \mathbf{p}_2)/2$ and $\boldsymbol{\varkappa}_2 = (\mathbf{p}_1 + \mathbf{p}_2)/3 - 2\mathbf{p}_3/3$].

In the following we will omit the color part of the wave functions in order to avoid encumbering the displayed equations. In the case being considered, the presence of the color part only leads to the appearance of the additional factor $\sqrt{3}$ in the expressions for the amplitudes describing the annihilation (creation) of mesons as $\bar{q}q$ states.

In the shell approximation used, the rho-meson wave function

$$|\rho(\widetilde{\bar{q}q}), m, \alpha, \mathbf{k}\rangle = \int \frac{d^3p_3}{(2\pi)^3}\frac{m_q}{E_q(\mathbf{p}_3)} \tag{7}$$
$$\times \int \frac{d^3p_{\bar{4}}}{(2\pi)^3}\frac{m_q}{E_q(\mathbf{p}_{\bar{4}})}(2\pi)^3\delta(\mathbf{k}-(\mathbf{p}_3+\mathbf{p}_{\bar{4}}))$$

[2)] In some studies (see, for example, [17]), this quantity was estimated at $z \simeq 0.5-0.8$.

$$\times \Phi_\rho(\boldsymbol{\varkappa}, \mathbf{k}) \sum_{\mu_3 \bar{\mu}_{\bar{4}}} (-1)^{1/2-\bar{\mu}_{\bar{4}}} \left(\frac{1}{2}\mu_3 \frac{1}{2} - \bar{\mu}_{\bar{4}} \middle| 1m\right)$$

$$\times \sum_{t_3 t_{\bar{4}}} (-1)^{1/2-\bar{t}_{\bar{4}}} \left(\frac{1}{2} t_3 \frac{1}{2} - \bar{t}_{\bar{4}} \middle| 1\alpha\right) b^\dagger_{\mathbf{p}_3 \mu_3 t_3} d^\dagger_{\mathbf{p}_{\bar{4}} \bar{\mu}_{\bar{4}} \bar{t}_{\bar{4}}} |0\rangle,$$

which is specified in the rho-meson rest frame (that is, at $\mathbf{k} \to 0$), differs from the pion wave function in (5) only in the replacement of the Clebsch–Gordan coefficient $(-1)^{1/2-\bar{\mu}_{\bar{4}}} \left(\frac{1}{2}\mu_3 \frac{1}{2} - \bar{\mu}_{\bar{4}} \middle| 00\right)$, which corresponds to the composition of the quark and antiquark spins to the total spin equal to zero, by the analogous coefficient $(-1)^{1/2-\bar{\mu}_{\bar{4}}} \left(\frac{1}{2}\mu_3 \frac{1}{2} - \bar{\mu}_{\bar{4}} \middle| 1m\right)$, which corresponds to the total rho-meson spin equal to unity, where m is the spin projection onto the quantization axis, which we choose to be aligned with the vector $\mathbf{k}$. Thus, the rho-meson polarization 4-vector ρ^μ (normalized, as a spacelike vector, by the condition $\rho^\mu \rho_\mu = -1$) is represented in the rho-meson rest frame ($\rho^\mu = \{0, \hat{\boldsymbol{\rho}}\}$) in the form of an expansion in three spherical components,

$$\hat{\boldsymbol{\rho}} = \sum_{m=0,\pm1} \rho^{(m)} \boldsymbol{\epsilon}^{(m)*}, \quad \boldsymbol{\epsilon}^{(\pm1)} = \mp(\hat{\mathbf{n}}_1 \pm i\hat{\mathbf{n}}_2)/\sqrt{2},$$

$$\epsilon^{(0)} = \hat{\mathbf{n}}_3.$$

By virtue of its orthogonality to the timelike vector $k^\mu = \{m_\rho, \mathbf{k} = 0\}$, it automatically satisfies the four-dimensional-transverseness condition

$$\rho^\mu k_\mu = 0. \tag{8}$$

In an arbitrary rest frame, $\mathbf{k} \neq 0$, and the polarization vector of the rho-meson state $|\rho, m, \alpha, \mathbf{k}\rangle$ is obtained by applying the corresponding Lorentz transformation to the spacelike vector $\{0, \hat{\boldsymbol{\rho}}\}$. The result has the form

$$\rho^\mu = \left\{ \frac{\mathbf{k} \cdot \hat{\boldsymbol{\rho}}}{m_\rho}, \hat{\boldsymbol{\rho}} + \left(\frac{\omega_\rho}{m_\rho} - 1\right)(\mathbf{k} \cdot \hat{\boldsymbol{\rho}})\hat{\mathbf{k}} \right\}, \tag{9}$$

where $\hat{\mathbf{k}}$ is the unit vector $\mathbf{k}/|\mathbf{k}|$. As a result, the vector in (9) also satisfies the condition in (8).

As is usually done, the wave packets $\Phi_\pi(\boldsymbol{\varkappa}, \mathbf{k})$, $\Phi_\rho(\boldsymbol{\varkappa}, \mathbf{k})$, and $\Phi_N(\boldsymbol{\varkappa}_1, \boldsymbol{\varkappa}_2; \mathbf{P})$, which appear in expressions (5), (7), and (6) for the state vectors $|\pi, \alpha, \mathbf{k}\rangle$, $|\rho, m, \alpha, \mathbf{k}\rangle$, and $|N, \mu, t, \mathbf{P}\rangle$, respectively, are chosen in the form of the Fourier transforms of the simplest functions in the translation-invariant shell model. Functions used in this model are characterized by only one phenomenological parameter, the quark-configuration radius b, which corresponds to the root-mean-square radius of the system. The meson wave function is dependent on the relative coordinate of quarks, $\boldsymbol{\rho} = \mathbf{r}_3 - \mathbf{r}_{\bar{4}}$, and is chosen in the form

$$\widetilde{\Phi}_M(\boldsymbol{\rho}) = (2\pi b_M^2)^{-3/4} e^{-\rho^2/4b_M^2}, \quad M = \pi, \rho, \tag{10}$$

where $b_M = b_\pi \approx b_\rho \approx 0.3$ fm. For the nucleon (baryon), $b \approx 0.6$ fm; the respective wave function in the translation-invariant shell model is taken in the form of the product of functions that are dependent on the relative coordinates $\boldsymbol{\rho}_1 = \mathbf{r}_1 - \mathbf{r}_2$ and $\boldsymbol{\rho}_2 = (\mathbf{r}_1 + \mathbf{r}_2)/2 - \mathbf{r}_3$; that is,

$$\widetilde{\Phi}_N(\boldsymbol{\rho}_1, \boldsymbol{\rho}_2) = \widetilde{\Phi}_N^{\mathrm{nr}(12)}(\boldsymbol{\rho}_1) \widetilde{\Phi}_N^{\mathrm{nr}(3)}(\boldsymbol{\rho}_2), \tag{11}$$

$$\widetilde{\Phi}_N^{\mathrm{nr}(12)}(\boldsymbol{\rho}_1) = (2\pi b^2)^{-3/4} e^{-\rho^2/4b^2},$$

$$\widetilde{\Phi}_N^{\mathrm{nr}(3)}(\boldsymbol{\rho}_2) = (3\pi b^2/2)^{-3/4} e^{-\rho^2/3b^2}.$$

If use is made of a covariant dynamical description, the time evolution of the wave packets $\Phi_\pi(\boldsymbol{\varkappa}, \mathbf{k})$, $\Phi_\rho(\boldsymbol{\varkappa}, \mathbf{k})$, and $\Phi_N(\boldsymbol{\varkappa}_1, \boldsymbol{\varkappa}_2; \mathbf{P})$ is determined by the exponential factors $\exp[i(-\omega_\pi)(\mathbf{k})x_0]$, $\exp[i(-\omega_\rho)(\mathbf{k})x_0]$, and $\exp[i(-E_N)(\mathbf{P})x_0]$, respectively, where $\omega_\pi(\mathbf{k}) = \sqrt{\mathbf{k}^2 + m_\pi^2}$, $\omega_\rho(\mathbf{k}) = \sqrt{\mathbf{k}^2 + m_\rho^2}$, and $E_N(\mathbf{P}) = \sqrt{\mathbf{P}^2 + M_N^2}$. By definition, the covariant normalization of the wave packets here depends on the total momentum of the respective hadron (in accordance with the covariant phase-space form $d^3k/(2\omega_M(\mathbf{k})(2\pi)^3)$, $M_N d^3P/(E_N(\mathbf{P}) \times (2\pi)^3)$. However, we use here the nonrelativistic shell wave functions (10) and (11), whose normalization features no dependence on the momenta $\mathbf{k}$ and $\mathbf{P}$. For the standard normalization conditions in Fock space,

$$\langle \pi, \alpha', \mathbf{k}' | \pi, \alpha, \mathbf{k} \rangle = 2\omega_\pi(\mathbf{k})(2\pi)^3 \delta^3(\mathbf{k} - \mathbf{k}') \delta_{\alpha\alpha'}, \tag{12}$$

$$\langle \rho, m', \alpha', \mathbf{k}' | \rho, m, \alpha, \mathbf{k} \rangle = 2\omega_\rho(\mathbf{k})(2\pi)^3 \delta^3(\mathbf{k} - \mathbf{k}') \delta_{mm'} \delta_{\alpha\alpha'},$$

$$\langle N, \mu', t', \mathbf{P}' | N, \mu, t, \mathbf{P} \rangle = \frac{E_N(\mathbf{P})}{M_N} (2\pi)^3 \delta^3(\mathbf{P} - \mathbf{P}') \delta_{\mu\mu'} \delta_{tt'},$$

to be valid in this case, we redefine the state vectors (5)–(7) by introducing appropriate additional factors in these expressions:

$$|\pi(\bar{q}q), \alpha, \mathbf{k}\rangle = \sqrt{2\omega_\pi(\mathbf{k})} |\widetilde{\pi(\bar{q}q), \alpha}, \mathbf{k}\rangle, \tag{13}$$

$$|\rho(\bar{q}q), m, \alpha, \mathbf{k}\rangle = \sqrt{2\omega_\rho(\mathbf{k})} |\widetilde{\rho(\bar{q}q), m, \alpha}, \mathbf{k}\rangle,$$

$$|N(3q), \mu, t, \mathbf{P}\rangle = \sqrt{E_N(\mathbf{P})/M_N} |\widetilde{N(3q), \mu}, t, \mathbf{P}\rangle.$$

In the nonrelativistic approximation, $E_q/m_q \approx 1$, which is quite acceptable in the region of low momenta, $|\mathbf{k}| \lesssim m_q$, characteristic of the virtual-pion cloud, the normalization conditions in (12) and (13) reduce

to the conventional nonrelativistic normalization conditions for wave packets,

$$\int |\Phi_\pi^{\rm nr}(\boldsymbol{\varkappa})|^2 d^3\varkappa/(2\pi)^3 \qquad (14)$$
$$= \int |\Phi_\rho^{\rm nr}(\boldsymbol{\varkappa})|^2 d^3\varkappa/(2\pi)^3 = 1,$$
$$\int |\Phi_N^{\rm nr(12)}(\boldsymbol{\varkappa}_1)|^2 d^3\varkappa_1/(2\pi)^3$$
$$= \int |\Phi_N^{\rm nr(3)}(\boldsymbol{\varkappa}_2)|^2 d^3\varkappa_2/(2\pi)^3 = 1,$$

where the functions $\Phi_M^{\rm nr}$ and $\Phi_N^{\rm nr}$ are the Fourier transforms of the corresponding nonrelativistic wave functions $\widetilde{\Phi}(\rho)$ defined above in (10) and (11).

We calculate the required matrix elements (4) in two steps. First, we evaluate transition amplitudes for one specific quark—for example, the third one. For the effective quark–meson vertex function, this yields

$$H^{(3)}_{Mqq(s)}(m,\alpha,\mathbf{k}) \qquad (15)$$
$$= \langle M,m,\alpha,\mathbf{k}|\langle q,t_4,\mu_4,\mathbf{p}_4|H_s|q,t_3,\mu_3,\mathbf{p}_3\rangle,$$

where $|q,t_3,\mu_3,\mathbf{p}_3\rangle = b^\dagger_{\mu_i t_i}(\mathbf{p}_i)|0\rangle$ and $|\bar{q},\ \bar{t}_3,\ \bar{\mu}_3,\ \mathbf{p}_3\rangle = d^\dagger_{\bar{\mu}_i\bar{t}_i}(\mathbf{p}_i)|0\rangle$ are the basis states in Fock space that correspond to a quark (antiquark) of momentum $\mathbf{p}_i$, spin projection (μ_i), and isospin projection (t_i). After that, the amplitude for the $N \to B + M$ transition is calculated as the matrix element of the operator $H^{(3)}_{Mqq}$ sandwiched between the quark wave functions for the nucleon (baryon),

$$\mathcal{M}(N \to M + B) = 3\langle B|H^{(3)}_{Mqq}|N\rangle, \qquad (16)$$

where the factor of 3 characterizes the number of quarks in the nucleon and reflects the fact that there are three identical matrix elements.

The calculation of the matrix element (15) in the first order in v/c (that is, for small $k, p_i \lesssim m_q$) leads to the following expression for the effective quark–pion vertex:

$$H^{(3)}_{\pi qq(s)}(\alpha,\mathbf{k}) = \frac{ig_s}{m_q}(2\pi)^3\delta(\mathbf{k}-(\mathbf{p}_3-\mathbf{p}_4)) \qquad (17)$$
$$\times (2\pi b_\pi^2)^{3/4}\sqrt{\omega_\pi(\mathbf{k})}\exp\left[-((\mathbf{p}_3+\mathbf{p}_4)/2)^2 b_\pi^2\right]$$
$$\times \left\langle \frac{1}{2}t_4\right| \tau_\alpha^{(3)\dagger}\left|\frac{1}{2}t_3\right\rangle$$
$$\times \left\langle \frac{1}{2}\mu_4\right| \boldsymbol{\sigma}^{(3)}\cdot(\mathbf{k}-(\mathbf{p}_3+\mathbf{p}_4))\left|\frac{1}{2}\mu_3\right\rangle + \mathcal{O}\left(\frac{v^2}{c^2}\right).$$

In deriving expression (17), we relied on the representation in (5) for the quark wave function for the pion and the wave function for a $\bar{q}q$ pair in the expansion (3) of the operator $H_{\rm pair}$. Integration with respect to quark momenta is performed with the aid of delta functions originating from the anticommutation relations in (2) for the creation and annihilation operators. As a result, the wave function for a $\bar{q}q$ pair is projected onto the pion wave function (for details, see [17]). Concurrently, use is made of the standard technique for rearranging angular, spin, and isospin momenta.

Further, we compare expression (17) with the analogous matrix element

$$H^{(3)}_{\pi qq({\rm PV})}(\alpha,\mathbf{k}) \qquad (18)$$
$$= \langle\pi^\alpha(\mathbf{k})|\langle q,t_4,\mu_4,\mathbf{p}_4|H_{\rm PV}|q,t_3,\mu_3,\mathbf{p}_3\rangle$$

of the operator of local pseudovector (PV) πqq coupling [12]. This operator has the form

$$H_{\rm PV} = \frac{f_{\pi qq}}{m_\pi}\int d^3x\bar{\psi}_q(x)\gamma^5\gamma^\mu\vec{\tau}\psi_q(x)\cdot\partial_\mu\vec{\varphi}_\pi(x), \qquad (19)$$

where use is made of the same basis states for quarks as in the matrix element (15), but the pion $|\pi^\alpha(\mathbf{k})\rangle = a^\dagger_\alpha(\mathbf{k})|0\rangle$ here is treated as an elementary particle without an internal structure:

$$H^{(3)}_{\pi qq({\rm PV})}(\alpha,\mathbf{k}) = i\frac{f_{\pi qq}}{m_\pi}(2\pi)^3\cdot\delta(\mathbf{k}-(\mathbf{p}_3-\mathbf{p}_4))$$
$$\times\left\langle\frac{1}{2}t_4\right|\tau_\alpha^{(3)\dagger}\left|\frac{1}{2}t_3\right\rangle\left\langle\frac{1}{2}\mu_4\right|\boldsymbol{\sigma}^{(3)}\cdot\left(\mathbf{k}\right. \qquad (20)$$
$$\left.-\frac{\omega_\pi(\mathbf{k})}{2m_q}(\mathbf{p}_3+\mathbf{p}_4)\right)\left|\frac{1}{2}\mu_3\right\rangle + \mathcal{O}\left(\frac{v^2}{c^2}\right).$$

Comparing expressions (17) and (20), we can see that the last factor on the right-hand side of (17) (spin matrix element) differs slightly from the analogous factor in (20); in order to remove this distinction, it is necessary to make the substitution

$$\boldsymbol{\sigma}^{(3)}\cdot(\mathbf{k}-(\mathbf{p}_3+\mathbf{p}_4)) \qquad (21)$$
$$\to \boldsymbol{\sigma}^{(3)}\cdot\left(\mathbf{k}-\frac{\omega_\pi(\mathbf{k})}{2m_q}(\mathbf{p}_3+\mathbf{p}_4)\right),$$

which is equivalent to introducing a correction to the effect of recoil in pion emission. Upon applying the substitution given by (21), we arrive at the transition amplitudes satisfying Galilei invariance.[3)]

[3)] Galilei invariance is violated in the πqq vertex function calculated on the basis of the $^3P_0$ model because the mass m_π of the physical pion, which is a (pseudo) Goldstone particle, is anomalously small in relation to the mass of a constituent-quark pair ($m_\pi \ll 2m_q$) generated by the Hamiltonian given by Eq. (1). We note that, if $m_M \approx 2m_q$ (this is so, for example, in the case of the ρ meson), a substitution of the form (21), which would then become $1 \to \omega_M/(2m_q) \approx m_M(2m_q)$, does no longer change anything.

Yet another distinction between expressions (17) and (20) is that, in the $^3P_0$ model, the vertex function (17) depends on the pion wave function $\Phi_\pi(\boldsymbol{\varkappa}) \sim e^{-\boldsymbol{\varkappa}^2 b_\pi^2}$. As a result, we arrive at a kernel that, in the coordinate representation, has the following nonlocal form:

$$\int \frac{d^3\varkappa}{(2\pi)^3} e^{i\boldsymbol{\varkappa}\cdot(\mathbf{r}_3-\mathbf{r}_4)} e^{-\boldsymbol{\varkappa}^2 b_\pi^2} \tag{22}$$
$$= (4\pi b_\pi^2)^{-3/2} \exp\left[-\frac{(\mathbf{r}_3-\mathbf{r}_4)^2}{4b_\pi^2}\right].$$

In the pointlike-pion limit $b_\pi \to 0$, expression (22) reduces to the delta function $\delta^3(\mathbf{r}_3-\mathbf{r}_4)$; that is, the πqq vertex function (17) becomes a local-coupling operator, as that in (20). In this limit, the phenomenological pseudovector coupling constant $f_{\pi qq}$ appears to be proportional to the scalar coupling constant g_s:

$$\frac{f_{\pi qq}}{(2\pi b_\pi^2 m_\pi^2)^{3/4}} \to \frac{g_s}{m_q}, \quad b_\pi \to 0. \tag{23}$$

Further, the averaging of the vertex functions (17) and (20) with the nucleon wave functions in the matrix element (16) results in that the quark constant $f_{\pi qq}$ transforms into the nucleon constant $f_{\pi NN}$; as a result, we arrive at a relation between g_s and $f_{\pi NN}$ that is valid for any finite value of the pion radius b_π (see below). It is the point where we generalize our previous consideration in [15,17], which was devoted to the pion and kaon channels.

The details of the calculation that are associated with projecting the $\bar{q}q^4$ quark system onto meson–nucleon channels were described previously in [17] (see also [15, 16]); for this reason, the exposition of this part here will be schematic, the more so as, in the model specified by Eqs. (1)–(7), this procedure reduces to the standard technique of the rearrangement of quark angular, spin, and isospin momenta and to the inclusion of (anti)commutation relations for creation and annihilation operators in Fock space.

We calculate the matrix elements

$$\mathcal{M}_s(N \to \pi + N) \tag{24}$$
$$= \langle \pi(q\bar{q}), \alpha, \mathbf{k}|\rangle N|H_s|N\rangle = 3\langle N|H^{(3)}_{\pi qq(s)}|N\rangle,$$
$$\mathcal{M}_{\rm PV}(N \to \pi + N) = \langle \pi^\alpha(\mathbf{k})|\langle N|H_{\rm PV}|N\rangle$$
$$= 3\langle N|H^{(3)}_{\pi qq({\rm PV})}|N\rangle,$$

relying on two different models of interaction that correspond to the Hamiltonians in (1) and (19) (here, $|N\rangle \equiv |N(3q), M, T_z, \mathbf{P}\rangle$). For the model employing a local (pseudovector) πqq interaction, $H_{\rm PV}$, the result is quite obvious: in the first order in v/c, we obtain the expression

$$\langle \pi^\alpha(\mathbf{k})|\langle N(3q), M', T_z', \mathbf{P}'|H_{\rm PV}|N(3q), M, T_z, \mathbf{P}\rangle = i\frac{5}{3}\frac{f_{\pi qq}}{m_\pi}\int \frac{d^3\varkappa_2}{(2\pi)^3}\Phi_N^{\rm nr(3)}(\boldsymbol{\varkappa}_2)\Phi_N^{\rm nr(3)}\left(\boldsymbol{\varkappa}_2+\frac{2}{3}\mathbf{k}\right) \tag{25}$$
$$\times \left\langle \frac{1}{2}M'\middle| \boldsymbol{\sigma}\cdot\left[\mathbf{k}-\frac{\omega_\pi(\mathbf{k})}{2m_q}\left(\frac{\mathbf{P}+\mathbf{P}'}{3}-2\boldsymbol{\varkappa}_2-\frac{2}{3}\mathbf{k}\right)\right]\middle|\frac{1}{2}M\right\rangle \left\langle \frac{1}{2}T_z'\middle|\tau_\alpha^\dagger\middle|\frac{1}{2}T_z\right\rangle,$$

which differs from the analogous expression for the local πNN vertex function,

$$\langle \pi^\alpha(\mathbf{k})|\langle N, M', T_z', \mathbf{P}'|\bar{\psi}_N(0)\gamma^\mu\gamma^5 \tag{26}$$
$$\times \vec{\tau}\psi_N(0)\cdot\partial_\mu\vec{\varphi}_\pi(0)|N, M, T_z, \mathbf{P}\rangle$$
$$= i\frac{f_{\pi NN}}{m_\pi}\left\langle \frac{1}{2}M'\middle|\boldsymbol{\sigma}\cdot\left[\mathbf{k}-\frac{\omega_\pi(\mathbf{k})}{2M_N}\right.\right.$$
$$\left.\left.\times\left(\mathbf{P}+\mathbf{P}'\right)\right]\middle|\frac{1}{2}M\right\rangle \left\langle \frac{1}{2}T_z'\middle|\tau_\alpha^\dagger\middle|\frac{1}{2}T_z\right\rangle,$$

only by the presence of the πNN form factor

$$F^{\rm (loc)}_{\pi NN}(\mathbf{k}^2) = \int \frac{d^3\varkappa_2}{(2\pi)^3}\Phi_N^{\rm nr(3)}(\boldsymbol{\varkappa}_2)\Phi_N^{\rm nr(3)}\left(\boldsymbol{\varkappa}_2+\frac{2}{3}\mathbf{k}\right) \tag{27}$$

in the vertex function (25).[4)]

From a comparison of expressions (25) and (26) for $\mathbf{k} \to 0$, we find that the πNN and πqq coupling constants are related by the well-known equation [12]

$$f_{\pi NN} = \frac{5}{3}f_{\pi qq}, \tag{28}$$

where the coefficient 5/3 is the spin–isospin part of the matrix element, this part being calculated by standard methods for summing Clebsch–Gordan co-

[4)] The term proportional to $\boldsymbol{\sigma}\cdot(2\boldsymbol{\varkappa}_2+\frac{2}{3}\mathbf{k})$ does not contribute to (25), since integration with respect to the angles in $\int \Phi_N^{\rm nr(3)}(\boldsymbol{\varkappa}_2)\Phi_N^{\rm nr(3)}\left(\boldsymbol{\varkappa}_2+\frac{2}{3}\mathbf{k}\right)\boldsymbol{\sigma}\cdot\left(\boldsymbol{\varkappa}_2+\frac{1}{3}\mathbf{k}\right)d^3\varkappa_2$, where $\Phi_N^{\rm nr(3)}$ are the Fourier transforms of the Gaussian functions in (11), annihilates this integral.

efficients appearing in the definition of the functions in (6).

By expressing $f_{\pi qq}$ in terms of $f_{\pi NN}$, we finally obtain an expression for the pseudovector πNN vertex function (26) in the form

$$\mathcal{M}_{\rm PV}(N\to\pi+N)=\frac{if_{\pi NN}}{m_\pi} \tag{29}$$
$$\times F^{\rm (PV)}_{\pi NN}(\mathbf{k}^2)\tau^\dagger_\alpha\boldsymbol{\sigma}\cdot\left[\mathbf{k}-\frac{\omega_\pi(\mathbf{k})}{2M_N}(\mathbf{P}+\mathbf{P}')\right].$$

A calculation of the matrix element for the same transition within the model of a scalar $\bar{q}q$ fluctuation (for relevant details, the interested reader is referred to [17]) leads to the expression

$$\mathcal{M}_s(N\to\pi+N)=\frac{5}{3}\frac{i\sqrt{3}g_s}{m_\pi m_q}(2\pi b_\pi^2m_\pi^2)^{3/4} \tag{30}$$
$$\times\left[1-\frac{y_\pi}{3}\varphi_{\pi NN}(0)\right](1-y_\pi)^{3/2}F^{(s)}_{\pi NN}(\mathbf{k}^2)$$
$$\times\tau^\dagger_\alpha\boldsymbol{\sigma}\cdot\left[\mathbf{k}-\frac{\omega_\pi(\mathbf{k})}{2M_N}(\mathbf{P}+\mathbf{P}')\right].$$

Here, we have made the substitution $M_N=3m_q$ and have introduced the notation

$$y_\pi=\frac{2}{3}x_\pi^2(1+2x_\pi^2/3)^{-1},\quad x_\pi=b_\pi/b, \tag{31}$$
$$\varphi_{\pi NB}(\mathbf{k})=3\omega_\pi(\mathbf{k})\left[M_N+M_B+\omega_\pi(\mathbf{k})\right]^{-1}.$$

The factor $\sqrt{3}$ in front of g_s on the right-hand side of (30) is the color contribution to the transition $N\to N+\pi$ [the result of summation over color in the pion wave function (5)]. Usually, this factor is included in the constant g_s by redefining it from the outset as

$$\tilde{g}_s=\sqrt{3}g_s. \tag{32}$$

In the two models in question (the local and the nonlocal one), the form factors $F^{\rm (PV)}_{\pi NN}$ and $F^{(s)}_{\pi NN}$ in the πNN vertex function are specified in the form of Gaussian functions, this being associated with the use of the oscillator basis (10), (11) in quark configurations of the translation-invariant shell model [see Eqs. (5)–(7)]; at the same time, any other (more realistic) wave functions—for example, wave functions that are used in covariant dynamical approaches [4]—are also compatible with the general form of expressions (5)–(7).

The form factor on the right-hand side of Eq. (30) is determined by an integral that is the generalization of (27) to the case of nonlocal interaction; that is,

$$F^{\rm (nonloc)}_{\pi NN}(\mathbf{k}^2)=\int\frac{d^3\varkappa_2}{(2\pi)^3}\Phi^{\rm nr(3)}_N(\boldsymbol{\varkappa}_2) \tag{33}$$
$$\times\Phi^{\rm nr(3)}_N\left(\boldsymbol{\varkappa}_2+\frac{2}{3}\mathbf{k}\right)\Phi^{\rm nr}_\pi\left(\boldsymbol{\varkappa}_2+\frac{1}{6}\mathbf{k}\right).$$

For the functions in (10)–(11), Eqs. (27) and (33) determine form factors of the following two types:

$$F^{\rm (loc)}_{\pi NN}(\mathbf{k}^2)=\exp\left(-\mathbf{k}^2b^2/6\right), \tag{34}$$
$$F^{\rm (nonloc)}_{\pi NN}(\mathbf{k}^2)=\exp\left[-\mathbf{k}^2b^2(1+y_\pi/4)/6\right].$$

In this case, the required form factors $F^{\rm (PV)}_{\pi NN}$ and $F^{(s)}_{\pi NN}$ are given by

$$F^{\rm (PV)}_{\pi NN}(\mathbf{k}^2)=F^{\rm (loc)}_{\pi NN}(\mathbf{k}^2), \tag{35}$$
$$F^{(s)}_{\pi NN}(\mathbf{k}^2)=\left[1-y_\pi\varphi_{\pi NN}(0)/3\right]^{-1}$$
$$\times\left[1-y_\pi\varphi_{\pi NN}(\mathbf{k})/3\right]F^{\rm (nonloc)}_{\pi NN}(\mathbf{k}^2).$$

From a comparison of expressions (29) and (30) considered in the limit $\mathbf{k}\to0$, we find that the coupling constants $f_{\pi NN}$ and $\tilde{g}_s$ are related by the equation

$$f_{\pi NN}=\frac{5}{3}\frac{\tilde{g}_s}{m_q}(2\pi b_\pi^2m_\pi^2)^{3/4} \tag{36}$$
$$\times\left[1-y_\pi\varphi_{\pi NN}(0)/3\right](1-y_\pi)^{3/2},$$
$$g_{\pi NN}=\frac{2M_N}{m_\pi}f_{\pi NN}.$$

As a matter of fact, this is a condition that normalizes the only phenomenological parameter of the $^3P_0$ model, $\tilde{g}_s=\sqrt{3}g_s$, to the experimental value of the πNN coupling constant $g_{\pi NN}$. Since Eq. (36) was derived within the constituent-quark model, its right-hand side also features a dependence on the parameters b, b_π, and m_q of this model, which are determined from an independent fit to the spectrum of hadrons.

We note that the bracketed factor on the right-hand side of (36) yields only a small correction at a realistic value of $x_\pi\approx0.5$–1. Discarding this factor, we obtain

$$\tilde{g}_s=\frac{3}{5}f_{\pi NN}(2\pi b_\pi^2m_\pi^2)^{-3/4}\left(1+\frac{2}{3}x_\pi^2\right)^{3/2}m_q, \tag{37}$$

which corresponds to a value of $\tilde{g}_s\simeq1.94m_q$ at $x_\pi=0.5$.

The right-hand side of (37) has a clear physical meaning. Here, $(2\pi b_\pi^2)^{-3/4}$ is the value of the pion wave function $\widetilde{\Phi}^{\rm nr}_\pi(\boldsymbol{\rho})$ at the origin. The same value determines the matrix element of the divergence of the axial current,

$$\langle0|\bar{\psi}_q(0)\gamma^5\gamma^\mu\partial_\mu\tau_\beta\psi_q(0)|\pi,\alpha,\mathbf{k}\rangle \tag{38}$$
$$=-i\delta_{\alpha\beta}m_\pi^2f_\pi.$$

This matrix element specifies the amplitude of weak pion decay. The weak-decay constant f_π can be calculated for the initial state (5) by using the wave function $\widetilde{\Phi}_\pi^{\rm nr}(\boldsymbol{\rho})$. This yields an expression that involves the value of this function at the origin. Specifically, we have

$$m_\pi^2 f_\pi = \sqrt{3}\sqrt{2m_\pi}\widetilde{\Phi}_\pi^{\rm nr}(0) m_{ud}, \qquad (39)$$

where $m_{ud} = (m_u + m_d)/2$, with m_u and m_d being the masses of light (current) quarks.[5)]

Once the constant g_s has been normalized to the known value of the πNN coupling constant, there appears the possibility of calculating, within the model of a $\bar{q}q$ scalar fluctuation, $N \to M + B$ vertex functions [the coupling constants f_{MNB} and the form factors $F_{MNB}(k^2)$] for any $\bar{q}q$ mesons $M = \pi$, ρ, π^*, K, K^*, ... and any $3q$ baryons $B = N$, Δ, $N_{1/2^+}(1440)$, $N_{1/2^-}(1535)$, Λ, Σ, ... For the coupling constants, we will concurrently obtain relations that, albeit being initiated by the original $SU(3)_F$-symmetric Hamiltonian (1), are beyond $SU(3)_F$ symmetry as such—for example, those that satisfy $SU(6)_{FS}$ symmetry. We have already realized this program in part for pion and kaons in [15–17].

Following the scheme outlined above, we will obtain the $N \to \rho + N$ rho-meson vertex function. In doing this, we start from the matrix elements

$$\mathcal{M}_s(N \to \rho + N) \qquad (40)$$
$$= \langle \rho(q\bar{q}), m, \alpha, \mathbf{k}|\langle N|H_s|N\rangle = 3\langle N|H^{(3)}_{\rho qq(s)}|N\rangle,$$
$$\mathcal{M}_V(N \to \rho + N)$$
$$= \langle \rho^{(m)\alpha}(\mathbf{k})|\langle N|H_V|N\rangle = 3\langle N|H^{(3)}_{\rho qq(V)}|N\rangle,$$

which are similar to those in (24). By H_V, we mean here the minimal (that is, the Dirac) interaction of a quark with a vector field,

$$H_V = g_{\rho qq}\int d^3x \bar{\psi}_q(x)\gamma^\mu \vec{\tau}\psi_q(x)\cdot\vec{\rho}_\mu(x). \qquad (41)$$

In the first order in v/c, this local interaction leads to the following ρqq vertex function:

$$H^{(3)}_{\rho qq(V)}(m, \alpha, \mathbf{k}) \qquad (42)$$
$$= \frac{g_{\rho qq}}{2m_q}(2\pi)^3\delta(\mathbf{k} - (\mathbf{p}_3 - \mathbf{p}_4))$$
$$\times \left\langle \frac{1}{2}t_4\right| \tau_\alpha^{(3)\dagger}\left|\frac{1}{2}t_3\right\rangle$$
$$\times \left\langle \frac{1}{2}\mu_4\right| \Big(\mathbf{p}_3 + \mathbf{p}_4 - i[\boldsymbol{\sigma}^{(3)}\times\mathbf{k}]\Big)\cdot\boldsymbol{\epsilon}^{(m)}\left|\frac{1}{2}\mu_3\right\rangle.$$

Applying Eq. (40), we obtain the $N \to \rho + N$ transition amplitude in the form

$$\langle \rho^{(m)\alpha}(\mathbf{k})|\langle N(3q), M', T_z', \mathbf{P}'|H_V|N(3q), M, T_z, \mathbf{P}\rangle$$
$$= \frac{g_{\rho qq}}{2m_q}\int\frac{d^3\varkappa_2}{(2\pi)^3}\Phi_N^{\rm nr(3)}(\boldsymbol{\varkappa}_2)\Phi_N^{\rm nr(3)}\left(\boldsymbol{\varkappa}_2 + \frac{2}{3}\mathbf{k}\right) \qquad (43)$$
$$\times\left\langle\frac{1}{2}M'\right|\left(\frac{\mathbf{P}+\mathbf{P}'}{3} - 2\boldsymbol{\varkappa}_2 - \frac{2}{3}\mathbf{k}\right.$$
$$\left. - \frac{5}{3}i\,[\boldsymbol{\sigma}\times\mathbf{k}]\right)\cdot\boldsymbol{\epsilon}^{(m)}\left|\frac{1}{2}M\right\rangle\left\langle\frac{1}{2}T_z'\right|\tau_\alpha^\dagger\left|\frac{1}{2}T_z\right\rangle.$$

Here, the expression in the lowest line [in a perfect analogy with the lowest line in (25)] is the spin–isospin part of the matrix element of the operator given by (42) and sandwiched between the nucleon wave functions (6), this spin–isospin part being calculated by standard methods of the shell model (for example, with the aid of the technique employing the fractional-parentage coefficients). In just the same way as in (25), we can discard the vector $2\boldsymbol{\varkappa}_2 + \frac{2}{3}\mathbf{k}$ in the lowest line of (43), since, for the functions in (11), its contribution vanishes upon integration of the whole expression with respect to the angles of the vector $\boldsymbol{\varkappa}_2$.

As a result, we find that, in the same order in v/c, the only distinction between the matrix element (43) of the local ρNN interaction for the $N \to \rho + N$ transition and the elementary ρNN vertex

$$\left\langle\rho^{(m)\alpha}(\mathbf{k})\right|\left\langle N, M', T_z', \mathbf{P}'\right|\bar{\psi}_N(0) \qquad (44)$$
$$\times\left(\gamma^\mu + \frac{\kappa_\rho}{2M_N}\sigma^{\mu\nu}\partial_\nu\right)$$
$$\times\vec{\tau}\psi_N(0)\cdot\vec{\rho}_\mu(0)\left|N, M, T_z, \mathbf{P}\right\rangle$$
$$= \frac{g_{\rho NN}}{2M_N}\left\langle\frac{1}{2}M'\right|(\mathbf{P}+\mathbf{P}' - (1+\kappa_\rho)$$
$$\times i\,[\boldsymbol{\sigma}\times\mathbf{k}])\cdot\boldsymbol{\epsilon}^{(m)}\left|\frac{1}{2}M\right\rangle\left\langle\frac{1}{2}T_z'\right|\tau_\alpha^\dagger\left|\frac{1}{2}T_z\right\rangle$$

is that the former includes the ρNN form factor [second line in (43)]

$$F^{(V)}_{\rho NN}(\mathbf{k}^2) \qquad (45)$$
$$= \int\frac{d^3\varkappa_2}{(2\pi)^3}\Phi_N^{\rm nr(3)}(\boldsymbol{\varkappa}_2)\Phi_N^{\rm nr(3)}\left(\boldsymbol{\varkappa}_2 + \frac{2}{3}\mathbf{k}\right),$$

[5)] The factor $\sqrt{2m_\pi}$ on the right-hand side of (39) is due exclusively to a change in the notation for the nonrelativistic pion wave function in (13). For the wave packet Φ_π, which satisfies the covariant normalization condition (12), Eq. (39) reduces to the form $m_\pi^2 f_\pi = \sqrt{3}\widetilde{\Phi}_\pi(0)m_{ud}$. As a result, the constant f_π does not vanish in the chiral limit $m_{ud} \to 0$ if $\widetilde{\Phi}_\pi(0) \neq 0$. We are grateful to V.E. Lyubovitsky for this valuable comment.

which, in this model, coincides with the πNN form factor (27).

Moreover, it follows from a comparison of expressions (43) and (44) that, in the quark model, the phenomenological parameter κ_ρ, which determines the coupling constant for the Pauli term of ρNN interaction, has a specific value,

$$1 + \kappa_\rho = 5, \tag{46}$$

which was obtained algebraically by using only the Dirac term in the interaction given by Eq. (41). We note that formula (46) for the rho-meson is an analog of formula (28) for the pion.

We derive a relation between the quark and nucleon coupling constants $g_{\rho qq}$ and $g_{\rho NN}$ for the ρ meson, following the same scheme of calculations as in deducing relation (28) for the pion. Substituting the relation $m_q = M_N/3$ into Eq. (43), we find that, in the limit $\mathbf{k} \to 0$ (that is, in the limit where the form factor reduces to unity), formulas (43) and (44) are identical if κ_ρ satisfies Eq. (46) and that the meson coupling constant takes the same value both for nucleons and for quarks:

$$g_{\rho NN} = g_{\rho qq}. \tag{47}$$

By using this relation, we can find that, in the model assuming a local ρqq interaction, the ρNN vertex function admits the representation

$$\mathcal{M}_V(N \to \rho + N) \tag{48}$$
$$= \frac{g_{\rho NN}}{2M_N}\tau_\alpha^\dagger \left(\mathbf{P} + \mathbf{P}' - 5i[\boldsymbol{\sigma} \times \mathbf{k}]\right) \cdot \boldsymbol{\epsilon}^{(m)} F^{(V)}_{\rho NN}(\mathbf{k}^2),$$

which coincides with the result obtained previously by Riska and Brown [12].

We calculate the same matrix element within the model of a $\bar{q}q$ scalar fluctuation by using a universal value of the scalar constant g_s. This value was earlier normalized to the pion coupling constant in Eqs. (36) and (37). We derive the operator $H^{(3)}_{\rho qq(s)}(m, \alpha, \mathbf{k})$ of effective ρqq coupling in just the same way as the analogous operator in (17) for πqq coupling by directly calculating the matrix element in (15) with the aid of the rho-meson wave function (7), the anticommutation relations (2) for creation and annihilation operators, and standard methods for transforming products of Clebsch–Gordan coefficients. In addition, we use the transverseness condition (8) for the rho-meson polarization vector in the region of small $|\mathbf{k}|/m_q \approx v/c$. For the ρqq vertex function, this leads to the expression

$$H^{(3)}_{\rho qq(s)}(m, \alpha, \mathbf{k}) = \frac{g_s}{m_q}(2\pi)^3 \delta(\mathbf{k} - (\mathbf{p}_3 - \mathbf{p}_4)) \tag{49}$$
$$\times (2\pi b_\rho^2)^{3/4}\sqrt{\omega_\rho(\mathbf{k})}\exp\left[-((\mathbf{p}_3 + \mathbf{p}_4)/2)^2 b_\rho^2\right]$$
$$\times \left\langle \frac{1}{2}t_4 \middle| \tau_\alpha^{(3)\dagger} \middle| \frac{1}{2}t_3 \right\rangle$$
$$\times \left\langle \frac{1}{2}\mu_4 \middle| \left(\mathbf{p}_3 + \mathbf{p}_4 - i\left[\boldsymbol{\sigma}^{(3)} \times \mathbf{k}\right]\right) \cdot \boldsymbol{\epsilon}^{(m)} \middle| \frac{1}{2}\mu_3 \right\rangle.$$

We can see that, in the model of a $\bar{q}q$ scalar fluctuation, the operator $H^{(3)}_{\rho qq(s)}$ of effective ρqq coupling has the same spin–isospin structure as the operator of local ρqq coupling (42) [compare the last two lines in Eqs. (42) and (49)].

The calculation of the matrix element for the $N \to \rho + N$ transition with this operator is performed in just the same way as for the $N \to \pi + N$ transition with the πqq-coupling operator (17). As a result, we arrive at the expression

$$\mathcal{M}_s(N \to \rho + N) \tag{50}$$
$$= \sqrt{3}g_s\frac{\sqrt{2m_\rho}}{M_N}(2\pi b_\rho^2)^{3/4}(1 - y_\rho)^{3/2}F^{(s)}_{\rho NN}(\mathbf{k}^2)$$
$$\times \tau_\alpha^\dagger \left(\mathbf{P} + \mathbf{P}' - 5i[\boldsymbol{\sigma} \times \mathbf{k}]\right) \cdot \boldsymbol{\epsilon}^{(m)},$$

which is similar to that in (30). Here, we have assumed as usual that $m_q = M_N/3$ and have employed the notation

$$y_\rho = \frac{2}{3}x_\rho^2\left(1 + \frac{2}{3}x_\rho^2\right)^{-1},$$

where $x_\rho = \dfrac{b_\rho}{b}$.

In this model, the form factors for local and nonlocal coupling in the amplitudes in (48) and (50) are expressed in terms of Gaussian functions as

$$F^{(V)}_{\rho NN}(k^2) = \exp\left[-\frac{k^2b^2}{6}\right], \tag{51}$$
$$F^{(s)}_{\rho NN}(k^2) = \exp\left[-\frac{k^2b^2(1 + y_\rho/4)}{6}\right].$$

In the limit $\mathbf{k} \to 0$, the amplitude in (50) determines the ρNN coupling constant in the model of a scalar fluctuation. Comparing Eq. (50) with Eqs. (44) and (48), we obtain the following expression for the ρNN coupling constant in terms of the scalar constant $\tilde{g}_s = \sqrt{3}g_s$ and the parameters of the rho-meson wave function in the constituent-quark model:

$$g_{\rho NN} = 2\tilde{g}_s\sqrt{m_\rho}(2\pi b_\rho^2)^{3/4}\left(1 + \frac{2}{3}x_\rho^2\right)^{-3/2}. \tag{52}$$

For the example of the rho meson, this demonstrates that the microscopic model being considered provides a universal basis for describing various meson clouds in the nucleon.

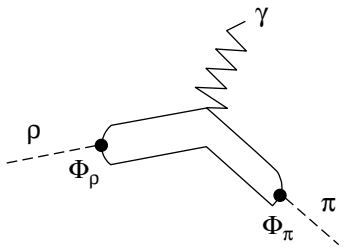

Fig. 2. Diagram for $\rho\pi\gamma$ coupling in the constituent-quark model.

Considering that, in our model, g_s is normalized to the pion constant $f_{\pi NN} = \dfrac{m_\pi}{2m_N} g_{\pi NN}$ [see relations (36), (37)], we arrive at the equation

$$\frac{g_{\rho NN}}{g_{\pi NN}} = \frac{1}{5}\left(\frac{m_\rho}{m_\pi}\right)^{1/2}\left(\frac{b_\rho}{b_\pi}\right)^{3/2}\left(\frac{1+\dfrac{2}{3}x_\pi^2}{1+\dfrac{2}{3}x_\rho^2}\right)^{3/2}, \tag{53}$$

which relates the constants $g_{\rho NN}$ and $g_{\pi NN}$ to each other and which follows from a microscopic consideration.

At $b_\rho = b_\pi$, the model predicts the following numerical values for the rho-meson constants:

$$g_{\rho NN} = \frac{g_{\pi NN}}{5}\left(\frac{m_\rho}{m_\pi}\right)^{1/2} = 6.35, \qquad 1+\kappa_\rho = 5. \tag{54}$$

This result does not differ very strongly from the value predicted by the well-known Kawarabayashi–Suzuki–Riazuddin–Fayyazuddin relation [27], $|g_{\rho NN}| = |g_{\rho\pi\pi}| = m_\rho/(\sqrt{2}f_\pi) \simeq 5.89$, as a consequence of low-energy theorems. For the sake of comparison, we indicate that, in the model proposed in [12], the quark vector coupling constant κ_ρ is a free parameter, its value being determined from a fit to the (model-dependent) coupling constant $g_{\rho NN}$ in the one-boson-exchange nucleon–nucleon potential. The resulting values of $g_{\rho NN}$ and κ_ρ, together with the form factor $F^{(s)}_{\rho NN}(k^2)$, are used in the following to describe the transverse part of the differential cross section for quasielastic rho-meson knockout from the nucleon with the subsequent conversion of the rho meson to a pion, $\rho + \gamma_T^* \to \pi$.

3. $\rho\pi\gamma$ ELECTROMAGNETIC FORM FACTOR AND CROSS SECTION FOR QUASIELASTIC RHO-MESON KNOCKOUT FOLLOWED BY RHO-MESON CONVERSION TO PIONS

Let us first consider the $\rho\pi\gamma$ electromagnetic vertex function. We will calculate it, assuming the minimal (Dirac) interaction of a quark with an electromagnetic field [see also formula (42) above]:

$$H_{\mathrm{em}(q)} = e\int d^3x\bar{\psi}_q(x)\gamma^\mu\left(\frac{1}{6}+\frac{\tau_z}{2}\right)\psi_q(x)A_\mu(x). \tag{55}$$

For one of the constituent quarks (we label it with the number 2), we obtain, in the lowest order in v/c, the transition amplitude [similarly to Eq. (43)]

$$H^{(2)}_{\mathrm{em}}(q,\lambda) = \left\langle q,\mu_2',t_2'\mathbf{p}_2'\right|\left(\frac{1}{6}+\frac{\tau_z^{(2)}}{2}\right)\frac{e}{2m_q} \times\left(\mathbf{p}_2+\mathbf{p}_2'-i[\boldsymbol{\sigma}^{(2)}\times\mathbf{q}]\right)\cdot\boldsymbol{\epsilon}_\gamma^{(\lambda)}\left|q,\mu_2,t_2,\mathbf{p}_2\right\rangle, \tag{56}$$

where $\boldsymbol{\epsilon}_\gamma^{(\lambda)}$ is the polarization vector of the virtual photon γ_T^*. Here, we are interested in the transverse polarizations ($\lambda = \pm 1$),

$$\boldsymbol{\epsilon}_\gamma^{(\lambda)}(\hat{\mathbf{q}}) = \mp\left\{\frac{1}{\sqrt{2}}, \pm i\frac{1}{\sqrt{2}}, 0\right\}, \tag{57}$$

since only transversely polarized photons γ_T^* make a nonzero contribution to the quark-spin-flip isovector $M1$ transition $\rho + \gamma^* \to \pi$. Calculating the matrix element for this transition, which corresponds to the diagram in Fig. 2, we obtain

$$\mathcal{M}(\vec{\boldsymbol{\rho}}+\vec{\gamma}\to\vec{\pi}) = 2\langle\vec{\pi},\mathbf{k}'|H^{(2)}_{\mathrm{em}}(q,\lambda)|\vec{\boldsymbol{\rho}},\mathbf{k}\rangle = eg_{\rho\pi\gamma}|\mathbf{q}|\boldsymbol{\epsilon}_\gamma^{(\lambda)}\cdot[\hat{\boldsymbol{\rho}}\times\hat{\mathbf{q}}][\vec{\rho}\times\vec{\pi}]_{I_z=0}F_{\rho\pi\gamma}(\mathbf{q}^2), \tag{58}$$

where the $\rho\pi\gamma$ coupling constant and the vertex form factor are expressed in term of the parameters of the constituent-quark model as

$$g_{\rho\pi\gamma} = C_{\rho\pi}\frac{\sqrt{m_\pi m_\rho}}{m_q}, \tag{59}$$

$$F_{\rho\pi\gamma}(\mathbf{q}^2) = \int\frac{d^3\varkappa}{(2\pi)^3}\Phi_\pi\left(\boldsymbol{\varkappa}-\frac{\mathbf{q}}{2}\right)\Phi_\rho(\boldsymbol{\varkappa}) = \exp\left[-\mathbf{q}^2b_\rho^2/4\right].$$

Here, $\vec{\rho}$ and $\vec{\pi}$ are isospin vectors, $\hat{\mathbf{q}} = \mathbf{q}/|\mathbf{q}|$ and $\hat{\boldsymbol{\rho}}$ are vectors of unit length, and we assume that $b_\rho = b_\pi$. Within this approach, the coefficient $C_{\rho\pi}$, which takes into account relativistic and other corrections, is a phenomenological parameter; in principle, it could be fitted to cross sections for other electromagnetic processes involving rho mesons (for example, to the decay width of the rho meson with respect to the channel $\pi + \gamma$). In the present study, we only estimated the coefficient $C_{\rho\pi}$ on the basis of data on quasielastic pion knockout induced by virtual photons γ_T^* and obtained the value of $C_{\rho\pi} = 1.7$ (see below). A total analysis of corrections contributing to the coefficient $C_{\rho\pi}$ is possible within relativistic models—for example, within the model used in [9].

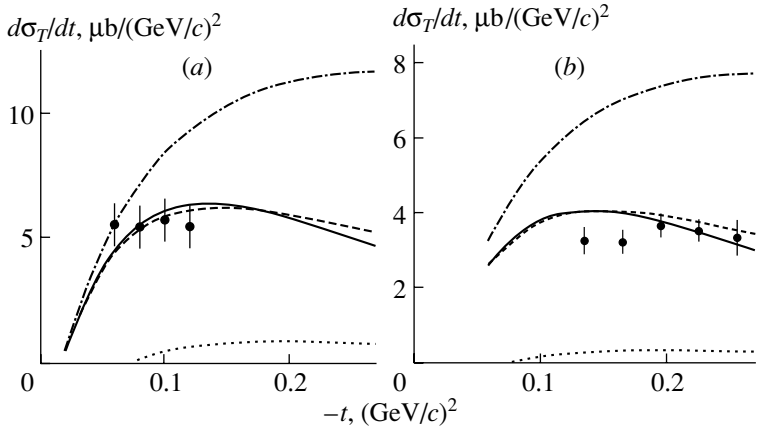

Fig. 3. Transverse part of the cross section for quasielastic pion knockout from a nucleon, $d\sigma_T/dt$, at the momentum transfers of $Q^2 = (a)$ 1.0 and (b) 1.6 $(\mathrm{GeV}/c)^2$. The displayed experimental data were borrowed from [22]. The total rho-meson-pole and pion-pole contribution calculated within various models of meson–nucleon coupling are represented by the dashed and the dash-dotted curve for the case where use is made of the monopole parametrization of the vertex form factors $F_{MNN}(k^2)$ $(M = \pi, \rho)$ for the cutoff parameter Λ set to 0.6 and 1.2 GeV/c, respectively, and by the solid curve for the case where the results were obtained on the basis of the microscopic quark model whose parameters were set to $b = 0.6$ fm and $b_\pi = b_\rho = 0.3$ fm. The dotted curve shows the contribution of the pion t-pole diagram alone.

Having the ρNB and $\rho\pi\gamma$ form factors at our disposal, we can obtain the required the differential cross section for pion electroproduction. In the general case, the differential cross section averaged over the azimuthal angle has the form

$$\frac{d\sigma}{dQ^2 dW dt} = \varepsilon J_0^2 + J_1^2, \qquad (60)$$

where ε is a parameter that characterizes the degree of the virtual-photon longitudinal polarization and J_i^2 is the square of the matrix element of the relevant current.

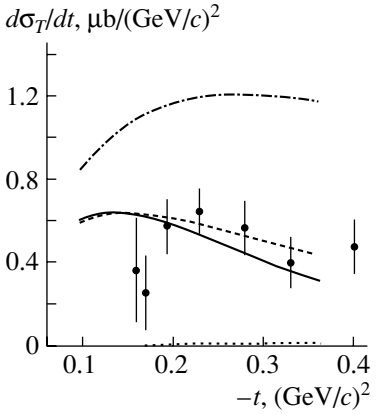

Fig. 4. Results of our calculations for the transverse part of the cross section for quasielastic pion knockout from a nucleon (the notation for the calculated curves is identical to that in Fig. 3) along with older experimental data from [20] at the momentum transfer of $Q^2 = 3.3\,(\mathrm{GeV}/c)^2$.

As was shown previously, the region $Q^2 \geq 1{-}3\ (\mathrm{GeV}/c)^2$ is dominated by the quasielastic-pion-knockout mechanism, in which case the main contribution to the cross section is generated by the t-channel pole mechanism, the longitudinal and the transverse part of the cross section receiving dominant contributions from, respectively, the diagram describing direct pion knockout and the diagram involving the rearrangement of the internal structure of the emitted meson— that is, the $\rho \to \pi$ conversion in the photon vertex. For rho-meson knockout followed by the conversion process $\rho \to \pi$, we ultimately obtain the matrix elements of hadron currents in the form

$$\begin{aligned}
&\langle N, M', T_z', p'|J_{(\lambda)}^{N\gamma^*\to N\pi}(t,\alpha)|N, M, T_z, p\rangle \qquad (61)\\
&= e g_{\rho\pi\gamma} g_{\rho NN} \frac{|\mathbf{q}||\mathbf{k}|}{t - m_\rho^2} F_{\rho\pi\gamma}(q^2) F_{\rho NN}(k^2) \frac{1+\kappa_\rho}{2M_N}\\
&\times \sqrt{2}(1 - \lambda 1\lambda|10)(-1)^{1/2-T_z'}(1/2T_z 1/2 - T_z'|1\alpha)\\
&\times \sqrt{2}(-1)^{\lambda}(1(M'-M)1(\lambda - M' + M)|1\lambda)\\
&\times \sqrt{2}(-1)^{1/2-M}(1/2 - M' 1/2M|1(M - M'))\\
&\times \sqrt{\frac{4\pi}{3}} Y_{1(\lambda - M' + M)}(\hat{\mathbf{k}}),
\end{aligned}$$

where $t = k_0^2 - \mathbf{k}^2$, $k_\mu = p_\mu - p'_\mu$, and α is the rho-meson (pion) isospin index. Upon performing summation and averaging over the spin projections of the initial (final) nucleon, we obtain the following result for the squared matrix element $\overline{|J_1|^2} =$

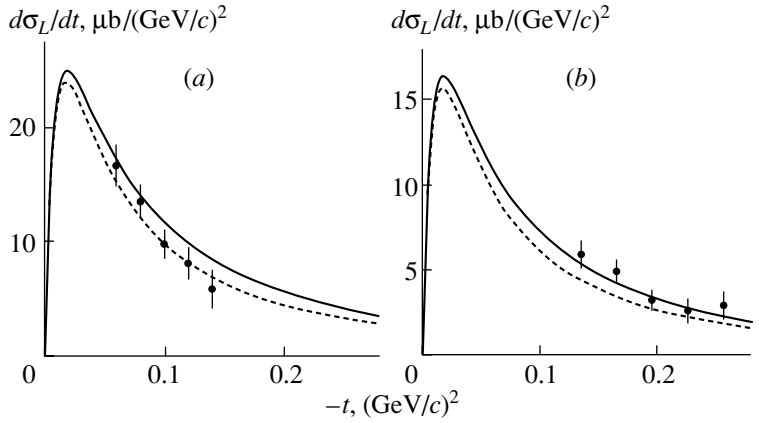

Fig. 5. Longitudinal part of the cross section for quasielastic pion knockout from a nucleon, $d\sigma_L/dt$, at the momentum transfers of $Q^2 = (a)\ 1.0$ and $(b)\ 1.6\ (\mathrm{GeV}/c)^2$. The displayed experimental data were borrowed from [22]. The notation for the calculated curves is identical to that in Fig. 3.

$(1/2)\overline{(J^2_{(\lambda=1)} + J^{*2}_{(\lambda=-1)})}$:

$$\frac{1}{2}\sum_{MM'}(J^2_{(\lambda=1)} + J^{*2}_{(\lambda=-1)}) = \left[eg_{\rho\pi\gamma}g_{\rho NN} \times \frac{|\mathbf{q}||\mathbf{k}|}{t-m_\rho^2}F_{\rho\pi\gamma}(q^2)F_{\rho NN}(k^2)\frac{1+\kappa_\rho}{2M_N}\right]^2 \times (1+\cos^2(\widehat{\mathbf{qk}})). \quad (62)$$

A transition from the expression for the currents to the momentum distribution of mesons and differential cross sections in the pole approximation is discussed in detail elsewhere [13]. The results obtained by calculating the cross sections for quasielastic rho-meson knockout are given in Figs. 3 and 4. Also presented here for the sake of comparison are the longitudinal components of the cross section for quasielastic pion knockout (Figs. 5 and 6). As to the electromagnetic form factors, the nonrelativistic constituent-quark model does not claim to provide a quantitative description of the "electromagnetic part" of the cross section at rather high values of $q^2 \sim 2$–$3\ (\mathrm{GeV}/c)^2$; in our calculations, we employed the latest experimental data [22] for $F_{\pi\pi\gamma}(q^2)$, assuming that $F_{\rho\pi\gamma}(q^2) \simeq F_{\pi\pi\gamma}(q^2)$.

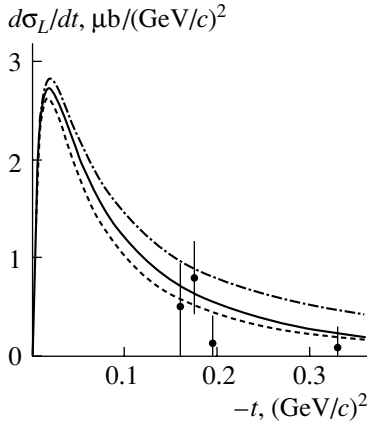

Fig. 6. Results of our calculations for the longitudinal part of the cross section for quasielastic pion knockout from a nucleon (the notation for the calculated curves is identical to that in Fig. 3) along with older experimental data from [20] at the momentum transfer of $Q^2 = 3.3\ (\mathrm{GeV}/c)^2$.

For a comparison of the shape of momentum distributions with theoretical results to be meaningful, available experimental data [20-22], against which we contrast our results (Figs. 3–6), must be refined substantially. At the same time, it is important that the absolute cross-section values are approximately in accord with experimental data, and this favors the statement, albeit at a qualitative level so far, that the microscopic $^3P_0$ model is universal.

In Figs. 3–6, the solid curves correspond the microscopic quark model at the parameter values of $b = 0.6$ fm and $b_\pi = b_\rho = 0.3$ fm, while the dashed and dash-dotted curves represent results obtained by using the monopole parametrization of the vertex form factors $F_{MNN}(k^2)$ $(M = \pi, \rho)$ with the cutoff parameter Λ set to 0.6 and 1.2 GeV/c, respectively. For a comparison to be convenient, the common vertex constants $g_{\rho NN} = 6.35$, $1 + \kappa_\rho = 5.0$, and $g_{\rho\pi\gamma} = 1.87$ (this corresponds to $C_{\rho\pi} = 1.7$), which were obtained within the quark model involving a $^3P_0$ scalar fluctuation (in this model, $g_{\rho NN}$ is normalized to the experimental value of $g_{\pi NN} = 13.5$), were used in all models.

4. CONCLUDING COMMENTS

The development of the microscopic formalism and the calculation of momentum distributions for channels involving an excited spectator baryon B

in the final state, $N \to B + \rho$ [$B = \Delta$, $N^*(3/2^-, 1/2^-)$, $N^{**}(1/2^+)$ (Roper)], are the most immediate task. Relevant experimental investigations are quite feasible at the Jefferson Laboratory. In the near future, a transition to an unpolarized electron and a polarized proton target in exclusive experiments (this is being planned at the present time) will furnish much richer information about virtual mesons in the nucleon that possess a nonzero intrinsic spin.

In all probability, investigation of quasielastic meson knockout induced by electrons and accompanied by the rearrangement of the internal state of the emitted meson can be extended by considering not only the spin-flip process $\rho \to \pi$ (this was done in the present article) but also a change in the intrinsic orbital angular momentum $l = 1$ of a meson—for example, in the electron-impact-induced transition of a virtual positive-parity b_1 meson in the nucleon to the $l = 0$ state (pion). As a result, a pion will be knocked out upon the absorption of a longitudinal virtual photon. The observable consequences of this will be similar to effects studied in detail in the theory of the quasielastic knockout of clusters from nuclei that is induced by protons of energy in the range 500–1000 MeV [19]. In particular, the relevant cross section will receive contributions both from the dominant $\pi + \gamma_L^* \to \pi$ amplitude and from the off-diagonal $b_1 + \gamma_L^* \to \pi$ amplitude, which can manifest itself via anisotropies of differential cross sections [19].

ACKNOWLEDGMENTS

This work was supported in part by the Russian Foundation for Basic Research (project no. 03-02-17394).

REFERENCES

1. L. Micu, Nucl. Phys. B **10**, 521 (1969); A. Le Yaouanc, L. Oliver, O. Péne, and J. Raynal, Phys. Rev. D **8**, 2223 (1973); **11**, 1272 (1975).
2. N. Isgur and J. Paton, Phys. Rev. D **31**, 2910 (1985).
3. S. Kumano and V. R. Pandharipande, Phys. Rev. D **38**, 146 (1988); S. Kumano, Phys. Rev. D **41**, 195 (1990).
4. E. S. Ackleh, T. D. Barnes, and E. S. Swanson, Phys. Rev. D **54**, 6811 (1996).
5. B. Desplanques, C. Gignoux, B. Silvestre-Brac, *et al.*, Z. Phys. A **343**, 331 (1992); F. Cano, P. Gonzalez, S. Noguera, and B. Desplanques, Nucl. Phys. A **603**, 257 (1996).
6. J. Güttner, G. Chanfray, H. J. Pirner, and B. Povh, Nucl. Phys. A **429**, 389 (1984); J. D. Sullivan, Phys. Rev. D **5**, 1732 (1972).
7. C. H. Llewelly Smith, Phys. Lett. B **128B**, 107 (1983).
8. M. Guidal, J.-M. Laget, and M. Vanderhaeghen, Nucl. Phys. A **627**, 645 (1997).
9. J. Speth and V. R. Zoller, Phys. Lett. B **351**, 533 (1995).
10. S. Capstick and W. Roberts, Phys. Rev. D **47**, 1994 (1993); **49**, 4570 (1994); nucl-th/0008028.
11. P. Stassart and Fl. Stancu, Phys. Rev. D **42**, 1521 (1990).
12. D. O. Riska and G. E. Brown, Nucl. Phys. A **679**, 577 (2001).
13. V. G. Neudatchin, N. P. Yudin, and L. L. Sviridova, Yad. Fiz. **60**, 2020 (1997) [Phys. At. Nucl. **60**, 1848 (1997)]; N. P. Yudin, L. L. Sviridova, and V. G. Neudatchin, Yad. Fiz. **61**, 1689 (1998) [Phys. At. Nucl. **61**, 1577 (1998)]; **62**, 694 (1999) [**62**, 645 (1999)].
14. V. G. Neudatchin, L. L. Sviridova, and N. P. Yudin, Yad. Fiz. **65**, 594 (2002) [Phys. At. Nucl. **65**, 567 (2002)].
15. I. T. Obukhovsky, V. G. Neudatchin, L. L. Sviridova, and N. P. Yudin, Yad. Fiz. **66**, 338 (2003) [Phys. At. Nucl. **66**, 313 (2003)].
16. I. T. Obukhovsky, L. L. Sviridova, and V. G. Neudatchin, Yad. Fiz. **66**, 2233 (2003) [Phys. At. Nucl. **66**, 2183 (2003)].
17. V. G. Neudatchin, I. T. Obukhovsky, L. L. Sviridova, and N. P. Yudin, Nucl. Phys. A **739**, 124 (2004).
18. V. G. Neudatchin, L. L. Sviridova, and N. P. Yudin, Yad. Fiz. **64**, 1680 (2001) [Phys. At. Nucl. **64**, 1600 (2001)].
19. N. F. Golovanova, I. M. Il'in, V. G. Neudatchin, *et al.*, Nucl. Phys. A **262**, 444 (1976); **285**, 531 (1977); V. G. Neudatchin, Yu. F. Smirnov, and N. F. Golovanova, Adv. Nucl. Phys. **11**, 1 (1979); V. G. Neudatchin, W. W. Kurovsky, A. A. Sakharuk, and Yu. M. Tchuvilsky, Phys. Rev. C **51**, 784 (1995); V. G. Neudatchin, A. A. Sakharuk, W. W. Kurovsky, and Yu. M. Tchuvil'sky, Yad. Fiz. **58**, 1234 (1995) [Phys. At. Nucl. **58**, 1155 (1995)].
20. C. J. Bebek, C. N. Brown, S. D. Holmes, *et al.*, Phys. Rev. D **17**, 1693 (1978).
21. P. Brauel, T. Canzler, D. Cords, *et al.*, Z. Phys. C **3**, 101 (1979).
22. J. Volmer, D. Abbott, H. Anklin, *et al.*, Phys. Rev. Lett. **86**, 1713 (2001).
23. S. Loucks, V. R. Pandharipande, and R. Schiavilla, Phys. Rev. C **49**, 342 (1994).
24. R. M. Mohring, D. Abbott, A. Ahmidouch, *et al.*, Phys. Rev. C **67**, 055205 (2003).
25. S. Okubo, Phys. Lett. **5**, 163 (1963); G. Zweig, CERN Report 8182/TH401 (1964); J. Iizuka, Prog. Theor. Phys. Suppl. **37–38**, 21 (1966).
26. C. Itzykson and J.-B. Zuber, *Introduction to Quantum Field Theory* (McGraw-Hill, New York, 1980; Mir, Moscow, 1984), Vol. 1, p. 234.
27. K. Kawarabayashi and M. Suzuki, Phys. Rev. Lett. **16**, 255 (1966); Riazuddin and Fayyazuddin, Phys. Rev. **147**, 1071 (1966).

Translated by A. Isaakyan

Physics of Atomic Nuclei, Vol. 68, No. 8, 2005, pp. 1395–1399. Translated from Yadernaya Fizika, Vol. 68, No. 8, 2005, pp. 1451–1455.

ELEMENTARY PARTICLES AND FIELDS
Experiment

Inclusive Deuteron Production in ^{16}Op Collisions at a Momentum of 3.25 GeV/c per Nucleon

E. Kh. Bazarov, V. V. Glagolev[1)], K. G. Gulamov, M. Yu. Kratenko, S. L. Lutpullaev, K. Olimov[*], Kh. Sh. Khamidov[2)], A. A. Yuldashev, and B. S. Yuldashev[2)]

Institute for Physics and Technology, Fizika-Solntse Research and Production Association, Uzbek Academy of Sciences, ul. Timiryazeva 2b, Tashkent, 700084 Republic of Uzbekistan

Received March 10, 2004; in final form, August 9, 2004

Abstract—Experimental data on inclusive deuteron production in ^{16}Op collisions at high energies were obtained for the first time under conditions of 4π geometry. An irregularity in the momentum spectrum of deuterons in the rest frame of oxygen nuclei is found in the range $0.40 \leq p \leq 0.55$ GeV/c, and the reasons for its appearance are discussed. The mean multiplicities of secondary fragments are correlated with the presence of deuterons in an event, these correlations being positive for fragments of charge in the range $z_f \leq 4$ and negative for fragments of charge in the range $5 \leq z_f \leq 7$. This is likely to be due to baryon-charge conservation. © *2005 Pleiades Publishing, Inc.*

INTRODUCTION

Investigation of mechanisms that are responsible for the fragmentation of relativistic nuclei interacting with nucleons and nuclei is one of the key problems of high-energy physics. In our opinion, the most efficient method for solving this problem is to study processes leading to the production of light fragments (^{1}H$_1$, ^{2}H$_1$, ^{3}H$_1$, ^{3}He$_2$, and ^{4}He$_2$). This is because the cross section for light-particle emission is commensurate with the total reaction cross section; therefore, the production of light particles is a characteristic feature of the nuclear-fragmentation process, which can be completely understood only upon establishing the mechanism of light-particle production. At the same time, it has been firmly established by now that a considerable part of light particles are emitted at the initial stage of the interaction of two nuclei. It follows that, in contrast to products originating from the decay of a thermalized residual nucleus, which forget the entire path of their formation almost completely, such particles carry direct information about interaction dynamics. We also note that data on deuteron production in hadron–nucleus collisions at high energies are scanty, the bulk of them stemming from the application of electronic procedures and covering a narrow solid angle. The entire momentum interval of deuteron production has not been considered either. Of course, this constrains substantially the range of useful information about the dynamics of deuteron formation. In view of this, it is of great interest to obtain new experimental data on deuteron emission from ^{16}Op collisions at high energies (under conditions of 4π geometry) for nearly the whole momentum interval of deuteron production, and this is precisely the objective of the present study.

Experimental data discussed below were obtained by exposing the 1-m hydrogen bubble chamber of the Laboratory of High Energies at the Joint Institute for Nuclear Research (JINR, Dubna) to a beam of ^{16}O nuclei accelerated at the Dubna synchrophasotron to a momentum of 3.25 GeV/c per nucleon. The data sample subjected to analysis in the present study consisted of 11 098 measured ^{16}Op events. We note that the use of beams of accelerated light nuclei in experiments with hydrogen bubble chambers makes it possible to identify all projectile fragments in charge and mass [1–3]. We considered fragments for which the measured track length satisfied the condition $L >$ 35 cm. This was necessary for reliably identifying fragments in mass. For this cut on the track length, the mean relative error in determining the momenta of all fragments does not exceed 3.4%.

In order to perform an ultimate mass identification of fragments, we introduced the following momentum intervals: singly charged fragments were identified as ^{2}H$_1$ for momenta in the range $p = 4.75$–7.8 GeV/c and as ^{3}H$_1$ for momenta in the region $p > 7.8$ GeV/c, while doubly charged fragments were classed with ^{3}He$_2$ for momenta in the range $p < 10.8$ GeV/c and

[1)]Joint Institute for Nuclear Research, Dubna, Moscow oblast, 141980 Russia.
[2)]Institute of Nuclear Physics, Uzbek Academy of Sciences, pos. Ulughbek, Tashkent 702132 Republic of Uzbekistan.
[*]e-mail: olimov@uzsci.net

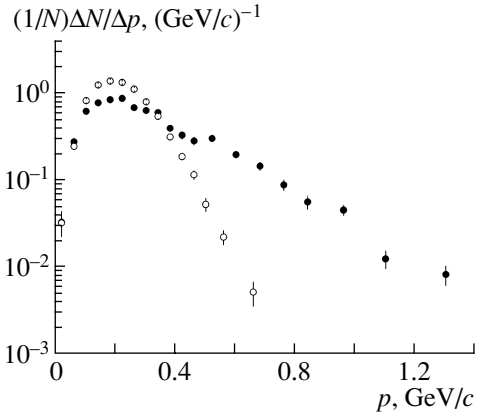

Fig. 1. Distribution of deuterons with respect to the total momentum in the rest frame of the oxygen nucleus: (closed circles) experimental data and (open circles) results obtained within the cascade–fragmentation–evaporation model.

with $^4He_2$ for momenta in the region $p > 10.8$ GeV/c. If the fragments for which the track lengths satisfy the condition $L > 35$ cm are identified by using these criteria, the admixture of isotopes close in mass does not exceed 4 to 5%. Positive singly charged relativistic particles of momentum in the range $1.75 < p < 4.75$ GeV/c were identified as protons. If protons are selected in this way, the admixture of positively charged pions can be disregarded. For multiply charged fragments ($z_f \geq 3$), no constraint was imposed on the track length, since no mass identification was performed for such fragments. In determining the mean multiplicities of singly and doubly charged fragments, we took into account the loss of these fragments at distances of $L \leq 35$ cm owing to their interaction with the chamber operating liquid (hydrogen). Other methodological features of our experiment were described elsewhere [1–3].

The experimental data in question are compared with the predictions of the cascade–fragmentation–evaporation model (CFEM) [4]. Within this model, the breakup of an excited thermalized residual nucleus, which is formed upon the completion of the intranuclear cascade, is a dominant mechanism of the production of all fragments, with the exception of protons, in the interactions of light nuclei with nucleons. For light nuclei, such as ^{16}O, the evaporation mechanism of fragment formation is disregarded, even for nucleons.

EXPERIMENTAL DATA AND THEIR ANALYSIS

The mean multiplicity of deuterons in the experiment proved to be $\langle n_d \rangle = 0.331 \pm 0.007$, which is about 1.4 times greater than its counterpart calculated on the basis of the cascade–fragmentation–evaporation model, $\langle n_d \rangle = 0.239 \pm 0.003$. The inclusive cross sections for deuteron production appeared to be 110.6 ± 2.3 mb in the experiment and 79.8 ± 1 mb in the cascade–fragmentation–evaporation model.

Figure 1 displays the normalized (to the total number of events) distribution of deuterons with respect to the total momentum in the rest frame of the oxygen nucleus. Also shown in this figure is the analogous spectrum obtained on the basis of the cascade–fragmentation–evaporation model, the calculated mean multiplicity of deuterons being normalized to their experimental mean multiplicity. The deuteron total momentum averaged over the experimental spectrum proved to be $\langle p \rangle = 0.341 \pm 0.005$ GeV/c, its counterpart calculated within the cascade–fragmentation–evaporation model being $\langle p \rangle = 0.223 \pm 0.002$ GeV/c, which is less than the above experimental value by a factor of about 1.53

Let us proceed to analyze the shape of the momentum spectra. As can be seen from Fig. 1, the calculated spectrum of p is smooth over the entire range of momentum (it peaks at $p \approx 0.20$ GeV/c and decreases fast toward $p \approx 0.7$ GeV/c). The experimental spectrum of p grows monotonically up to a maximum (at $p \approx 0.22$ GeV/c), whereupon it exhibits a pronounced irregularity ("shoulder") in the region $p = 0.40–0.55$ GeV/c; at momentum values in excess of $p \approx 0.6$ GeV/c, the spectrum in question decreases (approximately in proportion to an exponential), covering the momentum interval up to $p \approx 1.4$ GeV/c. From a comparison of these spectra, one can conclude that the cascade–fragmentation–evaporation model overestimates deuteron production in the range $0.10 < p < 0.35$ GeV/c, but that it underestimates the contribution of this process in the region $p > 0.4$ GeV/c. As was indicated in [5] in studying the structure functions for light fragments versus kinetic energy, this discrepancy is due to the disregard of the mechanism of fast-cascade-nucleon fusion in the model.

In order to clarify the reason behind the emergence of the irregularity in the momentum spectrum of deuterons in the range $p = 0.40–0.55$ GeV/c, we consider individually, in the rest frame of the oxygen nucleus, the momentum distributions of deuterons emitted into the forward and the backward hemisphere (Fig. 2). From Fig. 2, one can see that the momentum spectrum of deuterons emitted into the backward hemisphere is monotonic. The momentum spectrum of deuterons emitted into the forward hemisphere is rather hard, and the above irregularity in the

Table 1. Mean multiplicities of light fragments in events where there is a deuteron or where there is no deuteron

n_d		Fragment type			
		$^1H_1$	$^3H_1$	$^3He_2$	$^4He_2$
0	Expt.	1.28 ± 0.02	0.087 ± 0.004	0.088 ± 0.004	0.476 ± 0.011
	CFEM	1.52 ± 0.01	0.096 ± 0.002	0.137 ± 0.003	0.359 ± 0.005
≥ 1	Expt.	2.24 ± 0.04	0.232 ± 0.011	0.253 ± 0.012	0.806 ± 0.020
	CFEM	2.64 ± 0.03	0.156 ± 0.006	0.211 ± 0.007	0.356 ± 0.010

Table 2. Mean multiplicities of fragments in events where there is a deuteron or where there is no deuteron

n_d	Fragment charge						
	1	2	3	4	5	6	7
0	1.37 ± 0.03	0.56 ± 0.01	0.063 ± 0.003	0.035 ± 0.002	0.076 ± 0.003	0.216 ± 0.005	0.247 ± 0.006
≥ 1	2.47 ± 0.04	1.06 ± 0.02	0.12 ± 0.01	0.054 ± 0.005	0.067 ± 0.006	0.126 ± 0.008	0.022 ± 0.003

Table 3. Mean multiplicities of light fragments in the events involving the emission of a deuteron in the backward or in the forward direction in the rest frame of the oxygen nucleus

ϑ_d, deg	Fragment type			
	$^1H_1$	$^3H_1$	$^3He_2$	$^4He_2$
≤ 90	2.31 ± 0.04	0.215 ± 0.011	0.235 ± 0.012	0.746 ± 0.021
>90	2.35 ± 0.05	0.242 ± 0.019	0.251 ± 0.019	0.753 ± 0.029

Table 4. Mean multiplicity and mean total and transverse momenta of the deuteron in the rest frame of the oxygen nucleus versus the presence of a charged pion in an event

Quantity	Presence of a charged pion in an event			
	$n_{\pi^+} = 0$	$n_{\pi^+} \geq 1$	$n_{\pi^-} = 0$	$n_{\pi^-} \geq 1$
$\langle n \rangle$	0.287 ± 0.008	0.412 ± 0.018	0.292 ± 0.007	0.441 ± 0.023
$\langle p \rangle$, MeV/c	343 ± 6	345 ± 9	340 ± 5	358 ± 11
$\langle p_\perp \rangle$, MeV/c	252 ± 5	253 ± 8	250 ± 5	263 ± 9

momentum spectrum of all deuterons in the range $p = 0.40$–0.55 GeV/c becomes even more distinct there. It can be conjectured that this effect is due to a significant distinction between the mechanisms responsible for the forward and backward production of deuterons. The main contribution to the production of deuterons traveling in the backward direction comes from the evaporation mechanism and the mechanism of Fermi breakup. The production of deuterons traveling in the forward direction is due not only to these mechanisms but also to the fusion of fast cascade nucleons and the decays of relatively fast excited light fragments, as well as to a direct knockout of deuterons from the oxygen nucleus involved. These additional mechanisms can be responsible for the hardness of the deuteron momentum spectrum and for the emergence of the irregularity in it.

The experimental transverse-momentum ($p_\perp$) distribution of deuterons is shown in Fig. 3, along with the $p_\perp$ spectrum of deuterons that was calculated on the basis of the cascade–fragmentation–evaporation model. For the experimental spectrum, the mean value of the deuteron transverse momentum proved to be $\langle p_\perp \rangle = 0.252 \pm 0.005$ GeV/c, its coun-

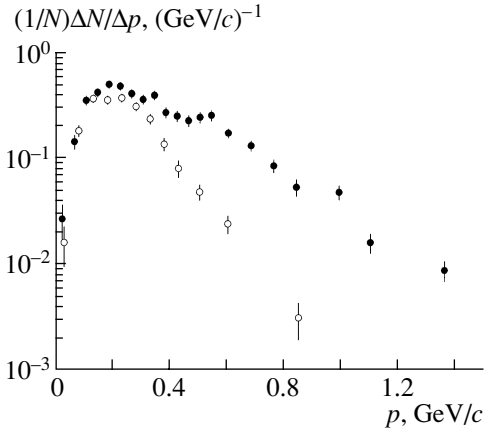

Fig. 2. Distribution of deuterons with respect to the total momentum in the rest frame of the oxygen nucleus: (closed circles) results for deuterons emitted into the forward hemisphere and (open circles) results for deuterons emitted into the backward hemisphere.

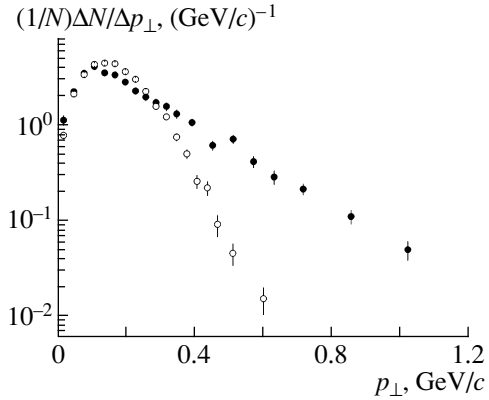

Fig. 3. Transverse-momentum distribution of deuterons: (closed circles) experimental data and (open circles) results of the calculation based on the cascade–fragmentation–evaporation model.

terpart in the cascade–fragmentation–evaporation model being $\langle p_\perp \rangle = 0.173 \pm 0.002$ GeV/c, which is less than the experimental value by a factor of about 1.46. As can be seen from Fig. 3, both the experimental and the calculated $p_\perp$ spectrum are rather smooth (this is not so only for the experimental spectrum in the vicinity of the point $p_\perp \approx 0.52$ GeV/c). The experimental $p_\perp$ spectrum covers the entire momentum range up to $p_\perp \leq 1.1$ GeV/c, while the calculated spectrum terminates at $p_\perp \leq 0.65$ GeV/c. For $p_\perp \geq 0.22$ GeV/c, the experimental $p_\perp$ spectrum has an approximately exponential character. For the calculated $p_\perp$, such a regime is realized in the region $p_\perp \geq 0.35$ GeV/c. The slope parameter for the calculated $p_\perp$ spectrum is severalfold as great as that for the experimental spectrum. From the comparison of these two spectra, we can conclude that the cascade–fragmentation–evaporation model fails to describe the experimental data being discussed.

Let us now proceed to consider associated multiplicities of secondary fragments versus the presence of a deuteron in an event. Table 1 gives the mean multiplicities of light fragments ($^1H_1$, $^3H_1$, $^3He_2$, and $^4He_2$) in events featuring a deuteron and events featuring no deuteron. Also displayed in this table are data calculated on the basis of the cascade–fragmentation–evaporation model. As can be seen from Table 1, the mean multiplicities of light fragments are correlated with the presence of a deuteron in an event. In the experiment, the mean multiplicities of $^1H_1$ and $^4He_2$ in events featuring the production of a deuteron are approximately 1.75 times greater than those in events featuring no deuteron. For the mirror nuclei of $^3H_1$ and $^3He_2$, the respective difference exceeds a factor of 2.7. It should be noted that, within the statistical errors, the mean multiplicities of these nuclei agree, irrespective of deuteron production in an event. Within the cascade–fragmentation–evaporation model, positive correlations between the mean multiplicities of fragments and the presence of a deuteron in an event are observed only for fragments whose mass numbers satisfy the inequality $A \leq 3$; for $^4He_2$ nuclei, there are no correlations within the statistical errors. We also note that, in contrast to what we observed experimentally, the mean multiplicities do not coincide for mirror nuclei within the model—the mean multiplicity of $^3He_2$ nuclei is approximately 1.4 times greater than the mean multiplicity of $^3H_1$. Irrespective of the presence of a deuteron in an event, the cascade–fragmentation–evaporation model overestimates the production of protons and underestimates the production of $^4He_2$ nuclei, this being probably due to the disregard of the α-cluster structure of the ^{16}O nucleus in the model. A strong discrepancy between the predictions of the cascade–fragmentation–evaporation model and experimental data was also observed previously for the yields of carbon isotopes [1].

The mean multiplicities of fragments whose charge satisfies the condition $1 \leq z_f < 7$ that are not separated in mass are displayed in Table 2 versus the presence of a deuteron in an event. We note that the mean multiplicity of singly charged fragments is given without allowance for the multiplicity of deuterons. In just the same way as in Table 1, we can see here correlations between mean multiplicities of fragments and the presence of a deuteron in an event. However, these correlations are positive for $z_f \leq 4$ fragments and are negative for $5 \leq z_f \leq 7$ fragments, this being probably due to baryon-charge conservation.

The mean multiplicities of light fragments ($^1H_1$, $^3H_1$, $^3He_2$, and $^4He_2$) are presented in Table 3 versus the deuteron emission angle in the rest frame of the oxygen nucleus. One can see that, within the statistical errors, the mean multiplicities of the fragments being considered are independent of the deuteron emission angle. With allowance for the significant distinction between the mechanisms of backward- and forward-deuteron production, this means that there is no interplay between the mechanisms of production of light fragments and deuterons.

Let us now consider the mean multiplicity of deuterons and their mean kinematical features versus the presence of a charged pion in an event. In order to eliminate the effect of the target-proton charge on the correlations being studied, we consider pions originating from the projectile—that is, fast ($p > 0.5$ GeV/c) positively and negatively charged pions produced predominantly in an inelastic charge-exchange process involving one or a few nucleons of the oxygen nucleus and constituting one of the steps of the intranuclear cascade ($p(n) \to n(p) + \pi^+(\pi^-)$). Table 4 displays the mean multiplicity of deuterons and the mean values of its total and transverse momenta versus the presence of a fast positively or negatively charged pion in an event. From this table, on can see that, within the statistical errors, the mean multiplicity of deuterons and its mean momentum features are independent of the sign of the pion charge and that the mean multiplicity of deuterons in events involving charged pions is approximately 1.45 times greater than that in events not involving the production of charged pions.

CONCLUSION

The production of deuterons in ^{16}Op collisions at a momentum of 3.25 GeV/c per nucleon has been studied for the first time under conditions of 4π geometry. The basic results of this investigation are the following. In the momentum range $0.40 < p < 0.55$ GeV/c, the momentum spectrum of forward deuterons in the rest frame of the oxygen nucleus exhibits a shoulder, which may be associated with the fusion of cascade nucleons, decays of relatively fast light fragments, and a direct knockout of a deuteron from the oxygen nucleus by the target proton. In order to clarify the role of these mechanisms and processes in the formation of the shoulder in the deuteron momentum spectrum, it is necessary to perform a detailed investigation of correlations between the shape of the momentum spectrum of forward deuterons (in the rest frame of the oxygen nucleus) and various topological channels of oxygen-nucleus breakup.

Mean multiplicities of fragments are correlated with the presence of a deuteron in an event. These correlations are positive for fragments of charge $z_f \leq 4$ and are negative for $5 \leq z_f \leq 7$ fragments. This is likely to be due to baryon-charge conservation. The mean multiplicities of light fragments are independent of the deuteron-production mechanism.

The cascade–fragmentation–evaporation model fails to reproduce our experimental data on deuteron production (multiplicities, momentum spectra, and correlations between the multiplicities of fragments of various types). From a comparison of the experimental data with the predictions of this model, one can conclude that, in order to obtain a realistic description of the production of light fragments in hadron–nucleus collisions at high energies, it is necessary to take into account both the contribution of the evaporation mechanism (even for nuclei as light as ^{16}O) and the contribution of the mechanism of fast-cascade-nucleon fusion, as well as the α-cluster structure of light nuclei.

REFERENCES

1. V. V. Glagolev, K. G. Gulamov, M. Yu. Kratenko, *et al.*, Pis'ma Zh. Éksp. Teor. Fiz. **58**, 497 (1993) [JETP Lett. **58**, 497 (1993)].
2. V. V. Glagolev, K. G. Gulamov, M. Yu. Kratenko, *et al.*, Pis'ma Zh. Éksp. Teor. Fiz. **59**, 307 (1994) [JETP Lett. **59**, 336 (1994)].
3. V. V. Glagolev, K. G. Gulamov, M. Yu. Kratenko, *et al.*, Yad. Fiz. **58**, 2005 (1995) [Phys. At. Nucl. **58**, 1896 (1995)].
4. A. S. Botvina, E. S. Golubeva, *et al.*, Preprint No. P-0657, IYaI AN SSSR (Inst. Nucl. Res., USSR Academy of Sciences, Moscow, 1990).
5. V. V. Glagolev, K. G. Gulamov, V. D. Lipin, *et al.*, Yad. Fiz. **62**, 1472 (1999) [Phys. At. Nucl. **62**, 1388 (1999)].

Translated by A. Isaakyan

Physics of Atomic Nuclei, Vol. 68, No. 8, 2005, pp. 1400–1404. Translated from Yadernaya Fizika, Vol. 68, No. 8, 2005, pp. 1456–1460.

ELEMENTARY PARTICLES AND FIELDS
Theory

Inclusive Production of Vector Charmonium in Two-Photon e^+e^- Annihilation

A. V. Luchinsky*

Institute for High Energy Physics, Protvino, Moscow oblast, 142281 Russia

Received January 13, 2004; in final form, November 24, 2004

Abstract—One of the processes involving the inclusive production of the vector-charmonium states J/ψ and $\psi(2S)$ in two-photon electron–positron annihilation at $\sqrt{s} = 10.6$ GeV is studied on the basis of the singlet model. Analytic expressions are derived for respective differential cross sections, and numerical values of the total cross sections are given, along with graphs that represent the distributions of cross sections in the scattering angle and in the vector-meson energy. It is shown that these distributions differ substantially from the analogous distributions for charmonium production in one-photon electron–positron annihilation. For this reason, the process under consideration can readily be isolated despite the smallness caused by an extra power of α. © *2005 Pleiades Publishing, Inc.*

1. INTRODUCTION

States of charmonium (that is, a meson consisting of c and $\bar{c}$ quarks—for example, J/ψ, $\psi(2S)$, or η_c particles) are of great theoretical and experimental interest: on one hand, these states can easily be isolated experimentally; on the other hand, a theoretical analysis of these states is considerably simplified owing to their nonrelativistic character. Within nonrelativistic QCD (NRQCD) [1, 2], charmonium production and decay can be systematically described in terms of series in the strong and electromagnetic coupling constants and in the c-quark velocity in the charmonium rest frame. At the same time, vector-charmonium production in electron–positron annihilation can be described within a model-independent approach because, in this case, all relevant parameters determined by perturbation theory cannot be obtained phenomenologically from experimental data on the rate of the decay $(c\bar{c}) \to e^+e^-$. For example, vector charmonium can emerge from electron–positron annihilation in the reaction $e^+e^- \to \gamma J/\psi$ [3, 4].

This may be the exclusive pair production of charmonuim states in electron–positron annihilation. This reaction has received considerable theoretical and experimental studies. For example, the BELLE Collaboration investigated the pair production of charmoniuum states in electron–positron annihilation at the c.m. energy of $\sqrt{s} = 10.6$ GeV [5] and obtained experimental data that disagree with the theoretical predictions based on NRQCD [6–13]. Attempts were made to explain this disagreement by taking into account the octet mechanism or the contribution of a two-photon intermediate state. Although those attempts did not remove the discrepancy between the theoretical predictions and experimental data completely, it was shown [6–13] that the contribution of the two-photon intermediate state may be sizable despite the suppression due to an extra power of α.

Yet another example is provided by the inclusive production of vector charmonium in electron–positron annihilation via the reaction

$$e^+e^- \to (c\bar{c})_V + \text{hadrons}.$$

Although this reaction has received much attention (see, for example, [8, 14–16]), the contribution of the two-photon intermediate state has not yet been taken into consideration. Despite an extra power of the small factor α, the two-photon process may contribute significantly to the cross section for the inclusive production of vector charmonium because, in this case, the square of the momentum of the photon fragmenting into the vector meson is equal to the mass squared of this meson: $p^2 = M_V^2 \ll s$ (for this reason, the contribution of purely electromagnetic processes to the exclusive production of two charmonia, which was considered in [6], is about 20%). It is the process that is considered in the present study.

The ensuing exposition is organized as follows. Expressions for relevant coupling constants are given in Section 2, and their relation to experimental data is considered there. Analytic expressions for differential cross sections are presented in Section 3. The respective numerical results are quoted in Section 4.

*e-mail: Alexey.Luchinsky@ihep.ru

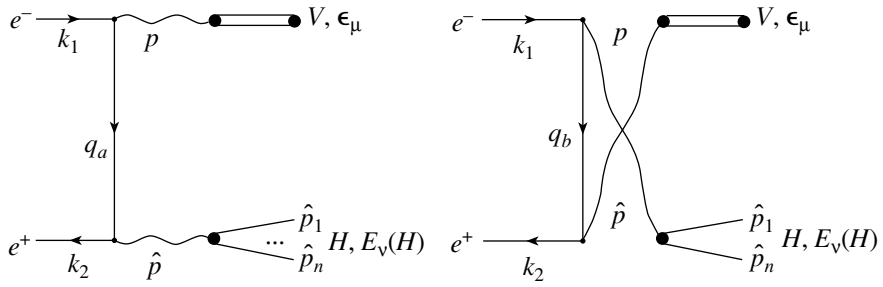

Fig. 1. Diagrams for the reaction $e^+e^- \to 2\gamma \to \gamma H$.

2. VERTICES

The matrix element for the decay of a vector meson V to an electron–positron pair can be represented in the form

$$\mathcal{M}_V = g_V \epsilon_\mu \bar{v}(k_2)\gamma^\mu u(k_1),$$

where $u(k_1)$ and $\bar{v}(k_2)$ are, respectively, the wave functions for the electron and the positron (whose masses are neglected); k_1 and k_2 are their momenta; ϵ_μ is the meson polarization vector; and g_V is the effective coupling constant, whose value can be determined from experimental data. The respective decay width is given by

$$\Gamma_V^{ee} = (2\pi)^4 \frac{1}{6M_V} \int d\Phi_2(p; k_1, k_2)|\mathcal{M}_V|^2, \quad (1)$$

where $p = k_1 + k_2$ is the momentum of the vector meson, $M_V = \sqrt{p}$ is its mass, and

$$d\Phi_n(P; p_1, \ldots, p_n) = \delta(P - \sum_{i=1}^n p_i) \prod_{i=1}^n \frac{d\mathbf{p}_i}{(2\pi)^3 \cdot 2E_i} \quad (2)$$

is the n-body Lorentz-invariant phase space. On the basis of Eq. (1), the effective coupling constant g_V can be expressed in terms of experimentally observable quantities as

$$g_V^2 = 12\pi \frac{\Gamma_V^{ee}}{M_V}. \quad (3)$$

The matrix element for the one-photon annihilation of an electron–positron pair to a given hadron state H has the form

$$\mathcal{M}(e^+e^- \to \gamma^* \to H)$$
$$= E_\mu(H)\bar{v}(k_2)\gamma^\mu u(k_1) = E_\mu(H)L^\mu,$$

where $E_\mu(H)$ is the effective polarization vector of the state H; this vector may depend on the number n of hadrons and on their momenta $(\hat{p}_1, \ldots, \hat{p}_n)$, spins, and masses. The inclusive annihilation cross section has the form

$$\sigma_H = \sum_H \sigma(e^+e^- \to \gamma^* \to H) = (2\pi)^4 \frac{1}{16(k_1k_2)}$$
$$\times L^\mu (L^\nu)^\dagger \sum_H \int d\Phi_n(\hat{p}; \{\hat{p}_i\}) E_\mu(H) E_\nu^*(H)$$
$$= \frac{\pi^4}{(k_1k_2)} L^\mu (L^\nu)^\dagger E_{\mu\nu}(\hat{p}),$$

where $\hat{p} = \sum_{i=1}^n \hat{p}_i$ is the total momentum of the hadron state and $\hat{s} = \hat{p}^2$. The last term in the above equation may depend only on the metric tensor $g_{\mu\nu}$, $\hat{s}$, and $\hat{p}$. Since it is transverse (that is, $E_{\mu\nu}(\hat{p})\hat{p}^\mu = 0$), it can be represented in the form

$$E_{\mu\nu}(\hat{p}) = \sum_H \int d\Phi_n(\hat{p}; \{\hat{p}_i\}) E_\mu(H) E_\nu^*(H) \quad (4)$$
$$= -a(\hat{s}) \left(g_{\mu\nu} - \frac{\hat{p}_\mu \hat{p}_\nu}{\hat{s}} \right).$$

The function $a(\hat{s})$ can be broken down into a resonance and a nonresonance part:

$$a(\hat{s}) = a^{\mathrm{r}}(\hat{s}) + a^{\mathrm{nr}}(\hat{s}).$$

The first component

$$a^{\mathrm{r}}(\hat{s}) = \sum_V \delta(\hat{s} - M_V^2) g_V^2$$

corresponds to the production of one vector meson V. Here, the coupling constant g_V is defined according

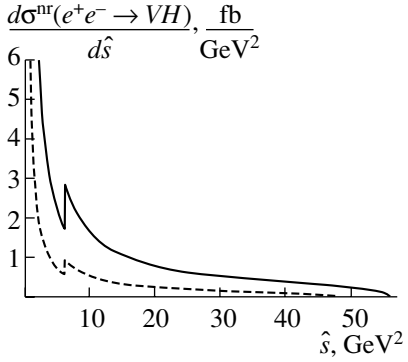

Fig. 2. Distribution in the invariant mass of the hadron state for (solid curve) $V = J/\psi$ and (dashed curve) $V = \psi(2S)$.

to (3), while $\delta(\hat{s}-M_V^2)$ is a narrow distribution $\hat{s}$ that is centered at the point $\hat{s}=M_V^2$ and which is characterized by a width $(\Gamma_V^{ee})^2$. The second component

$$a^{\rm nr}(\hat{s})=\sigma(e^+e^-\to\mu^+\mu^-)R(\hat{s})=\frac{\alpha^2}{6\pi^3}\frac{R(\hat{s})}{\hat{s}}$$

takes into account the production of any hadron state in a continuum. In determining the ratio $R(\hat{s})$, one can rely on experimental data, but we employ here the relation

$$R(\hat{s})=3\sum_q e_q^2, \tag{5}$$

which merely corresponds to the production of a pair of massless quarks (q and $\bar{q}$). It should be emphasized that analytic results given below are independent of the choice of specific expression for $R(\hat{s})$. For example, the hadron state H may involve either two or more than two particles.

3. INCLUSIVE PRODUCTION OF VECTOR CHARMONIUM

The diagrams describing the production of a vector charmonium V accompanied by a specific hadron state H are shown in Fig. 1. It should be noted that, although the contribution of processes involving a two-photon intermediate state is suppressed by an extra power of α in relation to the contribution of gluon-mediated hadron production, it may contribute significantly. The reason is that the momentum squared of the photon fragmenting into the vector meson is $p^2=M_V^2$ in the former case and satisfies the condition $s\gg M_V^2$ in the latter case.

The matrix element corresponding to the diagrams in Figs. 1*a* and 1*b* has the form

$$\mathcal{M}_{VH}=g_V\epsilon_\mu E_\nu(H)\bar{v}(k_2)\times\left[\frac{1}{q_a^2}\gamma^\nu\hat{q}_a\gamma^\mu+\frac{1}{q_b^2}\gamma^\mu\hat{q}_b\gamma^\nu\right]u(k_1)=g_V\epsilon_\mu E_\nu(H)L^{\mu\nu}.$$

For the inclusive cross section, we have

$$\sigma_{VH}=\sum_H\sigma(e^+e^-\to 2\gamma^*\to VH) \tag{6}$$
$$=\frac{2\pi^4g_V^2}{s}\epsilon_\mu\epsilon_\alpha^*\sum_H\int d\Phi_{n+1}(k_1+k_2;p,\{\hat{p}_i\})\times E_\nu(H)E_\beta^*(H)L^{\mu\nu}(L^{\alpha\beta})^\dagger.$$

The Lorentz-invariant phase space (2) satisfies the recursion relation

$$d\Phi_{n+1}(k_1+k_2;p,\{\hat{p}_i\})=(2\pi)^3d\hat{s}d\Phi_2(k_1+k_2;p,\hat{p})d\Phi_n(\hat{p};\{\hat{p}_i\}),$$

where $\hat{s}=\hat{p}^2=(\sum\hat{p}_i)^2$. Using this recursion relation and expression (4) for the virtual-photon polarization tensor, we can recast expression (6) into the form

$$\sigma_{VH}=\frac{\pi^2g_V^2}{8s}\int\limits_{\hat{s}_{\rm min}}^{\hat{s}_{\rm max}}d\hat{s}\frac{|\mathbf{p}|}{\sqrt{\hat{s}}}\int\limits_{-1}^{1}dxL_{\mu\nu}(L^{\mu\beta})^\dagger E_{\nu\beta}(\hat{p})=\frac{\pi^2g_V^2}{s}\int\limits_{\hat{s}_{\rm min}}^{\hat{s}_{\rm max}}d\hat{s}\lambda\left[\frac{\alpha^2}{6\pi^3}\frac{R(\hat{s})}{\hat{s}}+\sum_{V'}\delta(\hat{s}-M_{V'}^2)g_{V'}^2\right] \tag{7}$$
$$\times\int\limits_{-1}^{1}dx\frac{e_0^2(4-2e_0-e_1e_2)-(e_0^2-6e_0+e_1e_2+4)\lambda^2x^2-\lambda^4x^4}{(e_0^2-\lambda^2x^2)^2},$$

where $x=\cos\theta$ is the cosine of the scattering angle (that is, the angle between the momenta of the electron and the vector meson),

$$\lambda=\sqrt{1-\left(\frac{M_V}{\sqrt{s}}+\frac{\sqrt{\hat{s}}}{\sqrt{s}}\right)^2}\sqrt{1-\left(\frac{M_V}{\sqrt{s}}-\frac{\sqrt{\hat{s}}}{\sqrt{s}}\right)^2},$$

$$e_0=1-\frac{M_V^2}{s}-\frac{\hat{s}}{s},\qquad e_1=1+\frac{M_V^2}{s}-\frac{\hat{s}}{s},$$

$$e_2=1-\frac{M_V^2}{s}+\frac{\hat{s}}{s}.$$

The maximum value of $\hat{s}$ is $\hat{s}_{\rm max}=(\sqrt{s}-M)^2$; as for $\hat{s}_{\rm min}$, we consider two cases: $\hat{s}_{\rm min}=(2m_\pi)^2$ and $\hat{s}_{\rm min}=1\,{\rm GeV}^2$. In the former case, the ratio in (5) should in principle be corrected in order to take into account the π-meson form factor. However, we neglect these corrections because the form factor in

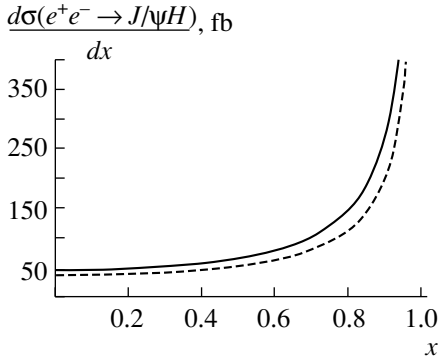

Fig. 3. Angular distribution for $V = J/\psi$: (solid curve) $\hat{s}_{\min} = (2m_\pi)^2$ and (dashed curve) $\hat{s}_{\min} = 1$ GeV^2.

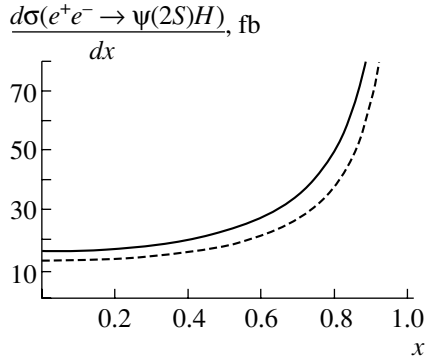

Fig. 4. Angular distribution for $V = \psi(2S)$ production: (solid curve) $\hat{s}_{\min} = (2m_\pi)^2$ and (dashed curve) $\hat{s}_{\min} = 1$ GeV^2.

question is close to unity. That term in expression (7) which corresponds to $V = V'$ must be divided by a factor of 2 in order to avoid the double counting of identical states.

Upon integration of the differential cross section (7) with respect to the scattering angle, we obtain the $\hat{s}$ distribution of the nonresonance component of the inclusive cross section:

$$\frac{d\sigma^{\rm nr}_{VH}}{d\hat{s}} = \frac{\alpha^2 g_V^2}{3\pi s\hat{s}} R(\hat{s})\lambda \left[\frac{e_0^2 - 2e_0 + 2}{e_0\lambda}\ln\frac{e_0+\lambda}{e_0-\lambda} - 2\right].$$

In the limit of low $\hat{s}$, the logarithmic term is dominant in the above expression, so that we have

$$\frac{d\sigma^{\rm nr}_{VH}}{d\hat{s}} \approx \frac{\alpha^2 g_V^2}{3\pi}\frac{R(\hat{s})}{\hat{s}}\frac{s^2+M^4}{s^2(s-M^2)}\ln\frac{(s-M^2)^2}{M^2\hat{s}},$$
$$\hat{s} \ll s, M^2.$$

The results of a numerical integration with respect to $\hat{s}$ are presented in the next section.

4. NUMERICAL RESULTS

The distributions of the nonresonance cross sections $\sigma^{\rm nr}_{VH}$ for $V = J/\psi$ and $\psi(2S)$ production with respect to the invariant mass of the hadron state are shown in Fig. 2. The distributions are seen to grow at low values of the invariant mass (or, in other words, near maximum values of the vector-meson energy in the c.m. frame). This shape of the distribution is governed by the virtual-photon and electron propagators, differing substantially from the shape of the analogous distributions for one-photon electron–positron annihilation.

The angular distributions of the cross sections for the inclusive production of J/ψ and $\psi(2S)$ at various values of $\hat{s}_{\min}$ are shown in Figs. 3 and 4, respectively. They also grow significantly in the vicinity of $x = 1$, in contrast to what we have in the case of one-photon annihilation.

The resonance and nonresonance contributions to the inclusive cross section for J/ψ and $\psi(2S)$ production are shown in the table for various values of $\hat{s}_{\min}$. The resonance contribution to the cross section involves all vector mesons V' whose production is allowed by the energy-conservation law (that is, whose mass satisfies the condition $M^2_{V'} < \hat{s}_{\max}$). The coupling constants $g_{V'}$ are determined by formula (3) with the meson masses and widths from [17]. The tabulated cross sections are an order of magnitude smaller than the cross sections for J/ψ and $\psi(2S)$ production in one-photon annihilation. However, the above distinctions between scattering-angle distributions and between the distributions in the vector-meson energy would make it possible to isolate the respective signal.

Table

V	$\sigma^{\rm r}_{VH}$, fb	$\sigma^{\rm nr}_{VH}$, fb	
		$\hat{s}_{\min} = (2m_\pi)^2$	$\hat{s}_{\min} = 1$ GeV^2
J/ψ	58.0	99.7	56.0
$\psi(2S)$	20.0	32.0	16.1

ACKNOWLEDGMENTS

I am grateful to A.K. Likhoded for stimulating discussions and enlightening comments.

This work was funded in part by the program for support of leading scientific schools (project no. 1303.2003.2).

REFERENCES

1. W. E. Caswell and G. P. Lepage, Phys. Lett. B **167B**, 437 (1986).
2. G. T. Bodwin, E. Braaten, and G. P. Lepage, Phys. Rev. D **51**, 1125 (1995); **55**, 5853(E) (1997); hep-ph/9407339.
3. BABAR Collab. (B. Aubert *et al.*), Phys. Rev. D **69**, 011103 (2004); hep-ex/0310027.
4. M. Benayoun *et al.*, Mod. Phys. Lett. A **14**, 2605 (1999); hep-ph/9910523.
5. BELLE Collab. (K. Abe *et al.*), Phys. Rev. Lett. **89**, 142001 (2002).
6. E. Braaten and J. Lee, Phys. Rev. D **67**, 054007 (2003); hep-ph/0211085.
7. K.-Y. Liu, Z.-G. He, and K.-T. Chao, Phys. Lett. B **557**, 45 (2003); hep-ph/0211181.
8. A. V. Berezhnoy and A. K. Likhoded, hep-ph/0303145.
9. F. Yuan *et al.*, Phys. Rev. D **56**, 321 (1997); hep-ph/9703438.
10. V. V. Kiselev, A. K. Likhoded, and M. V. Shevlyagin, Phys. Lett. B **332**, 411 (1994); hep-ph/9408407.
11. S. Baek *et al.*, J. Korean Phys. Soc. **33**, 97 (1998); hep-ph/9804455.
12. G. T. Bodwin, E. Braaten, and J. Lee, Phys. Rev. Lett. **90**, 162001 (2003); hep-ph/0212181.
13. A. V. Luchinsky, hep-ph/0301190.
14. E. Braaten and Yu-Qi Chen, Phys. Rev. Lett. **76**, 730 (1996); hep-ph/9508373.
15. P. L. Cho and A. K. Leibovich, Phys. Rev. D **54**, 6690 (1996); hep-ph/9606229.
16. K. Hagiwara *et al.*, Phys. Lett. B **570**, 39 (2003); hep-ph/0305102.
17. Particle Data Group (D. E. Groom *et al.*), Eur. Phys. J. C **15**, 1 (2000).

Translated by R. Rogalyov

Physics of Atomic Nuclei, Vol. 68, No. 8, 2005, pp. 1405–1413. From Yadernaya Fizika, Vol. 68, No. 8, 2005, pp. 1461–1469.

ELEMENTARY PARTICLES AND FIELDS
Theory

Special Case of Sunset: Reduction and ε Expansion*

A. I. Onishchenko[1)] and O. L. Veretin**

Institut für Theoretische Teilchenphysik, Universität Karlsruhe, Karlsruhe, Germany

Received March 30, 2004; in final form, September 22, 2004

Abstract—We consider two-loop sunset diagrams with two mass scales m and M at the threshold and pseudothreshold that cannot be treated by earlier published formulas. The complete reduction to master integrals is given. The master integrals are evaluated as a series in ratio m/M and in ε with the help of a differential-equation method. The rules of asymptotic expansion in the case when q^2 is at the (pseudo)threshold are given. © *2005 Pleiades Publishing, Inc.*

1. INTRODUCTION

The sunset diagram plays a key role in the two-loop calculations with masses. Despite the fact that a lot of investigation has been devoted to the sunset diagram, there still remain drawbacks. In [1], a general reduction procedure is given in the case when external momentum q and internal masses are arbitrary. But in the case when q^2 is equal to the threshold or one of the pseudothreshold values, the formula of [1] becomes inapplicable. Therefore, we turn to paper [2], where the reduction was given specifically for the (pseudo)threshold kinematics. However, even here in the two cases shown in the figure, the reduction of [2] requires additional analysis.

In the present paper, we consider calculation of these two special cases. These integrals naturally arise in the threshold problems with given mass hierarchy. An immediate typical example where it is the case is a problem of matching vector and axial QCD currents to NRQCD ones with two heavy-quark mass scales $m \ll M$. Another example is the calculation of masses of the heavy gauge bosons in the two-loop approximation [3], when q^2 is equal to m_Z^2 or m_W^2.

For the calculation of master integrals, there are mainly three methods: (i) direct evaluation using α or Feynman parameter representation; (ii) solving a master differential equation in external Mandelstam variables, which can be written for the master integrals of any Feynman graph; (iii) applying various asymptotic expansions [4, 5]; (iv) Mellin–Barnes representation. Here, we will demonstrate the strong and weak features of the first three methods using our particular problem as an example and will advocate that a certain mixing of these methods can give us a desired answer in the easiest way.

Now let us introduce the notation that will be used later in this paper and define the master integrals we are going to calculate. For the two-loop sunset with arbitrary masses and propagator indices, we have

$$J_{\nu_1\nu_2\nu_3}(q^2) = \frac{1}{\pi^d}\int\int \frac{d^dk\,d^dl}{[k^2-m_1^2]^{\nu_1}[(k-l)^2-m_2^2]^{\nu_2}[(l-q)^2-m_3^2]^{\nu_3}}, \quad (1)$$

where $d = 4 - 2\varepsilon$ is the dimension of spacetime.

We will discuss only two special cases of the sunset integrals which are shown in the figure:

(a) $m_1 = M,\ m_2 = 0,\ m_3 = m,\ q^2 = (M+m)^2$ (threshold case),

(b) $m_1 = m,\ m_2 = m,\ m_3 = M,\ q^2 = M^2$ (pseudothreshold case).

*This article was submitted by the authors in English.

1) On leave of absence from the Institute for High Energy Physics, Protvino, Russia, and the Institute for Theoretical and Experimental Physics, Moscow, Russia; e-mail: onish@particle.uni-karlsruhe.de

**e-mail: veretin@particle.uni-karlsruhe.de

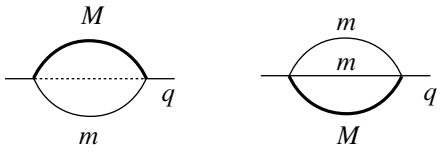

Case a: $q^2 = (m + M)^2$ Case b: $q^2 = M^2$

Sunset diagrams.

With the help of recurrence relations [6], which will be given in the next section, any integrals of the first type with arbitrary propagator indices can be reduced to two master integrals $J_{111}((m + M)^2)$ and $J_{112}((m + M)^2)$, whereas, in the second case, to two master integrals $J_{111}(M^2)$ and $J_{211}(M^2)$.

Another problem is the evaluation of the master integrals themselves. The general representation for the sunset diagram was obtained in [7] in terms of the hypergeometric Lauricella function. For practical purposes, however, one needs the ε expansion of these formulas.

The result for the threshold and pseudothreshold values of the sunset integrals with three arbitrary masses has been obtained in [8] up to $O(1)$ in ε expansion. From these results, we can easily obtain the finite parts of our integrals. However, we established that, in the reduction procedure for the matching of QCD to NRQCD currents, one has to know also the $O(\varepsilon)$ part for $J^{(a)}$ integrals and the $O(\varepsilon^2)$ part for $J^{(b)}$ integrals. It is not easy to push forward the approach of [8] in order to evaluate these needed parts. Instead, we use the differential-equation method [9–11] (see also [12]). We solve the differential equations as a series in m/M and the desired number of coefficients can always be obtained. In order to find the boundary conditions for the solutions, one can use two methods: the representation of [7] can be expanded in the limit $m/M \to 0$ and the asymptotic-expansion procedure can be applied at the threshold and pseudothreshold.

2. RECURRENCE RELATIONS AT THE THRESHOLD AND PSEUDOTHRESHOLD

Here we give the recurrence relations [6] for the sunsets of two types introduced earlier. While the derivation of these recurrence relations is straightforward, they have not been considered in the literature in detail until now. On the other hand, they represent the missing pieces to complete the generalized recurrence relations of Tarasov [1] and threshold relations of Davydychev and Smirnov [2] for the sunset diagrams in the case of threshold with one zero mass and pseudothreshold with two equal masses. Most of the formulas below can be derived just by combining and reexpressing the appropriate recurrence relations of [1, 2].

2.1. JM0m

In this case, some of the general relations obtained in [2] can be applied only after some transformations. The reason is that they become degenerate for this mass configuration. We present here an explicit solution:

$$(d - 2\nu_2 - 2)\nu_2 \mathbf{2}^+ = -2m^2\nu_3(\nu_3 + 1)\mathbf{3}^{++} + (d - 2\nu_3 - 2)\nu_3\mathbf{3}^+, \quad (2)$$

$$2M^2\nu_1(\nu_1 + 1)\mathbf{1}^{++} = 2m^2\nu_3(\nu_3 + 1)\mathbf{3}^{++} - (d - 2\nu_3 - 2)\nu_3\mathbf{3}^+ + (d - 2\nu_1 - 2)\nu_1\mathbf{1}^+, \quad (3)$$

$$2m^2(M + m)(3d - 2\nu_1 - 2\nu_3 - 7) \times \nu_3(\nu_3 + 1)\mathbf{3}^{++} = \Big[m\Big((d - \nu_3 - 3)(2d - \nu_1 - 2\nu_3 - 4) + (d - \nu_1 - \nu_3 - 2)(3d - 2\nu_2 - 2\nu_3 - 6)\Big) + M(2d - \nu_1 - 2\nu_3 - 5)(2d - \nu_1 - 2\nu_3 - 4)\Big]\nu_3\mathbf{3}^+ + (d - \nu_3 - 2)\Big(m(d - \nu_3 - 3) + M(2d - \nu_1 - 2\nu_3 - 5)\Big)\nu_1\mathbf{1}^+ + 2m^2 \times M\nu_1\nu_3(\nu_3 + 1)\mathbf{1}^+\mathbf{2}^-\mathbf{3}^{++} + \Big[-m(d - \nu_3 - 3) - M(2d - \nu_1 - 2\nu_3 - 5)\Big]\nu_1\nu_3\mathbf{1}^+\mathbf{2}^-\mathbf{3}^+, \quad (4)$$

$$2mM(m + M)(3d - 11)J_{212} = -(d - 3)\Big(m(d - 3) + M(2d - 7)\Big)J_{112} - (d - 3)\Big(m(2d - 7) + M(d - 3)\Big)J_{211} + \frac{m + M}{4m^2M^2}(d - 2)^2(2d - 7)J_{101}. \quad (5)$$

Here, as usual, $\mathbf{j}^+$ (or $\mathbf{j}^-$) means the operator raising (or lowering) the index on the jth line. In particular, (2) and (3) follow directly from [2].

With the help of (2)–(5), we reduce all integrals to three sunset diagrams J_{111}, J_{112}, and J_{211} plus products of one-loop tadpoles. In addition, there is a relation between these three sunset integrals and one of them can be eliminated,

$$M(m + 2M)J_{211} + m(M + 2m)J_{112} = \frac{3d - 8}{2}J_{111} + \frac{(d - 2)^2}{4mM(d - 3)}J_{101}. \quad (6)$$

This finishes the reduction procedure.

2.2. JmmM

Here, we are faced with the pseudothreshold problem, and again, in this case, the general recurrence relations by Tarasov [1] and those for the threshold problems by Davydychev and Smirnov [2] become degenerate. The reduction procedure for this type of integrals was studied in [13], where the topology with three and four lines was considered. The problem was solved by reduction to master integrals: sunset and the integral with additional massless line. These integrals were also considered in [14], where an asymptotic expansion was used. For completeness, we give reduction formulas which follow from [13], but we use a slightly different set of master integrals.

First, using relations

$$2m^2\nu_1(\nu_1+1)\mathbf{1}^{++} = (d-2\nu_1-2)\nu_1\mathbf{1}^{+} \quad (7)$$
$$-(d-2\nu_3-2)\nu_3\mathbf{3}^{+} + 2M^2\nu_3(\nu_3+1)\mathbf{3}^{++},$$
$$2m^2\nu_2(\nu_2+1)\mathbf{2}^{++} = (d-2\nu_2-2)\nu_2\mathbf{2}^{+} \quad (8)$$
$$-(d-2\nu_3-2)\nu_3\mathbf{3}^{+} + 2M^2\nu_3(\nu_3+1)\mathbf{3}^{++},$$

we reduce the indices of lines 1 and 2 to one or two. Thus, there remain only integrals $J_{11\nu_3}$, $J_{12\nu_3}$, and $J_{22\nu_3}$.

For $J_{12\nu_3}$, we have

$$4(M^2-m^2)\nu_3\mathbf{3}^{+} = \Big[\mathbf{1}^{-} - (d-3)\mathbf{2}^{-}\Big]\nu_3\mathbf{3}^{+} \quad (9)$$
$$-\mathbf{1}^{+}\mathbf{3}^{-} + d - 3\nu_3.$$

For $J_{22\nu_3}$, we have

$$4m^2(M^2-m^2)(d-\nu_3-3) = m^2 \quad (10)$$
$$\times(d-\nu_3-3)\mathbf{3}^{-} + \Big[m^2\Big(-3d^2 + d(13+7\nu_3)$$
$$-12-17\nu_3-4\nu_3^2\Big) + M^2(2d-\nu_3-6)$$
$$\times(d-\nu_3-2)\Big]\mathbf{1}^{-} + \Big[-m^2 + M^2(d-\nu_3-2)\Big]$$
$$\times(d-3)\nu_3\mathbf{3}^{+}\mathbf{1}^{-}\mathbf{2}^{-} + \Big[m^2(d-3)$$
$$-M^2(2d-\nu_3-6)\Big]\nu_3\mathbf{3}^{+}\mathbf{1}^{--}.$$

For $J_{11\nu_3}$, we have

$$4M^2(M^2-m^2)(d-\nu_3-3) \quad (11)$$
$$\times\nu_3(\nu_3+1)\mathbf{3}^{++} = \Big[-m^2(d-2\nu_3-3)$$
$$\times(2d-2\nu_3-5) + M^2\Big(3d^2 - d(17+7\nu_3) + 24$$
$$+19\nu_3+4\nu_3^2\Big)\Big]\nu_3\mathbf{3}^{+} + \Big[-m^2\Big(d^2 - d(3+5\nu_3)$$
$$+\nu_3(4\nu_3+11)\Big) - M^2(d-\nu_3-2)\nu_3\Big]\mathbf{2}^{+}$$
$$+\Big[-m^2(d-3) + M^2\nu_3\Big]\nu_3\mathbf{3}^{+}\mathbf{2}^{+}\mathbf{1}^{-}$$
$$+m^2(d-\nu_3-3)\mathbf{3}^{-}\mathbf{1}^{+}\mathbf{2}^{+}.$$

Finally, there is a relation between three integrals

$$M^2J_{112} + m^2J_{211} = \frac{3d-8}{4}J_{111} \quad (12)$$
$$-\frac{(d-2)^2}{8m^2(d-3)}J_{110}.$$

This finishes the reduction.

3. MASTER DIFFERENTIAL EQUATION

It is known that a general two-loop sunset topology has four master integrals [1]: one with unit powers of propagators and three with a dot placed on one of the lines. For master integrals considered in this paper, this number is, however, smaller, which is due to a symmetry of the mass distribution on the lines. In addition, in case of $JM0m$, the index of massless line can always be reduced to 1 (see [1]). It can be shown that these master integrals satisfy a system of linear nonhomogeneous differential equations in q^2 (q being external momentum) [11] or in masses [9]. However, in our case, we want to write differential equations in $r = m/M$, where m and M are internal masses and q^2 lies at threshold or pseudothreshold. Differential equations of this type were considered earlier in [15].

3.1. JM0m

In this case, we have two master integrals (J_{111} and J_{112}) and a system of two first-order equations. It is convenient to rescale integrals introducing $\tilde{J}_{111}$ and $\tilde{J}_{112}$ by

$$J_{111} = M^{2d-6}\Gamma^2(3-d/2)\tilde{J}_{111} \quad \text{and} \quad (13)$$
$$J_{112} = M^{2d-8}\Gamma^2(3-d/2)\tilde{J}_{112}.$$

Then the differential equations read

$$\begin{cases} (r+1)(r+2)\dfrac{\partial}{\partial r}\tilde{J}_{111} - 6r(r+1)\tilde{J}_{112} \\ -\Big(d+2(d-3)r-4\Big)\tilde{J}_{111} \\ -\dfrac{8r^{d-3}}{(d-4)^2(d-3)} = 0, \\ (r+1)(r+2)\dfrac{\partial}{\partial r}\tilde{J}_{112} + \dfrac{1}{r}(2r^2-5dr \\ +20r-4d+14)\tilde{J}_{112} - \dfrac{(d-3)(3d-8)}{2r}\tilde{J}_{111} \\ -\dfrac{8r^{d-5}}{(d-4)^2} = 0. \end{cases} \quad (14)$$

Using this system one can write the second-order differential equation for $\tilde{J}_{111}$:

$$(r+1)^2(r+2)^2\frac{\partial^2}{\partial r^2}\tilde{J}_{111} - \frac{2}{r}(r+1) \quad (15)$$

$$\times (r+2)^2\Big(d+(d-4)r-3\Big)\frac{\partial}{\partial r}\tilde{J}_{111}$$
$$+\frac{1}{r}(d-3)^2(r+2)^2(d-2r-4)\tilde{J}_{111}$$
$$-\frac{8}{(d-4)^2}(r+2)^2r^{d-4}=0.$$

As usual, we search for the solution to (15) as a linear combination of two solutions to the homogeneous equation and the solution to the nonhomogeneous equation. We will find the solution as a series in r, namely, in the following form:

$$\tilde{J}_{111}=\sum_i r^{\alpha_i}\left(\sum_{n=0}^{\infty}a_n^{(i)}(d)r^n\right). \qquad (16)$$

By substituting (16) into (15), we find for leading exponents α_i three allowed values $\alpha_1=0$, $\alpha_2=2d-5$, corresponding to the two independent solutions of the associated homogeneous equation, and $\alpha_3=d-2$, as required by the nonhomogeneous part of Eq. (15). So, the only thing we still need to do is to find the coefficients in front of two independent solutions to the homogeneous part of Eq. (15) using boundary conditions. One equation for these coefficients can be obtained from the value of the J_{111} master integral at $r=0$, which can be written in terms of Γ functions. One cannot use J_{112} at $r=0$ as the second boundary condition. The reason is that the latter integral becomes infrared divergent and this divergency is regularized by ε ($d=4-2\varepsilon$) and not by r as in the limit $r\to 0$. In order to obtain a second boundary condition, we need an explicit expansion of function J_{111} in r up to the third order, which can be obtained by analyzing the representation of this integral in terms of Appel function F_4 or performing an asymptotic expansion in small mass ratio r. Expansion of the Appel function will be considered in the Appendix, while the asymptotic expansion technique is discussed in Subsection 4.1.

Having obtained an expansion in r up to order $O(r^3)$ using one of the aforementioned methods, one can easily reconstruct all other expansion coefficients from the differential equation. Returning back to functions J_{111} and J_{112} instead of $\tilde{J}_{111}$ and $\tilde{J}_{112}$, we give the first seven coefficients of the expansion:

$$e^{2\varepsilon\gamma_{\rm E}}M^{-2+4\varepsilon}J_{111}=-\frac{1+r^2}{2\varepsilon^2} \qquad (17)$$
$$+\frac{(8L-5)r^2+2r-5}{4\varepsilon}-\frac{1}{8}(11+20\zeta_2)+\frac{5r}{4}$$
$$-\frac{1}{8}(16L^2-48L-12\zeta_2+7)r^2-\frac{2}{9}(9L^2+15L$$
$$+54\zeta_2-8)r^3+\frac{1}{8}(24L^2+20L+144\zeta_2-3)r^4$$
$$-\frac{2}{225}(450L^2+255L+2700\zeta_2-16)r^5$$
$$+\frac{1}{72}(360L^2+156L+2160\zeta_2-5)r^6+\varepsilon\Bigg(\frac{55}{16}$$
$$-\frac{25\zeta_2}{4}-\frac{11\zeta_3}{3}+\frac{1}{8}(20\zeta_2+11)r+\Bigg(\frac{4L^3}{3}$$
$$-6L^2+2(\zeta_2+7)L+\frac{1}{48}(276\zeta_2+208\zeta_3$$
$$+321)\Bigg)r^2+\Bigg(4L^3+\frac{2L^2}{3}+\left(40\zeta_2-\frac{238}{9}\right)L$$
$$-\frac{68\zeta_2}{3}-24\zeta_3+\frac{773}{54}\Bigg)r^3+\Bigg(-6L^3-\frac{L^2}{2}$$
$$+\left(\frac{463}{12}-60\zeta_2\right)L+17\zeta_2+36\zeta_3-\frac{4639}{144}\Bigg)r^4$$
$$+\Bigg(8L^3+\frac{23L^2}{15}+\left(80\zeta_2-\frac{22681}{450}\right)L-\frac{134\zeta_2}{15}$$
$$-48\zeta_3+\frac{1242497}{27000}\Bigg)r^5+\Bigg(-10L^3-\frac{19L^2}{6}$$
$$+\left(\frac{3751}{60}-100\zeta_2\right)L-\frac{5\zeta_2}{3}+60\zeta_3$$
$$-\frac{648161}{10800}\Bigg)r^6\Bigg)+O(r^7)+O(\varepsilon^2)$$

and

$$e^{2\varepsilon\gamma_{\rm E}}M^{4\varepsilon}J_{112}=-\frac{1}{2\varepsilon^2}+\frac{2L-1/2}{\varepsilon} \qquad (18)$$
$$+\frac{1}{4}(6\zeta_2+2)+4L-2L^2+(-2L^2-4L$$
$$-12\zeta_2+2)r+\left(3L^2+3L+18\zeta_2-\frac{1}{2}\right)r^2$$
$$+\left(-4L^2-\frac{8L}{3}-24\zeta_2+\frac{2}{9}\right)r^3+\Bigg(5L^2+\frac{5L}{2}$$
$$+30\zeta_2-\frac{1}{8}\Bigg)r^4+\Bigg(-6L^2-\frac{12L}{5}-36\zeta_2$$
$$+\frac{2}{25}\Bigg)r^5+\left(7L^2+\frac{7L}{3}+\frac{1}{18}(756\zeta_2-1)\right)r^6$$
$$+\varepsilon\Bigg(\frac{1}{12}(66\zeta_2+52\zeta_3+66)+8L+2L\zeta_2-4L^2$$
$$+\frac{4L^3}{3}+(4L^3+4L^2+40\zeta_2L-24L-8\zeta_2$$
$$-24\zeta_3+14)r+\Bigg(-6L^3-5L^2-60\zeta_2L+37L$$
$$-6\zeta_2+36\zeta_3-\frac{67}{2}\Bigg)r^2+\Bigg(8L^3+\frac{22L^2}{3}+80\zeta_2L$$
$$-\frac{440L}{9}+\frac{68\zeta_2}{3}-48\zeta_3+\frac{1277}{27}\Bigg)r^3$$

$$+\left(-10L^3-\frac{31L^2}{3}-100\zeta_2 L+\frac{1097L}{18}-42\zeta_2+60\zeta_3-\frac{4403}{72}\right)r^4+\left(12L^3+\frac{69L^2}{5}+120\zeta_2 L-\frac{5489L}{75}+\frac{318\zeta_2}{5}-72\zeta_3+\frac{75179}{1000}\right)r^5+\left(-14L^3-\frac{529L^2}{30}-140\zeta_2 L+\frac{6418L}{75}-\frac{1307\zeta_2}{15}+84\zeta_3-\frac{4823273}{54000}\right)r^6\Bigg)+O(r^7)+O(\varepsilon^2),$$

where $L=\log r$. The $O(1)$ part of J_{111} is in agreement with [8].

3.2. JmmM

This diagram was recently studied in [16] by means of the differential-equation method in the regime when $m \gg M$, while we are interested in the case $m \ll M$. Here, we also have two master integrals and a system of two differential equations. Again introducing rescaled functions according to (13), we have

$$\begin{cases}\dfrac{\partial}{\partial r}\tilde{J}_{111}-4r\tilde{J}_{211}=0,\\ (r^2-1)\dfrac{\partial}{\partial r}\tilde{J}_{211}+\dfrac{r^2(13-4d)+2d-7}{r}\tilde{J}_{211}\\ \quad+\dfrac{(d-3)(3d-8)}{4r}\tilde{J}_{111}-\dfrac{2r^{d-7}(r^d-2r^2)}{(d-4)^2}=0.\end{cases} \tag{19}$$

Using (19), the corresponding second-order differential equation for J_{111} looks like

$$(r^2-1)\frac{\partial^2}{\partial r^2}J_{111}-\frac{2(d-3)(2r^2-1)}{r}\frac{\partial}{\partial r}J_{111}+(d-3)(3d-8)J_{111}-\frac{8r^{d-6}(r^d-2r^2)}{(d-4)^2}=0. \tag{20}$$

To find a solution to this equation, we again use ansatz (16) for the most general form of solution at $r\to 0$. For leading exponents α_i, there are four allowed values $\alpha_1=0$, $\alpha_2=2d-5$, corresponding to the two independent solutions of the associated homogeneous equation, and $\alpha_3=d-2$, $\alpha_4=2d-4$, as required by the nonhomogeneous part of Eq. (20). All other steps in this case are in one-to-one correspondence with those considered in the previous subsection. The first boundary condition is given by the value of master integral J_{111} at $r=0$. In order to find the second boundary condition, we need an explicit expression for r expansion of J_{111} up to the third order, which can be obtained from threshold large-mass asymptotic expansion of J_{111}. As a result of all these steps, we have the following expressions for our master integrals:

$$e^{2\varepsilon\gamma_{\rm E}}M^{-2+4\varepsilon}J_{111}=-\frac{1+2r^2}{2\varepsilon^2}+\frac{4(4L-3)r^2-5}{4\varepsilon}-\frac{1}{8}(11+20\zeta_2)-(4L^2-12L-3\zeta_2+5)r^2-\frac{1}{4}(8L^2-12L+8\zeta_2+7)r^4-\frac{1}{18}(12L-11)r^6+\varepsilon\left(\frac{55}{16}-\frac{11\zeta_3}{3}-\frac{25\zeta_2}{4}+\left(\frac{8L^3}{3}-12L^2+4(\zeta_2+7)L+9\zeta_2+\frac{26\zeta_3}{3}-3\right)r^2-32\zeta_2 r^3+\left(4L^3-5L^2-\frac{7L}{2}+4\zeta_2-4\zeta_3+\frac{95}{8}\right)r^4+\frac{32\zeta_2 r^5}{5}+\frac{2}{9}(8L-9\zeta_2-14)r^6\right)+\varepsilon^2\left(\frac{949}{32}-\frac{55\zeta_2}{8}-\frac{55\zeta_3}{6}-\frac{1}{720}\pi^4\times(296r^4-578r^2+303)+\left(-\frac{4L^4}{3}+8L^3-4(\zeta_2+7)L^2+\frac{4}{3}(9\zeta_2-2\zeta_3+45)L+31\zeta_2+26\zeta_3+19\right)r^2+\frac{64}{3}(6L+12\log 2-11)\zeta_2 r^3+\left(-\frac{14L^4}{3}+6L^3+\left(\frac{3}{2}-2\zeta_2\right)L^2+\left(3\zeta_2+\frac{37}{4}\right)L-\frac{71\zeta_2}{4}+8\zeta_3-\frac{885}{16}\right)r^4-\frac{32}{75}(60L+120\log 2-77)\zeta_2 r^5+\frac{1}{324}(288L^3-792L^2-108(2\zeta_2+11)L+1926\zeta_2-1296\zeta_3+5417)r^6\right)+O(r^7)+O(\varepsilon^3) \tag{21}$$

and

$$e^{2\varepsilon\gamma_{\rm E}}M^{4\varepsilon}J_{211}=-\frac{1}{2\varepsilon^2}+\frac{4L-1}{2\varepsilon}+\frac{1}{2}+\frac{3\zeta_2}{2}+4L-2L^2-(2L^2-2L+2\zeta_2+1)r^2+\left(\frac{3}{4}-L\right)r^4+\left(\frac{5}{36}-\frac{L}{3}\right)r^6+\varepsilon\left(\frac{11}{2}+\frac{11\zeta_2}{2}+\frac{13\zeta_3}{3}+8L+2L\zeta_2-4L^2+\frac{4L^3}{3}-24\zeta_2 r+(4L^3-2L^2-6L+4\zeta_2-4\zeta_3+11)r^2+8\zeta_2 r^3 \tag{22}$$

$$+\frac{1}{9}(24L-27\zeta_2-38)r^4+\frac{8\zeta_2 r^5}{5}+\left(\frac{L}{45}-\zeta_2-\frac{83}{300}\right)r^6\Bigg)+\varepsilon^2\Bigg(\frac{49}{2}+\frac{37\zeta_2}{2}+\frac{37\zeta_3}{3}+\frac{289\pi^4}{720}-\frac{4}{3}L(\zeta_3-12)+4L\zeta_2-2L^2\zeta_2-8L^2+\frac{8L^3}{3}-\frac{2L^4}{3}+48\zeta_2(2L+4\log 2-3)r+\Bigg(-\frac{14L^4}{3}+\frac{4L^3}{3}-2(\zeta_2-3)L^2+2(\zeta_2+5)L-17\zeta_2+8\zeta_3-\frac{37\pi^4}{90}-53\Bigg)r^2-\frac{8}{3}(12L+24\log 2-13)\zeta_2 r^3+\Bigg(\frac{4L^3}{3}-3L^2-\left(\zeta_2+\frac{121}{18}\right)L+\frac{35\zeta_2}{4}-6\zeta_3+\frac{5219}{216}\Bigg)r^4-\frac{4}{75}(120L+240\log 2-199)\zeta_2 r^5+\Bigg(\frac{4L^3}{9}-\frac{5L^2}{9}-\frac{1}{450}(150\zeta_2+203)L+\frac{37\zeta_2}{180}-2\zeta_3+\frac{237511}{81000}\Bigg)r^6\Bigg)+O(r^7)+O(\varepsilon^3),$$

where $L=\log r$. The $O(1)$ part of J_{111} is in agreement with [8].

4. ASYMPTOTIC LARGE-MASS EXPANSION AT THE THRESHOLD

In this section, we consider an asymptotic large-mass expansion for the master integrals introduced above. The type of expansion one needs to perform in order to obtain an analytic expression for the master integral of case (b) was already considered in [17] and [14], and one may just follow along the lines of the procedure described there. However, in the case of master integral $JM0m$, a somewhat different prescription for setting loop momenta is required,[2)] and thus we will consider this case in detail below.

In order to establish the expansion procedure, we use an approach similar to [17]. In this regime, it is equivalent to the "strategy of regions" suggested in [18] for the large-mass expansion at the threshold. This approach was developed later in [19]. We consider a general case of threshold Feynman integral F_Γ, corresponding to a graph Γ when the masses M_i and external momenta Q_i are considered large with respect to small masses m_i and external momenta q_i. We are interested in the case when external momenta Q_i are on the following mass shell: $Q_i^2=(\sum_j a_{ij}M_j+\sum_k b_{ik}m_k)^2$. Here, a_{ij} and b_{ik} are some numbers. It is just the generalization of the on-mass-shell condition of [17]. Then the asymptotic expansion in the limit $Q_i, M_i\to\infty$ takes the following explicit form [4]:

$$F_\Gamma(Q_i,M_i,q_i,m_i;\varepsilon)\underset{M_i\to\infty}{\sim}\sum_\gamma \mathcal{M}_\gamma F_\Gamma(Q_i,M_i,q_i,m_i;\varepsilon). \tag{23}$$

Here the sum runs over subgraphs γ of Γ such that

(i) in γ, there is a path between any pair of external vertices associated with the large external momenta Q_i;

(ii) γ contains all the lines with large masses;

(iii) every connectivity component γ_j of the graph $\hat\gamma$ obtained from γ by collapsing all the external vertices with large external momenta to a point is 1 PI with respect to the lines with small masses.

Operator $\mathcal{M}_\gamma$ in (23) can be written as a product $\Pi_i\mathcal{M}_{\gamma_i}$ over different connectivity components, where $\mathcal{M}_{\gamma_i}$ are operators of Taylor expansion in certain momenta and masses. In what follows, we will distinguish the connectivity component γ_0, which is defined to contain all external vertices with large momenta. For connectivity components γ_i, different from γ_0, the corresponding operator $\mathcal{M}_{\gamma_i}$ performs a Taylor expansion of the Feynman integral F_{γ_i} in its small masses and external momenta. To describe the action of $\mathcal{M}_{\gamma_0}$, one uses a representation of the γ_0 component in terms of a union of its 1 PI components and cut heavy lines (that is a subgraph becomes disconnected after a cut line is removed). Here, we can again factorize $\mathcal{M}_{\gamma_0}$ and the Taylor expansion of the 1 PI components of γ_0 is performed as in the case of other connectivity components γ_i. As for the action of operator $\mathcal{M}$ on the cut lines, there are two different

[2)] Asymptotic expansions in momentum space are not invariant under the redefinition of loop momenta contrary to the expansions performed in the α representation for Feynman integrals. Therefore, special care should be taken in choosing a correct set of momenta.

cases. Let $P+k$ be the momentum of a line with large mass M_i, where P is a linear combination of large external momenta and k is a linear combination of loop momenta and small external momenta. Then the aforementioned two cases can be written as follows:

$P^2 = M_i^2$ and $\mathcal{M}$ for this line is given by

$$\mathcal{M} = \mathcal{T}_x \frac{1}{xk^2 + 2Pk}\bigg|_{x=1}. \qquad (24)$$

Here, $\mathcal{T}_x$ denotes the operator of Taylor expansion in x around $x = 0$.

$P^2 \neq M_i^2$ and the operator $\mathcal{M}$ reduces to the ordinary Taylor expansion in small (with respect to this line) external momenta.

As for the optimal set of internal loop momenta, we choose a rule when large external momenta are divided between lines with masses M_i and m_k in order to satisfy the following conditions: $P_i^2 = M_i^2$ and $P_k^2 = m_k^2$. We do not know whether such separation is always possible or not, but in most cases of interest it certainly works. As an example in the next subsection, we will consider an expansion for master integral $J_{111}((m+M)^2)$ from our case (a).

4.1. Second Boundary Condition for JM0m

For master integral J_{111}, according to our prescription for choosing internal momenta, we have the following expression:

$$J_{111} \qquad (25)$$
$$= \frac{1}{\pi^d}\int\int \frac{d^dk\,d^dl}{[k^2][(k+l)^2 + 2a(k+l,q)][l^2+2blq]}.$$

Here, q is an external momentum; $a = M/(M+m)$ and $b = -m/(M+m)$. From the general formula (23) in the asymptotic expansion of master integral J_{111} in the limit $m/M \to 0$, we have four subgraphs:[3)]

(i) graph Γ itself;

(ii) subgraph γ_1 consisting of lines with masses M and m;

(iii) subgraph γ_2 consisting of lines with masses M and zero;

(iv) subgraph γ_3 consisting of one heavy line.

For graph Γ, we expand the integrand around $m = 0$ with the result

$$\sum_{n=0}^{\infty} \frac{(-1)^n(2b)^n}{\pi^d} \qquad (26)$$
$$\times \int\int \frac{d^dk\,d^dl\,(l\cdot q)^n}{[k^2][(k+l)^2 + 2a(k+l,q)][l^2]^{n+1}}.$$

[3)] Here, Γ is the graph corresponding to Feynman integral J_{111}.

Each term in this expansion can be evaluated by rewriting it via scalar integrals with shifted spacetime dimension [1], and for the first three of them, we have

$$\frac{1}{\pi^d}\int\int \frac{d^dk\,d^dl\,(lq)}{[k^2][l^2]^2[(k+l)^2 + 2a(k+l,q)]} = -aq^2\mathrm{JV}^{d+2}_{222},$$

$$\frac{1}{\pi^d}\int\int \frac{d^dk\,d^dl\,(lq)^2}{[k^2][l^2]^3[(k+l)^2 + 2a(k+l,q)]} = -\frac{q^2}{2}\mathrm{JV}^{d+2}_{231} - \frac{q^2}{2}\mathrm{JV}^{d+2}_{132} + 4a^2q^4\mathrm{JV}^{d+4}_{333},$$

$$\frac{1}{\pi^d}\int\int \frac{d^dk\,d^dl\,(lq)^3}{[k^2][l^2]^4[(k+l)^2 + 2a(k+l,q)]} = -36a^3q^6\mathrm{JV}^{d+6}_{444} + 3aq^4\mathrm{JV}^{d+4}_{243} + 3aq^4\mathrm{JV}^{d+4}_{342},$$

where

$$\mathrm{JV}^d_{\nu_1\nu_2\nu_3} = \frac{1}{\pi^d}\int\int \frac{d^dk\,d^dl}{[k^2]^{\nu_1}[l^2]^{\nu_2}[(k+l)^2 + 2(k+l,q)]^{\nu_3}} \quad \text{and} \quad q^2 = M^2.$$

The latter can be easily expressed in terms of Γ functions for arbitrary values of ν_1, ν_2, and ν_3.

Subgraph γ_1 is equal to zero.

The Taylor expansion for subgraph γ_2 gives

$$\sum_{n=0}^{\infty} \frac{(-1)^n}{\pi^d}\int\int \frac{d^dk\,d^dl\,(k^2+2kl+2akq)^n}{[k^2][l^2+2alq]^{n+1}[l^2+2blq]} = 0. \qquad (27)$$

In the case of subgraph γ_3, we have the expression

$$\sum_{n=0}^{\infty} \frac{(-1)^n}{\pi^d}\int\int \frac{d^dk\,d^dl\,(l^2+2kl+2alq)^n}{[k^2][k^2+2akq]^{n+1}[l^2+2blq]}. \qquad (28)$$

Each term of this sum is just a product of two one-loop integrals and hence can be easily evaluated.

An expansion for subgraph γ_4 leads to the following result:

$$\sum_{n=0}^{\infty} \frac{(-1)^n}{\pi^d}\int\int \frac{d^dk\,d^dl\,((k+l)^2)^n}{[k^2][l^2+2blq][2a(k+l,q)]^{n+1}}. \qquad (29)$$

Here, we can see that it is the most difficult type of contribution from the point of view of computation, as we are dealing in this case with eikonal integrals. As one can easily see, the evaluation of each term from this contribution can be reduced to the evaluation of integrals of the following type:

$$\frac{1}{\pi^d}\int\int \frac{d^dk\,d^dl\,(kl)^m}{[k^2][l^2+2blq][(k+l,q)]^n}. \qquad (30)$$

In order to calculate these integrals, it is natural to express the products $(kl)^m$ in terms of traceless products $(kl)^{(m)} \equiv k^{(\alpha,m)} l_{(\alpha,m)}$[4]. Then we notice that integration over k of traceless products $k^{(\alpha,m)}$ times the part of integrand which depends only on k results in an expression proportional to the traceless product $q^{(\alpha,m)}$. Thus, we can replace the factor $(kl)^{(m)}$ by $(qk)^{(m)}(ql)^{(m)}/(qq)^{(m)}$ and finally replace the factors involved through ordinary products qk and lq. After performing these steps, we reduce the evaluation of integrals (30) to the integrals

$$\frac{1}{\pi^d}\int\int \frac{d^dk d^dl (lq)^m}{[k^2][l^2+2blq][(k+l,q)]^n}. \qquad (31)$$

These integrals with the use of integration-by-parts identities $(d-3-n)n^+ + (n+1)m^+n^{++} = 0$, where $n(m)^+$ are operators which increase corresponding indices n or m, can be further reduced to integrals of the form

$$\frac{1}{\pi^d}\int\int \frac{d^dk d^dl (lq)^m}{[k^2][l^2+2blq][(k+l,q)]}. \qquad (32)$$

To take these last integrals, one can first perform k_0 and l_0 integrations using the Cauchy theorem and the remaining angular integrations are trivial since there are no products kl in the integrand left.

However, as our calculations showed, it is far simpler just to calculate this master integral using asymptotic expansion up to the order $(m/M)^3$ and then use this result as the necessary boundary conditions for the solution to the master differential equation. It then takes much less effort to construct the expansion of this master integral up to any order in $r = m/M$ using the differential-equation method.

5. CONCLUSION

We considered two-loop sunset diagrams with two mass scales m and M at the threshold and pseudothreshold that cannot be treated by earlier published formulas [1, 2]. The complete reduction to the master integrals is given. The master integrals are evaluated as a series in ratio m/M and up to order in ε needed in applications with the help of the differential-equation method. The rules of asymptotic expansion in the case when q^2 is at the (pseudo)threshold are given.

[4] Here, α is a collective index representing m Lorenz indices $\alpha_1, \alpha_2, \ldots, \alpha_m$.

ACKNOWLEDGMENTS

We would like to thank K. Chetyrkin, A. Davydychev, V.A. Smirnov, M.Yu. Kalmykov, and O.V. Tarasov for fruitful discussions of the topics discussed in this paper and valuable comments. We also acknowledge Universität Karlsruhe for the warm hospitality.

APPENDIX

EXPANSION OF F_4 APPEL FUNCTION: SECOND BOUNDARY CONDITION FOR $JM0m$

In order to obtain the second boundary integral in the case of $JM0m$, we can use the representation of the sunset diagram in terms of the Lauricella function which can be obtained from [7]. However, since one mass is zero, the Lauricella function simplifies to the Appel function:

$$\begin{aligned} &e^{2\gamma\varepsilon} M^{-2+4\varepsilon} J_{111}(m, M, 0; q^2) \qquad (A.1)\\ &= -\left(\frac{m^2}{M^2}\right)^{1-\varepsilon} \Gamma^2(-1+\varepsilon)\\ &\times F_4\left(\begin{matrix}1, \varepsilon\\ 2-\varepsilon, 2-\varepsilon\end{matrix}; \frac{m^2}{M^2}, \frac{q^2}{M^2}\right)\\ &- \Gamma(1-\varepsilon)\Gamma(-1+\varepsilon)\Gamma(-1+2\varepsilon)\\ &\times F_4\left(\begin{matrix}-1+2\varepsilon, \varepsilon\\ \varepsilon, 2-\varepsilon\end{matrix}; \frac{m^2}{M^2}, \frac{q^2}{M^2}\right), \end{aligned}$$

and in our case $q^2 = (m+M)^2$. We need the expansion of this integral up to the order $O(r^3)$ and $O(\varepsilon)$. Then the remaining coefficients can be found from the differential equation.

In order to expand (A.1) in a series over m/M, we use the following representation for F_4:

$$\begin{aligned} &F_4\left(\begin{matrix}a, b\\ c, c'\end{matrix}; x, y\right) \qquad (A.2)\\ &= \sum_{k=0}^{\infty} \frac{(a)_k (b)_k}{(c)_k} \frac{x^k}{k!} {}_2F_1\left(\begin{matrix}a+k, b+k\\ c'\end{matrix}; y\right). \end{aligned}$$

In (A.2), function ${}_2F_1$ has to be transformed to the argument $1-y$. Then we have for the right-hand side $(r = m/M)$

$$\begin{aligned} &-r^{2-2\varepsilon}\Gamma^2(-1+\varepsilon) \sum_{k=0}^{\infty} \frac{(1)_k(\varepsilon)_k}{(2-\varepsilon)_k} \frac{r^{2k}}{k!} \qquad (A.3)\\ &\times \left\{ \Gamma\left(\begin{matrix}2-\varepsilon, 1-2\varepsilon-2k\\ 1-\varepsilon-k, 2-2\varepsilon-k\end{matrix}\right) {}_2F_1\left(\begin{matrix}1+k, \varepsilon+k\\ 2\varepsilon+2k\end{matrix}; -r(2+r)\right)\right.\\ &\left. + [-r(2+r)]^{1-2\varepsilon-2k}\, \Gamma\left(\begin{matrix}2-\varepsilon, 2\varepsilon+2k\\ 1+k, \varepsilon+k\end{matrix}\right)\right. \end{aligned}$$

$$\times {}_2F_1\left(\begin{smallmatrix}1-\varepsilon-k,2-2\varepsilon-k\\2-2\varepsilon-2k\end{smallmatrix};-r(2+r)\right)\Bigg\}$$
$$-\Gamma(-1+\varepsilon)\Gamma(1-\varepsilon)\Gamma(-1+2\varepsilon)$$
$$\times\sum_{k=0}^{\infty}(-1+2\varepsilon)_k\frac{r^{2k}}{k!}$$
$$\times\Bigg\{\Gamma\left(\begin{smallmatrix}2-\varepsilon,3-4\varepsilon-2k\\3-3\varepsilon-k,2-2\varepsilon-k\end{smallmatrix}\right){}_2F_1\left(\begin{smallmatrix}-1+2\varepsilon+k,\varepsilon+k\\2\varepsilon+2k\end{smallmatrix};-r(2+r)\right)$$
$$+[-r(2+r)]^{3-4\varepsilon-2k}\,\Gamma\left(\begin{smallmatrix}2-\varepsilon,-3+4\varepsilon+2k\\-1+2\varepsilon+k,\varepsilon+k\end{smallmatrix}\right)$$
$$\times {}_2F_1\left(\begin{smallmatrix}3-3\varepsilon-k,2-2\varepsilon-k\\4-4\varepsilon-2k\end{smallmatrix};-r(2+r)\right)\Bigg\}.$$

The first and third terms in (A.3) can be easily expanded since the series in k and the ${}_2F_1$ series can be truncated at the given order. In the second and fourth terms, we can still truncate the ${}_2F_1$ series; however, we cannot truncate the sum over k because of the factor $[-r(2+r)]^{-2k}$. Thus, we have to resum the whole k sum. Thus, in order $O(r^3)$, we have for the second term

$$\frac{(-r)^{-2\varepsilon}(+r)^{-2\varepsilon}}{2\sqrt{\pi}}\Gamma(2-\varepsilon)\Gamma^2(-1+\varepsilon)$$
$$\times\Gamma(-1/2+\varepsilon){}_2F_1\left(\begin{smallmatrix}3-3\varepsilon-k,2-2\varepsilon-k\\4-4\varepsilon-2k\end{smallmatrix};1\right)$$

and for the fourth term

$$\frac{(-r)^{-4\varepsilon}}{2\sqrt{\pi}\Gamma(\varepsilon)}\Gamma(2-\varepsilon)\Gamma^2(1-\varepsilon)\Gamma(-1+\varepsilon)$$
$$\times\Gamma(-3/2+2\varepsilon)\Gamma(-1+2\varepsilon){}_2F_1\left(\begin{smallmatrix}3-3\varepsilon-k,2-2\varepsilon-k\\4-4\varepsilon-2k\end{smallmatrix};1\right).$$

Each of these two terms has an imaginary part, but it cancels in the sum of the two. Adding contributions from the first and third terms of (A.3) and expanding in ε, we get the $O(r^3)$ term of formula (17).

REFERENCES

1. O. V. Tarasov, Nucl. Phys. B **502**, 455 (1997).
2. A. I. Davydychev and V. A. Smirnov, Nucl. Phys. B **554**, 391 (1999).
3. F. Jegerlehner, M. Y. Kalmykov, and O. Veretin, Nucl. Phys. B **641**, 285 (2002).
4. V. A. Smirnov, Phys. Lett. B **394**, 205 (1997).
5. V. A. Smirnov, in *Progress in Physics* (Birkhäuser Verlag, Basel, 1991), Vol. 14, p. 1; *Applied Asymptotic Expansions in Momenta and Masses* (Springer-Verlag, Berlin, 2002).
6. F. V. Tkachov, Phys. Lett. B **100B**, 65 (1981); K. G. Chetyrkin and F. V. Tkachov, Nucl. Phys. B **192**, 159 (1981).
7. F. A. Berends, M. Buza, M. Bohm, and R. Scharf, Z. Phys. C **63**, 227 (1994).
8. F. A. Berends, A. I. Davydychev, and N. I. Ussyukina, Phys. Lett. B **426**, 95 (1998).
9. A. V. Kotikov, Phys. Lett. B **254**, 158 (1991); **259**, 314 (1991); **267**, 123 (1991).
10. D. J. Broadhurst, J. Fleischer, and O. V. Tarasov, Z. Phys. C **60**, 287 (1993).
11. M. Caffo, H. Czyz, S. Laporta, and E. Remiddi, Nuovo Cimento A **111**, 365 (1998).
12. H. Czyz, A. Grzelinska, and R. Zabawa, Phys. Lett. B **538**, 52 (2002).
13. A. I. Davydychev and A. G. Grozin, Phys. Rev. D **59**, 054023 (1999).
14. L. V. Avdeev and M. Yu. Kalmykov, Nucl. Phys. B **502**, 419 (1997).
15. J. Franzkowski and J. B. Tausk, Eur. Phys. J. C **5**, 517 (1998).
16. M. Argeri, P. Mastrolia, and E. Remiddi, Nucl. Phys. B **631**, 388 (2002).
17. A. Czarnecki and V. A. Smirnov, Phys. Lett. B **394**, 211 (1997); V. A. Smirnov, Phys. Lett. B **394**, 205 (1997).
18. M. Beneke and V. A. Smirnov, Nucl. Phys. B **522**, 321 (1998).
19. V. A. Smirnov and E. R. Rakhmetov, Theor. Math. Phys. **120**, 870 (1999); **120**, 64 (1999).

Physics of Atomic Nuclei, Vol. 68, No. 8, 2005, pp. 1414–1416. Translated from Yadernaya Fizika, Vol. 68, No. 8, 2005, pp. 1470–1472.

FUTURE PUBLICATIONS

Method for Reconstructing Primary Event Parameters in a Water Cherenkov Telescope of the SuperKamiokande Type

A. M. Anokhina and V. I. Galkin

Methods for reconstructing energy, event type, and directions and vertices of electron and muon production in a water Cherenkov neutrino telescope that is similar in parameters to the SuperKamiokande setup are considered. Ultimate-resolution estimates obtained from a simulation are compared with the values declared for the SuperKamiokande.

Effect of the $a_1(1260)$ Resonance on the $\rho \to 4\pi$ and $\omega,\phi \to 5\pi$ Decay Widths

N. N. Achasov and A. A. Kozhevnikov

The contribution of the $a_1(1260)$ meson to the amplitudes of the decays $\rho(770) \to 4\pi$, $\omega(782) \to 5\pi$, and $\phi(1020) \to 5\pi$ is analyzed within the chiral model of pseudoscalar, vector, and axial-vector mesons, which is based on a generalized hidden local symmetry supplemented with terms induced by the Wess–Zumino anomaly. It is shown that the rate of these decays is enhanced upon taking into account the a_1 meson in intermediate states. For the a_1-meson mass between 1.23 GeV and $m_{a_1} = m_\rho\sqrt{2} = 1.09$ GeV, the enhancement factor falls within the interval from 1.3 to 1.9.

Prospects for Studying Penguin Decays in the LHCb Experiment

S. Ya. Barsuk, G. V. Pakhlova, and I. M. Belyaev

Investigation of loop penguin decays of charmed hadrons seems to provide a promising tool for testing the predictions of the standard model of electroweak and strong interactions and for seeking new phenomena beyond it. The possibility of studying the radiative penguin decays $B^0 \to \mathrm{K}^{0*}\gamma$, $B_s^0 \to \phi\gamma$, and $B^0 \to \omega\gamma$ and the gluonic penguin decays $B^0 \to \phi\mathrm{K}_\mathrm{S}^0$ and $B_s^0 \to \phi\phi$ in the LHCb experiment is discussed.

Diffractive Scattering of Loosely Bound Nuclei Involving Two Charged Clusters on Nuclei

V. V. Davidovsky, M. V. Evlanov, and V. K. Tartakovsky

A theory of diffractive interaction between nuclei and loosely bound nuclei featuring two charged clusters is developed with allowance for Coulomb interaction. The differential cross sections for the scattering of ^{6}Li, ^{7}Be, and ^{8}B nuclei on ^{12}C are calculated and compared with experimental data obtained recently.

Rarita–Schwinger Field: Dressing Procedure and Spin–Parity Component

A. E. Kaloshin and V. P. Lomov

A general form of the total nonrenormalized propagator for a massive Rarita–Schwinger field is obtained with allowance for all spin components. The dressing of two opposite-parity Dirac fermions in the presence of mutual transitions is the closest analogy of dressing in the ($s = 1/2$) sector of the Rarita–Schwinger field. A calculation of self-energy contributions confirms that the Rarita–Schwinger field involves, in addition to the leading spin of $s = 3/2$, two opposite-parity components of spin $s = 1/2$ parity.

Effects of Scalar (Pseudoscalar) Higgs Boson in the Process $e^+e^- \to b\bar{b}\nu\bar{\nu}$ at LEP II

A. A. Likhoded and A. E. Chalov

The possibility of imposing constraints on the couplings of the scalar (pseudoscalar) Higgs boson to b quarks by using data on the process $e^+e^- \to b\bar{b}\nu\bar{\nu}$ at the LEP II collider is considered. The effect of mixing of the scalar and a new hypothetical pseudoscalar state of the Higgs boson at the $Hb\bar{b}$ vertex is parametrized

1063-7788/05/6808-1414$26.00

as $\frac{m_b}{v}(a + i\gamma_5 b)$. In analyzing differential distributions for the process $e^+e^- \to b\bar{b}\nu\bar{\nu}$, the contribution of the fusion subprocess $WW \to H$ in the channel involving an electron neutrino is of importance, this contribution enhancing the sensitivity of data to the parameters under analysis. It is shown that data from the LEP II collider ($\sqrt{s} = 200$ GeV and $\int \mathcal{L}dt = 600$ pb^{-1}/experiment) would make it possible to constrain the parameters $\Delta a = a - 1$ and b at the level of $-0.75 \leq \Delta a \leq 1.4$ for the case of $b = 0$ and free Δa and at the level of $-0.97 \leq b \leq 0.97$ for the case of $\Delta a = 0$ and free b.

Gradient in the Distribution of Ultrahigh-Energy Particles

A. A. Mikhailov

Twenty-one pulsars from whose direction fluxes of ultrahigh-energy particles are enhanced within a narrow solid angle are discovered. An analysis of the directions of particle arrival from these pulsars shows that there are gradients in the particle distribution, their centers being coincident with the location of these pulsars. The problem of the origin of ultrahigh-energy cosmic rays is discussed.

Differential Analyzing Power in pp' Scattering on ^{28}Si Nuclei That Is Accompanied by the Excitation of High-Spin Particle–Hole States

A. V. Plavko and M. S. Onegin

The experimental energy dependence of the differential analyzing power is presented for the 5_1^-, $T = 0$ and 6_1^-, $T = 1$ nuclear levels and is contrasted against the results of calculations based on the DWBA-91 code. Information obtained for the nuclear structure from the analysis of inelastic scattering is discussed.

On the Generation of Hadronic Resonances in Heavy-Ion Collisions

I. I. Roizen

The problem of the role of microscopic kinetics in the production of short-lived (broad) hadronic resonances from subhadronic nuclear matter is discussed. A new approach to calculating the multiplicities of broad meson resonances that takes explicitly into account the possibility that massive constituent quarks play a key role at the last stage of the expansion and cooling of matter formed in central interactions of relativistic heavy ions is proposed. The resulting theoretical estimates are compared with known experimental data, and some quantitative and qualitative predictions are made.

Quantum Non-Markov Langevin Equations and Transport Coefficients

V. V. Sargsyan, Z. Kanokov, G. G. Adamian, and N. V. Antonenko

Quantum diffusion equations involving transport coefficients depending explicitly on time are derived from generalized non-Markov Langevin equations. Generalized fluctuation–dissipation relations and analytic formulas for calculating the friction and diffusion coefficients in nuclear processes are obtained. The asymptotic behavior of the transport coefficients and of the correlation functions is studied for a damped harmonic oscillator that is linearly related in momentum with a heat bath. The momentum relation with a heat bath is responsible for the emergence of the diffusion coefficient in the coordinate. The weakening of correlations in quantum dissipative systems is investigated.

Features of the Absorption of 2- to 40-TeV Cosmic-Ray Hadrons in Lead

L. G. Sveshnikova, V. I. Yakovlev, A. N. Turundaevsky, V. I. Galkin, S. I. Nazarov, D. M. Podorozhnyi, N. S. Popova, and T. M. Roganova

For the first time, 2- to 40-TeV hadronic cascades detected in a lead ionization calorimeter at the Tien Shan mountain research station of the Lebedev Institute of Physics are compared with modern calculations performed on the basis of the GEANT 3.21 package with allowance for the detection method. Earlier, these experimental data made it possible to conclude that a long-range component appeared in high-energy hadronic cascades. Methodological features of hadron detection in the calorimeter are investigated at TeV energies. It

is shown that both average hadronic cascades and various features of individual $E < 10$ TeV cascades are well described by calculations employing the QGSJET + FLUKA generators of nuclear interactions, but that they are not described if use is made of the GHEISHA generator at low energies. All details of experimental cascades whose energy is above 10 TeV could not be described.

Value of B_K from Experimental Data on the *CP* Violation in *K* Mesons and Up-to-Date Values of the CKM-Matrix Parameters

E. A. Andriyash, G. G. Ovanesyan, and M. I. Vysotsky

The difference between the quantity $\tilde{\epsilon}$ induced by the box diagram and the experimentally measured value of ϵ is determined and used to obtain the value of $\tilde{\epsilon}$ with a high precision. Present-day knowledge of the CKM-matrix elements (including B-factory data) enables us to obtain the value of the parameter B_K from the Standard Model expression for $\tilde{\epsilon}$: $B_K = 0.89 \pm 0.16$. It proves to be very close to the vacuum-insertion result, $B_K = 1$.

K-Matrix Approach to the Δ-Resonance Mass Splitting and Isospin Violation in Low-Energy πN Scattering

A. B. Gridnev, I. Horn, W. J. Briscoe, and I. I. Strakovsky

Experimental data on πN scattering in the elastic energy region, $T_\pi \leq 250$ MeV, are analyzed within the multichannel K-matrix approach with effective Lagrangians. Isospin invariance is not assumed in this analysis, and the physical values for masses of the particles involved are used. The corrections due to $\pi^+ - \pi^0$ and $p - n$ mass differences are calculated and found to be in reasonable agreement with NORDITA results. An analysis shows that the description of all experimental observables is good. From the data, new values for the masses and widths of the Δ^0 and Δ^{++} resonances were obtained. The isospin-symmetric version gives phase-shifts values close to the new solution for the πN elastic-scattering amplitude FA02 by the GW group on the basis of the latest experimental data. While our analysis leads to a considerably smaller ($\leq 1\%$) isospin violation in the energy interval $T_\pi \sim 30-70$ MeV as compared to 7% in the studies of W.R. Gibbs *et al.* and E. Matsinos, it confirms calculations based on chiral perturbation theory.

On the Basic Properties of the $A = 48$ Isobars

V. I. Isakov and Yu. N. Novikov

The binding energies of the $A = 48$ isobars and their charge radii are determined on the basis of self-consistent calculations and the concept of nuclear isobaric symmetry.

Experimental Data on Single-Spin Asymmetry and their Interpretations within the Chromomagnetic String Model

S. B. Nurushev and M. G. Ryskin

An attempt is made to interpret various existing experimental data on single-spin asymmetries in inclusive pion production by polarized proton and antiproton beams. The chromomagnetic string model is used as a basis for this analysis. The entire measured kinematic region is covered. The successes and failures of such an approach are outlined. The possible improvements of the model are discussed.

Constraints on Narrow Exotic States from Data on K^+p and $K^0_L p$ Scattering

R. L. Workman, R. A. Arndt, I. I. Strakovsky, D. M. Manley, and J. Tulpan

The effect of exotic $S = +1$ resonances Θ^+ and Θ^{++} on data on elastic K^+p scattering (total cross section) and the process $K^0_L p \to K^0_S p$ is considered. Data near the observed $\Theta^+(1540)$ resonance are examined for evidence of additional states. The width limit for a Θ^{++} state is reconsidered.